Parallel Relativistic Multiconfiguration Methods: New Powerful Tools for Heavy-Element Electronic-Structure Studies

---

Inaugural-Dissertation

zur

Erlangung des Doktorgrades der

Mathematisch-Naturwissenschaftlichen Fakultät

der Heinrich-Heine-Universität Düsseldorf

vorgelegt von

Stefan Knecht

aus Würzburg

Düsseldorf 2009

Aus dem Institut für Theoretische Chemie und Computerchemie
der Heinrich-Heine-Universität Düsseldorf

Gedruckt mit der Genehmigung der
Mathematisch-Naturwissenschaftlichen Fakultät
der Heinrich-Heine-Universität Düsseldorf

Externer Referent: Prof. Dr. Timo Fleig
Korreferentin: Prof. Dr. Christel M. Marian
Externer Referent: Prof. Dr. Lucas Visscher

Tag der mündlichen Prüfung: 29.10.2009

Little by little, one travels far.

J. R. R. Tolkien

Acknowledgment - Vielen Dank ...

... meinem Doktorvater Timo Fleig für die Möglichkeit dieses spannende Thema bearbeiten zu können, für die immerwährende Diskussionsbereitschaft, die bereitwilligen Erklärungen und nicht zuletzt die vermittelte Begeisterung für die Forschung an der Grenze von Chemie, Physik und Informatik.

... Christel M. Marian für die Zweitbetreuung dieser Arbeit, für die großartige Unterstützung vor allem im letzten Jahr und in den letzten Tagen dieser Arbeit sowie für die Einführung in die "chemische Sicht" allzu theoretischer Ergebnisse.

... Hans Jørgen Aagaard Jensen for inviting me to work with you in Odense many many times, for the great time as your Nanoquant student, for the patient introduction to the `DIRAC` code, for many fruitful discussions, for teaching me programming, for the great support from near and far, for your encouragement and hospitality!

... Lasse Kragh Sørensen für die großartige und unermüdliche Unterstützung während den letzten Tagen vor Abgabe dieser Arbeit, für die tolle wissenschaftliche Zusammenarbeit und für die vielen aufschlussreichen Diskussionen in den letzten vier Jahren. Ich danke Dir für Deine große Hilfsbereitschaft auch über das Fachliche hinaus! Du bist ein toller Zimmerkollege!

... Susanne Salzmann, für die große Hilfsbereitschaft zu allen Zeiten und Unzeiten und die leckere Versorgung mit "Notrationen".

... Emmanuel Fromager, for the great times we had together in Odense, for the nice discussions and for the table soccer sessions. I hope, we can continue on that soon...

... Martin Kleinschmidt, für Deine tolle Unterstützung bei kleinen und großen Computerprobemen, für Dein bereitwilliges Korrekturlesen und die vielen spaßigen Kickerspiele.

... Jörg Tatchen, für die vielen aufschlussreichen Diskussionen, netten Abendessen"sessions" und für Deine tollen Tipps zur Gestaltung meiner Bilder in dieser Arbeit.

... Stephan Raub, was soll ich sagen, ohne Deine unermüdliche Unterstützung als Technik-Support wäre diese Arbeit nur halb so dick, hat der Rechencluster GAUSS doch seine ganz eigenen Gesetze.

... Mihajlo Etinski für Deine immerwährende Bereitschaft für ein Kicker-Spiel!

... an die gesamte Gruppe der Theoretischen Chemie für die ganz besondere, freundschaftliche Arbeitsatmosphäre.

... the whole `DIRAC` family for making the annual meeting in Odense such a nice event

and your patience with my past, present, and future bugs in the code!
... meinen Freunden Markus, Christoph, Flo, Wolle, Mirko, Niko, Mathias, Marc und der ganzen Oustem Gang für die tollen Wander- und Segelurlaube. Ich hoffe, ich werde in Zukunft wieder mehr Zeit mit Euch verbringen können.
... Caesar Monauni, wir kennen uns zwar noch nicht, aber Dein Lachen hat mich ermuntert, weiterzuschreiben, wenn ich schon nicht mehr wollte...

... Susanne, weil ich ohne Dich nicht wäre, wo ich jetzt bin! Ich danke Dir für Deine unermüdliche Geduld mit mir und hoffe, wir finden jetzt wieder mehr Zeit füreinander...
... meiner Familie für die jahrelange Unterstützung, die liebevollen Carepakete. Eure uneingeschränkte Unterstützung und Euer Vertrauen in meine Fähigkeiten haben es mir ermöglicht, meinen eigenen Weg zu gehen und meine Träume zu verwirklichen.

Hiermit versichere ich, die hier vorgelegte Arbeit eigenständig und ohne unerlaubte Hilfe angefertigt zu haben. Die Dissertation wurde in der vorgelegten oder in ähnlicher Form noch bei keiner Institution eingereicht. Ich habe keine erfolglosen Promotionsversuche unternommen.

Düsseldorf, den

(Stefan Knecht)

List of papers included in the thesis

- **Paper 1**

  Large-scale parallel configuration interaction. I. Non-relativistic and scalar-relativistic general active space implementation with application to (Rb-Ba)$^+$.

  Stefan Knecht, Hans Jørgen Aagaard Jensen, and Timo Fleig, *J. Chem. Phys.*, **128** (2008) 014108.

  All calculations and the major part of the discussion and conclusion regarding the implementation and application of the parallel algorithm were provided by me. I contributed all (RbBa)$^+$ calculations and large parts of the discussion and conclusion.

- **Paper 2**

  Large-scale parallel configuration interaction. II. Two- and four-component double-group general active space implementation with application to BiH.

  Stefan Knecht, Hans Jørgen Aagaard Jensen, and Timo Fleig, *submitted to J. Chem. Phys.*.

  For this paper, I contributed all calculations in the implementation and application part. The discussion and conclusions for both the parallel implementation and application section concerning BiH were provided by me.

- **Paper 3**

  Four-component relativistic coupled cluster and configuration interaction calculations on the ground and excited states of the RbYb molecule.

  Lasse Kragh Sørensen, **Stefan Knecht**, Timo Fleig, and Christel M. Marian, *J. Phys. Chem.* **A**, Publication Date (Web): August 18, 2009, DOI: 10.1021/jp904914m.

  All CI calculations were provided by me. I contributed to the discussion of the photoassociation process and conclusions regarding the envisaged experiments.

- **Paper 4**

  The electronic structure of the triiodide ion from relativistic correlated calculations: A comparison of different methodologies.

  André Severo Pereira Gomes, Lucas Visscher, Hélène Bolvin, Trond Saue, **Stefan Knecht**, Timo Fleig, and Ephraim Eliav, *unpublished manuscript*.

The focus of this paper clearly lies on a comparison of different methodologies. My contributions comprise the CI calculations of I_3^- and I_3 and to a minor degree parts of the discussion and conclusions.

- **Paper 5**

  Four-component relativistic configuration interaction and coupled cluster calculations on the ground and excited states of the $(RbBa)^+$ molecule.

  Stefan Knecht, Lasse Kragh Sørensen, Hans Jørgen Aagaard Jensen, Timo Fleig, and Christel M. Marian, *submitted to J. Phys.* **B***: At. Mol. Opt. Phys.*.

  All CI calculations were provided by me. I contributed to the discussion of a non-radiative charge-transfer process and to the conclusions regarding the envisaged experiments.

Paper not included in the thesis

- **Paper 6**

  Quantum-chemical investigation of the structures and electronic spectra of the nucleic acid bases at the coupled cluster CC2 level.

  Timo Fleig, **Stefan Knecht**, and Christoph Hättig, *J. Phys. Chem.* **A**, **111** (2007) 5482.

Zusammenfassung

Im Zentrum dieser Arbeit steht die Entwicklung paralleler Algorithmen für relativistische Elektronenstrukturmethoden sowie deren Anwendung auf schwere Atome und kleine Moleküle mit schweren Elementen. Die Parallelisierungsarbeiten konzentrierten sich insbesondere auf das Verfahren der Konfigurationswechselwirkung (CI) und des Multiconfiguration-Self-Consistent-Field (MCSCF). Im Falle der erstgenannten Methode wurde im Zuge dieser Doktorarbeit eine parallele Implementierung des im Programmpaket `DIRAC` zur Verfügung stehenden relativistischen spinfreien (`LUCITA`) Algorithmus, d.h. ohne Einbezug der Spin-Bahn Wechselwirkung, als auch des voll relativistischen (`LUCIAREL`) Algorithmus realisiert. Für das voll relativistische MCSCF-Verfahren wurde eine Parallelisierung der wesentlichen Bestandteile, die auf Routinen des CI-Verfahrens zurückgehen, durchgeführt. Die Entwicklung der parallelen Algorithmen orientierte sich an den Maximen der Rechnerarchitektur- und Problemgrößenunabhängigkeit. Die erfolgreiche Umsetzung dieser Anforderungen konnte durch vergleichende Studien variabler Problemgrößen auf einem lokalen Rechencluster sowie auf dem Großrechner `JUMP` gezeigt werden. Mit den parallelisierten Programmen konnte ein nahezu optimaler Speedup erreicht werden. Der Zusammenhang zwischen Prozessoranzahl und Speedup verläuft über einen weiten Bereich linear (siehe Abbildung).

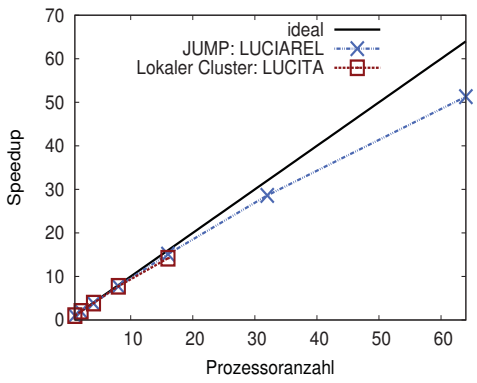

Abbildung: Exemplarischer Datensatz zur Illustration des mit der Parallelisierung erzielten Speedups.

Darüberhinaus wurde ein paralleles Programm auf der Basis der CI-Methode entwickelt, das einen einfachen Zugang zur Berechnung elektrischer und magnetischer Eigenschaften von Atomen und Molekülen bietet. Zudem ermöglicht es eine eindeutige Charakterisierung elektronischer Zustände im Rahmen spinorbasierter Methoden.

Die in dieser Arbeit vorgestellten Anwendungen befassen sich mit der genauen Ermittlung spektroskopischer Eigenschaften kleiner Moleküle mit schweren Elementen und schwerer Atome in ihren Grund- und elektronisch angeregten Zuständen. Hierbei wurde durch den Einsatz der parallelen relativistischen CI und MCSCF Methoden im Zusammenspiel mit großen, unkontrahierten Basissätzen und unter Anwendung des Konzeptes der generalisierten Räume (GAS) eine sehr hohe Genauigkeit erreicht. Im Fall des BiH Moleküls konnte eindrucksvoll demonstriert werden, dass eine simultane Behandlung der Elektronenkorrelation und Spin-Bahn Wechselwirkung unverzichtbar ist, um eine dem Experiment nahekommende Spin-Bahn Aufspaltung zwischen Grund- und erstem angeregten Zustand zu berechnen. Ein umfassender Vergleich verschiedener relativistischer Elektronenkorrelationsmethoden am Beispiel des I_3^- Anions und des I_3 Radikals zeigte, dass mit der parallelen voll relativistischen GASCI Methode eine Genauigkeit in der Berechnung der Elektronenstrukur und elektronischer Anregungsspektren der anionischen sowie der radikalischen Spezies erzielt werden kann, die an diejenige einer Multireferenz-Coupled Cluster Methode heranreicht. Auf der Basis hochgenauer CI-Potentialkurven und daraus abgeleiteter vibronischer Spektren konnte für das RbYb Molekül ein verbessertes Lasergetriebenes Zwei-Schritt Schema zur experimentellen Präparation des Moleküls in seinem rovibronischen Grundzustand ausgehend von ultrakalten Rb und Yb Atomen aufgestellt werden. In den Arbeiten am molekularen Kation $(RbBa)^+$ wurde der Einfluss energetisch niedrigliegender Ba $6s^15d^1$ Zustände auf einen möglichen Ladungstransfermechanismus unter Beteiligung strahlungsloser Prozesse in Stoßexperimenten ultrakalter Rb Atome und Ba^+ Ionen herausgestrichen. In ausführlichen GASCI-Studien am Th Atom konnten zwei Faktoren, welche notwendig sind für eine hochgenaue theoretische Beschreibung der niedrigsten elektronischen Zustände, identifiziert werden. Diese waren die Korrelation der äußeren "core" Elektronen sowie die Erweiterung des Referenzraumes um Konfigurationen mit Besetzung der $7p$ Schale. Das Bindungsbild des Urandimers U_2 wurde anhand von qualitativen relativistischen MCSCF Einzelpunktrechnungen untersucht und potentielle Grundzustandskonfigurationen wurden vorgestellt.

Summary

The development of parallel algorithms for relativistic electronic-structure theory methods and their application to heavy atoms and small molecular systems containing heavy elements is at the center of this work. The focus of the parallelization work has been put in particular on configuration interaction (CI) and multiconfiguration self-consistent-field (MCSCF) methods. In the course of this dissertation, parallel implementations have been completed for the relativistic spin-free CI code (`LUCITA`), where spin-orbit interaction is not taken into account, as well as for the fully relativistic CI code (`LUCIAREL`) which both are available in the `DIRAC` program package. In addition, the essential inner parts of the relativistic MCSCF implementation which are directly connected to CI contributions, have been parallelized. The development of the parallel algorithms thereby acted on the maxims of independence from the system architecture and problem sizes. These conditions have been successfully fulfilled in the current implementations as was shown for studies of varying complexity on both a local computer cluster and on the supercomputer `JUMP`. The speedup was found to be close to optimal as indicated by the almost linear increase of the speedup with an increasing number of processors (see Figure).

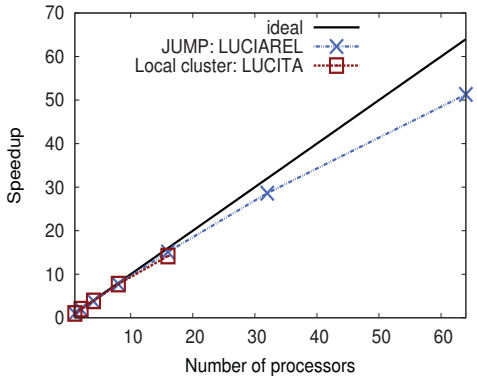

Abbildung: Speedup curves for the parallel implementations based on a sample data set.

Moreover, a parallel program has been developed that offers a computationally simple approach to calculate electric and magnetic properties of atoms and molecules at the

CI level of theory. In addition, it allows to unambiguously identify electronic states in the framework of spinor-based methods.

The applications presented in this thesis are concerned with an accurate determination of ground- and excited-state spectroscopic properties of heavy atoms and small molecules containing heavy elements. Very high accuracy has been achieved in applying relativistic CI and MCSCF methods with extensive, uncontracted basis sets and the concept of generalized active spaces (GAS). In the case of the BiH molecule it has been demonstrated, that, in order to obtain from theoretical calculations a spin-orbit splitting between the ground and first excited state which is on the order of the experimental value, it is mandatory to treat electron correlation and spin-orbit coupling simultaneously. A comprehensive comparison of different relativistic electron correlation methods using the example of the triiodide anion and its neutral radical counterpart revealed that the parallel GASCI method is capable of treating both systems adequately in their ground and excited states. The achieved accuracy was comparable to that of a genuine multi-reference coupled cluster method. On the basis of accurate CI potential energy curves and the derived vibrational data a revised laser-driven two-step mechanism was proposed to prepare RbYb molecules in their rovibronic ground state under laboratory conditions using ultracold Rb and Yb atoms. In the studies of the molecular cation $(RbBa)^+$ it has been discussed how the energetically low-lying Ba $6s^15d^1$ states could possibly contribute to a non-radiative charge-transfer mechanism in collision experiments of ultracold Rb atoms and Ba^+ ions. Extensive GASCI studies of the Th atom allowed to identify two contributions that are necessary to obtain a highly accurate description of the lowest electronic states; namely the correlation of the outer-core electrons as well as the extension of the reference space by configurations exhibiting a $7p$ occupation. The bonding picture of the uranium diatom U_2 has been studied in a qualitative manner by means of relativistic MCSCF single-point calculations. Possible electronic configurations of the electronic ground state were presented.

Contents

Chapter 1

Introduction

The primary goal in quantum chemistry is the calculation of the electronic structure of an atomic or molecular system in its ground and electronically excited states. While the theoretical framework for a description of objects at the macroscopic scale is provided by *classical mechanics*, the characterization of systems at the microscopic scale[1] such as atoms or molecules necessitates the theory of *quantum mechanics*. In the case of light elements the electronic structure can be determined from a solution of the Schrödinger equation [2]. For heavy elements, which are in the main focus of this thesis, the premises are different: electrons moving in the vicinity of a heavy nucleus can reach velocities close to the speed of light which requires the consideration of special relativity. The theory of special relativity was developed by A. Einstein [3] in order to correctly describe the dynamics of macroscopic objects moving at very high velocities. The important breakthrough to apply special relativity also to microscopic objects was achieved by P. A. M. Dirac [4–6] who successfully combined quantum mechanics and special relativity into a new theory – *relativistic quantum mechanics* – which is at the heart of relativistic quantum chemistry.

The "contributions"[2] of relativity to the atomic structure are twofold: Scalar-relativistic and magnetic effects. Both effects grow approximately quadratic with the

[1] Following Messiah [1] "microscopic scale" is to be understood as the one of atomic phenomena. The "macroscopic scale" is the one of phenomena observable with the naked eye or simple microscopes.

[2] In principle, there are no such contributions since our world is relativistic and a finite speed of light exists: $c \approx 137.0359895$ au. Relativistic effects can therefore be understood as anything that originates from the difference between this finite value and $c = \infty$ [7].

atomic number Z. Hence, relativistic effects are much more pronounced in heavier elements but can nevertheless be important for an accurate description of molecular systems composed only of light elements. Owing to the observed mass increase of the inner electrons moving at high velocities in heavy elements, the effective radii of the s and p shells shrink. As a result, the effective nuclear potential for other electrons is more efficiently screened which self-consistently leads to an energetic destabilization and radial expansion of the d and f shells [7]. If these so-called scalar-relativistic effects are for example neglected, it is impossible to explain the yellow color of gold in comparison to silver. The color of both metals originates from electronic transitions from the $(n-1)d$ shell to the Fermi-level that mainly possesses ns character. In gold ($n = 6$, $Z = 79$), the relativistic contraction and stabilization of the $6s$ shell reaches a maximum [8] whereas the $5d$ shell is considerably destabilized. Due to these favorable stabilization/destabilization effects gold absorbs light in the blue region of the visible spectrum of light and reflects yellow. By contrast, the analogous absorption in silver ($n = 5$, $Z = 47$) takes place in the UV as a result of the weaker relativistic effects for the $4d$ and $5s$ shells, respectively [7].

The second important phenomenon described by special relativity are magnetic couplings – the most important of which is the spin-orbit interaction – occurring in heavy elements. The spin-orbit interaction arises from a coupling of the electron spin to the induced magnetic field in the inertial frame of the electron due to its orbital motion in the field of other charged particles, nuclei and other electrons. Hence, neither the spin momentum s nor the orbital angular momentum l of an electron are "good" quantum numbers, but the sum $j = s + l$ still is. Striking examples for the consequences of spin-orbit interaction are a change of the ground state in the PtH molecule [9] and the lifting of the selection rules for electronic transitions between singlet and triplet states in a given system which would be formally spin-forbidden in a non-relativistic framework.

Both my development and application work presented in this thesis are based on Dirac's relativistic quantum mechanics which is, as indicated above, the most rigorous theoretical framework to take into account all these relativistic effects. Owing to the entanglement of spin and spatial symmetries the Hamiltonian and the wave function exhibit a four-component form. This is inevitably connected with an increase of the computational demand and complexity in solving the Dirac equation compared to the non-relativistic (one-component) Schrödinger equation as Dirac himself already stated in

1929 [6]:

> *"The underlying physical laws necessary for the mathematical theory of a large part of physics and the whole of chemistry are thus completely known, and the difficulty is only that the exact application of these laws leads to equations much too complicated to be soluble. It therefore becomes desirable that approximate practical methods of applying quantum mechanics should be developed, which can lead to an explanation of the main features of complex atomic systems without too much complications."*

Since then a variety of different approximate methods to account for relativity at a pseudo-relativistic one-component (scalar) or two-component (spin-orbit) or in particular four-component level of theory have been developed and implemented in quantum chemical codes, *i.e.*, `DIRAC` [10], `MOLFDIR` [11, 12], `REL4D` [13–15] as well as several others. To obtain an accurate and reliable description of the electronic structure of heavy-element systems it is, however, essential to take into account in such approaches not only relativity but also electron correlation, preferably on the same footing. The electron correlation energy of a given system is defined as the difference between the exact energy and the Hartree-Fock energy where the electron-electron interaction is approximated by a mean field. Electron correlation can formally be divided into a dynamic and a non-dynamic (or static) correlation part. While dynamic correlation is in general related to the short-range interaction of electrons – their mutual repulsion – static correlation becomes dominant for systems exhibiting, e.g. degeneracy or near-degeneracy of electronic states. The latter case is frequently encountered for d and f elements and their compounds due to several unpaired electrons in their valence shells. An adequate description of such electronic states surpasses the single reference determinant ansatz of the Hartree-Fock model and calls for a multiconfigurational treatment in its stead. The electronic-structure methods that will be applied in this thesis allow for an appropriate account of multi-reference problems as discussed in the respective sections.

Summing up, this thesis focuses on multiconfigurational approaches to the electronic-structure problem in heavy elements and heavy-element compounds within the four-component relativistic framework where electron correlation and magnetic couplings are treated simultaneously and on the same footing. This comes with the price of having to

deal with in general complex four-component orbitals and a substantial increase of the computational cost compared to less rigorous approaches where magnetic couplings are included *a posteriori* only in the electron correlation step. The main objective of my present work will therefore be to cope with the high computational demand of the chosen relativistic quantum chemical methodologies by devising efficient and general parallel algorithms for these. By these means, it will be possible to benefit from the huge computational power of today's supercomputers and clusters of standard PC's. The reported speedup benchmarks will clearly demonstrate the great potential of the novel parallel implementations on representative computer architectures. In this context, it will also be argued why the chosen parallelization approach is superior to previous concepts of related parallel implementations. Finally, it will be highlighted how my parallel approaches can decisively contribute to gain a deeper insight into selected problems of electronic-structure theory involving heavy elements which are currently of paramount interest in molecular physics and chemistry.

Layout of this thesis

The thesis is divided into three parts:

I The first part provides a short introduction to the physical framework of relativistic quantum chemistry and to the basic concepts of the relativistic quantum chemical configuration interaction (CI) and multiconfiguration self-consistent-field (MCSCF) methods.

II In the second part, a parallel algorithm suited for the available relativistic generalized active space CI (GASCI) implementations in the `DIRAC` software package [10] is described in full detail. Furthermore, the development of a parallel CI module for the calculation of atomic and molecular properties is presented.

III The third part is devoted to the application of the parallel multiconfiguration methods to fundamental physical and chemical questions regarding heavy atoms and small molecular compounds.

Part I

Theoretical Framework

Methodology

The basis for the development work and for the applications presented in this thesis are quantum chemistry methods in a relativistic four-component framework. The purpose of the following chapter is to acquaint the general reader with the basics of relativistic electronic structure theory and its implications for correlation methods. This introduction is certainly not intended to be exhaustive and for a detailed overview of the field of relativistic quantum chemistry the reader may refer to recent standard textbooks [16, 17]. The second chapter provides a short survey of the relativistic configuration interaction (CI) and multiconfiguration self-consistent-field (MCSCF) methods for which parallel algorithms were developed in this thesis.

Chapter 2

Relativistic Theory

This chapter will provide the basic framework for a discussion of important aspects of the relativistic CI and MCSCF methods and their application to electronic structure studies of atomic and molecular heavy-element systems. The starting point for a relativistic quantum mechanical description of an atomic or molecular system is the time-dependent Dirac equation, given here in its Hamiltonian form[1],

$$\hat{\mathcal{H}}\mathbf{\Psi}(\mathbf{r},t) = i\hbar\frac{\partial}{\partial t}\mathbf{\Psi}(\mathbf{r},t). \tag{2.1}$$

In typical quantum chemical calculations, however, stationary states are most often sought for, that is the eigenfunctions of a time-independent Hamiltonian. In these cases $\hat{\mathcal{H}}$ and the total energy E of the system are constants of the motion and Eq. (2.1) simplifies to,

$$\hat{\mathcal{H}}\Psi(\mathbf{r}) = E\Psi(\mathbf{r}), \tag{2.2}$$

and the wave function $\mathbf{\Psi}(\mathbf{r},t) = \Psi(\mathbf{r})\Phi(t)$ splits into a spatial part $\Psi(\mathbf{r})$ and a temporal part $\Phi(t)$ that is given by,

$$\Phi(t) = e^{Et/i\hbar}. \tag{2.3}$$

Moreover, focusing on solutions of the electronic structure of a molecular system it is convenient to work in the Born-Oppenheimer frame. In the Born-Oppenheimer approximation [18] it is assumed that the electrons follow the motion of the much heavier nuclei instantaneously such that the motion of the electrons and the nuclei may be treated separately. This implies a separation of the wave function $\Psi(\mathbf{r})$ into a nuclear part and an

[1]The above given form is equivalent to the covariant form of the Dirac equation.

electronic part which depends parametrically on the nuclear coordinates,

$$\Psi(\mathbf{r}) = \Theta(\mathbf{R})\Psi(\mathbf{r}';\mathbf{R}). \tag{2.4}$$

The set of solutions $\Psi(\mathbf{r}';\mathbf{R})$[2] obtained for fixed nuclei allows for the construction of potential energy curves (diatomic molecules) and potential energy surfaces (polyatomic molecules), respectively.

Up to now the Hamiltonian in Eq. (2.2) has not been further specified. In the following section a selection of four-component scalar-relativistic and relativistic Hamiltonians will be presented which were made use of in this thesis. In Section 2.2 the account for symmetry in a relativistic framework is briefly discussed. The chapter closes with considerations regarding a proper choice of basis sets in relativistic four-component calculations.

2.1 Hamiltonian Operators

Within the Born-Oppenheimer approximation a (non-)relativistic atomic or molecular Hamiltonian takes the form

$$\hat{\mathcal{H}} = \sum_i \hat{h}(i) + \frac{1}{2}\sum_{i\neq j} \hat{g}_{ij} + V_{NN} \tag{2.5}$$

where V_{NN} is the classical repulsion of the clamped nuclei, and $\hat{h}$ and $\hat{g}$ are one- and two-electron operators. The decision of working in a relativistic four-component framework therefore depends on the choice of $\hat{h}$ and $\hat{g}$ which will be covered below.

2.1.1 Four-Component Relativistic Hamiltonian

The cornerstone for a four-component relativistic theory is the free-particle Dirac operator[3] [4, 5],

$$\hat{h}_D^{free} = c(\boldsymbol{\alpha}\cdot\mathbf{p}) + \beta mc^2, \tag{2.6}$$

[2] For simplicity, the electronic wave function will hereafter be referred to as $\Psi(\mathbf{r})$.

[3] Here, the time-independent operator is given.

where $\mathbf{p}$ denotes the canonical momentum operator, c is the speed of light and m refers to the particle rest mass. Moreover, $\boldsymbol{\alpha} = (\alpha_x, \alpha_y, \alpha_z)$ and β are the 4×4 Dirac matrices,

$$\begin{aligned}
\alpha_x &= \begin{pmatrix} 0 & 0 & 0 & 1 \\ 0 & 0 & 1 & 0 \\ 0 & 1 & 0 & 0 \\ 1 & 0 & 0 & 0 \end{pmatrix} = \begin{pmatrix} \mathbf{0}_{2\times2} & \boldsymbol{\sigma}_x \\ \boldsymbol{\sigma}_x & \mathbf{0}_{2\times2} \end{pmatrix} \\
\alpha_y &= \begin{pmatrix} 0 & 0 & 0 & -i \\ 0 & 0 & i & 0 \\ 0 & -i & 0 & 0 \\ i & 0 & 0 & 0 \end{pmatrix} = \begin{pmatrix} \mathbf{0}_{2\times2} & \boldsymbol{\sigma}_y \\ \boldsymbol{\sigma}_y & \mathbf{0}_{2\times2} \end{pmatrix} \\
\alpha_z &= \begin{pmatrix} 0 & 0 & 1 & 0 \\ 0 & 0 & 0 & -1 \\ 1 & 0 & 0 & 0 \\ 0 & -1 & 0 & 0 \end{pmatrix} = \begin{pmatrix} \mathbf{0}_{2\times2} & \boldsymbol{\sigma}_z \\ \boldsymbol{\sigma}_z & \mathbf{0}_{2\times2} \end{pmatrix} \\
\beta &= \begin{pmatrix} 1 & 0 & 0 & 0 \\ 0 & 1 & 0 & 0 \\ 0 & 0 & -1 & 0 \\ 0 & 0 & 0 & -1 \end{pmatrix} = \begin{pmatrix} \mathbf{I}_{2\times2} & \mathbf{0}_{2\times2} \\ \mathbf{0}_{2\times2} & -\mathbf{I}_{2\times2} \end{pmatrix},
\end{aligned} \tag{2.7}$$

$\boldsymbol{\sigma}_x, \boldsymbol{\sigma}_y$ and $\boldsymbol{\sigma}_z$ are the Pauli spin matrices,

$$\boldsymbol{\sigma}_x = \begin{pmatrix} 0 & 1 \\ 1 & 0 \end{pmatrix}; \quad \boldsymbol{\sigma}_y = \begin{pmatrix} 0 & -i \\ i & 0 \end{pmatrix}; \quad \boldsymbol{\sigma}_z = \begin{pmatrix} 1 & 0 \\ 0 & -1 \end{pmatrix}, \tag{2.8}$$

and $\mathbf{0}_{2\times2}$ and $\mathbf{I}_{2\times2}$ are 2×2 zero and unity matrices, respectively. In order to facilitate comparisons with non-relativistic energies, it is common to subtract the constant rest-mass energy, *i.e.*, replacing β with $\beta' = \beta - \mathbf{I}_{4\times4}$. The 4×4 matrix form of the operator suggests that the associated wave function $\Psi(\mathbf{r})$ must be a four-component vector,

$$\Psi(\mathbf{r}) = \begin{pmatrix} \psi_1(\mathbf{r}) \\ \psi_2(\mathbf{r}) \\ \psi_3(\mathbf{r}) \\ \psi_4(\mathbf{r}) \end{pmatrix} = \begin{pmatrix} \psi^L(\mathbf{r}) \\ \psi^S(\mathbf{r}) \end{pmatrix}, \tag{2.9}$$

which can also be expressed using bi-spinors for the *large* (L) and *small* (S) component,

$$\psi^L = \begin{pmatrix} \psi^1(\mathbf{r}) \\ \psi^2(\mathbf{r}) \end{pmatrix} \quad \text{and} \quad \psi^S = \begin{pmatrix} \psi^3(\mathbf{r}) \\ \psi^4(\mathbf{r}) \end{pmatrix}. \tag{2.10}$$

The notion *large* and *small* component is related to their magnitude for the positive and negative energy solutions of the free-particle Dirac equation [16].

To be able to describe electrons bound in molecules by electromagnetic forces, it is essential to introduce external scalar (ϕ) and vector ($\mathbf{A}$) potentials in the free-particle Hamiltonian (Eq. (2.6)). To this end, the principle of minimal electromagnetic coupling [19] is applied,

$$\begin{aligned} \mathbf{p} &\rightarrow \mathbf{p} - q\mathbf{A} \\ E &\rightarrow E + q\phi, \end{aligned} \tag{2.11}$$

where q is the charge of the particle which must be specified explicitly [20]. For an electron this charge is $q = -e$ and the resulting one-electron Dirac Hamiltonian reads as,

$$\hat{h}'_D = c(\boldsymbol{\alpha} \cdot \mathbf{p}) + \beta' mc^2 + ec(\boldsymbol{\alpha} \cdot \mathbf{A}) - e\phi. \tag{2.12}$$

In a static potential, *e.g.* , the nuclear potential[4] $\hat{V}^{nuc} = \sum_{A=1}^{M} \hat{V}_A^{nuc}(\mathbf{r}_A)$ arising from the M clamped nuclei in the Born-Oppenheimer frame, where the vector potential $\mathbf{A}$ is zero the one-electron Dirac Hamiltonian simplifies to,

$$\hat{h}_D = c(\boldsymbol{\alpha} \cdot \mathbf{p}) + \beta' mc^2 + \hat{V}^{nuc}. \tag{2.13}$$

The Dirac Hamiltonian $\hat{h}_D$ in its above given form constitutes the natural choice as one-electron operator $\hat{h}$ (see Eq. (2.5)) for four-component relativistic calculations.

The treatment of electron-electron interaction in a many-electron system requires a two-electron operator. At present, the most elaborate two-particle operator for quantum chemical calculations is the so-called Coulomb-Breit operator [22][5] which, in the zero-

[4] A finite radial distribution of the nuclear charge is employed in general to avoid the problem of singularities at the nuclear center. It is of particular importance for calculations using Gaussian-type basis set expansions [16, 21].

[5] This operator nevertheless represents an approximation to a (not yet derived) Lorentz invariant two-electron operator within the framework of quantum electrodynamics (QED). The Coulomb-Breit operator is correct to $\mathcal{O}(\alpha^2)$ with $\alpha = \frac{1}{c}$ being the fine structure constant.

frequency limit, reads as,

$$\begin{aligned}\hat{g}_{ij}^{Breit} &= \hat{g}_{ij}^{Coulomb} + \hat{g}_{ij}^{Gaunt} + \hat{g}_{ij}^{gauge} \\ &= \frac{\mathbf{I}_{4\times4} \otimes \mathbf{I}_{4\times4}}{r_{ij}} - \frac{(c\boldsymbol{\alpha}_i)\cdot(c\boldsymbol{\alpha}_j)}{c^2 r_{ij}} - \frac{(c\boldsymbol{\alpha}_i\cdot\nabla_i)(c\boldsymbol{\alpha}_j\cdot\nabla_j)r_{ij}}{2c^2}. \end{aligned} \tag{2.14}$$

The Coulomb-Breit operator is composed of three terms, the non-relativistic Coulomb operator, the Gaunt or magnetic term [23, 24] and a gauge term that originates from the choice of the Coulomb gauge[6]. Due to the occurrence of integrals other than $\frac{1}{r_{ij}}$ in the gauge term, it is often neglected. Moreover, it can be shown that the Coulomb operator $\hat{g}_{ij}^{Coulomb}$ includes spin-same-orbit interaction [25, 26] but not spin-other-orbit effects which requires an inclusion of the Gaunt term. In this work electron-electron interaction will nevertheless be described by the Coulomb operator $\hat{g}_{ij}^{Coulomb}$ which is in most cases sufficient to obtain accurate results. The combination with the one-electron Dirac operator yields the Dirac-Coulomb Hamiltonian $\hat{\mathcal{H}}_{DC}$,

$$\begin{aligned}\hat{\mathcal{H}}_{DC} &= \sum_{i=1} \hat{h}_D(i) + \frac{1}{2}\sum_{i\neq j} \hat{g}_{ij}^{Coulomb} \\ &= \sum_{i=1} \left(c\boldsymbol{\alpha}_i\cdot\mathbf{p}_i + \beta_i' mc^2 + \hat{V}^{nuc}\,\mathbf{I}_{4\times4} \right) + \frac{1}{2}\sum_{i\neq j} \frac{\mathbf{I}_{4\times4}\otimes\mathbf{I}_{4\times4}}{r_{ij}}. \end{aligned} \tag{2.15}$$

The Dirac-Coulomb Hamiltonian $\hat{\mathcal{H}}_{DC}$ will predominantly be used in the correlated calculations of atomic and molecular systems presented in Part III. If applicable, the effect of the Gaunt interaction on the electronic structure of a given system will be examined at the uncorrelated level[7].

Finally, a word of caution may be given with respect to the solutions of the free-particle Dirac equation,

$$\hat{h}_D^{free}\Psi = E\Psi. \tag{2.16}$$

This wave equation exhibits a continuum of negative- and positive-energy solutions which are separated by $2mc^2$. The reason for this is that the free-particle Dirac equation provides a description of both electrons (positive-energy branch) and positrons (negative-energy branch). Upon invoking the minimal electromagnetic coupling (see Eq. (2.11)) and choosing the charge of an electron all solutions become electronic solutions. Positronic solutions

[6] This term vanishes in the so-called Lorentz gauge [16].

[7] The inclusion of the Gaunt interaction in post-Hartree-Fock calculations for the methods used here requires an integral transformation from the atomic to the molecular basis. This step is, at the time of writing this thesis, under development in the `DIRAC` program for the Gaunt integrals.

are then obtained either using the positronic charge ($q = +e$) or by charge-conjugation of the negative-energy solutions of the electronic problem [16, 27].

The solution spectrum of a many-electron Dirac Hamiltonian, for example the Dirac-Coulomb Hamiltonian (see Eq. (2.15)) exhibits the same positive and negative-energy branches as the corresponding spectrum of the free-particle Dirac Hamiltonian. It is therefore in principle possible to construct for a given electronic bound state an infinite number of degenerate states in which one particle is excited to the positive-energy continuum and a second particle is de-excited to the negative-energy continuum. In order to avoid this problem of continuum dissolution [28], also known as Brown-Ravenhall disease [29], a QED reinterpretation of the negative-energy states is required [16].

The `DIRAC` program is based on the so-called "empty Dirac" picture [16]. This corresponds to a treatment of the negative-energy states as virtual states in the Hartree-Fock optimization [30] and the application of a *minimax principle* [31]. The energy is minimized with respect to spinor rotations within the positive branch but maximized with respect to rotations involving positive- and negative-energy spinors. Hereafter, the negative-energy states may be discarded since a coupling between the states of the two energy branches was precluded. This approach can be regarded as a no-pair approximation *a posteriori* [32] which does not affect the four-component structure of the solution spinor. For a detailed discussion of a QED reinterpretation of the negative energy states, the reader may refer to Reference 16 and references therein.

2.1.2 Spin-Free Hamiltonian

Relativistic effects are typically considered to be twofold: (i) scalar-relativistic effects which are usually the largest and which are ascribed to the change in the kinematics of the electrons moving at significant fractions of the finite speed of light ($c \approx 137.035989$ au) [8]. (ii) spin-same and spin-other-orbit effects which are related to the coupling of the spin of an electron to an induced magnetic field caused by the movement in the fields of the charged nuclei or electrons. In the preceding section four-component Hamiltonians were presented which are suitable to encompass both types of relativistic effects outlined above. In this section, a modified Dirac Hamiltonian will be introduced which can be used to exclusively take account of the full scalar-relativistic effects while retaining a four-

component framework [26, 33][8]. Such an approach can particularly be useful to identify unambiguously spin-orbit effects on the electronic structure of a given system through a comparison of the modified to the full Dirac Hamiltonian. This objective requires a genuine separation of the spin-free and spin-dependent terms in the one-electron Dirac equation,

$$\begin{pmatrix} \hat{V}^{nuc} & c(\boldsymbol{\sigma}\cdot\mathbf{p}) \\ c(\boldsymbol{\sigma}\cdot\mathbf{p}) & \hat{V}^{nuc} - 2mc^2 \end{pmatrix} \begin{pmatrix} \psi^L \\ \psi^S \end{pmatrix} = E \begin{pmatrix} \psi^L \\ \psi^S \end{pmatrix}, \tag{2.17}$$

written here in the bi-spinor form. To begin with, it is shown to be advantageous [16] to introduce a pseudo-large component ϕ^L,

$$2mc^2\psi^S \equiv (\boldsymbol{\sigma}\cdot\mathbf{p})\phi^L, \tag{2.18}$$

which will have the same symmetry properties as the large component[9]. The major difficulty concerning a separation of scalar-relativistic and spin-orbit effects arises from the appearance of the spin in the kinetic energy operator $c(\boldsymbol{\sigma}\cdot\mathbf{p})$ (see Eq. (2.17)) which has to be dealt with in the following. An important tool to achieve a separation will thereby be the Dirac identity [16],

$$(\boldsymbol{\sigma}\cdot\mathbf{u})(\boldsymbol{\sigma}\cdot\mathbf{v}) = \mathbf{u}\cdot\mathbf{v} + i\boldsymbol{\sigma}\cdot\mathbf{u}\times\mathbf{v}. \tag{2.19}$$

By means of a non-unitary transformation which was proposed by Kutzelnigg [40] and Dyall [41],

$$\begin{pmatrix} \psi^L \\ \psi^S \end{pmatrix} = \begin{pmatrix} \mathbf{I}_{2\times2} & \mathbf{0}_{2\times2} \\ \mathbf{0}_{2\times2} & \frac{1}{2mc^2}(\boldsymbol{\sigma}\cdot\mathbf{p}) \end{pmatrix} \begin{pmatrix} \psi^L \\ \phi^L \end{pmatrix}, \tag{2.20}$$

and subsequent application of the Dirac identity (see Eq.2.19) a modified Dirac equation can be obtained,

$$\begin{pmatrix} \hat{V}^{nuc} & \hat{T} \\ \hat{T} & \frac{1}{4m^2c^2}(\boldsymbol{\sigma}\cdot\mathbf{p})\hat{V}^{nuc}(\boldsymbol{\sigma}\cdot\mathbf{p}) - \hat{T} \end{pmatrix} \begin{pmatrix} \psi^L \\ \phi^L \end{pmatrix} = E\tilde{G} \begin{pmatrix} \psi^L \\ \phi^L \end{pmatrix}. \tag{2.21}$$

Here, the non-relativistic kinetic energy operator $\hat{T}$ follows from the application of the Dirac identity on the kinetic energy term,

$$\frac{1}{2m}(\boldsymbol{\sigma}\cdot\mathbf{p})(\boldsymbol{\sigma}\cdot\mathbf{p}) = \frac{\mathbf{p}\cdot\mathbf{p}}{2m} = \hat{T}, \tag{2.22}$$

[8] There exist various Hamiltonian schemes to approximately include scalar relativistic effects in a one- and two-component framework [34–39] which will not be considered here.

[9] This choice for the pseudo-large component keeps the metric spin-free [16] as shown in the text.

and a modified metric $\tilde{G}$,

$$\tilde{G} = \begin{pmatrix} \mathbf{I}_{2\times 2} & \mathbf{0}_{2\times 2} \\ \mathbf{0}_{2\times 2} & \frac{T}{2mc^2} \end{pmatrix}, \tag{2.23}$$

which differs from unity was introduced.

A separation of spin-dependent and spin-free terms can now be performed on the basis of Eq. (2.21) by using the Dirac identity for the operator product $(\boldsymbol{\sigma}\cdot\mathbf{p})\hat{V}^{nuc}(\boldsymbol{\sigma}\cdot\mathbf{p})$,

$$(\boldsymbol{\sigma}\cdot\mathbf{p})\hat{V}^{nuc}(\boldsymbol{\sigma}\cdot\mathbf{p}) = \mathbf{p}\hat{V}^{nuc}\cdot\mathbf{p} + i\boldsymbol{\sigma}\cdot\mathbf{p}\hat{V}^{nuc}\times\mathbf{p}. \tag{2.24}$$

The resulting modified one-electron Dirac Hamiltonian consists of a sum of a spin-free and spin-dependent term,

$$\begin{aligned} \tilde{h}_D &= \tilde{h}_D^{sf} + \tilde{h}_D^{sd} \\ &= \begin{pmatrix} \hat{V}^{nuc} & \hat{T} \\ \hat{T} & \frac{1}{4m^2c^2}\left(\mathbf{p}\hat{V}^{nuc}\cdot\mathbf{p}\right) - \hat{T} \end{pmatrix} + \begin{pmatrix} \mathbf{0}_{2\times 2} & \mathbf{0}_{2\times 2} \\ \mathbf{0}_{2\times 2} & \frac{1}{4m^2c^2}\left(i\boldsymbol{\sigma}\cdot\mathbf{p}\hat{V}^{nuc}\times\mathbf{p}\right) \end{pmatrix} \end{aligned} \tag{2.25}$$

It should be emphasized that this separation requires no approximation and the separation is exact. The spin-free one-electron Dirac Hamiltonian $\tilde{h}_D^{sf}$ therefore provides an adequate basis for fully taking into account scalar-relativistic effects.

The modification of two-electron operators, for example the Coulomb operator $\hat{g}_{ij}^{Coulomb}$ (see Eq. (2.14)), and isolation of spin-free terms[10] can be achieved in a similar manner as for a one-electron operator. For this purpose, projectors on the large and pseudo-large components of the wave function are introduced,

$$\hat{\mathcal{P}}^{+} = \begin{pmatrix} \mathbf{I}_{2\times 2} & \mathbf{0}_{2\times 2} \\ \mathbf{0}_{2\times 2} & \mathbf{0}_{2\times 2} \end{pmatrix} \quad \text{and } \hat{\mathcal{P}}^{-} = \begin{pmatrix} \mathbf{0}_{2\times 2} & \mathbf{0}_{2\times 2} \\ \mathbf{0}_{2\times 2} & \mathbf{I}_{2\times 2} \end{pmatrix}. \tag{2.26}$$

These are used to define the transformation operators for the ith electron,

$$\hat{\mathcal{T}}_i = \hat{\mathcal{P}}_i^{+} + \frac{1}{2mc}(\boldsymbol{\Sigma}\cdot\mathbf{p})\hat{\mathcal{P}}_i^{-}, \tag{2.27}$$

where $\boldsymbol{\Sigma}$ is the four-component spin-operator,

$$\boldsymbol{\Sigma} = \left[\begin{pmatrix} \boldsymbol{\sigma}_x & \mathbf{0}_{2\times 2} \\ \mathbf{0}_{2\times 2} & \boldsymbol{\sigma}_x \end{pmatrix}, \begin{pmatrix} \boldsymbol{\sigma}_y & \mathbf{0}_{2\times 2} \\ \mathbf{0}_{2\times 2} & \boldsymbol{\sigma}_y \end{pmatrix}, \begin{pmatrix} \boldsymbol{\sigma}_z & \mathbf{0}_{2\times 2} \\ \mathbf{0}_{2\times 2} & \boldsymbol{\sigma}_z \end{pmatrix} \right]. \tag{2.28}$$

[10] A detailed account of the procedure can be found for example in references [16, 41].

The ansatz for a spin-free modification of the Coulomb operator (or any other two-electron operator) is then given by,

$$\tilde{g}_{ij}^{Coulomb} = \hat{\mathcal{T}}_i \hat{\mathcal{T}}_j \hat{g}_{ij}^{Coulomb} \hat{\mathcal{T}}_j \hat{\mathcal{T}}_i. \tag{2.29}$$

Application of the Dirac identity (see Eq. (2.19)) to Eq. (2.29) and elimination of the resulting spin-dependent terms yields an expression for the spin-free Coulomb operator, $\tilde{g}_{ij}^{Coulomb,sf} =$

$$\left(\hat{\mathcal{P}}_i^+ \hat{\mathcal{P}}_i^-\right) \begin{pmatrix} \frac{1}{r_{ij}} & \left(\frac{1}{4m^2c^2}\right) \mathbf{p}_j \cdot \left(\frac{1}{r_{ij}}\right) \mathbf{p}_j \\ \left(\frac{1}{4m^2c^2}\right) \mathbf{p}_i \cdot \left(\frac{1}{r_{ij}}\right) \mathbf{p}_i & \left(\frac{1}{16m^4c^4}\right) \mathbf{p}_j \cdot \left[\mathbf{p}_i \cdot \left(\frac{1}{r_{ij}}\right) \mathbf{p}_i\right] \mathbf{p}_j \end{pmatrix} \begin{pmatrix} \hat{\mathcal{P}}_j^+ \\ \hat{\mathcal{P}}_j^- \end{pmatrix}. \tag{2.30}$$

It should be noted that the use of quaternion algebra as implemented in DIRAC[11] [30] allows to cast both Eq. (2.25) and the corresponding modified equation for the Coulomb operator (not shown here) in a very simple form. The elimination of the spin-dependent parts in this formalism corresponds to zeroing out the quaternion imaginary parts in the operator matrix [33].

Having a modified one-electron Dirac Hamiltonian and two-electron Coulomb operator at hand, the total spin-free Dirac-Coulomb operator can be written as,

$$\tilde{\mathcal{H}}_{DC}^{sf} = \sum_{i=1} \tilde{h}_D^{sf}(i) + \frac{1}{2} \sum_{i \neq j} \tilde{g}_{ij}^{Coulomb,sf}. \tag{2.31}$$

The associated spin-free wave function for this operator,

$$\tilde{\Psi} = \begin{pmatrix} \psi^L \\ \phi^L \end{pmatrix}, \tag{2.32}$$

is purely real and the four-component (molecular) spinors can be classified according to a specific boson irrep[12]. From this it follows that after the transformation to a molecular orbital (MO) basis and invoking the no-pair approximation, any non-relativistic electron correlation method built on a MO-formalism can be combined with the spin-free Dirac-Coulomb equation. In the present work the GASCI program LUCITA will be employed for a discussion of scalar-relativistic effects based on results obtained with the spin-free Dirac-Coulomb operator $\tilde{\mathcal{H}}_{DC}$ as given in Eq. (2.31).

[11] The DIRAC program is based on a quaternion algebra formalism. A quaternion number Q can be written as $Q = r + si + tj + uk$, where r, s, t, u are real numbers and the quaternion units i, j and k anticommute, $ij = k, jk = i, ki = j$ and fulfill the relation $i^2 = j^2 = k^2 = -1$ [16].

[12] Relevant aspects with regard to molecular symmetry in a four-component framework are discussed in Section 2.2.2.

2.2 Symmetry

2.2.1 Time Reversal

Due to the entanglement of spin and spatial symmetry in the relativistic case which can easily be seen from Eq. (2.6), spin restrictions are not applicable to relativistic wave functions. However, as stated by Kramers, in the absence of an external magnetic field the energy levels of a fermion system are at least doubly generate [42]. This allows for a construction of a Kramers-restricted basis of fermion functions $\{\varphi, \bar{\varphi}\}$ where each fermion function φ_p is related to its energy-degenerate partner (Kramers partner) $\varphi_{\bar{p}}$ through time reversal,

$$\hat{\mathcal{K}}\varphi_p \;=\; \varphi_{\bar{p}} \qquad \hat{\mathcal{K}}\varphi_{\bar{p}} = -\varphi_p \qquad \hat{\mathcal{K}}(a\varphi_p) = a^*\hat{\mathcal{K}}\varphi_p, \tag{2.33}$$

with a being a complex number. The time-reversal operator $\hat{\mathcal{K}}$ is an antilinear operator that reverses the time arrow, flips the spin $\boldsymbol{\sigma}$, changes the sign of all velocities $\mathbf{v}$ but keeps positions $\mathbf{r}$ invariant [16],

$$\hat{\mathcal{K}}\varphi_p(t) = \varphi_{\bar{p}}(-t); \quad \hat{\mathcal{K}}\boldsymbol{\sigma}\hat{\mathcal{K}}^{-1} = -\boldsymbol{\sigma}; \quad \hat{\mathcal{K}}\mathbf{v}\hat{\mathcal{K}}^{-1} = -\mathbf{v}; \quad \hat{\mathcal{K}}\mathbf{r}\hat{\mathcal{K}}^{-1} = \mathbf{r}. \tag{2.34}$$

In the four-component relativistic framework the time-reversal operator is given by,

$$\hat{\mathcal{K}} := -i\boldsymbol{\Sigma}_y\hat{\mathcal{K}}_0 = -i\begin{pmatrix} \boldsymbol{\sigma}_y & \mathbf{0}_{2\times2} \\ \mathbf{0}_{2\times2} & \boldsymbol{\sigma}_y \end{pmatrix}\hat{\mathcal{K}}_0, \tag{2.35}$$

where $\boldsymbol{\Sigma}_y$ is the y component of the total spin operator $\boldsymbol{\Sigma}$ and $\hat{\mathcal{K}}_0$ is the complex conjugation operator. It should be noted that because of its antilinear property $\hat{\mathcal{K}}$ is not an observable and therefore does not have a corresponding eigenvalue K.

Working in a Kramers-paired spinor basis allows to take advantage of time-reversal symmetry to recover to some extent computational savings that were lost compared to a non-relativistic framework where spin-restriction can be exploited. For example, it can be shown [16, 43] that the matrix representation of a Hermitian one-particle operator $\hat{\Omega}$ in a Kramers-restricted basis takes the following form of a general 2×2 matrix for the components of a Kramers pair,

$$\boldsymbol{\Omega} = \begin{pmatrix} \left\langle \varphi_p \middle| \hat{\Omega} \middle| \varphi_q \right\rangle & \left\langle \varphi_p \middle| \hat{\Omega} \middle| \varphi_{\bar{q}} \right\rangle \\ \left\langle \varphi_{\bar{p}} \middle| \hat{\Omega} \middle| \varphi_q \right\rangle & \left\langle \varphi_{\bar{p}} \middle| \hat{\Omega} \middle| \varphi_{\bar{q}} \right\rangle \end{pmatrix} = \begin{pmatrix} \Omega_{pq} & \Omega_{p\bar{q}} \\ \Omega_{\bar{p}q} & \Omega_{\bar{p}\bar{q}} \end{pmatrix} = \begin{pmatrix} \Omega_{pq} & \Omega_{p\bar{q}} \\ -t\Omega^*_{p\bar{q}} & t\Omega^*_{pq} \end{pmatrix}, \tag{2.36}$$

where $t = \pm 1$ indicates the symmetry of the operator under time reversal,

$$\hat{\mathcal{K}}\hat{\Omega}\hat{\mathcal{K}}^{-1} = t\hat{\Omega}. \tag{2.37}$$

By defining $\Omega_{pq} = A_{pq}, \Omega_{p\bar{q}} = B_{pq}$ for all Kramers pairs in the basis $\{\varphi, \bar{\varphi}\}$ and after a suitable reordering, the matrix $\mathbf{\Omega}$ can be written as,

$$\mathbf{\Omega} = \begin{pmatrix} \mathbf{A} & \mathbf{B} \\ -t\mathbf{B}^* & t\mathbf{A}^* \end{pmatrix}. \tag{2.38}$$

For the particular case of Hermitian operators that are symmetric under time reversal ($t = +1$) the resulting matrix in Eq. (2.38) can be cast in a block-diagonal form by introducing quaternion algebra [16]. Applying the quaternion unitary matrix,

$$\mathbf{U} = \frac{1}{\sqrt{2}} \begin{pmatrix} \mathbf{I} & j\mathbf{I} \\ j\mathbf{I} & \mathbf{I} \end{pmatrix}, \tag{2.39}$$

the matrix $\mathbf{\Omega}$ is transformed to,

$$\mathbf{U}^\dagger \mathbf{\Omega} \mathbf{U} = \begin{pmatrix} \mathbf{G} & \mathbf{0} \\ \mathbf{0} & -k\mathbf{G}k \end{pmatrix}, \tag{2.40}$$

where $\mathbf{G}$ is a quaternion Hermitian matrix. The structure of the resulting matrix also indicates the double degeneracy of the eigenvalues of $\mathbf{\Omega}$. Moreover, the block-diagonal form of the matrix allows to diagonalize the sub-blocks independently which can lead in general to considerable computational savings.

2.2.2 Double Group Symmetry

In the preceding chapter it was demonstrated how time-reversal symmetry can be exploited to reduce the computational demand in a relativistic implementation of many-body methods. In order to make use of molecular symmetry one needs to resort to double point groups rather than the well-known single point groups because of the transformation properties of fermion (spin $\frac{1}{2}$) particles. There are two cases to consider for many-particle systems which will consist of either an *even* or *odd* number of spin $\frac{1}{2}$ particles [16]. In the first case, the total spin is an integer and the many-particle wave function transforms as one of the well-known single group irreducible representations (boson irreps). In the case of an odd number of fermion particles the total spin is half integer which requires

a rotation of 4π around an arbitrary axis to yield the identity operation E. Thus, it follows that an operation $\bar{E}$, corresponding to a rotation by 2π, needs to be added to the single group of order n. The expanded group then has the order $2n$ (double group). The additional irreps with a negative sign for the $\bar{E}$ operation are called fermion irreps. A further elaboration on the theory of double groups is beyond the scope of this introductory section and the reader may refer to standard textbooks on group theory, *e.g.* [44].

It is nevertheless useful to discuss important implications arising from the application of molecular symmetry for the matrix elements of a totally symmetric operator $\hat{\Omega}$ (with symmetry under time reversal $t = 1$, see Eq. (2.36)) in a basis of Kramers-paired spinors. Although time reversal is not an element of a double group [45], there is a connection between the structure of the fermion irreps and the group theoretical properties of the Kramers pairs. The following considerations are not restricted to the binary double group D_{2h}^* and its subgroups but these are most often implemented [46], for example in the `DIRAC` program and have been used in the applications. According to Wigner [47] three different classes exist[13]: (i) the Kramers partner φ_p and $\varphi_{\bar{p}}$ belong to different rows of a doubly degenerate fermion irrep (double groups D_{2h}^*, D_2^*, and C_{2v}^*). By symmetry, the matrix elements $\Omega_{p\bar{q}}$ are zero. (ii) φ_p and $\varphi_{\bar{p}}$ are members of two different one-dimensional fermion irreps (C_{2h}^*, C_2^*, and C_s^*). Again, the matrix elements $\Omega_{p\bar{q}}$ are zero by symmetry. (iii) φ_p and $\varphi_{\bar{p}}$ belong to the same one-dimensional irrep (C_i^* and C_1^*) which implies in general that $\Omega_{p\bar{q}} \neq 0$ and a block-diagonal form of $\mathbf{\Omega}$ necessitates a quaternion rotation of the Kramers pairs (see Section 2.2.1). By contrast, it can be shown [30] that, starting from a quaternion formalism, the algebra reduces for the first two cases, (i) and (ii), to a real and complex algebra, respectively. Hence, the above characterized double groups are often referred to as *real*, *complex* and *quaternion* double groups.

2.3 Basis Sets

In non-relativistic (molecular) calculations using expansions in finite basis sets it is nowadays standard to employ contracted basis sets of Gaussian-type orbitals in various different "flavors"[14]. In relativistic calculations, on the other hand, in particular in four-component

[13] A nice discussion on this topic can be found in the textbook of Dyall and Fægri, Chapter 10.1 [16].
[14] See for example the basis set data base in Reference 48.

calculations the application of contracted basis sets is rather nontrivial[15] and most often uncontracted basis sets are employed in its stead [16]. For example, all calculations presented in this thesis have been carried out using Gaussian-type basis sets in uncontracted form with exponents optimized for the relativistic case [50]. The preference of specifically optimized exponents over those from "standard" basis sets can be rationalized by considering, *e.g.* the splitting of shells with $l > 0$ into two components which may have their radial maxima far apart[16], and the relativistically contracted inner shells which require in general higher exponents.

The introduction of uncontracted basis sets in four-component calculations is in particular motivated by the imperative necessity to fulfill the *kinetic balance* condition [51],

$$\chi^S = (\boldsymbol{\sigma} \cdot \mathbf{p})\chi^L, \tag{2.41}$$

where χ^S and χ^L denote basis functions for the small Ψ^S and large component Ψ^L of the four-component wave function. Eq. (2.41) imposes an important condition on the choice of basis sets for the large and small component. The above given relation has to be satisfied in order to yield the correct non-relativistic limit for the kinetic energy [16]. For instance, it was proven that, if and only if the basis sets χ^S and χ^L are related by Eq. (2.41) the kinetic energy is a maximum [52] and that any other connection will lead to a lowering of the kinetic energy in the non-relativistic limit and to variationally unstable results. The kinetic balance condition is taken into account in calculations using the `DIRAC` program which assumes uncontracted basis sets for the large component basis. The corresponding set for the small component is generated by means of a restricted kinetic balance approach [53].

[15] A suitable scheme to make use of contracted basis sets in four-component calculations is based on the application of the *atomic* kinetic balance [49].

[16] An illustrative example is given in Figure 6.3 (page 69) for the splitting of the $6p_{1/2,3/2}$ components in the Bi atom.

Chapter 3

Relativistic Correlation Methods

This chapter will discuss important aspects of relativistic large-scale configuration interaction (CI) and multiconfiguration self-consistent-field (MCSCF) methods for which parallel algorithms were developed in this thesis. Moreover, the implementations of these methods in the `DIRAC` program were used to perform a major part of the applications presented in Part III.

The simplest and basic starting point for describing the electronic structure of atoms and molecules is the Hartree-Fock model where the motion of each electron is characterized by a mean-field repulsion of all other electrons. In reality, the movements of the electrons are, however, correlated and, as electron correlation effects are in most cases significant for chemical properties, it is essential to cover these accurately. Moreover, electron correlation can be thought of as being divided into a dynamic and a non-dynamic (or static) correlation part. Dynamic correlation is in general related to the short-range interaction of electrons while static correlation becomes dominant for systems exhibiting, e.g., degeneracy or near-degeneracy. For heavy atoms or molecules containing heavy elements multiple occurrences of near-degenerate configurations are more likely than for systems with only light elements because of the small energetic separation of s, p, d and f shells and considerable spin-orbit coupling[1].

A CI method is a straightforward approach to include dynamic correlation in the wave function after the Hartree-Fock step. It is based on the idea of a linear parametrization of the wave function Ψ through an expansion in a set of M N-particle functions

[1]Spin-orbit coupling leads to an energetic splitting of shells with $l > 0$ which may thus increase the state density, *i.e.*, the number of states per energy window.

Φ_i,

$$\Psi = \sum_i^M C_i \Phi_i. \tag{3.1}$$

This leads to a matrix eigenvalue problem for the operator $\hat{\mathcal{H}}$,

$$\mathbf{HC} = E\mathbf{C}, \tag{3.2}$$

where **C** is the CI coefficient vector and E the corresponding eigenvalue. Since in most cases only a sub-set of m solutions is required for the full eigenvalue problem, iterative subspace diagonalization schemes were proposed [54–56] to reduce the computational scaling from roughly M^3 to M^2. In the following section basic features of the string-driven relativistic direct CI algorithm of the program module `LUCIAREL`, which was developed by Fleig and co-workers [57–60], will be presented. The algorithm takes advantage of an iterative Davidson diagonalization scheme [54] that was extended to a complex-valued algebra [61]. For a detailed account of the underlying theory and implementation of `LUCIAREL` the reader may refer to the literature given above. A description of the CI program `LUCITA` which was used to carry out spin-free calculations can be found in References 60 and 62[2].

Returning to the initial problem of taking into account electron correlation, the MCSCF model is well-known to be capable of describing strong static correlation effects [64]. A four-component Kramers-restricted MCSCF (KR-MCSCF) method [43, 61, 65] is therefore an adequate means to simultaneously account for both static electron correlation and relativistic effects already in the orbital optimization step. In Section 3.2 a brief introduction to the KR-MCSCF method will be given where the main focus lies on direct CI contributions to the optimization procedure.

3.1 Kramers-Restricted Configuration Interaction

The relativistic double group program `LUCIAREL` fully exploits the advantages of a genuine string-based implementation where explicit comparisons of configurations in the determination of coupling coefficients are avoided. This guarantees efficiency even when

[2] A comprehensive introduction to the non-relativistic pre-cursor CI algorithms is provided in references [55, 63].

higher-order excitations are taken into account. In non- or scalar-relativistic CI a Slater determinant is the product of an α-string and a β-string, and has a specific M_S value [63]. In a basis of Kramers-paired spinors $\{\varphi_p, \varphi_{\bar{p}}\}$ in a relativistic implementation, the two strings are replaced by an $\mathcal{S}$-string of j Kramers spinors $\{\varphi_p\}$ and a $\bar{\mathcal{T}}$-string of $N-j$ Kramers partners $\{\varphi_{\bar{p}}\}$,

$$\begin{aligned} \hat{\mathcal{S}}^\dagger \,|\, vac \,\rangle &= \hat{a}^\dagger_{S_1} \hat{a}^\dagger_{S_2} \ldots \hat{a}^\dagger_{S_j} \,|\, vac \,\rangle \\ \hat{\bar{\mathcal{T}}}^\dagger \,|\, vac \,\rangle &= \hat{a}^\dagger_{\bar{T}_1} \hat{a}^\dagger_{\bar{T}_2} \ldots \hat{a}^\dagger_{\bar{T}_{N-j}} \,|\, vac \,\rangle \,, \end{aligned} \tag{3.3}$$

where N is the total number of electrons for a given system. A general Slater determinant $|\mathcal{S}\bar{\mathcal{T}}\rangle$ can then be written in terms of these strings according to,

$$|\, \mathcal{S}\bar{\mathcal{T}} \,\rangle = \hat{\mathcal{S}}^\dagger \hat{\bar{\mathcal{T}}}^\dagger \,|\, vac \,\rangle \,. \tag{3.4}$$

By means of an auxiliary bookkeeping number M_K (Kramers projection value),

$$M_K = \frac{n_{\text{unbarred}} - n_{\text{barred}}}{2} = \frac{j - (N-j)}{2} = j - N/2, \tag{3.5}$$

it is possible to arrange all determinants which may be built from an initial set of Kramers pairs in individual subsets each with a characteristic M_K value.

The decisive step of any iterative sub-space diagonalization method (see also Section 4.1.1) is the computation of the linear transformation of the current trial vector $\mathbf{b}_n$ in a given iteration,

$$\boldsymbol{\sigma}_n \;=\; \mathbf{H}\mathbf{b}_n, \tag{3.6}$$

where $\mathbf{H}$ is the Hamiltonian, *e.g.* the Dirac-Coulomb Hamiltonian $\hat{\mathcal{H}}_{DC}$ (see Eq. (2.15)), in matrix representation[3]. In second quantization, this operator can be written as [43,57],

$$\begin{aligned} \hat{\mathcal{H}}_{DC} \;=\; & \sum_{pq} \left[h_{pq} \hat{X}^+_{pq} + \frac{1}{2} \left(h_{\bar{p}q} \hat{X}^+_{\bar{p}q} + h_{p\bar{q}} \hat{X}^+_{p\bar{q}} \right) \right] \\ & + \frac{1}{2} \sum_{pqrs} \left[(pq|rs)\, \hat{x}^{++}_{pq,rs} + (\bar{p}q|rs)\, \hat{x}^{++}_{\bar{p}q,rs} + (p\bar{q}|rs)\, \hat{x}^{++}_{p\bar{q},rs} \right] \\ & + \frac{1}{4} \sum_{pqrs} (\bar{p}q|r\bar{s})\, \hat{x}^{++}_{\bar{p}q,r\bar{s}} \\ & + \frac{1}{8} \sum_{pqrs} \left[(\bar{p}q|\bar{r}s)\, \hat{x}^{++}_{\bar{p}q,\bar{r}s} + (p\bar{q}|r\bar{s})\, \hat{x}^{++}_{p\bar{q},r\bar{s}} \right] . \end{aligned} \tag{3.7}$$

[3]Further considerations with regard to the Dirac-Coulomb-Gaunt or Dirac-Coulomb-Breit operator (Eq. (2.14)) can be found for example in Reference 16.

Here, Kramers-restricted single $\hat{X}^{s}_{pq}$ (with $s = \pm$) and double replacement operators $\hat{x}^{s_1,s_2}_{pq,rs}$ (with $s_1, s_2 = \pm$) have been employed which were defined by Aucar *et al.* [66]. Their explicit form is given in Eq. (3.8) and Eq. (3.9), respectively, in terms of creation and annihilation operators,

$$\hat{X}^{s}_{pq} = a^{\dagger}_{p}a_{q} + sa^{\dagger}_{\bar{q}}a_{\bar{p}} \qquad \hat{X}^{s}_{p\bar{q}} = a^{\dagger}_{p}a_{\bar{q}} - sa^{\dagger}_{q}a_{\bar{p}} \qquad \hat{X}^{s}_{\bar{p}q} = a^{\dagger}_{\bar{p}}a_{q} - sa^{\dagger}_{\bar{q}}a_{p}, \tag{3.8}$$

and,

$$\hat{x}^{s_1,s_2}_{pq,rs} = \hat{X}^{s_1}_{pq}\hat{X}^{s_2}_{rs} - \delta_{rq}a^{\dagger}_{p}a_{s} - s_1\delta_{r\bar{p}}a^{\dagger}_{\bar{q}}a_{s} - s_2\delta_{\bar{s}q}a^{\dagger}_{p}a_{\bar{r}} - s_1s_2\delta_{\bar{p}\bar{s}}a^{\dagger}_{\bar{q}}a_{\bar{r}} = \hat{x}^{s_2,s_1}_{rs,pq}, \tag{3.9}$$

where the sign indices s and $s_1, s_2 = \pm$, respectively, indicate the symmetry of the operators under time reversal and Hermitian conjugation[4]. The remaining double replacement operators with bars can be obtained from the operator $\hat{x}^{s_1,s_2}_{pq,rs}$ given in Eq. (3.9) through application of the auxiliary bar-reversal operator $\hat{K}_p$ [16],

$$\hat{K}_p a_p = a_{\bar{p}} \qquad \hat{K}_p a_{\bar{p}} = -a_p \qquad \hat{K}_p a_q = a_q. \tag{3.10}$$

It can now be shown [57] that the Hamiltonian $\hat{\mathcal{H}}_{DC}$ in Eq. (3.7) may be reformulated by rewriting it in terms of ΔM_K partitions,

$$\hat{\mathcal{H}}_{DC} = \sum_{+2}^{\Delta M_K=-2} \hat{H}_{\Delta M_K} \tag{3.11}$$

with

$$\hat{H}_{\Delta M_K=+2} = \sum_{pqrs} \frac{1}{8} (p\bar{q}|r\bar{s})\, \hat{x}^{++}_{p\bar{q}r\bar{s}} \tag{3.12}$$

$$\hat{H}_{\Delta M_K=+1} = \sum_{pq} \frac{1}{2} h_{p\bar{q}} \hat{X}^{+}_{p\bar{q}} + \sum_{pqrs} \frac{1}{2} (p\bar{q}|rs)\, \hat{x}^{++}_{p\bar{q}rs} \tag{3.13}$$

$$\hat{H}_{\Delta M_K=0} = \sum_{pq} h_{pq} \hat{X}^{+}_{pq} + \sum_{pqrs} \left[\frac{1}{2} (pq|rs)\, \hat{x}^{++}_{pqrs} + \frac{1}{4} (\bar{p}q|r\bar{s})\, \hat{x}^{++}_{\bar{p}qr\bar{s}} \right] \tag{3.14}$$

$$\hat{H}_{\Delta M_K=-1} = \sum_{pq} h_{\bar{p}q} \hat{X}^{+}_{\bar{p}q} + \sum_{pqrs} \frac{1}{2} (\bar{p}q|rs)\, x^{++}_{\bar{p}qrs} \tag{3.15}$$

$$\hat{H}_{\Delta M_K=-2} = \sum_{pqrs} \frac{1}{2} (\bar{p}q|\bar{r}s)\, x^{++}_{\bar{p}q\bar{r}s} \tag{3.16}$$

[4]Since all components in Eq. (3.7) are symmetric under time reversal it follows that the total operator $\hat{\mathcal{H}}_{DC}$ is also symmetric with respect to reversal of motion which is equivalent to the commutation relation $\left[\hat{\mathcal{H}}_{DC}, \hat{\mathcal{K}}\right] = 0$.

Table 3.1: Excitation class ordered operators in second quantization and the corresponding integrals. The original table was taken from Reference 58.

Operator	Integral class	Kramers flip type
$a_p^\dagger a_q$	h_{pq}	$\Delta M_k = 0$
$a_{\bar{p}}^\dagger a_{\bar{q}}$	$h_{\bar{p}\bar{q}}$	$\Delta M_k = 0$
$a_p^\dagger a_r^\dagger a_s a_q$	$(pq\|rs)$	$\Delta M_k = 0$
$a_{\bar{p}}^\dagger a_{\bar{r}}^\dagger a_{\bar{s}} a_{\bar{q}}$	$(\bar{p}\bar{q}\|\bar{r}\bar{s})$	$\Delta M_k = 0$
$a_p^\dagger a_{\bar{r}}^\dagger a_s a_{\bar{q}}$	$(p\bar{q}\|\bar{r}s)$	$\Delta M_k = 0$
$a_p^\dagger a_{\bar{q}}$	$h_{p\bar{q}}$	$\Delta M_k = +1$
$a_{\bar{p}}^\dagger a_q$	$h_{\bar{p}q}$	$\Delta M_k = -1$
$a_p^\dagger a_r^\dagger a_s a_{\bar{q}}$	$(p\bar{q}\|rs)$	$\Delta M_k = +1$
$a_{\bar{p}}^\dagger a_{\bar{r}}^\dagger a_{\bar{s}} a_q$	$(\bar{p}q\|\bar{r}\bar{s})$	$\Delta M_k = -1$
$a_p^\dagger a_r^\dagger a_{\bar{s}} a_{\bar{q}}$	$(p\bar{q}\|r\bar{s})$	$\Delta M_k = +2$
$a_{\bar{p}}^\dagger a_{\bar{r}}^\dagger a_s a_q$	$(\bar{p}q\|\bar{r}s)$	$\Delta M_k = -2$

The partitioning scheme is based on a classification of the individual operator elements $\hat{X}_{pq}^{s}$ and $\hat{x}_{pq,rs}^{s_1,s_2}$, respectively, according to their action on a given Slater determinant, *i.e.*, the number of induced Kramers flips. These flips have their correspondence in spin-flips in a non-relativistic formalism and replace a barred spinor by an unbarred spinor and vice versa. Table 3.1 compiles the operator types derived from the Kramers-restricted single and double replacement operators and their associated integral classes with respect to the Kramers flip type.

In order to illustrate the computation of the linear transformation in Eq. (3.6), the part of the Dirac-Coulomb Hamiltonian that changes the M_K-value by a single unit $\Delta M_K = +1$ (see Eq. (3.13)) shall be considered here:

$$\hat{H}_{\Delta M_K=+1} = \sum_{pq} \frac{1}{2} h_{p\bar{q}} \hat{X}_{p\bar{q}}^{+} + \sum_{pqrs} \frac{1}{2} (p\bar{q}|rs)\, \hat{x}_{p\bar{q}rs}^{++}. \tag{3.17}$$

Taking only the first term (given in bold face) for the Kramers-restricted double replacement operator into consideration,

$$\hat{x}_{p\bar{q}rs}^{++} = \mathbf{\hat{a}_p^\dagger \hat{a}_r^\dagger \hat{a}_s \hat{a}_{\bar{q}}} - \hat{a}_q^\dagger \hat{a}_r^\dagger \hat{a}_s \hat{a}_{\bar{p}} + \hat{a}_p^\dagger \hat{a}_{\bar{s}}^\dagger \hat{a}_{\bar{r}} \hat{a}_{\bar{q}} - \hat{a}_q^\dagger \hat{a}_{\bar{s}}^\dagger \hat{a}_{\bar{r}} \hat{a}_{\bar{p}}, \tag{3.18}$$

the real part of this sigma-vector fragment can be written as[5],

$$\sigma^r_{\Delta M_K=+1}(\mathcal{S}\bar{\mathcal{T}}) = \sum_{pqrs}\sum_{\mathcal{U}\bar{\mathcal{V}}} \left\{ (p\bar{q}|rs)^r \, A^{\mathcal{S}\bar{\mathcal{T}},\mathcal{U}\bar{\mathcal{V}}}_{p\bar{q}rs} b^r_{\mathcal{U}\bar{\mathcal{V}}} + (p\bar{q}|rs)^i \, A^{\mathcal{S}\bar{\mathcal{T}},\mathcal{U}\bar{\mathcal{V}}}_{p\bar{q}rs} b^i_{\mathcal{U}\bar{\mathcal{V}}} \right\}, \tag{3.19}$$

where $A^{\mathcal{S}\bar{\mathcal{T}},\mathcal{U}\bar{\mathcal{V}}}_{p\bar{q}rs} = \langle \mathcal{S}\bar{\mathcal{T}}|\hat{a}^\dagger_p \hat{a}^\dagger_q \hat{a}_r \hat{a}_{\bar{s}}|\mathcal{U}\bar{\mathcal{V}}\rangle$ is the coupling coefficient for the complex integral $(p\bar{q}|rs)$ between the Slater determinants $|\mathcal{S}\bar{\mathcal{T}}\rangle$ and $|\mathcal{U}\bar{\mathcal{V}}\rangle$. It is contracted with the complex CI expansion coefficient $b_{\mathcal{U}\bar{\mathcal{V}}}$ for this particular determinant and the integral.

The definition of orbital spaces in `LUCIAREL` takes advantage of the concept of generalized active spaces (GAS) [57]. The wave function may be specified by an arbitrary number of active orbital spaces with arbitrary electron occupation constraints thus providing maximum flexibility for the envisaged electronic-structure problem. The GAS partitioning can, furthermore, be exploited to create an implicit blocking of the Slater determinants that are included in the CI expansion. In addition to its M_K value, any determinant $|\Phi_\nu\rangle = |\mathcal{S}_\nu\bar{\mathcal{T}}_\nu\rangle$ can also be classified according to the occupation type (T) in the various active orbital spaces and double point group symmetry (S) of its creator string for the occupied unbarred Kramers spinors $\hat{\mathcal{S}}^\dagger$ and the corresponding creator string for the occupied barred Kramers spinors $\hat{\bar{\mathcal{T}}}^\dagger$. A given block of determinants of the complete CI vector is thus characterized by the occupation types and symmetries of its unbarred and barred string components, and the Kramers projection M_K. As introduced for the spin-free analogue in Paper 1 such a group of determinants is labeled in general as (occupation)-type-(occupation)-type-symmetry-symmetry ($TTSS$) block. Since the Hamiltonian is totally symmetric the block partitioning will be the same for both the sigma vector $\boldsymbol{\sigma}_n$ and the current trial vector $\mathbf{b}_n$. The $TTSS$ blocking is used in the algorithm to skip all the coupling coefficients which are zero because the type-type of the $\boldsymbol{\sigma}_n$-block differ by more than two electrons from the type-type of the $\mathbf{b}_n$-block or because the two blocks have different symmetries. As will be discussed in Section 4.1 the $TTSS$ blocks played a central role in the development of a parallel algorithm.

[5]The superscript ^{r} denotes the real part and ^{i} the imaginary part of a generally complex quantity as for example the integral $(p\bar{q}|rs)$.

3.2 Kramers-Restricted Multiconfiguration Self-Consistent-Field

The general formalism of a KR-MCSCF method has been developed by Jensen and coworkers [43] and an implementation in the DIRAC program has been reported by Thyssen *et al.* [61, 65]. The emphasis is put in this section on CI-based contributions to the KR-MCSCF optimization algorithm as parallel algorithms for these were devised in this thesis.

The aim of a relativistic KR-MCSCF calculation is the optimization of a multiconfigurational trial function,

$$| \Psi (\boldsymbol{\delta}, \boldsymbol{\kappa}) \rangle = \sum_{\nu} \frac{c_\nu + \delta_\nu}{\sqrt{1+\delta^2}} | D_\nu(\boldsymbol{\kappa}) \rangle , \tag{3.20}$$

which depends on the complex configurational ($\boldsymbol{\delta}, \delta = ||\boldsymbol{\delta}||$) and orbital rotation parameters ($\boldsymbol{\kappa}$) gathered in a column vector $\boldsymbol{\lambda} = [\boldsymbol{\delta}, \boldsymbol{\kappa}, \boldsymbol{\delta}^*, \boldsymbol{\kappa}^*]^T$. Moreover, $\mathbf{c}$ is a coefficient vector in configuration space and $| D_\nu(\boldsymbol{\kappa}) \rangle$ refers to, *e.g.* a Slater determinant composed of atomic or molecular spinors. The trial function is obtained from an optimization of the energy functional $E(\boldsymbol{\lambda})$ for a given spin-dependent Hamiltonian $\hat{H}$,

$$E(\boldsymbol{\lambda}) \;=\; \left\langle \Psi (\boldsymbol{\delta^*}, \boldsymbol{\kappa^*}) \middle| \hat{H} \middle| \Psi (\boldsymbol{\delta}, \boldsymbol{\kappa}) \right\rangle . \tag{3.21}$$

In order to achieve a good approximation to $E(\boldsymbol{\lambda})$ a restricted-step second-order optimization scheme can be employed. A second-order Taylor expansion of $E(\boldsymbol{\lambda})$ around the current expansion point (CEP) ($\boldsymbol{\lambda} = \mathbf{0}$) in the parameter space $\boldsymbol{\Gamma} = [\lambda \; \boldsymbol{\kappa}]$ yields [43],

$$E^{(2)}(\boldsymbol{\lambda}) = E(\mathbf{0}) + \boldsymbol{\lambda}^\dagger \mathbf{E}^{[1]} + \frac{1}{2} \, \boldsymbol{\lambda}^\dagger \, \mathbf{E}^{[2]} \, \boldsymbol{\lambda}, \tag{3.22}$$

where $\mathbf{E}^{[1]}$ and $\mathbf{E}^{[2]}$ are the gradient and the Hessian, respectively, at the CEP. They are given by

$$\mathbf{E}^{[1]} \;=\; \begin{pmatrix} \frac{\partial E}{\partial \Gamma^*} \\ \frac{\partial E}{\partial \Gamma} \end{pmatrix}_{\lambda=0} \quad \text{and} \quad \mathbf{E}^{[2]} \;=\; \begin{pmatrix} \frac{\partial^2 E}{\partial \Gamma^* \partial \Gamma} & \frac{\partial^2 E}{\partial \Gamma^* \partial \Gamma^*} \\ \frac{\partial^2 E}{\partial \Gamma \partial \Gamma} & \frac{\partial^2 E}{\partial \Gamma \partial \Gamma^*} \end{pmatrix}_{\lambda=0} . \tag{3.23}$$

To ensure convergence towards the electronic ground state wave function in the no-pair approximation[6] by means of a fully relativistic optimization algorithm, application of the so-called *minimax principle* [31, 43] is required. From this, it follows that

[6] A brief discussion on the interpretations of the negative-energy solutions of the Dirac equation can be found in Section 2.1.

the energy has to be minimized with respect to electronic-electronic orbital rotations and configuration coefficients and maximized with respect to electronic-positronic orbital rotations. Invoking the no-pair approximation, the step that predicts the lowest energy value $E^{(2)}(\boldsymbol{\lambda})$ in Eq. (3.22) represents the optimal step for minimization. This condition yields a modified Newton-type of equation [67, 68] for the optimal step $\boldsymbol{\lambda}^{\nu}$,

$$\boldsymbol{\lambda}^{\nu} \;=\; -\left(\mathbf{E}^{[2]} - \nu\mathbf{I}\right)^{-1}\mathbf{E}^{[1]}, \tag{3.24}$$

where a level shift parameter ν has been introduced. The solution of Eq. (3.24) defines one macro iteration after which all orbital and configuration coefficients are updated to define the next CEP and to determine a new set of one- and two-electron integrals from the rotated orbitals.

In order to facilitate a (relativistic) MCSCF for larger systems it is mandatory to make use of a direct technique which refrains from an explicit evaluation of the Hessian matrix $\mathbf{E}^{[2]}$ [69] in expression (3.24). This can be achieved by expanding the optimal step vector $\boldsymbol{\lambda}^{\nu}$ in a set of trial vectors[7] $\{\mathbf{b}_n\}$

$$\boldsymbol{\lambda}^{j} = \sum_{n}^{N_b^j} a_n^j\, \mathbf{b}_n, \tag{3.25}$$

with N_b^j being the dimension of the trial vector in micro iteration j. The optimal expansion coefficients $\{a_n^j\}$ in Eq. (3.25) are likewise obtained from the solutions of the *projected* linear equations,

$$a_n^j = -\left(\mathbf{E}^{[2j]} - \nu_j\mathbf{I}\right)^{-1}\mathbf{E}^{[1j]}, \tag{3.26}$$

where the reduced gradient and Hessian elements read as

$$\mathbf{E}^{[1j]} \;=\; \mathbf{b}_n^{\dagger}\mathbf{E}^{[1]} \tag{3.27}$$

$$\mathbf{E}^{[2j]} \;=\; \mathbf{b}_m^{\dagger}\,\mathbf{E}^{[2]}\,\mathbf{b}_n \;= \mathbf{b}_m^{\dagger}\,\boldsymbol{\sigma}_n. \tag{3.28}$$

Hence, a direct KR-MCSCF algorithm comprises a dual-level structure. The macro iterations represent the outer part aiming at the convergence towards a desired local minimum on the parameter surface and the micro iterations provide the optimal step for each of the macro iterations.

[7] A separate set of trial vectors is used for the electronic-electronic, electronic-positronic, and configurational parameters.

According to Eq. (3.28) central elements of a micro iteration are successive linear transformations for each $\mathbf{b}_n$

$$\boldsymbol{\sigma}_n = \mathbf{E}^{[2]}\ \mathbf{b}_n, \tag{3.29}$$

where the resulting $\boldsymbol{\sigma}_n$ vectors contain both orbital and configurational contributions due to the coupling of all subspaces by the Hessian. This is illustrated by picking out a single sigma vector and casting Eq. (3.29) in a form that identifies the individual orbital and configurational parts (denoted by the superscripts ^{o} and ^{c}),

$$\begin{pmatrix} \boldsymbol{\sigma}^c \\ \boldsymbol{\sigma}^o \\ \boldsymbol{\sigma}^{c*} \\ \boldsymbol{\sigma}^{o*} \end{pmatrix} = \begin{pmatrix} \mathbf{E}^{[2]c^*,c} & \mathbf{E}^{[2]c^*,o} & \mathbf{E}^{[2]c^*,c^*} & \mathbf{E}^{[2]c^*,o^*} \\ \mathbf{E}^{[2]o^*,c} & \mathbf{E}^{[2]o^*,o} & \mathbf{E}^{[2]o^*,c^*} & \mathbf{E}^{[2]o^*,o^*} \\ \mathbf{E}^{[2]c,c} & \mathbf{E}^{[2]c,o} & \mathbf{E}^{[2]c,c^*} & \mathbf{E}^{[2]c,o^*} \\ \mathbf{E}^{[2]o,c} & \mathbf{E}^{[2]o,o} & \mathbf{E}^{[2]o,c^*} & \mathbf{E}^{[2]o,o^*} \end{pmatrix} \cdot \begin{pmatrix} \mathbf{b}^c \\ \mathbf{b}^o \\ \mathbf{b}^{c*} \\ \mathbf{b}^{o*} \end{pmatrix}. \tag{3.30}$$

Typically, only the upper half of Eq. (3.30) needs to be evaluated since the remaining parts follow from complex conjugation [61]. For a given determinant $|\,\Phi_\mu\,\rangle$, configurational trial vector $|\,\mathbf{B}\,\rangle = \sum_\mu b_\mu\,|\,\Phi_\mu\,\rangle$, and one-index transformed Hamiltonian[8] $\tilde{\hat{H}}$ the configurational parts of the sigma vector in Eq. (3.30) are composed of two CI sigma-vector contributions [43, 61],

$$\boldsymbol{\sigma}^c_\mu \;=\; \left\langle \Phi_\mu \left| \hat{H} \right| \mathbf{B} \right\rangle \;+\; \left\langle \Phi_\mu \left| \tilde{\hat{H}} \right| \mathbf{c}^k \right\rangle, \tag{3.31}$$

where $|\,\mathbf{c}^k\,\rangle$ is the CEP vector of the kth macro iteration. The calculation of the orbital parts requires the evaluation of CI density and transition density matrices between the CEP vector $|\,\mathbf{c}^k\,\rangle$ and a given configurational trial vector $|\,\mathbf{B}\,\rangle$ [43, 61],

$$\boldsymbol{\sigma}^o_{rs} \;=\; -\;\left\{ \left\langle \mathbf{c}^k \left| \left[\hat{X}^-_{sr}, \hat{H} \right] \right| \mathbf{B} \right\rangle \;+\; \left\langle \mathbf{B} \left| \left[\hat{X}^-_{sr}, \hat{H} \right] \right| \mathbf{c}^k \right\rangle \right\} \;-\; \left\langle \mathbf{c}^k \left| \left[\hat{X}^-_{rs}, \tilde{\hat{H}} \right] \right| \mathbf{c}^k \right\rangle, \tag{3.32}$$

where the Kramers single replacement operators $\hat{X}^-_{rs}$ and $\hat{X}^-_{sr}$ are defined by Eq. (3.8) in the preceding section.

The MCSCF gradient $\mathbf{E}^{[1]}$ in Eq. (3.28) consists similarly of a configurational (Eq. (3.33)) and orbital part (Eq. (3.34)). The evaluation of the corresponding terms is equivalent to the computation of a CI sigma vector and density matrix [43, 61],

$$\mathbf{E}^{[1]c}_\mu \;=\; \left\langle \Phi_\mu \left| \hat{H} \right| \mathbf{c}^k \right\rangle - E^{[0]} c^k_\mu \tag{3.33}$$

$$\mathbf{E}^{[1]o}_{rs} \;=\; -\;\left\langle \mathbf{c}^k \left| \left[\hat{X}^-_{sr}, \hat{H} \right] \right| \mathbf{c}^k \right\rangle. \tag{3.34}$$

[8] For more details about the evaluation of the individual terms, for example the one-index transformed Hamiltonian, the reader may refer to Reference 43.

In its present form the KR-MCSCF program in DIRAC takes advantage of the direct CI techniques implemented in LUCIAREL. The CI program is invoked to compute sigma vectors and (transition) density matrices which occur in the expressions for the orbital and configurational parts of the gradient and Hessian. On this account, the second-order optimization scheme in the KR-MCSCF module greatly benefits from a parallelization of these tasks which is subject of Section 4.1.2 and Section 4.3, respectively.

Part II

Method Development

Parallel Implementations and Method Development

The development of a parallel algorithm described in this thesis comprises implementations for large-scale GASCI programs both at the scalar-relativistic and fully relativistic four-component level and in parts for a relativistic large-scale KR-MCSCF program. Moreover, a new and parallel program module which allows for the computation of atomic and molecular properties at the two- and four-component CI level has come into implementation.

My entire development work has been and is carried out within a local version of the relativistic quantum chemistry program suite `DIRAC` [10]. This program package has been developed over the years by a team of main and contributing authors[9] and recently I joined this team with the contribution of my parallel implementation of the CI program `LUCITA` to the latest `DIRAC08` release making it thus available to a wider public.

At the beginning of my PhD in August 2005, operative implementations of both CI programs `LUCITA` and the relativistic counterpart `LUCIAREL` as well as of the KR-MCSCF module (see Figure 3.1) have been completed with major contributions [60] of my supervisor Timo Fleig. Their potential was indicated in several applications [57–59, 71–73]. However, in consideration of the rapid advance of massively parallel computer architectures as illustrated in Figure 3.2 where the state-of-the-art is depicted for the years 2005 and 2009, a parallel GASCI implementation is an effective means of further extending the applicability of the CI approach. It allows not only to quicken the calculation process in itself, ideally scaling with the number of processors, but also to introduce important savings with regard to hardware requirements per processor.

[9] For a yet incomplete list of current main and contributing authors follow the link in Reference 70.

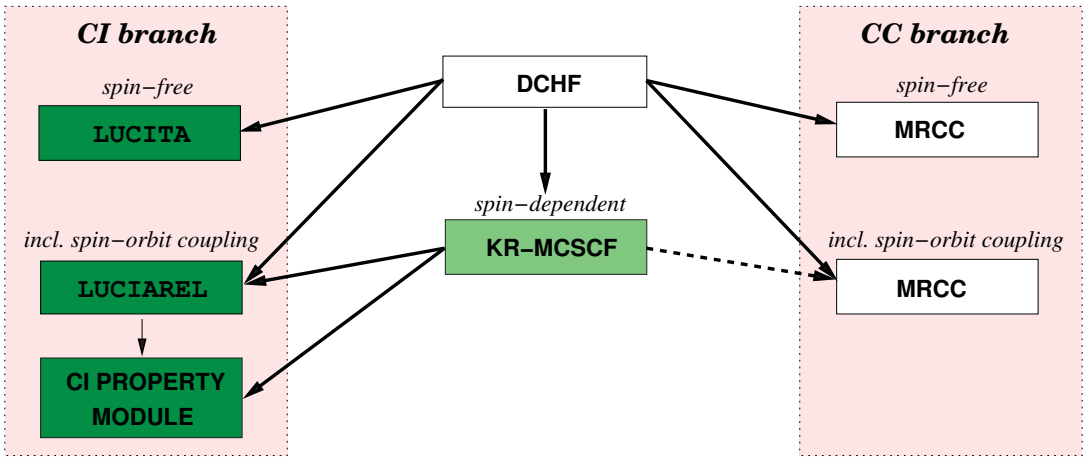

Figure 3.1: An overview of a selection of CI and CC branches in DIRAC and their interrelations. The dark green boxes denote fully parallelized program parts. The partially parallelized KR-MCSCF module is marked with a light green box.

Particular emphasis was therefore put on the design of my parallel CI algorithm which I have developed in collaboration with Prof. H. J. Aa. Jensen during several stays in his group in Odense at the University of Southern Denmark, such that the improved programs can be applied effectively on a supercomputer as well as on today's standard Linux clusters. Important features of this algorithm are discussed in Section 4.1. Sample speed-up tests which simulate large-scale applications are provided in Section 4.2. By means of the current parallel implementations and further code revisions on my part for the CI programs LUCITA and LUCIAREL, elaborate spin-free and relativistic MRCI calculations have become possible. Such applications had been entirely out of reach with the serial implementation whereas they can even be considered as standard now for di- and triatomic molecules containing heavy elements. Illustrative examples are included in the application part of this work, *e.g.* in Section 6.2 or Section 7.2. As the KR-MCSCF program resorts to LUCIAREL for CI-related steps[10] the parallelization of these tasks was greatly facilitated (see Section 4.3).

To summarize, Figure 3.1 displays the branch of MRCI and MCSCF modules I have been working on during my PhD. The dark green boxes mark my fully parallelized GASCI and CI property programs whereas the light green box refers to the KR-MCSCF module which is parallelized to a large extent. I furthermore show in Figure 3.1 the connection of the GASCI/MCSCF modules to one of the MRCC branches in DIRAC that

[10] A second CI program is in use for testing purposes.

has been and is developed with the collaboration of Timo Fleig and my fellow PhD student Lasse K. Sørensen [74–76]. Since the key structures of these programs bear a close resemblance to the corresponding GASCI superstruction, my parallel algorithms presented in the following provide a promising basis for a future parallelization of the MRCC codes.

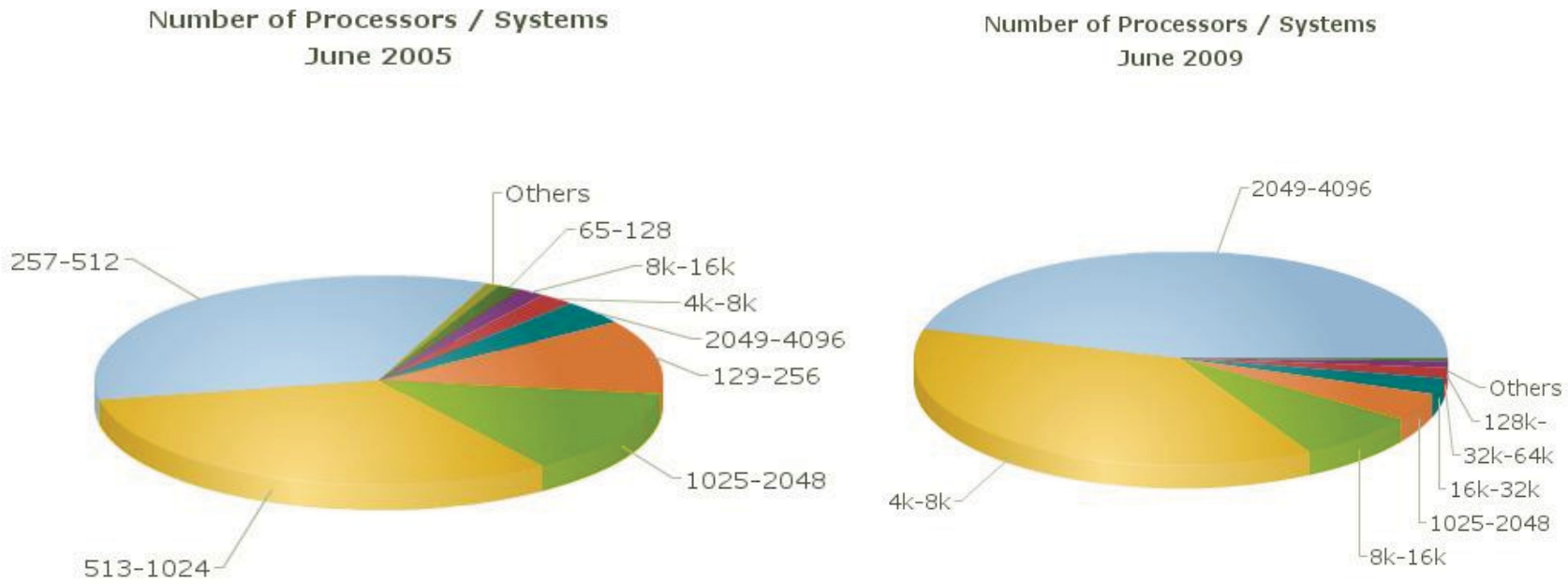

Figure 3.2: Comparison of processor share for all supercomputers compiled in the Top500 list in June 2005 and June 2009. The charts are taken from Reference 77. Unit: $1\text{k} = 10^3$ processors.

Chapter 4

Parallel Relativistic CI Implementation

This chapter summarizes the essentials of my generalized parallel CI algorithm (Section 4.1) and its performance for the resulting parallel MRCI implementations in the spin-free and spin-dependent case (Section 4.2), where a great deal of details is omitted and left to the papers 1 and 2. My contributions towards a fully parallelized KR-MCSCF program are outlined in Section 4.3. In this context, the missing links to complete the parallelization of the MCSCF module are elucidated.

4.1 Parallelization Scheme

The parallel algorithm that applies to both CI implementations is based on an extended usage of functionalities of the message-passing interface (MPI)-1 and MPI-2 libraries [78]. This strategy does not only allow for completely retaining the efficiency of the sequential precursor method (for a given process) but, in addition, facilitates further algorithmic improvements in the future.

4.1.1 General Considerations

As the most used computer architectures for scientific computing change every few years (one example: single core → dual core → quad core → etc.), it has been a major design

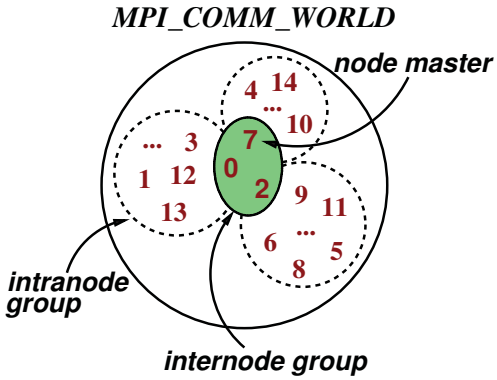

Figure 4.1: Process partitioning for different communication and resource patterns applied in the parallel implementations. Each number corresponds to a unique process that is contained in the global group of all processes MPI_COMM_WORLD.

goal for me that the algorithm must be flexible and adaptable, such that it will be able to run efficiently on all the most common computer architectures. This design goal was achieved by using a dual-level structure consisting of *intranode* and *internode* groups as depicted in Figure 4.1. The typical computer architecture fits into the template n nodes with m cores, where a node is defined as a (sub)system with shared memory and shared disks. Usually, the bandwidth for *internode* communication is much slower than for *intranode* communication. A parallel calculation with, say, 32 tasks on a true shared memory machine would then correspond to $n = 1, m = 32$, while the same job on a Linux-based cluster with quad cores would correspond to $n = 8, m = 4$. To this end, a node master was chosen for each set of m cores that exclusively takes care of expensive communication tasks among the n nodes. The node-master concept proved to be particularly useful in the $\boldsymbol{\sigma}$-vector evaluation (see Section 4.1.2).

The central idea of the algorithm is that in order to minimize time-consuming communication tasks, each core p is statically assigned all coefficients related to a specific subset of all the Slater determinants, $\mathbf{b}_n(p)$ for all $\mathbf{b}_n$ vectors as well as $\boldsymbol{\sigma}_n(p)$ for all $\boldsymbol{\sigma}_n$ vectors. In this context, the *TTSS* blocking of the vectors $\mathbf{b}_n$ and $\boldsymbol{\sigma}_n$ which was introduced in Section 3.1 plays an essential role. By using the *TTSS* blocks as units to create a close to optimal *static* block distribution, it is of the utmost importance to predict well *a priori* the computational load arising from each *TTSS* block. At the outset of a calculation each *TTSS* block of nonzero length is assigned to a specific process as indicated by the arrows in Figure 4.2, thereby taking account of a block-"weight" criterion. This individual block-"weight" criterion is calculated from an estimation of the respective

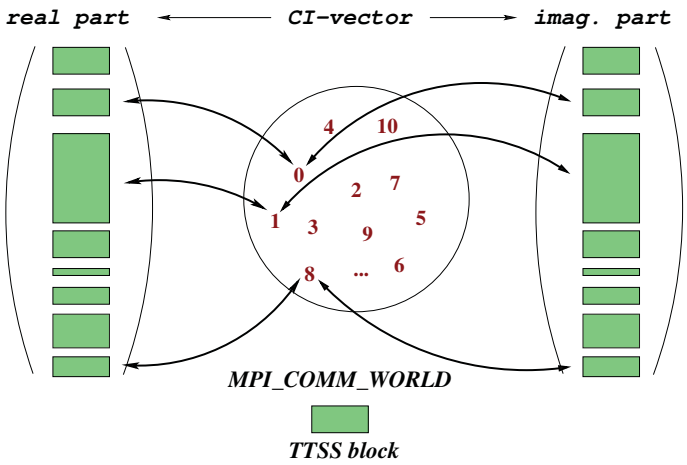

Figure 4.2: Static *TTSS*-block assignment among all available processes as central parallelization pattern. Each number corresponds to a unique process contained in the global group of all processes MPI_COMM_WORLD. The process holding the *TTSS* block with the real part of the coefficients also treats the corresponding non-zero imaginary part if applicable (only for `LUCIAREL` and complex matrix double groups).

computational load in the dominating linear transformation step $(60 - 80\%)$ of a Davidson iteration and the number of determinants in a given *TTSS* block. Achieving an even "weight" distribution of the *TTSS* blocks among all processes ensures a decent static load balancing. The performance of this approach is demonstrated in Section 4.2 on the basis of two representative parallel test simulations in the spin-free and spin-dependent case, respectively.

Each generalized Davidson iteration, sketched in a flow chart diagram in Figure 4.3, consists of two distinct parts, each with different requirements. The parallelization of the important $\boldsymbol{\sigma}_n$-vector step (green box in Figure 4.3), is discussed in detail in Section 4.1.2. The second main part is comprised by the subspace operations such as the determination of the current residual (see Figure 4.3). Two of the computationally most expensive subspace tasks are

$$\tilde{H}_{kl} = \boldsymbol{\sigma}_k^\dagger \mathbf{b}_l = \sum_p^{N_{proc}} \boldsymbol{\sigma}_k^\dagger(p)\mathbf{b}_l(p) = \sum_p^{N_{proc}} \tilde{H}_{kl}(p) \tag{4.1}$$

$$\tilde{S'}_{kn} = \mathbf{b}_k^\dagger \mathbf{b'}_n = \sum_p^{N_{proc}} \mathbf{b}_k^\dagger(p)\mathbf{b'}_n(p) = \sum_p^{N_{proc}} \tilde{S'}_{kn}(p) \tag{4.2}$$

which are needed, respectively, for the subspace eigenvalue problem and for the Gram-Schmidt orthogonalization of a new trial vector $\mathbf{b'}_n$ to previous trial vectors. Since the computations of $\tilde{H}_{kl}(p)$ and $\tilde{S'}_{kn}(p)$ can be carried out locally on each process, with this

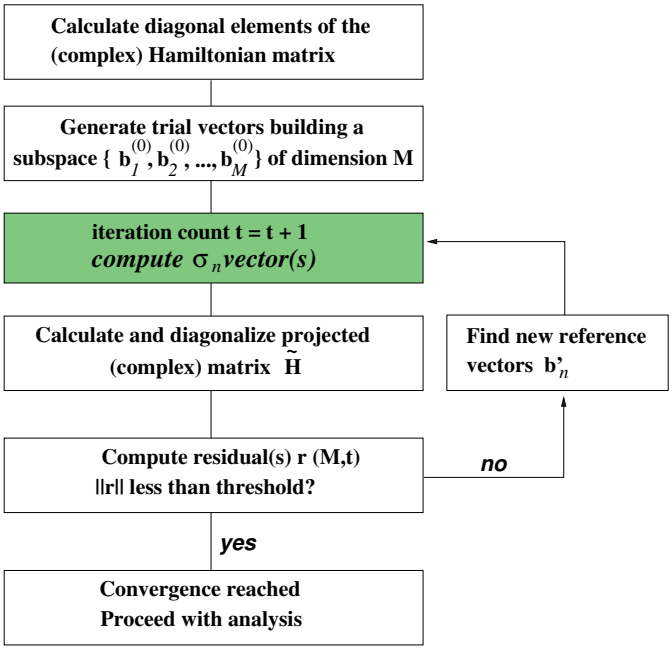

Figure 4.3: Flow chart of the iterative generalized Davidson diagonalization method as implemented in `LUCITA` and `LUCIAREL`.

design no long vectors but only scalars as $\tilde{H}_{kl}(p)$ and $\tilde{S}_{kn}(p)$ need to be communicated for the subspace tasks by means of fast global reduction operations (MPI_allreduce). The only complication that arose for these tasks in the spin-dependent case were due to the fact that the vectors and scalars are then generally complex-valued.

The application of a static distribution scheme of *TTSS* blocks as well as of a dual-level communication model comes in handy to introduce further computational savings and cut down hardware requirements. These are summarized in the following[1]:

1. *disk storage.* The organization of *TTSS* blocks in batches, where a batch is defined as the maximum sum of *TTSS* blocks that fits into the core memory, originated already from the sequential precursor algorithm. For the parallel algorithm described here, the individual number of batches on a given process however decreases significantly as the total number of processes increases. This reduction was achieved by explicitly setting the length of all *TTSS* blocks to zero that are not assigned to a given process. The total input/output (I/O) cost for each process was thereby greatly reduced, in particular for the subspace operations as these local steps are typically processed in terms of batches.

[1]Further details can be found in Paper 1 and Paper 2.

In addition, file sharing based on the established *intranode* group was enabled among the m cores minimizing the internal I/O load. If, on the other hand, a global file system is provided it may optionally be utilized for a full file-sharing model among all processes by use of MPI file-I/O techniques. A shareable file which contains all $\mathbf{b}_n$-*TTSS* blocks was of particular use in the $\boldsymbol{\sigma}_n$-vector computation since costly *internode* communication (see Sec. 4.1.2 for more details) could be avoided.

2. *two-electron integrals.* As a natural consequence of the static *TTSS*-block distribution a significant reduction of one- and two-electron integrals that have to reside in core memory of a given processor, was accomplished. A processor stores only those integrals that are required to calculate the respective $\boldsymbol{\sigma}_n$-*TTSS* blocks in the linear transformation step.

3. *shared memory.* Since the m cores of a single node representing an *intranode* group share core memory (but often not memory cache) one could take into account shared-memory like access algorithms based on MPI-2 one-sided communication routines (MPI_get, MPI_accumulate) for memory demanding quantities such as the two-electron integrals and the required blocks of the $\mathbf{b}_n$ vector. By these means, only a single copy of, *e.g.* the essential two-electron integrals (see preceding paragraph), needs to be kept in core memory of a given *intranode* group. To ensure in general high efficiency a passive target communication model (MPI_win_lock(MPI_lock_shared)) was implemented as visualized by the one-directional arrows in Figure 4.4. A deeper understanding of an optimal performance of such a one-sided communication model is of particular importance since it shall be employed for the final parallelization of the KR-MCSCF program (see Section 4.3). Elaborate test studies on cache-based multi-core systems, today's most common system architecture, are being carried out at the time of writing this thesis.

In summary, it can be stated that the parallel algorithm which I outlined above is universally applicable to any (large-scale) eigenvalue problem that can be solved iteratively. A prerequisite is, however, that the Hamilton matrix, respectively, the solution vector can be divided in some way into subunits. In the present case, this requirement was met through the *TTSS*-block partitioning of the CI vector and sigma vectors.

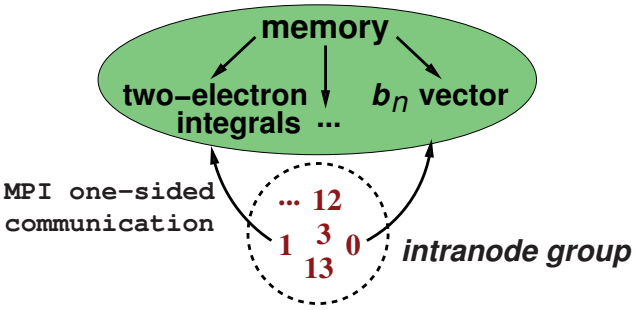

Figure 4.4: Shared-memory access pattern for memory demanding quantities. Each number corresponds to a unique process that belongs to a given *intranode* group.

4.1.2 Sigma-Vector Evaluation

In Paper 1 and Paper 2 different approaches to an efficient parallelization scheme for the $\boldsymbol{\sigma}_n$ task [79–82] were discussed at length. In these papers the superiority of a distributed data model on which I will elaborate in the following was justified in agreement with Gan *et al.* [80]. In the conclusion of this section I illustrate the decisive drawback of an alternative approach, namely the replicated data model.

In Figure 4.5, the calculation of a sigma-vector $\boldsymbol{\sigma}_n$ is outlined as it is implemented for the present GASCI algorithms. Each segment, here a *TTSS* block, of the complete sigma vector $\boldsymbol{\sigma}_n$ is coupled through the Hamiltonian matrix (cf Eq. (3.19)) to the same *TTSS* block of $\mathbf{b}_n$, but also to specific other $\mathbf{b}_n$-*TTSS* blocks. To compute a full sigma-vector *TTSS* block locally on its statically designated process (see Figure 4.2) using a distributed data model, therefore necessitates for each process the collection of all those $\mathbf{b}_n$-*TTSS* blocks that couple to the $\boldsymbol{\sigma}_n$-*TTSS* blocks assigned to this process, prior to the actual "matrix × vector" contraction (code line 25 in Fig. 4.5). For this purpose, a global communication step among all node masters was introduced at the beginning of each sigma-vector evaluation where lists of required $\mathbf{b}_n$-*TTSS* blocks for each partial *intranode* linear transformation are utilized. These `INTEGER` lists, which are of dimension [number of *TTSS* blocks] are constructed at the outset of the diagonalization procedure and kept in main memory.

The essential gathering step can efficiently be carried out using either a collective communication (MPI_bcast) or one-sided communication (MPI_get) approach[2]. The current collection algorithm was designed such that the *internode* communication is min-

[2]The latter approach is under development.

```
For each process (which is assigned a specific subset of all TTSS blocks):
if distributed data approach then
  loop {TTSS blocks}
    if global file system then
      if my b_n-TTSS block then
        store block into the globally accessible file BBLOCKS
      end if
    else
      if my process is node master then
        if this b_n-TTSS block is on my node then
          scatter this block to relevant node masters with MPI_bcast
          (unless one-sided communication is used)
        else if this block is needed for my node then
          gather this b_n-TTSS block from another node master
          using either MPI_bcast or MPI_get
          store block into the intranode specific file BBLOCKS
        end if
      end if
    end if
  end loop[TTSS blocks]
end if
loop {my σ-batches of σ_n-TTSS blocks}
  loop {my b-batches of b_n-TTSS blocks}
    read this b-batch from the BBLOCKS file
    loop {all my connecting b_n-TTSS blocks in current b-batch}
      loop {my σ_n-TTSS blocks in current σ-batch}
        add contribution to current σ_n-vector TTSS block
      end loop[my σ_n-TTSS blocks in current σ-batch]
    end loop[all my connecting b_n-TTSS blocks in current b-batch]
  end loop[my b-batches of b_n-TTSS blocks]
  if replicated data model then
    sum up contributions to my σ_n-TTSS blocks from all processors using either
    MPI_reduce or MPI_allreduce
  end if
end loop[my σ-batches of σ_n-TTSS blocks]
```

Figure 4.5: Simplified pseudo-code visualization of the evaluation of the linear transformation step $\boldsymbol{\sigma}_n = \mathbf{H}\,\mathbf{b}_n$, as implemented in `LUCITA` and `LUCIAREL`. The two main approaches to a parallelization of this task, namely a distributed and replicated data model, are indicated in the algorithm.

imized. For example, the communication group consisting of all node masters is further split (MPI_comm_split) whenever a *TTSS* block is not required for the sigma-vector evaluation of a given *intranode* group. The actually communicated $\mathbf{b}_n$-*TTSS* blocks are stored for each *intranode* group in a shared coefficient file `BBLOCKS` that is accessible by all individual processes on this node via MPI file-I/O routines.

A major advantage of the presented strategy is that costly global communication inside the sigma-vector loop structure (see Figure 4.5) is avoided. Global (blocking) communication would have led to an intrinsic barrier and therefore in general to idling times and considerable performance loss. This, on the other hand, applies to the second, alternative algorithm ("replicated data model" in Figure 4.5) where each process computes all $\boldsymbol{\sigma}_n$ contributions from *its* $\mathbf{b}_n$-*TTSS* blocks. Unless all active $\boldsymbol{\sigma}_n$-*TTSS* blocks fit into memory on all nodes, the $\boldsymbol{\sigma}_n$-*TTSS* blocks must be added up with an MPI_reduce or MPI_allreduce call at the end of each $\boldsymbol{\sigma}$-batch (after code line 28 in Figure 4.5) which would become a barrier and cause idling time.

4.2 Parallel Performance

The overall performance of the parallel algorithm presented in the preceding section was examined on the basis of extensive large-scale test applications both in the spin-free and spin-dependent case in Paper 1 and Paper 2, respectively. In what follows, I will thus restrict myself to a discussion of two representative examples.

The `LUCITA` performance test was carried out on a Linux-based cluster (`Horseshoe`) that is made up of 200 nodes of two Intel Woodcrest (2.66 GHz; dual core version) processors each, equipped with either 4GB (160 nodes) or 8GB (40 nodes) of shared main memory and a dual Gigabit ethernet connection, respectively. The nodes are interconnected by Gigabit switches and provided with local disks. The second system is an IBM p6 575 cluster (`Jump`) consisting of symmetric multiprocessor nodes with each node holding 32 simultaneous multithreaded Power6 processors running at 4.7 GHz. Each node has a ten Gigabit ethernet access to a general parallel file system (GPFS) and the nodes are interconnected by an InfiniBand connection for MPI communication.

The speedup $\mathcal{S}(p, N)$ which is used to evaluate the performance of the parallel

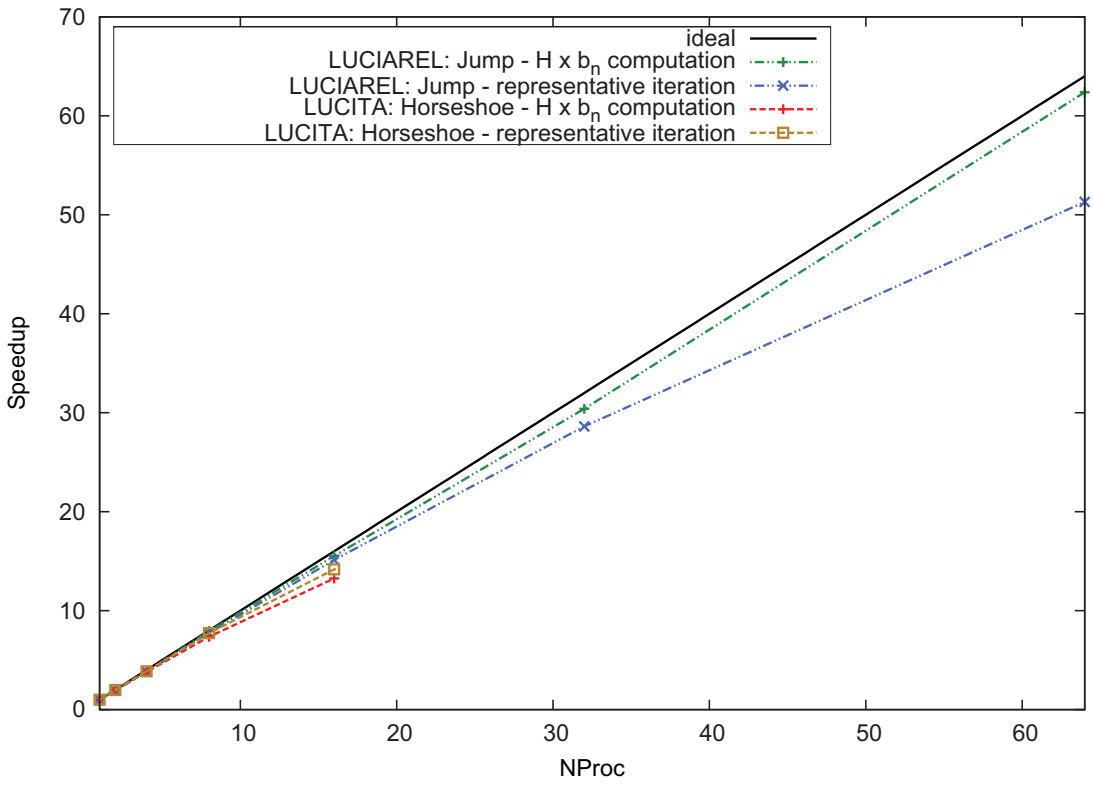

Figure 4.6: Parallel performance plots for MRCI calculations on the ground state of H_2O (`LUCITA`; point group C_{2v}; DZ basis) and BiH (`LUCIAREL`; double point group C_2^*; TZ basis). The `LUCITA` performance test comprises roughly 1.5×10^9 determinants whereas the CI expansion spans approximately 428×10^6 determinants in the `LUCIAREL` test case. Details on the computer architectures of the Linux-based cluster `Horseshoe` and the supercomputer `Jump` are given in the text.

implementations is defined as

$$\mathcal{S}(p, L) = \frac{T(1, L)}{T(p, L)}, \tag{4.3}$$

where $T(p, L)$ is the time required to solve a problem of size L on p processors.

Figure 4.6 displays the speedup for the linear transformation step ("H x $\mathbf{b}_n$" computation) and for a representative Davidson iteration that were obtained for a spin-free `LUCITA` benchmark calculation (roughly 1.5×10^9 determinants) on the ground state of the water molecule (C_{2v} symmetry) and a `LUCIAREL` benchmark calculation ($\approx 428 \times 10^6$ determinants) on the ground state of the bismuth hydride molecule (double point group C_2^*). The shown examples are calculated for the respective test cases **B** in Paper 1 and Paper 2, and for further computational details the reader is referred to the papers.

The depicted LUCITA benchmark test was carried out applying an "*n nodes using m = 1 core on each node*" allocation scheme which was found to yield in general the best performances on Linux-based clusters (see Paper 1 and Paper 2)[3]. As for the present case, an excellent scalability is obtained with regard to both the $\boldsymbol{\sigma}$-vector computation and the total Davidson iteration. The speedup for $n = 16$ processors is 13.25 (H x $\mathbf{b}_n$ step) and 14.18, respectively, which exemplifies the effectiveness of the static load-balancing scheme. The higher $\mathcal{S}$ value for the total Davidson iteration compared to the value for the $\boldsymbol{\sigma}$-vector step originates mostly from an intrinsic I/O parallelization. As a result of the *TTSS*-block distribution, the I/O intense Davidson subspace-vector tasks (cf Eq. (4.1)) are spread out to the local disks of the individual processors.

The remaining two curves in Figure 4.6 demonstrate the speedup for the LUCIAREL benchmark test performed on the supercomputer Jump for up to 64 processors. The scaling for the $\boldsymbol{\sigma}$-vector step is almost perfect with a speedup of $\mathcal{S} = 62.38$ for 64 processors. A drop in the speedup is, however, observed with regard to a total iteration, in particular for a larger number of processors, that is 28.62 (32 processors) and 51.30 (64 processors), respectively. These findings were partly ascribed to the increasing GPFS load, most notably in the Davidson subspace-operation parts where large chunks of *TTSS* blocks are read in and written almost simultaneously by all processes (see preceding paragraph).

Summarizing, the performance of the parallel implementations of the MRCI programs LUCITA and LUCIAREL based on the idea of distributed data model combined with a static load-balancing scheme is excellent. As visualized by the lines nearly parallel to optimum performance in Figure 4.6 for up to 32 processors, the algorithm works properly on two of the most wide-spread types of system architectures.

4.3 Outlook for a Parallel KR-MCSCF

The constitutive elements of a restricted-step second-order MCSCF optimization algorithm that is implemented for the KR-MCSCF module in the DIRAC software package, were outlined in Section 3.2. Table 4.1 summarizes the various CI contributions to the

[3] Arising difficulties on multi-core machines that are associated with an application of an "*n nodes using m > 1 core on each node*" scheme, are explained in full detail in Paper 1 and Paper 2. Moreover, an in-depth study of this topic was recently published by Kleinschmidt and co-workers [83].

Table 4.1: Direct CI contributions to the MCSCF gradient and Hessian. The original table is taken from Reference 84.

Gradient $\mathbf{E}^{[1]}$	Config. part $\mathbf{E}^{[1]c}$	CI sigma vector $\hat{H} \mid c^{(k)} \rangle$
Gradient $\mathbf{E}^{[1]}$	Orbital part $\mathbf{E}^{[1]o}$	CI density matrices $\left\langle c^{(k)} \middle\| \left[\hat{X}^{-}_{sr}, \hat{H}\right] \middle\| c^{(k)} \right\rangle$
Hessian $\mathbf{E}^{[2]}$	Config. part $\mathbf{E}^{[2]c,c/o}$	CI sigma vector $\hat{H} \mid c^{(k)} \rangle$
		CI sigma vector $\hat{H} \mid B \rangle$
Hessian $\mathbf{E}^{[2]}$	Orbital part $\mathbf{E}^{[2]o,c/o}$	CI density matrices $\left\langle c^{(k)} \middle\| \left[\hat{X}^{-}_{sr}, \tilde{\hat{H}}\right] \middle\| c^{(k)} \right\rangle$
		CI transition densities $\left\langle c^{(k)} \middle\| \left[\hat{X}^{-}_{sr}, \hat{H}\right] \middle\| B \right\rangle$

calculation of both the MCSCF gradient $\mathbf{E}^{[1]}$ and Hessian $\mathbf{E}^{[2]}$ (see Eq. (3.28)) where the superscripts ^{c} and ^{o} refer to the configurational and orbital parts of the respective quantities.

As the parallelization of the sigma-vector evaluation was already presented in Section 4.1.2, I proceed with the calculation of CI (transition) density matrices. Replacing the integrals $(p\bar{q}|rs)^{r,i}$ in the expression for the computation of a $\boldsymbol{\sigma}$-vector fragment in Eq. (3.19) with the expansion coefficients of the left-hand side determinants $b^{r,i}_{\mathcal{S}\bar{\mathcal{T}}}$ yields an expression for the corresponding two-particle density matrix fragment (real part),

$$\rho^{++(r)}\,(p\bar{q}rs) \;=\; \sum_{\mathcal{U}\bar{\mathcal{V}}} \sum_{\mathcal{S}\bar{\mathcal{T}}} \{ b^{r}_{\mathcal{S}\bar{\mathcal{T}}}\; A^{\mathcal{S}\bar{\mathcal{T}},\mathcal{U}\bar{\mathcal{V}}}_{p\bar{q}rs}\; b^{r}_{\mathcal{U}\bar{\mathcal{V}}} \;+\; b^{i}_{\mathcal{S}\bar{\mathcal{T}}}\; A^{\mathcal{S}\bar{\mathcal{T}},\mathcal{U}\bar{\mathcal{V}}}_{p\bar{q}rs}\; b^{i}_{\mathcal{U}\bar{\mathcal{V}}} \}. \tag{4.4}$$

A comparison of Eqs. (3.19) and (4.4) then reveals that in the latter case (density matrix case) the contraction runs now over coefficients rather than integrals which makes the evaluation procedure for both tasks almost identical. Transition densities are likewise obtained by substituting the ket vector in Eq. (4.4) with the appropriate CI expansion of the reference vectors.

The similarity between the $\boldsymbol{\sigma}$-vector and density-matrix construction suggests a static assignment of $\mathbf{b}_n$-*TTSS* blocks (see Section 4.1.1) for the parallelization of the latter task. Hence, each process is assigned a corresponding set of *TTSS* blocks of the bra ($b^{r,i}_{\mathcal{S}\bar{\mathcal{T}}}$) *and* ket vector ($b^{r,i}_{\mathcal{U}\bar{\mathcal{V}}}$). In contrast to the $\boldsymbol{\sigma}$-vector computation only partial density-matrix elements are calculated and the initial gathering step (code lines 2-19 in Figure 4.5) is omitted. To subsequently obtain the full density matrix, the individual elements are

summed up using either MPI_reduce (only on the master process) or MPI_allreduce (on all processes) in an extra loop running over the density matrix elements. This scheme avoids any global communication within the density-matrix evaluation which would otherwise introduce a barrier and cause idling time. By contrast, the computational overhead of the additional summation step is comparatively small.

My development of parallel algorithms for the $\boldsymbol{\sigma}$-vector and density-matrix evaluation completes the parallelization of the essential inner parts of the MCSCF algorithm, namely the CI tasks, the integral transformation at the outset of each macro iteration and the computation of generalized Fock matrices[4]. It remains then to devise a parallel algorithm for the outer structure of the large-scale second-order MCSCF algorithm. This includes a suitable handling of memory demanding quantities such as for example the complete set of one- and two-electron integrals or the current expansion point vector $|\, c^{(k)} \,\rangle$. Since, at present, the master process invokes the slave processes only at each of the above mentioned entry points to the inner parts, all these quantities have to be kept in core memory of a single process. In a future parallel scheme, the memory requirements for the individual processes could be alleviated, *e.g.* by introducing a shared-memory like model within an *intranode* group (see Figure 4.4).

[4] A parallelized integral-transformation module as well as a parallelized module for the generation of Fock matrices were already available in DIRAC.

Chapter 5

Parallel CI Property Module

In this chapter I present the implementation of a parallelized module which is part of the DIRAC program package and can be used to compute first-order time-independent properties of atomic and molecular compounds at the CI level. In the following section, a general definition of atomic and molecular properties is given as well as a brief overview of different approaches to their computational evaluation. The second section comprises the details of our parallel algorithm. Finally, a first application is presented and technical issues that were encountered in the course of this work are explained in more detail.

5.1 Theoretical Considerations

Besides the derivation of spectroscopic properties as for example the equilibrium bond distance R_e or the harmonic frequency ω_e, the determination of electric, magnetic and optical properties is an important aspect in theoretical studies of atomic and molecular compounds. A molecular (atomic) property can be defined as the response of the electronic structure of a given system to an applied external perturbation $V(\lambda)$ that is characterized by its perturbation strength λ. As an example, time-independent first-order properties may be derived from the experiment in accordance with the so-called empirical definition [85]:

$$\mathbf{E^{(1)}} := \lim_{\lambda \to 0} \lim_{\lambda' - \lambda \to 0} \frac{E(\lambda') - E(\lambda)}{\lambda' - \lambda}. \tag{5.1}$$

The full Hamiltonian of the perturbed system may be decomposed into a sum of the

zeroth-order (unperturbed) Hamiltonian and the perturbation operator,

$$\hat{H}(\lambda) = \hat{H}_0 + V(\lambda). \tag{5.2}$$

Furthermore, the total energy $E(\lambda)$ may be expressed as a Taylor expansion in terms of the perturbation strength λ:

$$\begin{aligned} E(\lambda) &= \sum_{n=0}^{\infty} \frac{1}{n!} \left(\frac{d^n E(\lambda)}{d\lambda^n} \right)_{\lambda=0} \cdot \lambda^n \\ &= E^{(0)} + \mathbf{E^{(1)}}\lambda + \frac{1}{2}\lambda^2 \mathbf{E^{(2)}} + \dots \end{aligned} \tag{5.3}$$

Molecular properties of order n of a system in a given quantum state are therefore defined as the nth-order expansion coefficients $\left(\frac{d^n E}{d\lambda^n}\right)_{\lambda=0}$ of the power series in Eq. 5.3. Correspondingly, molecular properties for time-independent perturbations may also be obtained directly from the energy derivatives at zero perturbation strength [86]:

$$\begin{aligned} \mathbf{E^{(1)}} &= \left. \frac{dE(\lambda)}{d\lambda} \right|_{\lambda=0} \\ \mathbf{E^{(2)}} &= \left. \frac{d^2 E(\lambda)}{d\lambda^2} \right|_{\lambda=0} \\ &\vdots \quad \vdots \quad \vdots \\ \mathbf{E^{(n)}} &= \left. \frac{d^n E(\lambda)}{d\lambda^n} \right|_{\lambda=0} \end{aligned} \tag{5.4}$$

To evaluate the energy derivatives either a numerical or analytical approach could be employed.

The numerical method is based on a sufficiently large series of energy calculations of the perturbed system where the perturbation $V(\lambda)$ has been added to the zeroth-order Hamiltonian $\hat{H}_0$ for a given set of small and finite perturbation strengths λ (finite-field technique). The nth-order derivatives may then be found through a polynomial fit of the λ-dependent function of the total energy E(λ). In so doing, the polynomial pre-factors straightforwardly deliver the desired nth-order properties. Particular care must thereby be taken of the energy convergence in the wave function optimization step. The approximation of higher-order (> first-order) derivatives by numerical differentiation typically calls for an energy convergence to at least 10^{-10} $\mathrm{E_h}$. A general discussion on the applicability of the finite-field method for the calculation of molecular properties may be found for example in [86]. In Ref. 87, T. Saue addresses the numerical approach in

particular with regard to relativistic four-component calculations. The numerical differentiation technique has been successfully employed in this work. With due attention to these caveats, ground-state dipole moment functions of RbYb (see Paper 3) and $(RbBa)^+$ (see Paper 5) were calculated using a highly sophisticated coupled cluster approach.

Since the CI property module in its present implementation is restricted to the calculation of first-order properties for time-independent perturbations the evaluation of the first-order energy derivation shall in the following be examined in more detail.

The analytical method requires the explicit differentiation of the energy with respect to the perturbation strength and involves in general considerable, additional programming effort. The Hellmann-Feynman theorem, on the other hand, may equally well be used to compute the first-order derivative. It states that the first-order energy derivative $\mathbf{E^{(1)}}$ can be derived from the expectation value of the perturbation operator $\hat{H}_1$,

$$\begin{aligned} \mathbf{E^{(1)}} &= \left.\frac{dE(\lambda)}{d\lambda}\right|_{\lambda=0} = \left\langle \Psi \left| \frac{\partial \hat{H}(\lambda)}{\partial \lambda} \right| \Psi \right\rangle \\ &= \left\langle \Psi \left| \hat{H}_1 \right| \Psi \right\rangle, \end{aligned} \tag{5.5}$$

given that Ψ is an exact, normalized eigen state of the full Hamiltonian $\hat{H}(\lambda)$. As exact solutions of the full Hamiltonian $\hat{H}(\lambda)$ are in practice mostly not available, approximate wave functions which depend on a set of variation parameters $\alpha(\lambda)$ must be taken into account instead. The resulting first-order energy derivative then reads:

$$\mathbf{E^{(1)}} = \left.\frac{\partial E(\lambda)}{\partial \lambda}\right|_{\lambda=0} + \sum_k \left.\frac{\partial E(\alpha)}{\partial \alpha_k}\right|_{\lambda=0} \left.\frac{d\alpha_k}{d\lambda}\right|_{\lambda=0}. \tag{5.6}$$

It follows from Eq. 5.6 that the Hellmann-Feynman theorem may likewise be satisfied for approximate wave functions if the wave function is variational with respect to $\alpha(\lambda)$,

$$\left.\frac{\partial E(\alpha)}{\partial \alpha_k}\right|_{\lambda=0} = 0, \tag{5.7}$$

or if the parameters $\alpha(\lambda)$ do not depend on the perturbation

$$\left.\frac{d\alpha_k}{d\lambda}\right|_{\lambda=0} = 0. \tag{5.8}$$

It can be shown [88] (and references therein) that the second term in Eq. 5.6 indeed vanishes for wave functions obtained from either HF or MCSCF optimizations. In this case, there are no objections to the expectation-value approach to first-order properties.

This situation is, on the other hand, not given upon including dynamic electron correlation through, *e.g.* , a restricted CI expansion where neither Eq. 5.7 nor Eq. 5.8 are fulfilled. On this account, corrections of Brillouin-type [88] to the Hellmann-Feynman theorem were derived and, furthermore, their significance was investigated by reference to benchmark studies [85]. In this work, Diercksen *et al.* concluded on the basis of, admittedly, very limited CI wave functions that the extent of a correction term to the Hellmann-Feynman theorem strongly depends on the role played by correlation effects for the calculation of a given property. If correlation effects are only of minor importance for a given first-order property, similar results from the finite-field technique and the expectation-value approach could be expected. In a later work, Ernzerhof *et al.* [89], however, stated that, although the Hellmann-Feynman theorem does formally not hold for CI wave functions other than Full CI, there is in itself no argument for an *a priori* preference of the derivative approach to the expectation-value approach. The latter method has indeed been proven to yield reliable predictions of first-order properties in many different cases [85, 90–92]. As my present relativistic implementation also exploits the Hellmann-Feynman theorem a similar performance could be expected.

Finally, it is worthwhile to mention that both time-independent and time-dependent general-order properties can be calculated in the more sophisticated framework of response theory [93, 94]. This method is currently implemented in the `DIRAC` program for HF and DFT response calculations at the one-, two- and four-component level. In future work, this approach shall be extended to MCSCF response functions at the two- and four-component level.

5.2 Implementation for One-Particle Operators

After having established the theoretical framework for the evaluation of first-order properties at the CI level, I consider in this section characteristics of my parallel implementation of a two- and four-component CI property module based on an expectation-value approach. The implementation of the module is adapted to the parallelized CI program `LUCIAREL`, thus taking advantage of all its features which are described in Chapter 4 and Paper 2. As pointed out in the preceding section, the underlying Hellmann-Feynman theorem is a computationally simple means to calculate first-order properties at the cor-

related level for arbitrary time-independent perturbations of one-particle operators. It may be used with due care, though, since the expectation-value approach is fully valid only for wave functions that satisfy Eq. 5.7 or Eq. 5.8.

The operating sequence of a property evaluation essentially consists of three parts on which I shall elaborate in the following. In a first step the symmetries of the relevant set of $\{\hat{f}_1, \hat{f}_2, \ldots, \hat{f}_M\}$ one-particle operators are determined in the respective abelian sub-double group which may have to be applied in the CI algorithm In addition, the one-electron integrals are sorted for their convenient use in the CI program. The second part comprises the actual calculation of the elements of the property matrix $\mathbf{P}$ where the results for the kth operator $\hat{f}_k$ are stored separately for a subsequent manipulation of the data. The remaining part encompasses distinct routines which can be used to, *e.g.* , further analyze the computed properties or simply write them to file in an ordered, human-readable format.

The basic idea of my approach is to compute the linear transformation $\boldsymbol{\sigma}_i^{(k)} = \hat{f}_k|\mathbf{C}_i >$ for the kth perturbation operator and to make use of the resulting $\boldsymbol{\sigma}_i^{(k)}$ vector to calculate the respective property matrix entry by means of a simple dot product $\left\langle \boldsymbol{\sigma}_i^{(k)}|\mathbf{C}_i \right\rangle$. An alternative procedure could be to use the various one-particle density matrices $\mathbf{D}$ derived from all possible C-vector combinations. In this scheme, the desired property matrix element would thus be obtained from the trace $tr(\mathbf{F}_k)$ of the matrix $\mathbf{F}_k = \mathbf{f}_k \times \mathbf{D}$. This approach has been employed for example in the property module of the DFT/MRCI program of Grimme and co-workers [95]. The density-matrix based scheme should be advantageous in particular if a large number of properties needs to be calculated for a relatively small set of eigenvectors. By contrast, my $\boldsymbol{\sigma}$-vector driven approach comes in handy for a comparatively large number of C-vectors and a limited set of property operators. For example, if one assumes six one-particle operators and 100 CI vectors, a total of $\frac{100\times101}{2} = 5050$ one-particle densities would have to be calculated. In the present approach this reduces to 600 $\boldsymbol{\sigma}$-vector computations and the computation of the corresponding dot products.

As briefly mentioned above, additional steps of low computational cost are required in my present implementation prior to the actual evaluation of the property matrix. In Figure 5.1 the procedure of the symmetry assignment and the ensuing rearranging step of the one-electron integrals is outlined in a pseudo-code illustration for a given one-particle

1. **loop** {M one-particle operators $\hat{f}$ }
2. **loop** {all active spinors φ_p, $\varphi_{\overline{p}}$}
3. **loop** {all active spinors φ_p, $\varphi_{\overline{p}}$}
4. identify the index pair (a,b) pointing to the largest absolute element $abs(f_k^{\mathsf{max}}(a,b))$ in the kth operator matrix $\mathbf{f}_k$
5. **end loop**[all active spinors φ_p, $\varphi_{\overline{p}}$]
6. **end loop**[all active spinors φ_p, $\varphi_{\overline{p}}$]
7. use double-group multiplication table to obtain the symmetry $\Gamma_{\hat{f}_k}$ of $\hat{f}_k$:
8. $\Gamma_{\hat{f}_k} = \Gamma_{\varphi_a}^{-1} \otimes \Gamma_{\varphi_b}$
9. store $\Gamma_{\hat{f}_k}$ in array $\mathsf{fsym}[M]$ and rearrange one-electron integrals in $\mathbf{f}_k$ according to the excitation class formalism
10. **end loop**[M one-particle operators $\hat{f}$]

Figure 5.1: Pseudo-code visualization of the identification of the operator symmetry in the applied abelian sub-double group in `LUCIAREL`.

operator $\hat{f}_k$. For the following a Kramers-paired spinor basis $\{\varphi_p,\ \varphi_{\overline{p}}\}$ is assumed. A straightforward way of finding the symmetry $\Gamma_{\hat{f}_k}$ of an operator $\hat{f}_k$ in the respective sub-double group arises from its matrix elements. First of all the index pair (a,b) of Kramers-paired spinors is determined that combines into the largest value $abs(f_k^{\mathsf{max}}(a,b))$ in the total operator matrix. Since the symmetry representations of the Kramers spinors are known through the specification of symmetry descriptors in the program input the required symmetry of the operator is obtained by a direct product (line 8 in Figure 5.1):

$$\Gamma_{\hat{f}_k} = \Gamma_{\varphi_a}^{-1} \otimes \Gamma_{\varphi_b}. \tag{5.9}$$

The result of Eq. 5.9 is afterwards stored in an integer array $\mathsf{fsym}[M]$ for later use in the property matrix evaluation. Knowing the symmetry of the kth operator $\hat{f}_k$ it is now possible to sort the one-electron integrals according to the excitation class formalism [58] (see also Section 3.1) on which the CI program is based. It should be noted that the above described initial part of the property module is not parallelized since it does not involve any heavy computational task.

In what follows I shall deal with the essential inner parts of my property module which are illustrated in Figure 5.2. The key concept of my parallel implementation is in close accordance with the parallelization approach for the CI programs `LUCITA` and `LUCIAREL` which is introduced in Section 4.1. In the present case, the information about

the symmetry of the N C-vectors is read by the master process from an input file and stored in an integer array csym$[N]$. Next, both arrays csym$[N]$ and fsym$[M]$ are communicated to all processes and, furthermore, all M reordered one-electron integral matrices f_k. The efficient collective communication routine MPI_bcast can be used in this case where for the latter elements a sub-communicator of MPI_COMM_WORLD composed of all node masters[1] is employed. In order to proceed with the scattering process of all C-vectors to the node masters the necessary even-distribution lists of active $TTSS$ blocks[2] needs to be set up. Thereby, an individual list is required for each new symmetry that is either stored in csym$[N]$ or arises from the direct product of the operator and C-vector symmetry representations (line 8 in Figure 5.2).

The actual evaluation of the elements of the property matrix $\mathbf{P}$ comprises a nested loop structure of C-vectors and one-particle operators. I designed the algorithm such that occurrences of global communication inside the loop structure are minimized as these constitute natural barriers in the computation step. A further exchange of single C-vector $TTSS$ blocks among the node masters in the linear transformation step (see line 9 in Figure 5.2) is, however, unavoidable because of the coupling of different C-vector $TTSS$ blocks to a given $\boldsymbol{\sigma}$-vector $TTSS$ block through the Hamiltonian $\hat{f}_k$. For a detailed discussion of the parallelization scheme of the $\boldsymbol{\sigma}$-vector computation the reader is referred to Section 4.1.2.

A property matrix element is derived in parts on each process from the dot product of the resulting, partial $\boldsymbol{\sigma}$ vector and a given C-vector (see line 13 in Figure 5.2), if and only if both parts exhibit identical symmetry. The final step of the property matrix evaluation involves the summation of the partial matrices on the master process. To this end, the efficient collective communication routine MPI_reduce with MPI_sum as reduce operation is applied. After the completion of the full property matrix $\mathbf{P}$ the individual properties can be extracted and further worked on in suited analysis routines. So far, I completed analysis tools for the calculation of the ground state dipole moment and of transition dipole moments between ground and excited states from which possible oscillator strengths are computed. Furthermore, a routine in which Ω quantum numbers are assigned to C-vectors is implemented.

[1] The concept of node masters for the communication of large data sets such as integrals or C-vectors is explained in more detail in Section 4.1.

[2] A definition of $TTSS$ blocks into which a C- and $\boldsymbol{\sigma}$ vector are decomposed is given in Section 4.1.

1. store symmetry of N C-vectors in array csym$[N]$
2. communicate symmetry arrays for C vectors (csym$[N]$) and one-particle operators (fsym$[M]$) to all processes via MPI_bcast with the communicator MPI_COMM_WORLD; distribute reordered one-electron integrals $\mathbf{f}$ to node masters using MPI_bcast with a purpose-built sub-communicator of MPI_COMM_WORLD
3. set up even-distribution lists of active $TTSS$ blocks for each distinct symmetry that results from either csym$[N]$ or any direct product of fsym$[M]$ and csym$[N]$
4. scatter C vector(s) to node masters with respect to the distribution lists using MPI_bcast with a purpose-built sub-communicator of MPI_COMM_WORLD
5. **loop** $\{N$ C-vectors$\}$
6. symmetry of ith C-vector: $\Gamma_{\mathrm{C}_i} =$ csym$[i]$
7. **loop** $\{M$ one-particle operators $\hat{f}\}$
8. calculate ith $\sigma^{(k)}$ vector of symmetry $\Gamma_{\sigma_i^{(k)}} = \Gamma_{\hat{f}_k} \otimes \Gamma_{\mathrm{C}_i}$:
9. $|\sigma_i^{(k)}\rangle = \hat{f}_k|\mathrm{C}_i\rangle$
10. **loop** $\{N$ C-vectors$\}$
11. symmetry of jth C-vector: $\Gamma_{\mathrm{C}_j} =$ csym$[j]$
12. **if** $\Gamma_{\sigma_i^{(k)}} = \Gamma_{\mathrm{C}_j}$ **then**
13. compute dot product $\langle\sigma_i^{(k)}|\mathrm{C}_j\rangle$ and store in property matrix $\mathbf{P}_{\mathrm{process}}$
14. **end if**
15. **end loop**[N C-vectors]
16. **end loop**[M one-particle operators $\hat{f}$]
17. **end loop**[N C-vectors]
18. sum up partial property matrices $\mathbf{P}_{\mathrm{process}}$ to complete property matrix $\mathbf{P}$ to be kept on the master process using MPI_reduce with MPI_COMM_WORLD

Figure 5.2: Pseudo-code visualization of the parallelized property matrix evaluation as implemented in the framework of the CI program `LUCIAREL`. Global communications and those among the node masters are displayed in red. In the linear transformation step (line 9) additional communication among the node masters is taking place (see Section 4.1 for further details).

It is worthwhile to mention that the one-electron integrals for essential perturbation operators such as the electric dipole operator $\hat{\mu}_{el} = \{\hat{x}, \hat{y}, \hat{z}\}$ (length representation) or the zth-component of the total angular momentum operator $\hat{j}_z = \hat{s}_z + \hat{l}_z$ as well as of many more operators are readily accessible in the DIRAC program package[3]. Moreover, the integral routine takes care of the appropriate form of the one-electron integrals in particular with respect to time-reversal symmetry and their real or complex valued representation.

5.3 Initial Applications

The CI property module presented in the preceding section is a versatile program that can be used with any one-particle perturbation operator. An application of the property module which proved to be extremely useful is the unambiguous assignment of J and Ω quantum numbers to electronic ground and excited states of atoms and molecules. As neither atomic nor linear symmetry is available in the current implementation of LUCIAREL I pursue an expectation-value approach for the determination of the J and Ω quantum numbers. In this particular case, the expectation value of the $\hat{j}_z$ or $\hat{J}_z$ operator needs to be calculated over a given electronic state. Various examples for practical applications can be found throughout the present work, in particular in Section 8.1 and 7.2 where I took advantage of this technique to clearly identify individual electronic states in the dense electronic spectra of the thorium atom and $(RbBa)^+$ molecule, respectively.

At the time of writing this thesis, a correct symmetry handling of one-electron integrals for operators which are not totally symmetric was not provided by the underlying CI program. This restriction currently limits the applicability of my parallel property module. For instance, the calculation of transition dipole moments (TDMs), from which oscillator strengths of electronic transitions can be computed, is of great interest in theoretical studies as these quantities can be used for a direct comparison with experimental spectra. The calculation of the individual components of the electric dipole operator $\hat{\mu}_e = \{\hat{x}, \hat{y}, \hat{z}\}$ (length representation) which are required to determine the TDM (see also Appendix A.3), however, involves non-totally symmetric operators $(\hat{x}, \hat{y})$. This applies to all abelian double groups which are currently implemented for LUCIAREL. The next

[3] A complete list of implemented one-electron operators in the DIRAC program is available in the DIRAC manual which can be downloaded from Reference 10.

step will therefore be to program a new and general integral routine that allows to treat any one-electron operator irrespective of its symmetry. Upon completion this will greatly enhance the direct applicability of my parallel property module to the calculation of, *e.g.* electric and magnetic properties of molecular (or atomic) systems.

Part III

Applications

Applications in Heavy-Element Electronic-Structure Studies

My parallel MRCI implementations presented in this thesis have been applied to a wide variety of atomic and molecular di- and triatomic systems containing heavy elements. The applications comprise calculations of ground and excited states, their precise characterization, and determination of spectroscopic properties.

In the following chapter, two molecular systems that comprise heavy p-block elements are considered. In Section 6.1, I address the question of an accurate theoretical description of the ground and first excited state of bismuth monohydride (BiH). Moreover, my contributions to an elaborate investigation of the electronic structure of the triiodide anion are presented in Section 6.2. In this latter work, particular emphasis was put on the assessment of various relativistic correlated *ab initio* and DFT methods. In Chapter 7 I present the lower electronic spectra and spectroscopic properties of two new molecular species, namely RbYb (Section 7.1) and $(RbBa)^+$ (Section 7.2), which play an important role in ongoing experimental ultracold molecular physics studies. The final chapter is addressed to atomic and molecular actinide compounds. In Section 8.1 I turn to the calculation of the lower *gerade* electronic states of the thorium atom which served the purpose of a methodological calibration in view of a future study of the thorium diatom. I conclude this part of my thesis with some comments on my MCSCF calculations on the uranium diatom (U_2) (Section 8.2).

Chapter 6

p-Block Main Group Molecules

The main group atoms branch out into two blocks in the periodic table as displayed in Figure 6.1 [96]. The s block is composed of the first two groups and, in addition, the element He. The p block includes the main-group elements of the groups 13-18. The late p-block elements (fifth- to seventh-row) are of particular interest for theoreticians working in the field of relativistic electronic structure theory since their ground state is to a considerable extent determined by spin-orbit coupling[1]. The energetic splitting and the different radial extent of the (partially) occupied valence $np_{1/2}$ and $np_{3/2}$ spinors ($n = 5, 6, 7$) are thus expected to play a key role in the bonding pattern of these elements. Furthermore, excitation energies to low-lying electronically excited states in such molecular compounds are significantly affected by spin-orbit coupling.

In the following Section 6.1 I discuss the spectroscopic parameters of the spin-orbit split ground state and first excited state in BiH derived from my four-component MRCI calculations. Their accurate determination comprises most of the application part in Paper 2. The second half of this chapter is dedicated to the triiodide anion (I_3^-). The core topic of Paper 4 was the assessment of different relativistic methodologies with regard to an adequate description of the electronic structure as well as spectroscopic properties of the ground and lower electronically excited states of I_3^- and its neutral, radical parent system I_3. In Section 6.2 a representative selection of the results for I_3^- is presented from which the pros and cons of each method can be deduced.

[1]Exceptions are, *e.g.* , bismuth and in general the noble gas atoms which have a $6p^3$ and np^6 configuration resulting in a ^4S and ^1S state, respectively. A ^4S state as well as ^1S states are merely shifted in energy by, in a perturbative sense, higher-order magnetic couplings.

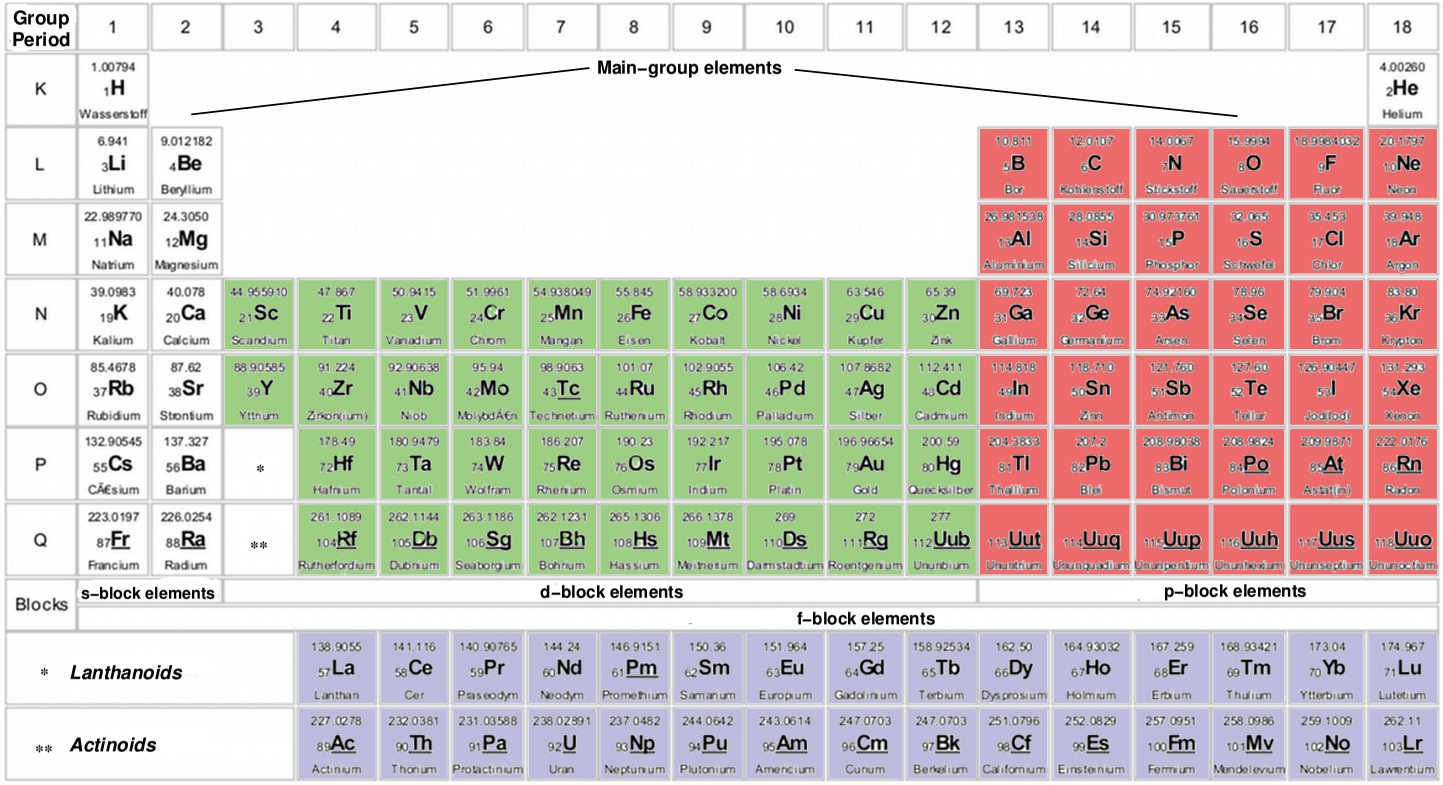

Figure 6.1: Periodic table of elements and its decomposition into s (white coloring), p (red coloring), d (green coloring) and f (blue coloring) blocks. The original figure is taken from Reference 97.

6.1 Bismuth Monohydride (BiH)

Molecular compounds of the sixth-row p block elements, in particular the monohydrides, have been subject to a variety of theoretical studies [39,98–109] where spin-orbit coupling was taken into account in different approximate ways. There are only few investigations [110–112] that include spin-orbit coupling in a more rigorous manner. The appealing nature of the hydrides for theoreticians originates in the simplicity of the hydrogen atom and its possibility to approach the heavier nucleus much more closely than any other element, thus acting as a probe. These systems are, therefore, ideal candidates to study relativistic effects on the (σ-)bonding and electronic structure.

The main objectives of my study in Paper 2 on bismuth monohydride (BiH) were on the one hand to provide spectroscopic properties from correlated relativistic calculations, and on the other hand to shed light on the spin-orbit splitting of the molecular electronic ground state ($\Omega = 0^+$) and first excited state $\Omega = 1$. This investigation which was accomplished by means of our new parallel four-component MRCI program `LUCIAREL` described in Chapter 4, represented the first of unprecedented rigor on this topic. In a scalar-relativistic picture, the molecule has a $^3\Sigma^-$ ground state which dissociates in the atomic limit to Bi (^4S_u) and H (^2S_g). Figure 6.2 shows the ground-state potential curve calculated at the spin-free MRCI SD10(6in5)SD/TZ level[2]. The valence electronic configuration of this state can be written in terms of scalar-relativistic orbitals as $\sigma^2\pi^2$. Upon inclusion of spin-orbit coupling the $^3\Sigma^-$ state, however, splits according to Hund's coupling case (c) [113, 114] into two components: X 0^+ and A 1. Their potential energy curves are displayed in Figure 6.2.

The resulting electronic configurations of the split states exhibit in the approximate $\lambda\omega$-projection notation a $\sigma^2_{1/2}\pi^2_{1/2}\pi^0_{3/2}$ and $\sigma^2_{1/2}\pi^1_{1/2}\pi^1_{3/2}$ occupation pattern, respectively. The value of their large energetic separation, $T_e = 4923$ cm^{-1}, is well-known from experiment [115]. In earlier theoretical works [98, 100, 109] which were primarily based on the assumption of separability of spin-orbit coupling and electron correlation, the prediction of the splitting exhibited significant deviations from the experimental value. Hence, a computational approach that treats both electron correlation and relativistic effects on

[2]An introduction to my notation of MRCI excitation schemes used throughout this thesis is provided in Appendix A.1.

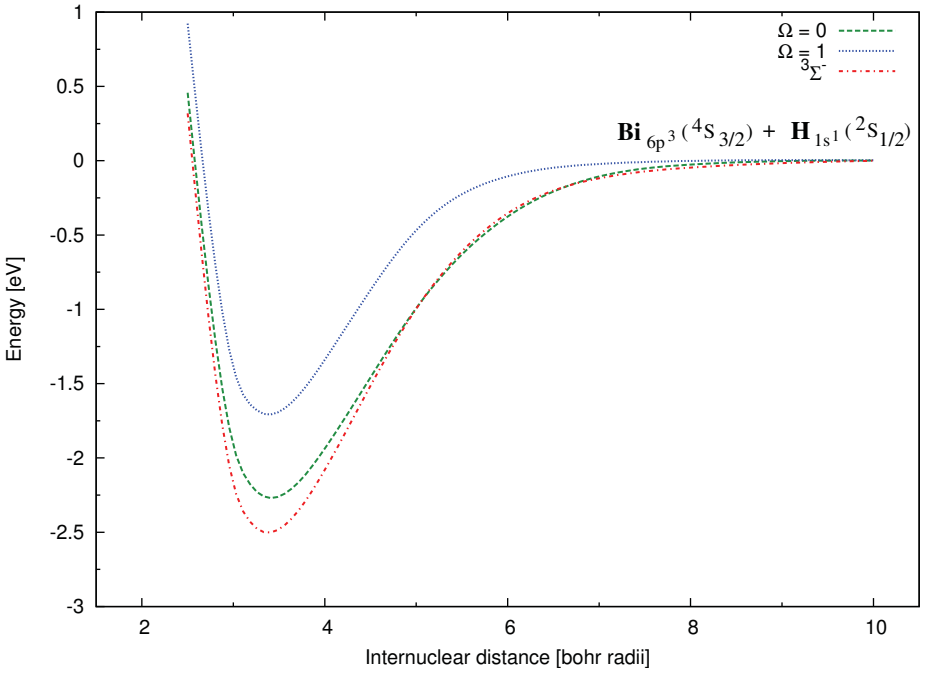

Figure 6.2: Potential energy curves of the electronic X 0^+ ground and A 1 first excited state of BiH obtained from four-component SD10(6in5)SD/TZ calculations. For comparison, the potential energy curve of the electronic $^3\Sigma^-$ ground state of BiH is included in the picture. It was derived from spin-free MRCI SD10(6in5)SD/TZ calculations where scalar-relativistic effects were taken into account. In the latter case the atomic dissociation limit corresponds to Bi (^4S_u) and H (^2S_g) (not shown) and in the spin-dependent case to Bi ($^4S_{3/2}$) + H ($^2S_{1/2}$). Details on the computational levels and basis set are given in the text.

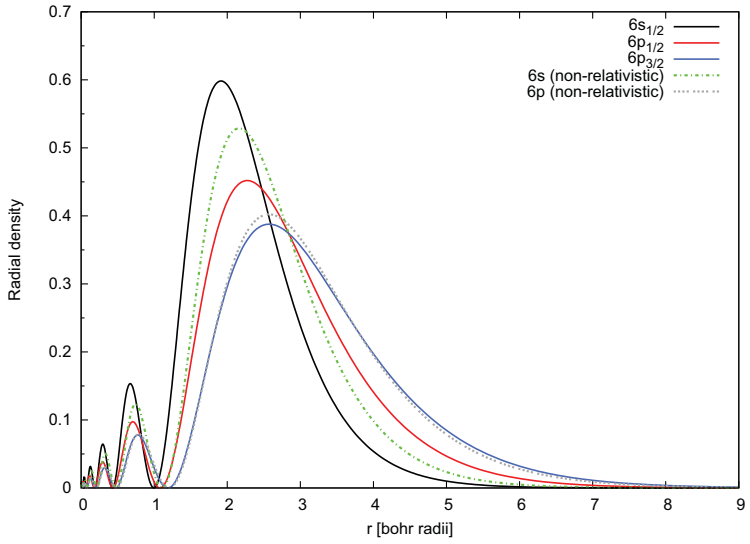

Figure 6.3: Large component radial density distribution for valence orbitals of Bi. Solid lines indicate relativistic spinors and dashed lines non-relativistic orbitals.

an equal footing is indicated and was therefore applied in this thesis. To emphasize the importance of an appropriate consideration of relativistic effects in BiH, I show in Figure 6.3 the large-component radial densities for the relativistic atomic valence spinors[3] of Bi that were obtained from numerical DHF calculations using the atomic DHF program `GRASP` [116]. Relativistic effects that influence the molecular electronic structure may in general be traced back to characteristics of the atomic electronic structure of its constituents. To this end, such an analysis is a valuable means.

As can be readily seen from Figure 6.3 spin-orbit coupling leads to a considerable splitting of the valence Bi $6p_{1/2}$ and $6p_{3/2}$ spinors. The relative displacement of the radial density maximum of the $6p_{3/2}$ spinors to the $6p_{1/2}$ spinor amounts to 0.29 bohr whereas the positions of the radial density maxima of the relativistic $6p_{3/2}$ spinors and the non-relativistic $6p$ orbitals coincide. It can thus be concluded from this comparison that spin-orbit coupling is expected to play a decisive role not only for the molecular electronic structure but also for the bonding in BiH. The depicted splitting therefore suggests the use of a molecular one-particle basis that has been optimized taking account of spin-orbit interactions.

[3]The additional non-relativistic densities were simulated by increasing the speed of light from 137 a.u. to 10^6 a.u..

This requirement was met in the study described in Paper 2 as it was carried out in a four-component framework using the Dirac-Coulomb Hamiltonian. Kramers-paired spinors for the subsequent MRCI correlation calculations were obtained from all-electron average-of-configuration four-component Hartree-Fock calculations. Close to the molecular equilibrium structure, an open-shell state-averaging over all electronic configurations with two electrons distributed among two Kramers pairs (2in2) ensured a balanced description of all electronic states arising from the $\pi_{1/2}\pi_{3/2}$ occupation manifold. Furthermore, basis sets in uncontracted form of either triple-ζ (TZ) or quadruple-ζ (QZ) quality [117, 118] were employed for both atoms.

Table 6.1: Spectral constants for $^{209}Bi^{1}H$ - ground and excited states from the present MRCI study in comparison with previous theoretical calculations and experimental data. Details on the basis sets and excitation schemes used in the computations are given in the text. SF: spin-free Dirac-Coulomb calculation.

Method/basis set	$X\ 0^+$			$A\ 1$		T_e [cm^{-1}]
	R_e [Å]	ω_e [cm^{-1}]	D_e [eV]	R_e [Å]	ω_e [cm^{-1}]	
SF-SD10(6in5)MRSD/TZ[a]	1.787	1814	2.56			
SD10(6in5)MRSD/TZ	1.801	1700		1.787	1742	4617
SD10(6in5)MRSD/TZ[b]	1.806	1692	2.27	1.792	1732	4529
SD10(6in5)MRSD/QZ	1.790	1702		1.775	1754	4780
CCSD(T)/TZ [119]	1.803	1695				
CCSD(T)/MRCIS [109]	1.800	1716	2.38	1.790	1741	4328
MRD-CI [100]	1.867	1632	2.28	1.854	1618	4303
experiment [115, 120]	1.809	1699	≤ 2.9	1.788	1734	4923

[a] Spectroscopic parameters for the $^3\Sigma^-$ are presented.

[b] An adequate one-particle basis to dissociate the molecule was generated by (4in4) average-of-configurations DHF calculations.

Table 6.1 compiles the equilibrium bond lengths (R_e), harmonic frequencies (ω_e), dissociation energy (D_e) and adiabatic excitation (T_e) for the ground and first excited state of BiH from a selection of my MRCI data in comparison with other theoretical studies and the experiment. For the applied computational level SD10(6in5)MRSD a

CAS-like active space was chosen that comprises the six valence electrons distributed in the $6s_{1/2}$, $\sigma_{1/2}$, $\pi_{1/2}$, $\pi_{3/2}$, $\sigma^*_{1/2}$ Kramers pairs (6in5). Core-valence and core-core correlation is taken into account by allowing at most two holes in the underlying Bi $5d$ shell (SD10). Furthermore, single and double as well as combined triple and quadruple excitations from the combined spaces into the virtual spinor space make it possible to recover essential parts of dynamic correlation[4]. A complete table with further results employing different active space models and correlation levels can be found in Paper 2.

The observed bond elongation in the order of 0.02 Å for the molecular ground state upon inclusion of spin-orbit coupling is consistent with previous theoretical findings [105, 109, 112]. The decrease of 0.29 eV in the dissociation energy, on the other hand, contradicts to the results by Han and co-workers [112]. They report even a slight increase of D_e in the order of 0.08 eV comparing their scalar-relativistic CCSD(T) results with the corresponding two-component CCSD(T) values using averaged relativistic effective core potentials. It should be considered, however, that for one thing they make use of an effective one-electron spin-orbit operator to generate a molecular two-component spinor basis, and for another thing, as the authors write themselves, they apply a too small basis set for obtaining accurate numbers. By contrast, my approach is more rigorous since the difference between the spin-free and the four-component calculations merely bases on an exact separation of spin-dependent terms in the Dirac equation for the former computational scheme. Although the ground state of the Bi atom ($^4S_{3/2}$) is not spin-orbit split, spin-orbit coupling will lead to an energy lowering at the atomic limit. In view of my current results, this lowering does not seem to be fully quenched at the molecular minimum.

The values for R_e and ω_e for both the ground and first excited state computed at the four-component SD10(6in5)MRSD level are close to the available experimental data. Sørensen *et al.* [119] calculated ground state properties at the four-component CCSD(T)/TZ level which agree perfectly with my SD10(6in5)MRSD/TZ data. These findings thus confirm the good quality of the present MRCI calculations. Moreover, the computed dissociation energy of 2.27 eV is in agreement with the one-component CCSD(T)/two-component MRCIS results of Stoll and co-workers [109] and also with the

[4] An energy cutoff threshold in the virtual spinor space of 18 E_h was used. Details on the notation of my wave function models can be found in Appendix A.1.

Table 6.2: Atomic and atomic-like (value taken at R = 20 bohr) excitation energies T_e in cm^{-1} for the lowest $Bi_{6p^3}(^4S_{3/2}) \rightarrow Bi_{6p^3}(^2D_{3/2,5/2})$ and $Bi_{6p^3}(^4S_{3/2}) \rightarrow Bi_{6p^3}(^2P_{1/2,3/2})$ transitions calculated at the MRCI X2C-G (5in4)MRSD/TZ, (5in4)MRSD/TZ, SD10(5in4)MRSD/TZ and SD10(6in5)MRSD/TZ levels, respectively. Details on the basis set and computational levels are given in the text.

	$J = 1.5$	$J = 1.5$	$J = 2.5$	$J = 0.5$	$J = 1.5$
Method / T_e [cm^{-1}]	$\Omega^a = 0^+$	$\Omega^b = 2$			
X2C-G (5in4)MRSD/TZ[c]	0	11825	16339	21944	33773
(5in4)MRSD/TZ	0	11905	16436	22040	33999
SD10(5in4)MRSD/TZ	0	11763	16205	22677	33710
SD10(6in5)MRSD/TZ	0	11771			
experiment [122]	0	11419.04	15437.50	21660.91	33164.81

[a] Additional molecular states that correlate to the atomic dissociation channel Bi ($^4S_{3/2}$) + H ($^2S_{1/2}$) are $\Omega = 0^-, 1, 1, 2$.

[b] Additional molecular states that correlate to the atomic dissociation channel Bi ($^2D_{3/2}$) + H ($^2S_{1/2}$) are $\Omega = 0^+, 0^-, 1, 1$.

[c] Exact-Two-Component Hamiltonian including Gaunt corrections.

spin-orbit MRD-CI value of Alekseyev *et al.* [100]. From the experiment [121] only an upper limit of 2.9 eV is available.

What about the spin-orbit splitting T_e between the X 0^+ ground and A 1 first excited state? Inspecting Table 6.1 it becomes evident that my more sophisticated four-component MRCI approach clearly outperforms all previous theoretical studies on the spin-orbit splitting T_e. My best estimate for T_e = 4780 cm^{-1} (SD10(6in5)MRSD/QZ) differs only by ca. 140 cm^{-1} from the experiment. Possible future improvements to close the gap to the experimental splitting are outlined in more detail in Paper 2. For example, a series of MRCI calculations where higher excitations (SDTQ) from the reference space were taken into account revealed the importance of such correlation contributions for an adequate description both of the shape and relative position of the respective electronic potential wells of the ground and first excited state. Furthermore, it is shown that core-valence correlation from the Bi 5d shell suffices to account for the largest corrections to all spectroscopic constants (R_e, ω_e and T_e) determined from corresponding valence CI calculations.

In addition to the study of spectroscopic properties of BiH I carried out atomic two- and four-component MRCI calculations on the lower atomic excitation spectrum of Bi which should give an idea of the performance of my MRCI approach and give an example of the possible accuracy in heavy-atom calculations. The excitation energies for the four lowest transitions in Bi are listed in Table 6.2 in comparison with the experimental data. All states are characterized as internal Bi $6p$ excitations. The atomic-like SD10(6in5)MRSD/TZ excitation energy for the first electronic transition was derived from a molecular calculation at a Bi-H distance of R = 20 bohr. It almost matches its corresponding atomic SD10(5in4)MRSD/TZ value[5]. A difference of only 8 cm^{-1} indicates that the atomic dissociation limit is reached at an internuclear distance of R = 20 bohr. The calculated excitation energies obtained with (SD10(5in4)MRSD/TZ) and without ((5in4)MRSD/TZ) inclusion of core-valence and core-core correlation are in very good agreement with the experiment. The largest deviation amounts up to 1000 cm^{-1} ($\approx$ 4.5%) for the $J = 0.5$ state at the SD10(5in4)MRSD/TZ level. Including spin-other-orbit effects yields a lowering of the excitation energies on the order of 80-200 cm^{-1}. A similar trend was also observed for the spin-orbit splitting $X\ 0^+$ - $A\ 1$ in the BiH molecule (see Paper 2). Spin-other-orbit contributions were thereby added in the exact two-component Hamiltonian (X2C) scheme of Ilias and Saue [27, 123] via atomic mean-field integrals generated with the AMFI [124–126] code.

[5]The active space (5in4) consists of the Bi $6s6p$ shell where the five valence electrons were freely distributed. Core-valence and core-core correlation was included from the Bi $5d$ shell. Single and double excitations from the combined spaces into the virtual space truncated at 18 E_h accounted for dynamic correlation. A general introduction to my notation of wave function models can be found in Appendix A.1.

6.2 Triiodide Anion (I_3^-)

The photodissociation process of the triiodide anion (I_3^-) in solution provides an efficient and facile access to the unstable I_2^- radical anion for solution chemistry: $I_3^- + h\nu \rightarrow I_2^- + I$. The absorption spectrum of I_3^- exhibits two broad absorption bands in the ultraviolet (UV) region centered at $\approx$ 360 and 290 nm which correspond to transitions from the $^1\Sigma_g^+$ (0_g^+) ground state to the $^3\Pi_u$ (0_u^+) and $^1\Sigma_u^+$ (0_u^+) excited states. The dynamics of the photoinduced dissociation process in solution have been extensively studied in the past using time-resolved pump-probe techniques [127] at the femtosecond time scale [128–133].

For the isolated I_3^- molecule in the gas phase, the photodissociation process and its associated dynamics, however, change to a considerable extent. Upon excitation with UV or visible light a variety of decay channels leading to different fragments are energetically accessible [134]. The potential two- and three-body dissociation channels and the resulting fragments are illustrated in Figure 6.4.

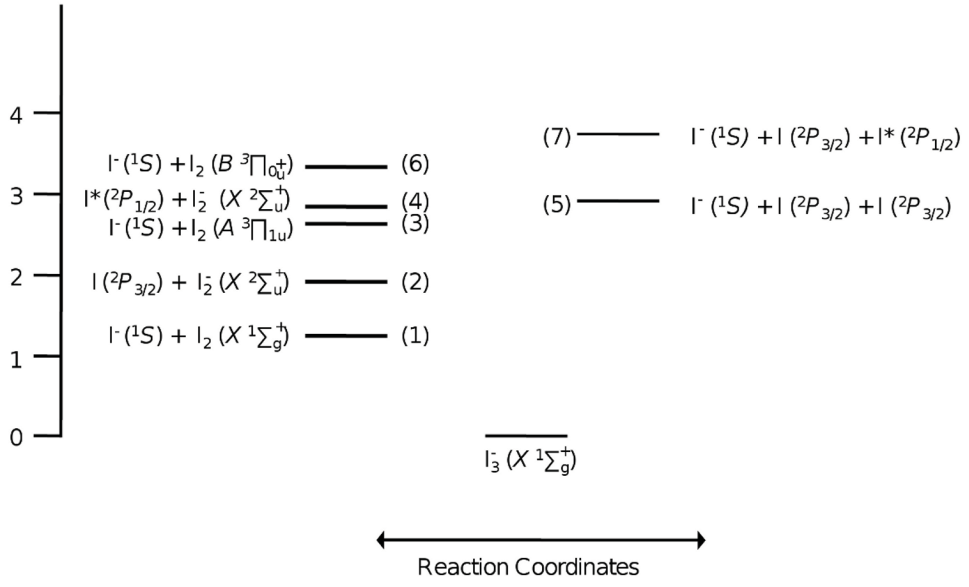

Figure 6.4: Energy level diagram for I_3^-. The asymptotic energies of the respective decay channels are drawn relative to the ground state of I_3^-. The numbering (1), (2), ..., of the channels relates to their ascending energetic order. Two-body dissociation channels are shown on the left of I_3^-, three-body dissociation channels to the right. The figure is based on a graphics in Reference 134.

Given the variety of possible decay channels, an important aspect in experimental gas-phase measurements of the I_3^- photodissociation dynamics is the branching ratio

between competing two-body and three-body dissociation pathways [134–138]. The simultaneous occurrence of such competitive channels is indicative of the involvement of distinct non-adiabatic dynamics [138, 139] during the photochemical decay of I_3^-. In this context, theoretical wave-packet dynamics simulations are highly desirable to get a deeper insight in this complex photodissociation process. To avoid artifacts in the dynamics, the whole of the potential energy surfaces has to be calculated accurately which is, from a computational point of view, a demanding task.

The main objective of the study in Paper 4 was therefore to provide an assessment of different methodologies (TDDFT, SO-CASPT2, MRCI and IHFSCC)[6] that could be appropriate to describe the electronic structure of the triiodide species at all points on the potential energy surfaces. In a later step, the most suitable approach shall thus be employed to calculate the desired potentials. The relativistic IHFSCC method [144–146], which served in the presented study as a reference for the calculation of the low-lying electronic states of I_3^- is a true multireference coupled cluster method. It is fully size-extensive for both ground and excited states and includes electron correlation to infinite order whereas, *e.g.* SO-CASPT2 does it only to second order. Further details on this method can be found in References [144–146] and in Paper 4.

Compared to the wealth of experimental data on the triiodine species, relatively few theoretical studies have been performed in the past. Kosloff and coworkers [139] presented an extensive study of the potential energy curves of the I_3^-, I_2 and I_2^- species, which are, as indicated in Figure 6.4, likely to be involved in the photodissociation dynamics of I_3^-. Their results, obtained with a combination of spin-free MRCI calculations and a diatomics-in-molecule (DIM) treatment where spin-orbit effects were included, may, however, be somewhat flawed due to the relatively small basis set used in the DIM treatment. More recently, Nakanishi *et al.* [138] performed spin-orbit-CI calculations which explored not only the potential along the symmetric stretch of I_3^- but also along the asymmetric stretch coordinate. This theoretical investigation, however, still leaves room for improvement, given the modest basis sets and the relatively limited accuracy warranted by the spin-orbit-CI method used. Although I_3^- is a closed-shell molecule, a key prerequisite for a

[6] TDDFT: time-dependent DFT [140]; SO-CASPT2: spin-orbit complete active space perturbation theory to 2nd order [141–143]; MRCI: my parallel multireference CI program `LUCIAREL` (see Chapter 4); IHFSCC: intermediate Hamiltonian Fock-space coupled cluster [144–146].

Table 6.3: Ground-state spectroscopic constants of I_3^- calculated with the DFT, MRCI, SO-CASPT2 and IHFSCC methods.

Method	R_e [Å]	ω_e [cm^{-1}]
DFT	3.007	102
MRCI	2.982	108
SO-CASPT2	2.888	119
IHFSCC	2.946	114
spin-free MRCI [139]	2.930	114
DIM+SO [139]	2.966	95
experiment [147][a]	2.93	112±1

[a] Crystal structure data of $(C_2H_5)_4NI_3$ salt.

thorough investigation of I_3^- and its decay products is to account for spin-orbit coupling. The reason is that I_3^- is composed of the relatively heavy element iodine ($Z = 53$) for which spin-orbit effects are intrinsically important and, by being present, will play a role in selection rules for relaxation processes after photoexcitation. For this purpose and for reasons of computational efficiency, the exact two-component Hamiltonian (X2C) scheme of Iliaš and Saue [27, 123] was used in the present investigation for the IHFSCC and MRCI calculations. Two-electron spin-same-orbit and spin-other-orbit contributions were included via atomic mean-field integrals obtained with the AMFI [124–126] code.

Table 6.3 compiles the spectroscopic constants of the $\Omega = 0_g^+$ electronic ground state of I_3^- derived from calculations employing various methods. My MRCI approach[7] yields a fairly good agreement with the solid state data which has to be used since experimental gas-phase data are available neither for the equilibrium bond length R_e nor the harmonic frequency ω_e. The deviations from the experiment for both R_e (+0.05 Å) and ω_e (-4 cm^{-1}) are comparable to those for SO-CASPT2 and the generally more accurate IHFSCC method. DFT, on the other hand, shows larger discrepancies.

Benchmark calculations of the vertical electronic spectra of I_3^- at both a fixed inter-

[7] A computational scheme with a CAS space composed of 16 electrons distributed in 9 Kramers-paired spinors (16in9) from which up to two particles in the external space (cutoff threshold 3 E_h) were allowed, was employed in combination with a TZ basis set [117, 148]. To list all computational details for the various methods would go beyond the scope of this discussion and the reader is referred to Paper 4.

nuclear distance (r = 2.93 Å; experimental R_e) and at the respective equilibrium distance of a given method are discussed at length in Paper 4. In order to be useful in modeling the dissociation process of I_3^- the potential surfaces of the excited states far removed from the ground state equilibrium region have to be properly described. On this account, bond length r_e as well as "adiabatic" (T_e) excitation energies were calculated for geometries limited to displacements along the symmetric stretch coordinate. The calculated spectroscopic constants for a given excited state, which are listed in Table 6.4, may thus differ from their true values since the chosen restriction merely represents a cut through the full multidimensional surface.

To facilitate the comparison between the methods, statistical measures of the errors for each method[8] with reference to IHFSCC are given at the bottom of Table 6.4. My MRCI calculations tend to yield slightly longer bonds than their IHFSCC counterparts, with an average deviation $\bar{\Delta}$ of 0.14 Å. A reverse trend is observed for the SO-CASPT2 results which underestimates the bond length compared to IHFSCC by about 0.036 Å. TDDFT, on the other hand, gives too long bond lengths, with $\bar{\Delta} \simeq 0.2$ Å, in line with the overestimation that was observed for the ground state.

My MRCI approach also performs well for the calculation of the "adiabatic" excitation energies exhibiting a small mean error $\bar{\Delta}$ though the errors are not completely systematic ($|\bar{\Delta}| \neq \bar{\Delta}_{\mathrm{abs}}$). By contrast, SO-CASPT2 in general yields too high excitation energies. However, the small standard deviation Δ_{std} associated with a one-to-one correspondence of $\bar{\Delta}_{\mathrm{abs}}$ and $\bar{\Delta}$ points to a rather systematic behavior. Although TDDFT seems to capture the essentials of the other methods for the lowest states, it is obviously less reliable from a quantitative point of view.

In summary it can be said, therefore, that the agreement between the different methodologies employed is very good in particular for the wave function-based approaches, as is their agreement with experimental results. The IHFSCC method which is considered to yield the most accurate results, is, however, not applicable to the complete potential energy surface due to the presence of intruder states which prohibit a convergence at large internuclear distances. Thus, either my MRCI or the SO-CASPT2 approach remain as potential candidates for the computation of complete potential energy surfaces of I_3^- (and

[8]This procedure follows the approach of Helgaker and coworkers [149]. A definition of the statistical measures can be found in Appendix A.2.

Table 6.4: Bond length (r_e in Å) and "adiabatic" (T_e) excitation energies (in eV) for the ten lowest excited states of I_3^-, calculated with the TDDFT, MRCI, SO-CASPT2 and IHFSCC methods. The lowest, optically active 0_u^+ state is shown in boldface. Statistical measures of the error compared to IHFSCC are also shown (see text for discussion).

	TDDFT			MRCI			SO-CASPT2			IHFSCC		
State	Ω	r_e	T_e	Ω	r_e	T_e	Ω	r_e	T_e	Ω	r_e	T_e
1	2_g	3.442	1.19	0_u^-	3.501	1.53	1_u	3.366	1.82	0_u^-	3.419	1.45
2	1_g	3.462	1.29	1_u	3.503	1.53	2_g	3.233	1.82	1_u	3.414	1.46
3	0_u^-	3.720	1.38	2_g	3.383	1.64	0_u^-	3.362	1.83	2_g	3.245	1.59
4	1_u	3.696	1.38	1_g	3.421	1.71	1_g	3.251	1.87	1_g	3.255	1.71
5	2_u	3.615	1.41	2_u	3.644	1.89	1_u	3.481	2.18	0_g^-	3.358	2.07
6	1_u	3.669	1.52	1_u	3.657	1.89	2_u	3.472	2.21	1_g	3.512	2.20
7	0_g^-	3.554	1.68	0_g^-	3.478	2.16	0_g^-	3.272	2.28	2_u	3.448	2.22
8	1_g	3.771	1.81	1_g	3.562	2.22	1_g	3.315	2.32	0_g^+	3.240	2.24
9	0_g^+	3.388	1.88	0_g^+	3.388	2.28	0_g^+	3.242	2.38	1_u	3.462	2.26
10	$\mathbf{0_u^+}$	**3.513**	**2.10**	$\mathbf{0_u^+}$	**3.731**	**2.36**	$\mathbf{0_u^+}$	**3.501**	**2.64**	$\mathbf{0_u^+}$	**3.496**	**2.61**
$\bar{\Delta}$		0.198	-0.42		0.142	-0.06		-0.036	0.15			
Δ_{std}		0.080	0.24		0.058	0.18		0.067	0.15			
$\bar{\Delta}_{\text{abs}}$		0.198	0.42		0.142	0.13		0.045	0.17			
Δ_{max}		0.301	0.83		0.235	0.37		0.197	0.38			

I_3, see also Paper 4). In this context, SO-CASPT2 exhibits two interesting advantages: for one thing, it is computationally much more efficient than MRCI, and for another its error seems to be more systematic for all electronic states considered. In view of the large number of single-point calculations ($> 10^6$) that have to be carried out to obtain a dense and suitable grid of the potential energy surfaces for ensuing dynamics simulations, the former holds as a strong argument. If, on the other hand, computational power is not a limiting factor, my parallel MRCI approach could be in particular cases the more suitable choice.

Chapter 7

Ultracold Molecules

The discovery of methods for cooling, trapping, and manipulating atoms led to a revolution in atomic physics. It has stimulated researchers to pursue the creation and study of ultracold molecular gases (exhibiting translational temperatures < 1mK) aiming at for example a controlled chemistry at the quantum level [150] and the possibility of testing, e.g., fundamental symmetries in nature through measurements of a postulated electric dipole moment of an electron [151, 152] or the space-time variation of fundamental constants such as the fine-structure constant α [153, 154]. The production of ultracold molecules can be achieved in a variety of ways, such as photoassociation [155], buffer gas cooling (sympathetic cooling) [156], Stark deceleration of polar molecules via time-modulated electric fields [157] and magnetically tunable Feshbach resonances [158].

Theoretical contributions to the field of (ultra-)cold molecules are of value in many different respects. Among the most important is the determination of accurate molecular potential energy curves of ground and relevant electronically excited states. In the long-range limit atom-atom and atom-ion interactions are well described by $1/r^6$ and $1/r^4$ potentials, respectively, using perturbation methods whereas at short range Coulombic forces dominate where advanced methods of molecular electronic structure theory come into play. In the following section, I introduce the essentials of our high-level four-component theoretical study on the RbYb molecule (Paper 3), a new molecular species composed of an alkaline atom and a lanthanides atom[1] that has been produced for the first time at the ultracold regime in the group of Axel Görlitz at the University of Düsseldorf [159]. I will

[1]The Yb atom has the valence electronic configuration $[Xe]4f^{14}6s^2$ which bears a close resemblance to the earth-alkaline atoms.

in particular focus on our results of the spectral constants (equilibrium bond lengths, harmonic vibrational frequencies, dissociation and excitation energies) as well as vibrational states and Franck-Condon factors which may help to guide the experimentalists in their future work on an efficient formation of ultracold RbYb molecules.

Section 7.2 comprises an overview over our recent four-component MRCI and CC investigations of the molecular ion $(RbBa)^+$. A four-component spin-free pilot survey of $(RbBa)^+$ is provided in Paper 1 and this study has recently been extended to account for spin-orbit interactions in Paper 5. $(RbBa)^+$ will be involved for example in experimental studies of elastic and inelastic collisions between a singly trapped ultracold ion (here Ba^+) and an atomic Bose-Einstein condensate consisting of Rb atoms [160]. In order to explain a possible charge-transfer mechanism in the collision experiments on the basis of the molecular ground and excited-state potentials necessitates the inclusion of spin-orbit interaction in the electronic-structure calculations as will be emphasized in this section.

7.1 Rubidium Ytterbium (RbYb)

To the date a large fraction of investigated systems in the (ultra-)cold molecular sciences is comprised by alkali metal diatomics, both homonuclear and heteronuclear [150, 161]. The RbYb molecule belongs to a new class of heteronuclear diatomics that due to their unpaired electron(s) may be trapped and manipulated using magnetic fields [159]. They are, for example, promising candidates for an experimental search for a permanent electric dipole moment of the electron or for producing lattice-spin models [162] for quantum computing. Recently, the thermalization of various bosonic and fermionic Yb isotopes through collisions with ultracold Rb has been shown by Görlitz and his co-workers [163], giving first insights into the long-range behavior of the RbYb potential. Based on this work, the controlled production of electronically excited RbYb* molecules by single-photon photoassociation techniques has been demonstrated [159], and continued efforts include the conservative trapping of the Rb-Yb mixture. Ultimately, the investigations aim at a molecular Bose-Einstein condensate with adjustable dipolar interaction and a new approach to measuring the electron electric dipole moment.

The main objective of the theoretical study on the RbYb molecule (see Paper 3) was to gain insight into its electronic structure applying accurate and highly sophisticated relativistic electronic structure methods. To the best of my knowledge, this molecule has not been investigated theoretically before. On the basis of our achieved results, a laser-driven two-step mechanism was proposed to prepare RbYb molecules in the rovibronic ground state under laboratory conditions using ultracold Rb and Yb atoms. The new data on vibrational levels and overlap between vibrational levels which were derived from my MRCI ground and excited state potentials thereby gave rise to a revision of the mechanism initially suggested by Nemitz [164].

Due to the energetic vicinity of the Rb $5s$ $5p$ $4d$ $6s$ $6p$ and Yb $6s$ $6p$ $4f$ $5d$ shells, a large variety of excited states are expected to constitute the lower part of the electronic spectrum of RbYb. An overview over the atomic configurations and terms as well as the associated molecular states in the $\Lambda - S$ coupling picture is given in Table 7.1. Since the experimental photoassociation process for preparing RbYb molecules requires only the lowest four excited states I refrained from calculating the complete lower electronic spectrum. A qualitative picture of the molecular electronic excited states correlating to

Table 7.1: A selection of molecular electronic states in the $\Lambda - S$ coupling picture and associated atomic dissociation channels in an energy range of $\approx$ 25000 cm^{-1}. Molecular electronic states correlating to atomic channels with intra-atomic Yb $f - d$ excitations, e.g. $Yb_{4f^{13}5d^16s^2}$ are not considered.

Atomic $^{(2S+1)}L_J$	Molecular $^{(2S+1)}\Lambda_\Omega$
$Rb_{5s^1}(^2S_{1/2}) + Yb_{6s^2}(^1S_0)$	$^2\Sigma^+_{1/2}$
$Rb_{5p^1}(^2P_{3/2,1/2}) + Yb_{6s^2}(^1S_0)$	$^2\Pi_{3/2,1/2}$, $^2\Sigma^+_{1/2}$
$Rb_{5s^1}(^2S_{1/2}) + Yb_{6s^16p^1}(^3P_{2,1,0})$	$^4\Pi_{5/2,3/2,1/2,-1/2}$, $^2\Pi_{3/2,1/2}$, $^4\Sigma^+_{3/2,1/2}$, $^2\Sigma^+_{1/2}$
$Rb_{4d^1}(^2D_{5/2,3/2}) + Yb_{6s^2}(^1S_0)$	$^2\Delta_{5/2,3/2}$, $^2\Pi_{3/2,1/2}$, $^2\Sigma^+_{1/2}$
$Rb_{6s^1}(^2S_{1/2}) + Yb_{6s^2}(^1S_0)$	$^2\Sigma^+_{1/2}$
$Rb_{5s^1}(^2S_{1/2}) + Yb_{6s^15d^1}(^3D_{3,2,1})$	$^4\Delta_{7/2,5/2,3/2,1/2}$, $^2\Delta_{5/2,3/2}$, $^4\Pi_{5/2,3/2,1/2,-1/2}$, $^2\Pi_{3/2,1/2}$ $^4\Sigma^+_{3/2,1/2}$, $^2\Sigma^+_{1/2}$
$Rb_{6p^1}(^2P_{3/2,1/2}) + Yb_{6s^2}(^1S_0)$	$^2\Pi_{3/2,1/2}$, $^2\Sigma^+_{1/2}$
$Rb_{5s^1}(^2S_{1/2}) + Yb_{6s^16p^1}(^1P_1)$	$^2\Pi_{3/2,1/2}$, $^2\Sigma^+_{1/2}$

the $Rb_{5p^1}(^2P_{3/2,1/2}) + Yb_{6s^2}(^1S_0)$ and $Rb_{5s^1}(^2S_{1/2}) + Yb_{6s^16p^1}(^3P_{2,1,0})$ atomic dissociation channels can be found in Paper 3.

In order to calibrate and test the accuracy of my four-component MRCI approach using the Dirac-Coulomb Hamiltonian for the calculation of ground and low-lying excited state potentials of RbYb, spin-free (not shown here) and spin-dependent CCSD and CCSD(T) calculations were carried out for the molecular electronic $\Omega = 0.5$ (denoted in the following by 1 0.5) ground state. The results of these benchmark calculations are compiled in Table 7.2. Since RbYb is a characteristic, weakly bound van der Waals complex as indicated by the large equilibrium bond distance $R_e = 8.88$ bohr and the low dissociation energy ($D_e < 900$ cm^{-1}) the spectroscopic constants shown in Table 7.2 were counterpoise (CP) corrected [165] to account for the basis set superposition error. Uncontracted basis sets of triple-ζ quality (TZ) were used for both atoms consisting of $\{30s24p16d13f3g1h\}$ functions for Yb [166] and $\{28s20p14d1f\}$ functions for Rb [167]. Core-valence correlation was taken into account from the Rb $4p$ shell. In case of my MRCI approach this was achieved by including single holes in the Rb $4p$ shell. The CAS-like active space comprised the Rb $5s5p$ and the Yb $6s6p$ shells where the three valence electrons were freely distributed (3in8). Single and double excitations from the

Table 7.2: Spectroscopic values for the 1 0.5 ground state calculated at the CCSD/TZ and CCSD(T)/TZ and MRCI S6(3in8)MRSD/TZ level with nine explicitly correlated electrons and including spin-orbit coupling. A spinor basis was derived from average-of-configurations DCHF calculations, distributing either three electrons in two Kramers pairs (3in2) or three electrons in five Kramers pairs (3in5). A CP-correction was carried out in the spin-dependent case only for the MRCI data.

Method	av. in DCHF	R_e[bohr]	ω_e [cm^{-1}]	D_e [cm^{-1}]
CCSD(T)/TZ	(3in2)	8.98	28.620	795
CCSD/TZ	(3in5)	9.15	25.572	654
CCSD(T)/TZ	(3in5)	8.89	30.214	828
S6(3in8)MRSD/TZ	(3in5)	8.85	29.751	865
S6(3in8)MRSD/TZ (CP)	(3in5)	8.88	29.458	844

combined spaces into the virtual Kramers-paired spinor space accounted for dynamical electron correlation. The threshold for the truncation of the virtual spinors was set at 7.8 E_h. A one-particle spinor basis for the ensuing MRCI S6(3in8)MRSD calculations was obtained from average-of-configurations HF with an averaging over all states arising from a distribution of three electrons among five Kramers pairs, namely Rb $5s$ and Yb $6s6p^2$.

As can be seen from Table 7.2, my MRCI S6(3in8)MRSD/TZ calculations reproduce very well the ground state spectroscopic parameters derived from the CCSD(T)/TZ (3in5) calculations. The CP correction is small which indicates the use of a balanced basis set. In Paper 3 the effect of correlating the Yb $4f$ electrons at the CCSD(T)/TZ level was found to be of minor importance despite the fact that the inclusion of this primarily atomic shell causes a slight reduction of the harmonic frequency ω_e and the dissociation energy D_e. A comparison of the CCSD(T)/TZ calculations using different one-particle spinor bases (see Table 7.2) furthermore reveals that the choice of the averaging has a significant effect. Although the CCSD(T) calculations based on a (3in5) averaged spinor basis yield the most attractive potential, the results need to be regarded with caution because of the use of a single-reference method. This choice of one-particle basis is more appropriate for a multireference correlation approach. Furthermore, CCSD(T) is typically expected to yield larger binding energies than CI. A thorough analysis of the MRCI wave function

[2] A (3in8) averaging, where the Rb $5p$ spinors are included, was not possible along the entire potential energy curve due to strong mixing with the Yb $5d$ spinors.

Table 7.3: Atomic and atomic-like (value taken at R = 30 bohr) excitation energies T in cm^{-1} for the lowest $Rb_{5s^1}(^2S_{1/2}) \rightarrow Rb_{5p^1}(^2P_{3/2,1/2})$ transitions calculated at the MRCI S1/TZ, S6(1in4)SD/TZ and S6(3in8)SD/TZ levels, respectively. Details on the computational levels are given in the text.

	$J = 0.5$	$J = 0.5$	$J = 1.5$	
Method / T [cm^{-1}]	$\Omega = 0.5$	$\Omega = 0.5$	$\Omega = 1.5$	$\Omega = 0.5$
S1/TZ	0	10692	10875	10875
S6(1in4)MRSD/TZ	0	12636	12857	12857
S6(3in8)MRSD/TZ	0	12662	12879	12883
experiment [168]	0	12579	12817	12817

reveals, however, substantial multiconfigurational character in the bonding region. The leading configuration consists of a doubly occupied Yb 6s Kramers pair and a bonding orbital composed of Rb 5s and Yb 6$p_{1/2}$. In addition, large coefficients are found for single excitations from the bonding orbital as well as double excitations from the Yb 6s shell. The simultaneous occurrence of polarizing and correlating excitations are indicative of the importance of triples as observed in the CC calculations.

The high quality of my chosen MRCI S6(3in8)MRSD/TZ computational scheme is also mirrored in the atomic-like (value taken at R = 30 bohr) excitation energies T for the lowest $Rb_{5s^1}(^2S_{1/2}) \rightarrow Rb_{5p^1}(^2P_{3/2,1/2})$ transitions. In Table 7.3 I compare these results to both atomic MRCI and experimental data. If core-valence correlation is neglected in the atomic S1/TZ (one electron CI) calculation not only the excitation energies are considerably underestimated by ≈ 2000 cm^{-1}. The fine-structure splitting of the $^2P_{3/2,1/2}$ term is also too small by almost 23 %. However, taking into account single excitations from the outer-core Rb 4p shell (S6(1in4)MRSD/TZ) results in a significant improvement towards the experimental values. Excitation energies and the fine-structure splitting differ from the experimental data by about 40 - 60 cm^{-1} and 15 cm^{-1}, respectively. A similar performance is observed for their atomic-like counterparts derived from the molecular S6(3in8)MRSD/TZ calculation. The agreement with the experimental excitation energies becomes slightly worse by about 22-26 cm^{-1}, yet an excellent spin-orbit splitting of 218 cm^{-1} is obtained. In summary, it can be stated that with my MRCI S6(3in8)MRSD/TZ scheme high accuracy can be achieved both for ground and low-lying excited states of

the RbYb molecule. For one thing the computed spectroscopic constants of the ground state are in good agreement with the corresponding CCSD(T) values, for another thing a balanced description of the atomic limit is reached[3].

Finally, I will briefly discuss a possible two step-mechanism for the production of ultracold RbYb molecules in the rovibronic ground state. This mechanism is sketched in Figure 7.1. Each of the steps (first step: (1) and (2); second step: (3) and (4) in Figure 7.1) could experimentally be realized by the so-called STIRAP (STImulated Raman Adiabatic Passage) process [169, 170]. The STIRAP process is a sophisticated laser technique that uses a coupled intermediate state to achieve an almost adiabatic transfer from the initial to the desired final molecular state.

Since all electronic transitions are dipole allowed, the transition probability is expected to be primarily dominated by the vibrational overlaps between the electronically excited- and ground-state potential wells. For this purpose, vibrational wave functions, eigenvalues and Franck-Condon factors (FCFs)[4] (see also Appendix A.3) were computed with the program `LEVEL` [171] for the isotopes ^{87}Rb and ^{176}Yb which are mainly used in the experiment. As could be expected from the small geometric shift between the minima of the ground state and the uppermost 3 0.5 state (see Figure 7.1), large FCFs[5] ($\approx 2 \times 10^{-1}$) are found between the rovibronic ground state ($\nu_{1\ 0.5} = 0$) and the lowest vibrational levels ($\nu_{3\ 0.5} = 0 - 4$) of the 3 0.5 state. However, none of these levels has non-negligible FCFs with the highest vibrational level ($\nu_{1\ 0.5} = 69$) from which the second excitation process ((3) in Figure 7.1) is likely to take place. These findings therefore suggest a revision of the scheme proposed by Nemitz [164], who based the original mechanism on preliminary potential energy curves [172]. In agreement with the computed FCFs either the first excited state 2 0.5 or the second excited state 1 1.5 should be used as intermediate states. The FCFs for the absorption ((3)) and emission ((4)) were found to be on the order of 10^{-2} and $10^{-4} - 10^{-6}$, respectively, for both excited states which thus make them more favorable candidates for the final STIRAP process. This picture can, however, change depending on how well the ground state is determined. For example, a shorter equilibrium bond distance for the ground state would favor the first two

[3] Spectroscopic constants for the excited states are available in Paper 3.

[4] A detailed introduction to the Franck-Condon principle and the computation of Franck-Condon factors can be found for example in [115].

[5] A list of the most important FCFs is reported in Paper 3.

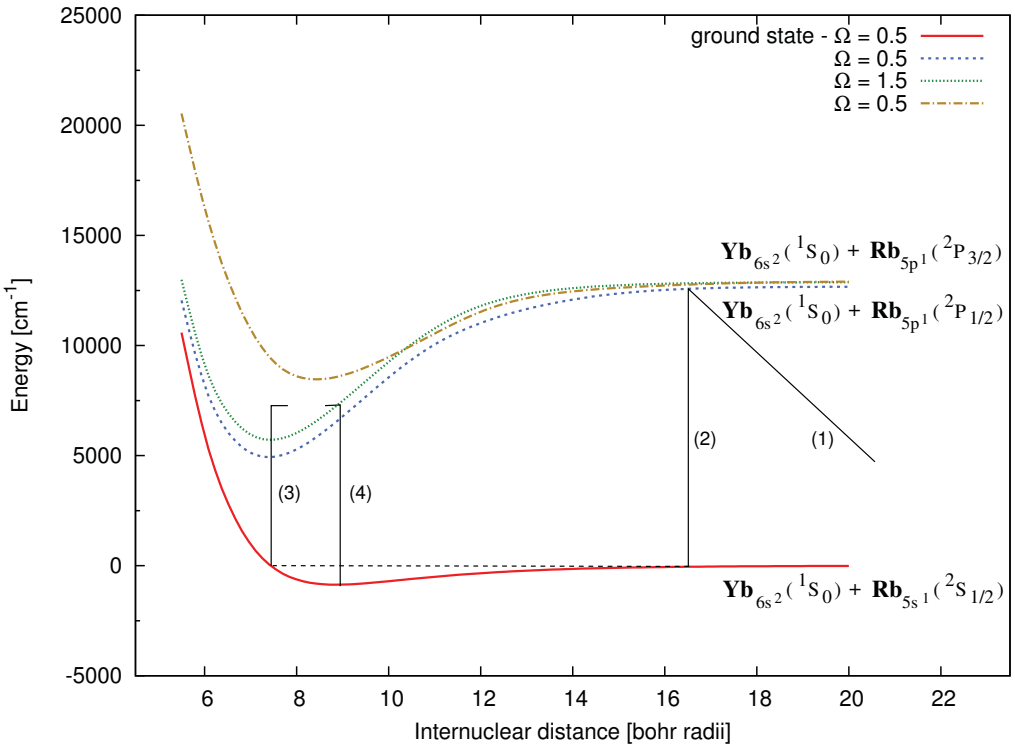

Figure 7.1: Potential energy curves of the ground and low-lying states of RbYb computed at the MRCI S6(3in8)MRSD/TZ level. Atomic dissociation channels for the states are shown. The transitions (1) and (2) are part of the first STIRAP process [170] (initial photoassociation), (3) and (4) refer to the corresponding second two-photon process.

excited states whereas a longer would favor the third excited state. In view of the results presented here, an experimental approval of the revised mechanism is highly probable.

7.2 The Molecular Ion $(RbBa)^+$

Investigations on the collision kinetics of heavy ionic and neutral main-group atoms at ultracold temperatures is a field of growing interest in experimental physics. These studies aim at a profound understanding of the collision processes and products, and ultimately at a controlled chemistry at the quantum level [150] and the possibility of testing fundamental symmetries in nature [151, 152]. Particular aspects of inelastic and elastic cold collisions are, *e.g.* a concurrent charge-transfer process resulting in a loss of the initial ion (for example Ba^+) or the formation of a postulated mesoscopic molecular bound state arising from a single trapped ion in a sea of ultracold atoms [173]. In this context, the collision kinetics and electronic potential energy curves of the molecular benchmark system $(RbBa)^+$ [160], initially starting from a Ba^+ ion that interacts with a Bose-Einstein condensate of neutral Rb atoms, are of great interest. It is valence isoelectronic with the $(MgK)^+$, $(MgCs)^+$ and $(CaNa)^+$ systems which have been considered in earlier experiments [174–176][6]. The associated theoretical investigations were mainly carried out using large-core pseudopotentials and neglecting spin-orbit coupling. In these systems, the lowest-lying electronic states are characterized as Σ states, which is also true for the $(RbBa)^+$ molecular ion (see Paper 1) and most likely also for another heavier species of interest, $(MgCs)^+$. The neglect of spin-orbit interaction is reasonable in the determination of such Σ states, since it affects these states only through higher-order couplings to excited states of different angular momentum projection onto the internuclear axis. For the $(RbBa)^+$ molecular ion, however, electronic states of projection $\Lambda > 0$ play a role for the lowest dissociation channels to the different atomic fragments as I have shown in Paper 1. An understanding of experiments involving the lower dissociation channels of $(RbBa)^+$ which come to lie in an energy window of about 2 eV, therefore necessitates inclusion of spin-orbit interaction in the electronic-structure calculations.

The main objective of my initial study on $(RbBa)^+$ in Paper 1 was thus to provide a survey of the molecular potentials for the lowest electronic states at a high level of accuracy with respect to the treatment of dynamic electron correlation using a spin-free MRCI approach. Figure 7.2 displays the scalar-relativistic nine lowest-lying molecular electronic states of the $(RbBa)^+$ ion derived from spin-free MRCI S16(2in7)MRSD/ANO-

[6]The investigations including the Mg-containing molecular ions have been collision experiments performed at room temperature.

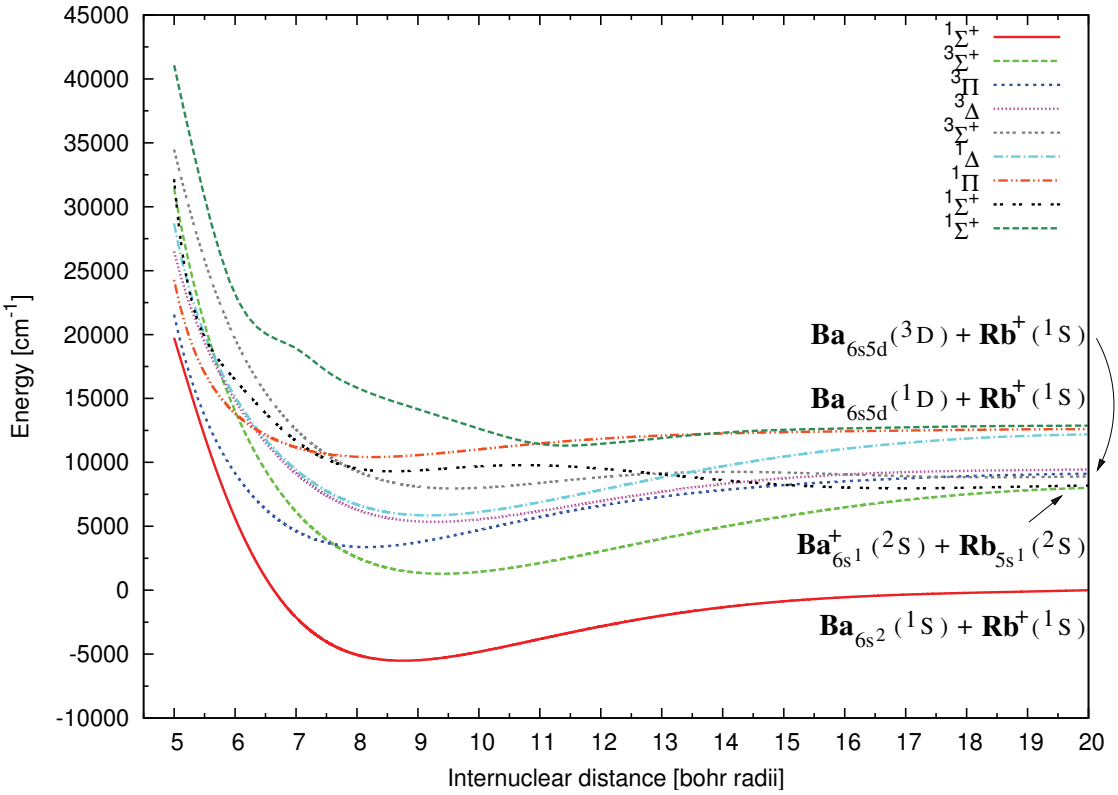

Figure 7.2: Potential energy curves of the ground and low-lying states ($\Lambda - S$ designation) of $(RbBa)^+$ computed at the spin-free MRCI SD16(2in7)MRSD/ANO-RCC level (see text for more details). Atomic dissociation channels for the states are shown in the picture.

RCC calculations[7].

The objective of the second study presented in Paper 5 has been to investigate the electronic excited states lying close to the Rb + Ba^+ entrance channel (see Figure 7.2) and expected to have a complicated distance dependence, to form a firm basis for design of ultracold collision experiments for this system. One aim in the study in Paper 5, which I will discuss here, was the search for possible charge transfer mechanism from Rb to Ba^+ by a characterization of the excited states. To obtain this objective the scalar relativistic study (Paper 1) was extended to also include the spin-orbit interaction, which is imperative for an understanding of the charge transfer mechanisms in $(RbBa)^+$ at ultracold experimental conditions.

[7]The ANO-RCC basis sets for both atoms Rb and Ba were taken from Reference [177] and applied in uncontracted form. The spin-free MRCI calculations included the correlation of the Rb $4s4p$ as well as the Ba $5s5p$ outer-core shell. The active space comprised the Ba $6s5d$ shell where the two valence electrons were freely distributed. Further details are given in Paper 1. A guideline for my notation of MRCI wave function models can be found in Appendix A.1.

Table 7.4: A selection of molecular electronic states in the $\Lambda - S$ coupling picture and associated atomic dissociation channels in an energy range of up to ≈ 14000 cm^{-1}.

Atomic $^{(2S+1)}L_J$	Molecular $^{(2S+1)}\Lambda_\Omega$
$Rb^+_{5s^0}$ $(^1S_0)$ + Ba_{6s^2} $(^1S_0)$	$^1\Sigma^+_{0^+}$
Rb_{5s^1} $(^2S_{1/2})$ + $Ba^+_{6s^1}$ $(^2S_{1/2})$	$^3\Sigma^+_{1,0^-}$, $^1\Sigma^+_{0^+}$
$Rb^+_{5s^0}$ $(^1S_0)$ + $Ba_{6s^15d^1}$ $(^3D_{1,2,3})$	$^3\Delta_{3,2,1}$, $^3\Pi_{2,1,0^+,0^-}$, $^3\Sigma^+_{1,0^-}$
$Rb^+_{5s^0}$ $(^1S_0)$ + $Ba_{6s^15d^1}$ $(^1D_2)$	$^1\Delta_2$, $^1\Pi_1$, $^1\Sigma^+_{0^+}$
$Rb^+_{5s^0}$ $(^1S_0)$ + $Ba_{6s^16p^1}$ $(^3P_{0,1,2})$	$^3\Pi_{2,1,0^+,0^-}$, $^3\Sigma^+_{1,0^-}$

Table 7.4 compiles the atomic configurations and terms as well as their corresponding molecular states that form the lower part of the electronic spectrum of the $(RbBa)^+$ molecular ion up to $\approx$ 14000 cm^{-1} above the ground state. These molecular states include also the Σ states correlated with the entrance channel for the envisaged collision experiments involving an ultracold ionized trapped barium atom and a Bose-Einstein condensate of neutral rubidium atoms. In the following I shall elaborate on the results that were obtained for all the molecular states located below the entrance channel plus d channels associated with the $Rb^+_{5s^0}(^1S_0)$ + $Ba_{6s^15d^1}(^3D_{1,2,3}$; $^1D_2)$ atomic limits listed in Table 7.4.

In the MRCI study at the spin-free computational level reported in Paper 1 I used the ANO-RCC basis sets [177] for both atoms. Extensive atomic and molecular test calculations, however, revealed that with Dyall's latest basis sets of triple-ζ quality for Rb and Ba [167] (in the following denoted by TZ) higher accuracy can be achieved in the calculations including spin-orbit coupling. Both basis sets were applied in uncontracted form. The Ba TZ basis set was further augmented with one diffuse d, f, and g function with exponents of 0.036645714, 0.3000341, and 0.76354824, respectively. This was done in order to properly describe excitations to the Ba $5d$ shell in the molecular ion $(RbBa)^+$. A molecular one-particle Kramers-paired spinor basis was obtained from closed-shell Dirac-Coulomb HF calculations at the various internuclear distances. Average-of-configurations HF calculations with an averaging over the Ba $6s5d$ and Rb $5s$ shell were not possible at all internuclear distances because of strong mixing with the Ba $6p$ and Rb $5p$ shell. All these valence shells were included in the active space in the ensuing MRCI correlation

Table 7.5: Excitation energies T in cm^{-1} for the lowest $Ba_{6s^2}(^1S_0) \rightarrow Ba_{6s^15d^1}(^3D_{1,2,3})$, $Ba_{6s^2}(^1S_0) \rightarrow Ba_{6s^15d^1}(^1D_2)$ and $Ba_{6s^2}(^1S_0) \rightarrow Ba_{6s^16p^1}(^3P_{0,1,2})$, electronic transitions calculated at the atomic MRCI S6(2in9)SD/TZ and atomic-like S12(2in13)SD/TZ (molecular calculation; values taken at $R = 50$ bohr) levels. The active space in the atomic calculation includes the same Ba shells and the same truncation threshold for the virtual spinors as in the molecular case. Details on the molecular computational level are given in the text. The MRCI results are compared to previous theoretical and experimental data. In the atomic-like "J states" (Ω) the individual M_j components are almost degenerate at $R = 50$ bohr with deviations on the order of $4 - 8$ cm^{-1} from the lowest to highest M_j component. Here, the energies of the lowest M_j values are shown in the table.

	$^1S_0$	$^3D_{1,2,3}$			$^1D_2$	$^3P_{0,1,2}$		
Method	$J = 0$	$J = 1$	$J = 2$	$J = 3$	$J = 2$	$J = 0$	$J = 1$	$J = 2$
Experiment [178]	0	9034	9216	9597	11395	12266	12637	13515
Atomic calculations								
S6(2in9)SD/TZ	0	8627	8809	9175	11197	12732	13091	13944
FSCCSD [145]	0	9075	9260	9639	11621	12423	12802	13793
IHFSCCSD [145]	0	9117	9296	9677	11426	12397	12728	13610
Molecular calculation at $R = 50$ bohr								
S12(2in13)SD/TZ	0	8619	8812	9174	11198	12736	13109	13936

step yielding a distribution of two valence electrons in 13 Kramers pairs (2in13). Core-valence correlation was taken into account from the outer-core Rb $4p$ and Ba $5p$ shell (S12). Single and double excitations from the combined spaces into the virtual spinor space which was limited to virtual Kramers pairs below a threshold of 18 E_h[8], ensured a proper accounting of dynamic electron correlation. This computational model is dubbed as MRCI S12(2in13)MRSD/TZ[9].

In order to validate the chosen molecular MRCI setup it is useful to examine its performance in the atomic limit. Table 7.5 compiles the results of atomic and atomic-like excitation energies of the lowest Ba atomic transitions as well as previous theoretical work and experimental data. Comparisons of the atomic MRCI S6(2in9)MRSD/TZ and the

[8]Virtually no difference in the computed excitation energies was observed for a benchmark test using a cut-off threshold of 42 E_h.

[9]A general introduction to my notation of MRCI schemes can be found in Appendix A.1

atomic-like molecular MRCI S12(2in13)SD/TZ results show that the dissociation limit is reached at an internuclear separation of 50 bohr. From previous studies on transition metals it is known that $ns^2(n\text{-}1)d^m \rightarrow ns^1(n\text{-}1)d^{m+1}$ excitations are difficult to describe in general within an MRCI approach because of the slow convergence of the dynamical electron correlation contributions [179]. Multireference CC approaches, such as for example the Fock-space CCSD (FSCCSD) or the intermediate Hamiltonian IHFSCCSD methods [144–146], are better at describing dynamical electron correlation energies. They are therefore expected to yield closer agreement with experiments, as the results in Table 7.5 confirm. In view of these difficulties for MRCI the deviations of my computed ^3D and ^1D excitation energies from the experimental values on the order of a few 100 cm^{-1} are satisfactory. The fine-structure splittings of these terms are even reproduced within a few tens of cm^{-1}(see Table 7.5). Furthermore, the good agreement of the calculated $Ba_{6s^1 6p^1}(^3P)$ energies with the experiment shows that the chosen basis set and correlation treatment are adequate.

In addition to the energetic location of the low-lying neutral Ba channels, the differential ionization potential of Rb and Ba is of vital importance for an unbiased description of the $(RbBa)^+$ molecular states. The computed ΔIP (IP(Ba)-IP(Rb)) value of 8454 cm^{-1} is in excellent agreement with experiment (8344 cm^{-1}) [180]. This ΔIP was calculated as the excitation energy in the atomic-like limit at 50 bohr of a molecular calculation. The Ba^+ + Rb entrance channel is thus placed only slightly below the $Ba_{6s^1 5d^1}(^3D_1)$ + $Rb^+_{5s^0}$ atomic channel. This is in contrast to the lighter homologs $(NaCa)^+$, $(MgK)^+$ and $(MgCs)^+$ where the corresponding energy gap is much larger.

Contrary to the ground state[10], accounting for spin-orbit coupling in the excited states yields a more complex picture for the potential energy curves of the electronic excited states of the molecular ion $(RbBa)^+$ compared to the spin-free calculations (Paper 1). The avoided crossings between the $^3\Sigma^+_{0^-}$-$^3\Pi_{0^-}$ states and the $^3\Sigma^+_1$-$^3\Pi_1$ states are easily discernible in Figure 7.3 and in the enlargement of the critical region in Figure 7.4. Of course, in the spin-free calculations all these curves cross as illustrated in Figure 7.2, and it is thus evident that a proper treatment of spin-orbit coupling is mandatory for explanation and prediction of outcomes of ultracold reactive collisions of Ba^+ on a Rb Bose-Einstein condensate. An even more pronounced avoided crossing between the $^1\Sigma^+$ of the entrance

[10]The reader is referred to Paper 5 for a detailed discussion of the ground state.

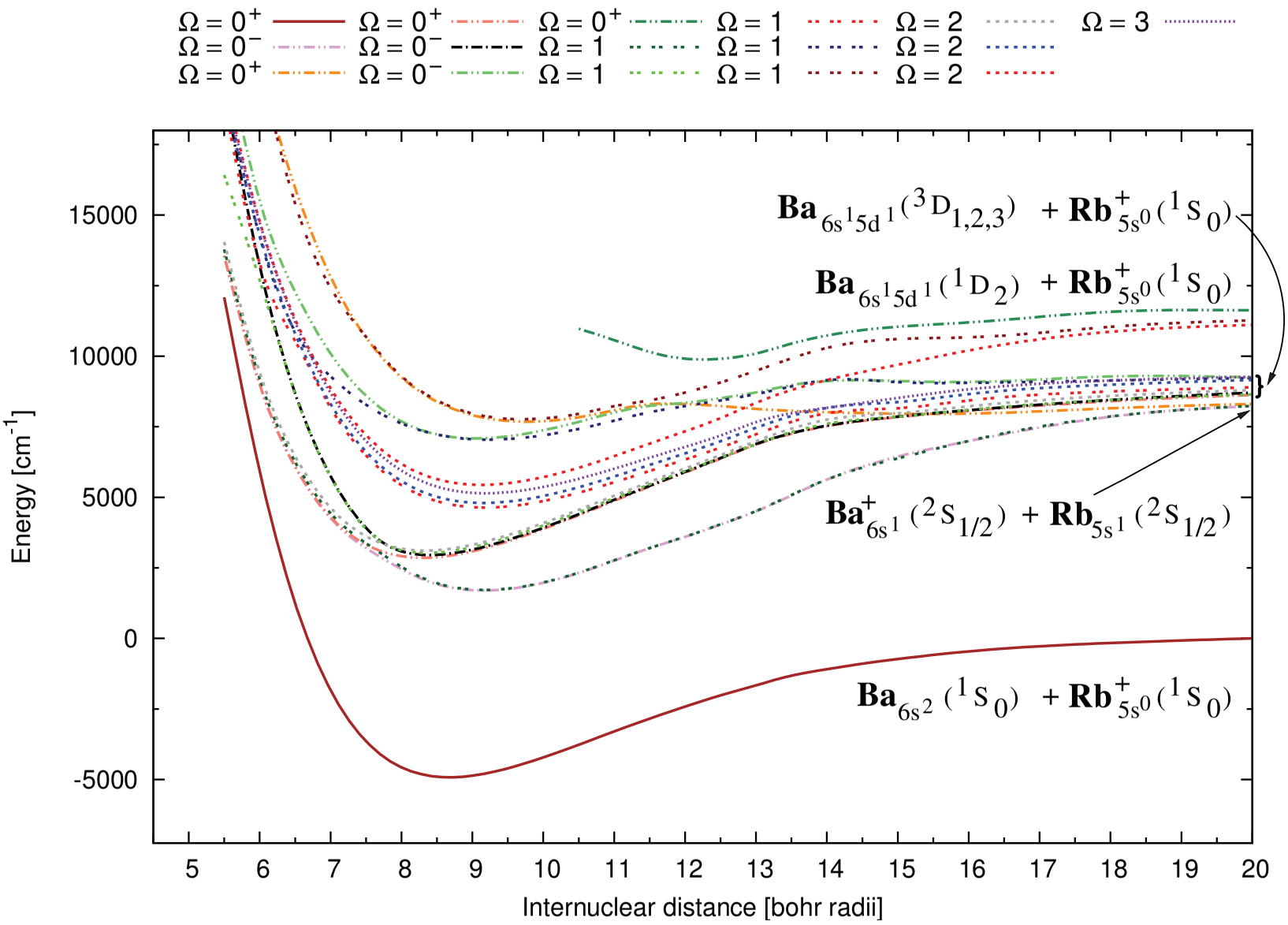

Figure 7.3: Potential energy curves of the ground and low-lying states (Ω designation) of $(RbBa)^+$ computed at the four-component MRCI S12(2in13)SD/TZ level (see text for more details). Atomic dissociation channels for the states are indicated in the picture (see Table 7.4 for details).

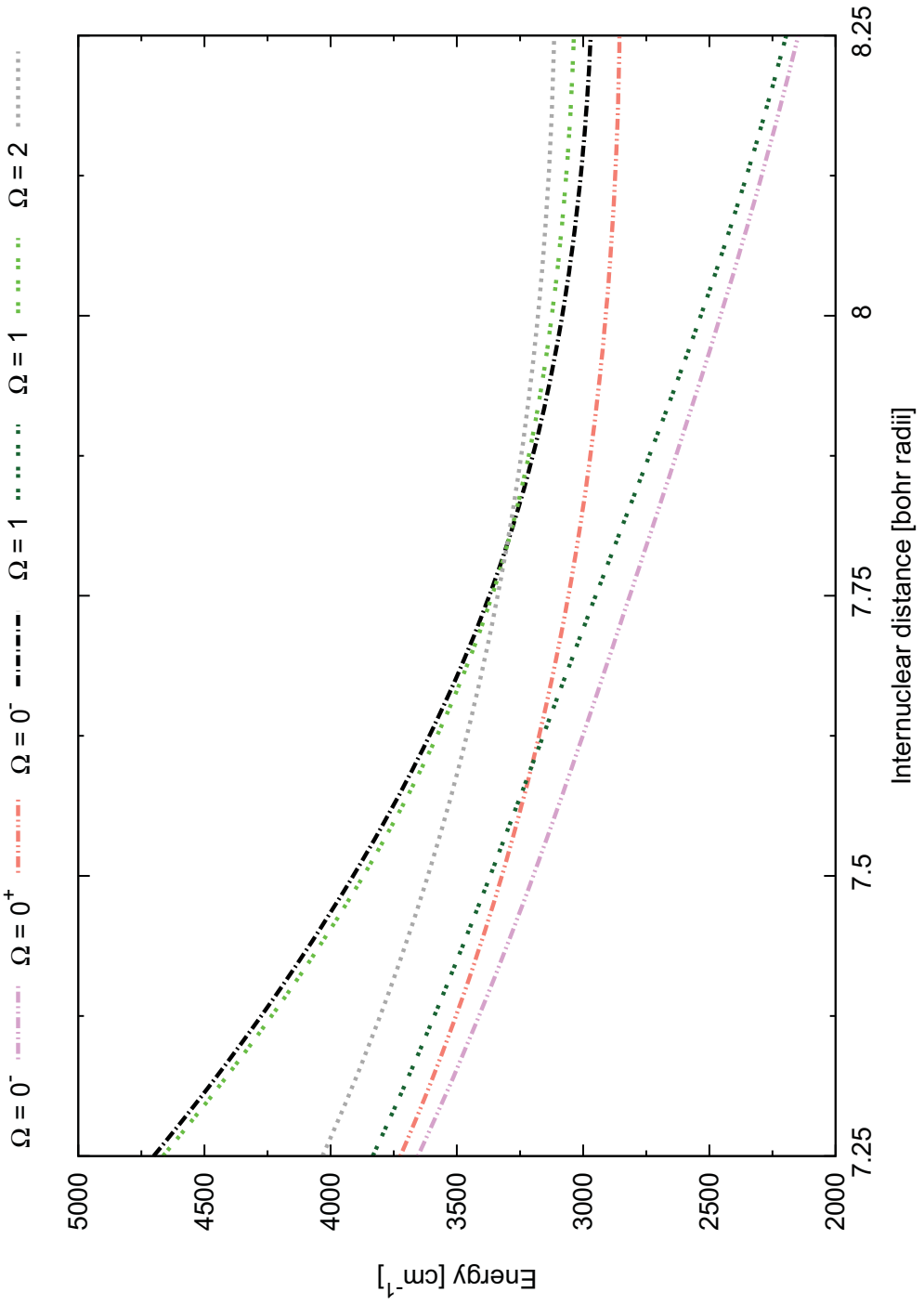

Figure 7.4: Close up of the avoided crossings between the $^3\Sigma^+_{1,0^-}$ Rb + Ba^+ entrance channels and and low-lying charge transfer $^3\Pi_{1,0^-}$ states of the Rb^+ and $Ba_{6s^1\,5d^1}(^3D)$ atomic channels.

channel and the $^1\Sigma^+$ of the $Ba_{6s^15d^1}(^1D)$ channel is also visually identifiable in Figure 7.3. Unlike the above mentioned avoided crossings this one would also be present in a non-relativistic or scalar-relativistic calculation (see Figure 7.2). The spin-orbit splitting of the calculated scalar-relativistic states is sizeable, in particular for the $^3\Delta$ and $^3\Pi$ states which are split into their $\Omega = 1, 2, 3$ and $\Omega = 0^+, 0^-, 1, 2$ components (see Figure 7.3). The splitting of the $^3\Delta$ and $^3\Pi$ into their Ω components is on the order of of 250 and 80 cm^{-1}, respectively, at the ground state equilibrium bond distance. While some of the Ω components are degenerate in the atomic limit because they belong to the same atomic J level, the molecular field gives rise to a spin-orbit splitting also of these components.

Most of the electronically excited states exhibit strong multiconfigurational character and are thus more difficult to describe in a molecular orbital picture. Their electronic structure will therefore be discussed in a more qualitative way. The lowest excited $\Omega = 0^-$ and $\Omega = 1$ states correlate to a $^3\Sigma^+$ state in the Λ-S representation (see Table 7.4). In the dissociation limit their electronic structure corresponds to $Ba^+ + Rb$. At shorter nuclear distances more and more $Ba_{6s^15d^1_\sigma}(^3D)$ character is mixed in. In the Franck-Condon region the wave function has nearly equal contributions from these two configurations. At about 7.75 bohr the $^3\Sigma^+$ components undergo an avoided crossing with the $\Omega = 0^-$ and $\Omega = 1$ of a $^3\Pi$ state (see Figure 7.4). The $^3\Pi$ state has a significantly shorter equilibrium distance than the other states originating from the $Ba_{6s^15d^1}(^3D) + Rb^+$ channel which can be traced back to the strong admixture of Ba $6p_\pi$ and Rb $5p_\pi$ character into the Ba $5d_\pi$ spinor.

The non-adiabatic interaction between the $^3\Sigma^+$ and $^3\Pi$ states is anticipated to have significant impact on the charge-transfer process. In the entrance channel the system is prepared initially in a highly excited vibrational level of the $^3\Sigma^+$ potential. At short internuclear separation the non-adiabatic interaction yields a finite probability for a non-radiative transition to the $^3\Pi$ potential which in turn can relax to the electronic ground state by emission of a photon.

At an internuclear distance of 15 to 16 bohr it is furthermore seen that the $^1\Sigma^+$ entrance channel crosses the $\Omega = 0^+$ of a $^3\Pi$ state (see Figure 7.3). While it would formally not be allowed for two $\Omega = 0^+$ state to cross it appears that for this charge transfer process the non-adiabatic coupling matrix element or off diagonal element between the two states is so small that hardly any effect can be seen. A clear avoided crossing in the 12 to 13

bohr range between the $^1\Sigma^+$ and the higher lying $\Omega = 0^+$ of a $^1\Sigma^+$ from the $Ba_{6s^1 5d^1}(^1D)$ but also $\Omega = 0^+$ of a $^3\Pi$ of the $Ba_{6s^1 6p^1}(^3P)$ (not shown in Figure 7.3) are observed. These avoided crossings are responsible for the metastable character of the $^1\Sigma^+$ entrance channel state. This is in sharp contrast to what is observed in the lighter homologs where the $^1\Sigma^+$ state is a purely dissociative state.

Summarizing, the non-adiabatic interaction in the short range of the potential (see Figure 7.4) between the $^3\Sigma^+_{1,0^-}$ and $^3\Pi_{1,0^-}$ states is expected to lead to a non-radiative charge transfer from the $^3\Sigma^+_{1,0^-}$ entrance channel to the $^3\Pi_{1,0^-}$ states. While transition from the $^3\Pi_{1,0^-}$ states to the ground state in $(RbBa)^+$ is also in a scalar-relativistic approximation electric dipole and spin forbidden, the large mixing of the Ba $5d_\pi$ with the close lying Ba $6p_\pi$ and Rb $5p_\pi$ spinors induced by spin-orbit coupling will greatly decrease the radiative lifetime. The expected fast non-radiative charge transfer to the $^3\Pi_{1,0^-}$ states may experimentally, however, not be desirable since it will irreversibly 'destroy' the Ba ion. In order to go from the present qualitative analysis to a more quantitative predictions of life times requires the knowledge of the transition dipole moments which are currently not available yet (see Section 5.3 for a discussion). Since Ba is a special case among the alkaline earth metals with its low lying D shell it presents a unique opportunity to study non-radiative charge transfer processes in the excited state manifold thereby making $(RbBa)^+$ experimentally very interesting.

Finally, I show in Figure 7.5 the dipole moment curve of the molecular ground state of $(RbBa)^+$ calculated at the four-component CCSD(T) level with origin at the center of mass. The dipole moment was computed for each point by means of the finite-field technique[11] as described in full detail in Paper 5. For a charge distribution corresponding purely to Rb^+ and Ba a dipole moment of around 14 Debye could be expected at an internuclear separation of 8.75 bohr (see Figure 7.5). Due to a partial electron transfer from Ba to Rb^+ in the ground state (see Paper 5 for more details) the dipole moment of the electronic ground state is, however, significantly lower at the equilibrium distance. It should be noted that in perfect agreement with the theory, an asymptotic behavior of the dipole moment is obtained for large internuclear distances.

[11] See Section 5.1 for a discussion of the finite-field technique.

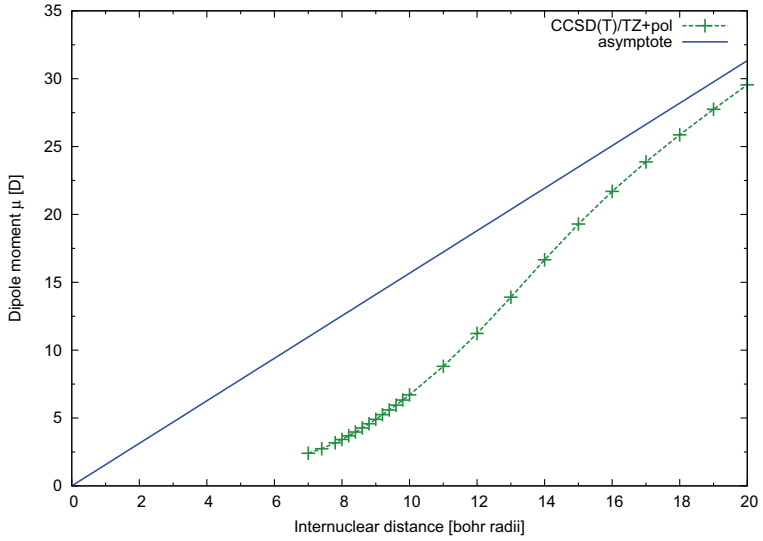

Figure 7.5: Four-component CCSD(T) dipole moment curve (in Debye) of the molecular ground state with calculated with 14 explicitly correlated electrons. The straight line (blue) indicates the asymptotic limit of the dipole moment μ for a charged system in the center-of-mass coordinates.

Chapter 8

Actinide Compounds

The actinide elements comprise the lower row of the f block in the periodic system of elements (see Figure 6.1 in Section 6). Owing to the fact that many of the relativistic effects roughly scale as Z^2 for isoelectronic valence shells these effects will be much more pronounced for the actinide ($5f$) than the lanthanide ($4f$) elements [8]. The so-called "direct" relativistic effect which has its origin in the relativistic mass increase results in a significant contraction and energetic stabilization of in particular the s and $p_{1/2}$ orbitals[1] (see Figure 6.3 in Section 6.1 for an illustrative example). In consequence of the more efficient screening of the effective potential through the s and p shell, the d and f shells will be energetically destabilized and expand radially ("indirect" relativistic effect). Moreover, spin-orbit coupling yields a splitting of all shells with $l > 0$, *e.g.* for the $5f$ in the actinides: $5f \rightarrow 5f_{7/2}, 5f_{5/2}$.

All these effect lead to a unique situation in the early actinide elements including thorium and uranium where different empty and (partially) filled shells ($7s$, $7p$, $6d$ and $5f$) are in principle available for chemical activity. Experimental and in particular spectroscopic work on actinide compounds is, however, rather scarce owing to the toxicity and radioactivity of these materials. Theoretical calculations on the other hand can help to gain insight into the complex electronic structure of actinide systems and on this basis to explain the chemical behavior of actinide atoms, ions, complexes and molecular compounds.

[1] These orbitals have a greater density close to the nucleus and therefore experience a considerable fraction of the effective nuclear potential.

In the following Section 8.1 I present my MRCI results on the lower even-parity electronic spectra of the thorium atom. Besides a thorough investigation of various correlation effects, a comparison is drawn to experimental data and previous theoretical work. Moreover, I outline a future investigation on the Th diatom Th_2. A discussion of the bonding picture in the uranium diatom U_2 that has been observed experimentally for the first time in the mid 1970's [181] comprises Section 8.2. As shall be explained there, my own contributions are limited to a qualitative study.

8.1 Thorium

Thorium is the first of the $5f$-block elements (see also Figure 6.1 in Chapter 6) and exhibits, unlike its lighter $4f$-block homologue cerium ($^1G_4$: $4f^15d^16s^2$), an electronic ground state configuration with an empty f shell: $6d^27s^2$ ($^3F_2$) [182]. The lowest electronic states are of even-parity and are derived from the configurations $6d^27s^2$ and $6d^37s^1$ resulting in a wealth of ^3F, ^3P, ^5F, ^1D, ^1G and ^5P states (LS coupling picture). The first electronically excited state with an f^1 occupation pattern ($5f^16d^17s^2$ $^3H_4$) is of odd-parity and is located 7795 cm^{-1} above the electronic ground state [182].

The validity of the LS coupling picture is, however, in general lifted for a heavy element such as thorium. The strong spin-orbit coupling significantly mixes terms of different configurations and LS values leaving only the total angular momentum J as a good quantum number. For this purpose, I have computed the lower electronic spectrum of the thorium atom by means of my parallel spin-dependent MRCI program `LUCIAREL` in a 4-component framework using the Dirac-Coulomb Hamiltonian. By these means, a treatment of both electron correlation and relativistic effects on the same footing is ensured. To correctly describe the spin-orbit coupling of the ground state and excited states the Dirac-Coulomb Hamiltonian suffices since it contains the leading spin-orbit terms for heavy elements, namely the one-electron spin-orbit and the two-electron spin-same-orbit terms [25, 26]. Taking into account the spin-other-orbit term which is derived from the Gaunt operator yields a reduction of 41 cm^{-1} on the spin-orbit splitting of the $6d$ Kramers pairs at the (uncorrelated) SCF level. This decrease corresponds to 1.6% of the total splitting which is still below the accuracy we may typically achieve for relative energies.

The energetic vicinity of the $7s$, $7p$, $6d$ and $5f$ shell in the actinide elements [183] leads in general to a great many of configurations that are mostly characterized by a large number of partially occupied shells. This trend holds true also for the present system where such a variety of configurations is already found in the lower part of the atomic spectrum. A summary of configurations[2] for excitation energies of up to 25 000 cm^{-1} is given in Table 8.1. As a result of the high M_J degeneracy of states with high angular

[2]The presented list may be incomplete, though. In Reference 182 further configurations provided with large error bars are reported.

Table 8.1: Even-parity and odd-parity ground and excited levels of the thorium atom and their respective electronic configuration. The table is taken from Reference 182 but only states below an energetic threshold of 25000 cm^{-1} are shown. Excitation energies are given in cm^{-1}.

even parity levels			odd parity levels		
configuration	level	excitation energy	configuration	level	excitation energy
$6d^2 7s^2$	$^3F_2$	0	$5f6d7s^2$	$^3H_4$	7795
$6d^3 7s$	$^5F_1$	5563	$6d7s^2 7p$	$^3F_2$	10783
$5f7s^2 7p$	$^3G_3$	18432	$6d^2 7s7p$	$^5G_2$	14465
$6d^4$	$^5D_0$	21176	$5f6d^2 7s$	$^5H_3$	15619
$5f6d7s7p$	$^5I_4$	22098			

momentum the calculation of but a few electronic states necessitates for the present approach the computation of many eigenvectors. The reason for this is the lack of full atomic symmetry in the CI program `LUCIAREL` and the use of binary double groups in its stead. Every M_J component of an atomic J state is thus determined as an individual eigenvector in the CI optimization. I therefore confine myself to a discussion of the ground and lowest electronically excited states originating from the even-parity levels ^3F, ^3P, ^5F based on my MRCI results. These states are ascribed particular importance to the bonding in the thorium diatom Th_2 [184].

The following section comprises details on the basis sets and computational schemes that were employed in this study. In Section 8.1.2, I discuss the performance of my MRCI excitation energies in comparison to previous theoretical work as well as to experiment. Finally, I outline my ongoing study of the thorium diatom Th_2 using the present four-component MRCI approach.

8.1.1 Computational Details

All calculations in the present investigation were performed using uncontracted basis sets. I made use of Dyall's double-ζ (DZ) and triple-ζ (TZ) basis set [185] where valence-correlating functions for the Th $6d$, $7s$ and $5f$ shells were added. The smaller DZ basis comprises $\{26s23p17d12f1g\}$ functions and the more elaborate TZ basis a set of $\{33s29p20d14f4g1h\}$ functions. The TZ basis set is comparable in size with the "large-size" Th basis set of Noro *et al.* [186] and with the ANO-type basis set optimized by Roos

and coworkers [187].

The calculations were carried out in the abelian double point group C_{2h}^{*}. An unambiguous assignment of the J quantum number to each individual electronic state was accomplished by means of my parallel CI property module which is presented in Section 5. An appropriate one-particle Kramers-paired spinor basis for the ensuing correlation step was obtained from all-electron average-of-configuration four-component Hartree-Fock calculations [188]. The open-shell state-averaging was defined over all even-parity electronic configurations with a Th $6d^x7s^y$ ($x = 2, 3, 4;\ y = 0, 1, 2;\ x + y = 4$) occupation manifold by distributing four electrons among six *gerade* Kramers pairs. This technique ensures a balanced description of the ground state and lowest excited even-parity states (cf. Table 8.1) that stem from these configurations.

I considered five different GAS set-ups in the MRCI studies all of which are compiled in Table 8.2. In the (4in6)SD calculations single and double excitations (SD) into the virtual spinor space are taken into account from a complete-active-space (CAS) spanned by the six Th $7s$ and $6d$ Kramers pairs where four electrons are freely distributed (4in6). The remaining computational schemes are of restricted-active-space type with a maximum number of holes in GAS I, no restrictions in GAS II, and with a maximum number of particles in GAS III. A detailed introduction to my notation can be found in Appendix A.1. To account for core-valence correlation single excitations from the Th $6s6p$ shells[3] are taken into consideration in the MRCI S8(4in6)MRSD calculations. The GAS set-ups S6(4in6)MRSD and S6(4in9)MRSD, respectively, differ in the size of the CAS (and the virtual space). The extended (4in9) active space includes the Th $7p$ shell thus implicitly accounting for reference configurations with a $7p$ occupation. As will be discussed in Section 8.1.2 the resulting correlation effects are indicative of having a significant impact on an accurate description of the lower electronic spectrum. Finally, in a fifth GAS scheme, henceforth referred to as S6(4in6)SDT($7p$)MRSD, higher excitations are taken into account from the combined reference configurations (GAS I and GAS II) into the Th $7p$ shell (GAS III) by allowing single, double and triple excitations into GAS III.

[3] In this work the $6s6p$ shells will be referred to as "core" shell, although for the early actinides these shells are sometimes denoted as "semi-core" or "subvalence" [189,190]. The numerical Dirac-Hartree-Fock orbital binding energies are -2.066 au ($6s_{1/2}$), -1.318 au ($6p_{1/2}$), -1.002 au ($6p_{3/2}$), -0.230 au ($6d_{3/2}$), -0.211 au ($6d_{5/2}$) and -0.204 au ($7s_{1/2}$) [183], respectively.

In the correlation step the virtual spinor space (GAS III or GAS IV) was limited to an energy threshold of either 11 E_h or 42 E_h, a procedure that is routinely performed when uncontracted basis sets are used [73]. Nonetheless, an error estimation will be given on the basis of a comparison of a low-cutoff and corresponding high-cutoff calculation. To allow for a reliable comparison of the performance of the different computational schemes using either basis sets, DZ and TZ, a statistical analysis of the deviations of the calculated spectra from the experiment was carried out. This procedure follows the idea of Helgaker *et al.* [149] and is described in Appendix A.2. The calculated quantities were added at the bottom of Table 8.3.

8.1.2 Lower Even-Parity Atomic Electronic States

The MRCI results for the lowest electronic states of even-parity of the thorium atom as well as experimental data are compiled in Table 8.3. From an inspection of Table 8.3 some general trends can immediately be deduced: the excitation energies calculated at the (4in6)MRSD level agree reasonably well with experiment for most of the states under consideration[4]. Taking into account core-valence correlation leads for the most part to a different ordering of the atomic states due to a significant shift in the excitation energies. In agreement with Hund's second rule [113] and the jj-coupling rules [191] all computational models yield the $J = 2$ state originating from the ^3F as the electronic ground state.

As can be inferred from the mean error $\bar{\Delta}$ excitation energies are in general underestimated within all MRCI models and basis sets. The calculations using a DZ basis set show a smaller mean error than their corresponding TZ counterparts which should be considered as a fortunate error compensation. Nonetheless, the relatively small Δ_{std} (< 700 cm^{-1}) which I find for all models, points to a more systematic origin of the errors in spite of the rather complicated interactions between various electronic configurations. As a further indication of this hypothesis, for all but one exception, namely (4in6)SD/TZ, a mean absolute error is obtained that is identical to $\bar{\Delta}$. A key issue could thus be whether it is possible to predict a correct ordering of the various J states from the present CI approaches.

[4]The good performance of the (4in6)SD approach is likely to be fortuitous though.

Table 8.2: Generalized Active Spaces (GAS) and occupation constraints for Th ground- and excited-state calculations in C_{2h}^{*} double-group symmetry using uncontracted DZ and TZ basis sets (see text for more details), respectively. The minimum and maximum number of electrons are accumulated values, *i.e.*, by adding the number of electrons in this and all preceding GA spaces.

S8(4in6)MRSD

GA Space	Kramers pairs per irrep		Min./max. accum. el.		
	E_{1g}	E_{1u}	Min. el.	Max. el.	Shell types
I	1	3	6[a]	8	$6s6p$
II	6	0	10	12	$6d7s$
III	$X^{b,c}$	$Y^{b,c}$	12	12	virtual Kramers pairs

S6(4in6)MRSD

GA Space	Kramers pairs per irrep		Min./max. accum. el.		
	E_{1g}	E_{1u}	Min. el.	Max. el.	Shell types
I	0	3	5	6	$6p$
II	6	0	8	10	$6d7s$
III	$X^{b,c}$	$Y^{b,c}$	10	10	virtual Kramers pairs

S6(4in9)MRSD

GA Space	Kramers pairs per irrep		Min./max. accum. el.		
	E_{1g}	E_{1u}	Min. el.	Max. el.	Shell types
I	0	3	5	6	$6p$
II	6	3	8	10	$6d7s7p$
III	$X^{b,c}$	$Y^{b,c}$	10	10	virtual Kramers pairs

S6(4in6)SDT($7p$)MRSD

GA Space	Kramers pairs per irrep		Min./max. accum. el.		
	E_{1g}	E_{1u}	Min. el.	Max. el.	Shell types
I	0	3	5	6	$6p$
II	6	0	7	10	$6d7s$
III	0	3	8	10	$7p$
IV	$X^{b,c}$	$Y^{b,c}$	10	10	virtual Kramers pairs

[a] The Th $6s6p$ Kramers pairs are always doubly occupied in the **(4in6)MRSD** calculations.

[b] DZ basis set: X = 27 and Y = 47 (11 E_h threshold).

[c] TZ basis set: X = 52 and Y = 62 (11 E_h threshold), and
X = 68 and Y = 81 (42 E_h threshold).

To begin with, I turn towards the (4in6)MRSD calculations where only the four valence electrons were considered in the correlation treatment. At this computational level I find an excellent agreement with the experimental data as confirmed by the small standard deviations of 280 cm^{-1} and 372 cm^{-1}, respectively, for both basis sets. A striking feature in both cases is, however, a distinct underestimation of the excitation energies of the $J = 3$ and $J = 4$ states ($\Delta_{max} = 741$ cm^{-1} resp. 764 cm^{-1}) that originate from the same ^3F term as the electronic ground state ($J = 2$). This in turn results in a reverse order of the two lowest electronically excited states $J = 0$ and $J = 3$. Taking account of correlation contributions from the underlying Th $6s6p$ (S8(4in6)MRSD) and Th $6p$ shell (S6(4in6)MRSD), respectively, yields, on the other hand, the correct order of the $J = 0$ and $J = 3$ states.

In addition, the inclusion of the outer core shells of thorium has a more significant impact on the lower electronic spectrum as a whole which manifests itself in both a notable increase of $\bar{\Delta}_{abs}$ of up to 798 cm^{-1}(S8(4in6)MRSD/TZ) and a maximum absolute error of 1768 cm^{-1}(S8(4in6)MRSD/TZ). Inspecting Table 8.3, it becomes evident that all states are shifted to a large extent towards the lower end of the spectrum except for the above mentioned $J = 3$ and $J = 4$ states for which I find the opposite effect. By drawing a comparison between the excitation energies obtained at the S8(4in6)MRSD computational level which takes into account single excitations from Th $6s$ and $6p$ and those derived from a S6(4in6)MRSD calculation (only Th $6p$) I can conclude that the differential correlation effects arising from the Th $6s$ shell are relatively small.

Further calculations of the ground and four lowest excited states where Th $6s6p$ core-core correlation was included[5] yielded a decrease of the excitation energies for the $J = 0, 2, 1$ states on the order of 30 - 100 cm^{-1}. The $J = 3$ state, on the other hand, exhibited a slight increase by 40 cm^{-1} towards the experimental value. In summary it can be said, therefore, that explicitly correlating the outer core electrons of thorium in general entails a significant reordering of the electronic states in the lower excitation spectrum. It furthermore results in a modest agreement with the experiment for distinct states irrespective of the basis set. In what follows, I will only consider core-valence correlation contributions from the Th $6p$ shell. As stated above, they account for a major part of the

[5]The results are not listed in Table 8.3. These were obtained from a SD8(4in6)MRSD/TZ calculation where at most two holes in GAS I were allowed.

relaxation effects.

As a next step, the effect of extending GAS II to comprise the Th $7p$ shell (S6(4in9)MRSD) was examined. With this particular choice of a CAS-like reference space I allow for reference configurations with, *e.g.* a Th $6p7p$ or Th $7p^2$ occupation pattern. The resulting correlation contributions lead to a significant improvement of the description of the lower excited states. Both the mean absolute error as well as the standard deviation decrease by 26% respective 18% comparing the S6(4in9)MRSD/TZ calculation with its S6(4in6)MRSD/TZ reference. This trend is perfectly consistent with what is observed for the DZ basis set. It is worth noting that the extension of the reference space results in an increase of the excitation energies on the order of 150-300 cm^{-1} for all but the previously mentioned $J = 3$ and $J = 4$ states. These states are hardly affected. The observed singular increase is therefore indicative of a particular importance of relaxation effects relevant for the electronic ground state of thorium arising from configurations with a Th $7p$ occupation. This proposition is in agreement with the findings of Bauschlicher and co-workers [179] who studied the issue of differential correlation contributions for first-row transition metals in regard to an accurate description of states with a $d^n s^2$ $d^{n+1}s^1$ and $d^{n+2}s^0$ occupation pattern. In this work, they also pointed out the particular importance of $s^2 \rightarrow p^2$ reference configurations for the description of $d^n s^2$ states.

To further investigate this interesting aspect I carried out complementary MRCI calculations where the Th $7p$ shell was placed in an extra GA space (S6(4in6)SDT($7p$)MRSD). At this level up to three particles in GAS III are taken into consideration which should to a great extent account for the suggested relevant relaxation contributions. In both cases using either basis set the picture obtained from the large-space (4in9) calculations is indeed retained, however, at a considerably lower computational cost[6]. As can be seen from Table 8.3 Δ_{std} and $\bar{\Delta}_{\mathrm{abs}}$ only slightly change by 11 cm^{-1} and 20 cm^{-1} in case of the TZ basis. Moreover, additional test calculations with an extended virtual space to include all Kramers pairs up to an energy threshold of 42 $E_h$show that the error from a calculation using a lower threshold of 11 E_h is negligible. Raising the cutoff value to 42 E_h results in a minor decrease of both Δ_{std} and $\bar{\Delta}_{\mathrm{abs}}$ by 11 cm^{-1} and 6 cm^{-1} as

[6] A S6(4in9)MRSD/TZ calculation comprises for example a configuration space of $\approx 32 \times 10^6$ determinants whereas in a S6(4in6)SDT($7p$)MRSD/TZ calculation the configuration space reduces to 25×10^6 determinants.

Table 8.3: Lowest excited even-parity states of thorium with empty $5f$ shell. For details on the MRCI schemes and basis sets (DZ and TZ) used the reader is referred to the text. Experimental data are taken from Ref. 182. Deviations (Δ) of the theoretical results from experimental data were quantified with statistical measures. Excitation energies and statistical measures are given in cm^{-1}

		(4in6)MRSD		S8(4in6)MRSD		S6(4in6)MRSD		S6(4in9)MRSD		S6(4in6)SDT($7p$)MRSD			
configuration	$^{2S+1}L_J$	DZ	TZ	DZ	TZ	DZ	TZ	DZ	TZ	DZ	TZ	TZ[a]	experiment
		Th atom. Ground state $6d^27s^2\ ^3F_2$											
$6d^27s^2$	$^3P_0$	2542	2804	1932	2104	2103	2259	2375	2433	2330	2416	2414	2558
$6d^27s^2$	$^3F_3$	2300	2296	2611	2633	2586	2598	2617	2625	2605	2620	2622	2869
$6d^27s^2$	$^3P_2$	3364	3522	3135	3203	3253	3311	3487	3463	3446	3447	3446	3688
$6d^27s^2$	$^3P_1$	3452	3727	2958	3099	3125	3262	3445	3470	3389	3448	3447	3866
$6d^27s^2$	$^3F_4$	4221	4198	4781	4774	4746	4725	4796	4769	4781	4762	4765	4962
$6d^3(^4F)7s$	$^5F_1$	5583	5756	4222	3869	4419	4177	4918	4477	4823	4442	4439	5563
$6d^3(^4F)7s$	$^5F_2$	6167	6305	4948	4594	5137	4896	5644	5203	5558	5167	5213	6362
$\bar{\Delta}$		-319	-180	-754	-798	-642	-662	-369	-489	-419	-509	-503	
Δ_{std}		280	372	489	664	406	535	230	440	259	451	440	
$\bar{\Delta}_{\mathrm{abs}}$		325	305	754	798	642	662	369	489	419	509	503	
Δ_{max}		741	764	1414	1768	1225	1466	718	1159	804	1195	1149	

[a] A higher cutoff threshold of 42 E_h in the virtual spinor space has been employed.

Table 8.4: A comparison of the lowest excited even-parity states of thorium computed at the MRCI S6(4in6)SDT(7p)MRSD/TZlevel with CASPT2/RASSI-SO [187], FSCC, IHFSCC [192] results and experimental data [182]. Excitation energies are given in cm^{-1}.

configuration	level	MRCI	CASPT2/RASSI-SO	FSCC	IHFSCC	experiment
		Th atom. Ground state $6d^2 7s^2\ {}^3F_2$				
$6d^2 7s^2$	$^3P_0$	2414	2258	3920	3630	2558
$6d^2 7s^2$	$^3F_3$	2622	2742	2783	2976	2869
$6d^2 7s^2$	$^3P_2$	3446	3146	4775	4339	3688
$6d^2 7s^2$	$^3P_1$	3447	3307	5485	5396	3866
$6d^2 7s^2$	$^3F_4$	4765	4759	5025	5033	4962
$6d^3(^4F)7s$	$^5F_1$	4439	4436	-	-	5563
$6d^3(^4F)7s$	$^5F_2$	5213	5323	-	-	6362

indicated in Table 8.3.

What about the question of predicting a correct ordering of the various atomic states that was raised in the beginning? Both computational schemes S6(4in9)MRSD/TZ and S6(4in6)SDT(7p)MRSD/TZ yield a similar overall picture of the lower part of the electronic excitation spectrum. Concerning for example the spin-orbit split lower $J = 2$ and $J = 1$ states that stem from the non-relativistic ^3P term a correct energetic order is predicted at both computational levels. The excitation energies for the second $J = 1$ and $J = 2$ excited states, on the other hand, come out too low by approximately 1000 cm^{-1} which entails the $J = 1$ state being wrongly placed below the $J = 4$ state. A related issue is encountered for the above mentioned lower $J = 2$ and $J = 1$ atomic states when either a S6(4in9)MRSD/DZ or a S6(4in6)SDT(7p)MRSD/DZ MRCI model is applied. To summarize, neither computational model is able to yield a correct ordering of all lowest atomic states of even-parity although with regard to the excitation energies the overall agreement with the experiment is very good.

Moreover, S6(4in6)SDT(5f 7p)MRSD/DZ calculations (results are not shown in Table 8.3) where the Th 5f shell was included in GAS III, did not reveal any significant improvements for the excitation energies. The contributions of reference configurations with 5f occupation are thus only of minor importance for the calculation of the lower even-parity excitation spectrum of the Th atom.

Finally, Table 8.4 lists the excitation energies for the lowest six transitions from my present best approach (S6(4in6)SDT(7p)MRSD/TZ and cutoff threshold at 42 E_h) in comparison with previous theoretical studies. My excitation energies are in very good agreement with the corresponding data reported by Roos and coworkers [187]. They included scalar-relativistic effects through the use of a Douglas-Kroll-Hess (DKH) [35,37] Hamiltonian in a combined CASPT2/RASSI-SO approach[7] using an ANO-type of basis set to compute the excitation spectrum. My present calculations, however, achieve this in a rigorous "one-step" manner where electron correlation and relativistic effects are treated on the same footing. It is therefore worth drawing a comparison with the results of the generally more accurate Fock-space CC (FSCC) and intermediate Hamiltonian FSCC calculations (IHFSCC) by Eliav *et al.* [192] where they made use of a Dirac-Coulomb-Breit Hamiltonian and an extensive basis set including up to l functions. Obviously, both FSCC calculations yield a slightly better agreement with the experimental data for those states which originate from the spin-orbit split ground state term ^3F. By contrast the remaining three atomic states are much worse described as indicated in Table 8.4. Summing up, among the considered theoretical approaches, the best overall agreement with the experimental data is obtained within my S6(4in6)SDT(7p)MRSD/TZ computational scheme. In addition, despite the general trend to underestimate individual excitation energies of the lowest even-parity states of Th the fine-structure splitting is very well reproduced in my MRCI calculations. For example, I calculate a splitting of 774 cm^{-1} between the $J = 1$ and $J = 2$ states of the ^5F term which is experimentally determined as 799 cm^{-1}.

8.1.3 Future Prospects

In view of the encouraging results that I obtained for the thorium atom it is worth considering to extend the investigation to a study of the thorium diatom. This system was examined in detail in a recent work by Roos *et al.* [184] using a CASPT2/RASSI-SO approach as described in the preceding section. They report the formation of a quadruple bond between the two thorium atoms as well as a rather large dissociation energy of 3.28 eV. Furthermore, they indicate a $\Omega = 1_g$ state as the electronic ground state of the

[7] In the restricted-active space state interaction (RASSI) method spin-orbit (SO) coupling is included in a variation-perturbation approach [143, 193].

molecule. It is, however, natural to ask whether a two-step approach to include spin-orbit coupling may give reliable predictions for such a molecular system composed of two heavy centers.

As a starting point, I examined the performance of the four-component Dirac-Coulomb/MRCI/TZ approach in the molecular case where a S12(8in12)SDT(7p)MRSD computational model shall finally be employed to mimic the corresponding atomic computational scheme. At the present stage, dynamical electron correlation is not taken into account, *i.e.*, excitations into the virtual Kramers-paired spinor space are neglected. In subsequent calculations the energetic cutoff threshold in the virtual space will gradually be raised to 14 E_h which will finally include 170 virtual Kramers-paired spinors in the correlation step. For the present test purposes the one-particle basis is generated by means of a (8in12) average-of-configurations DHF calculation. At a later stage, it is envisaged to perform state-specific MCSCF calculations which should provide a suitable spinor basis for a study of the molecular ground state.

Table 8.5 compiles a preliminary list of molecular electronic states which are found to form the lower electronic spectrum of the diatom Th_2 at the "uncorrelated" CI level. All states displayed differ in at most 0.5 eV in energy. In the calculations a Th-Th distance of 2.76 Å was chosen which corresponds to the ground state equilibrium bond distance computed by Roos *et al.* [184].

Besides the Ω designation of the various molecular states, the composition of the individual electronic states is reported in Table 8.5 in terms of natural spinor occupation numbers of the involved Kramers pairs. For this purpose, the (partially) occupied Kramers pairs are characterized with respect to their approximate $\lambda\omega$-projection notation. At the given computational level the lowest electronic states of Th_2 are of *ungerade* symmetry, namely $\Omega = 0_u$, 1_u and 3_u. Interestingly, none of these states were found in the earlier CASPT2/RASSI-SO study. A striking feature in the electronic configurations of the shown molecular states is furthermore that all these states exhibit an occupation of the predominantly antibonding ($7s\sigma_{1/2u}$) spinor which would be indicative of a bond order < 4. A possible explanation for this finding could be that the average-of-configurations approach used at present to generate a one-particle basis spuriously favors the occupation of this particular spinor. However, in view of the preliminary status of my calculations, it would be premature to conclude at this stage. Upon accounting for dynamic electron

Table 8.5: Molecular states of the thorium diatom Th_2 within an energy range of 0.5 eV calculated at the "uncorrelated" S12(8in12)SDT($7p$)MRSD computational level. Natural spinor occupation numbers for the individual Ω states are presented.

Ω	natural spinor occupation numbers
0_u	$(7s\sigma_{1/2g})^{1.85}$ $(6d\sigma_{1/2g})^{0.98}$ $(6d\delta_{3/2g})^{1.19}$ $(6d\delta_{5/2g})^{0.67}$ $(6d\pi_{1/2u})^{1.13}$ $(6d\pi_{3/2u})^{0.85}$ $(7s\sigma_{1/2u})^{1.01}$
1_u	$(7s\sigma_{1/2g})^{1.85}$ $(6d\sigma_{1/2g})^{0.98}$ $(6d\delta_{3/2g})^{1.15}$ $(6d\delta_{5/2g})^{0.70}$ $(6d\pi_{1/2u})^{1.13}$ $(6d\pi_{3/2u})^{0.87}$ $(7s\sigma_{1/2u})^{1.02}$
3_u	$(7s\sigma_{1/2g})^{1.85}$ $6d(\sigma_{1/2g})^{0.98}$ $(6d\delta_{3/2g})^{0.93}$ $(6d\delta_{5/2g})^{0.93}$ $(6d\pi_{1/2u})^{0.98}$ $(6d\pi_{3/2u})^{0.99}$ $(7s\sigma_{1/2u})^{1.02}$
0_g	$(7s\sigma_{1/2g})^{1.81}$ $(6d\sigma_{1/2g})^{0.96}$ $(6d\delta_{3/2g})^{0.84}$ $(6d\pi_{1/2u})^{1.72}$ $(6d\pi_{3/2u})^{1.15}$ $(7s\sigma_{1/2u})^{1.02}$
0_g	$(7s\sigma_{1/2g})^{1.80}$ $(6d\sigma_{1/2g})^{0.97}$ $(6d\delta_{3/2g})^{0.84}$ $(6d\pi_{1/2u})^{1.70}$ $(6d\pi_{3/2u})^{1.15}$ $(7s\sigma_{1/2u})^{1.02}$
1_g	$(7s\sigma_{1/2g})^{1.81}$ $(6d\sigma_{1/2g})^{0.98}$ $(6d\delta_{3/2g})^{0.71}$ $(6d\delta_{5/2g})^{0.35}$ $(6d\pi_{1/2u})^{1.40}$ $(6d\pi_{3/2u})^{1.34}$ $(7s\sigma_{1/2u})^{1.10}$
0_u	$(7s\sigma_{1/2g})^{1.81}$ $(6d\sigma_{1/2g})^{0.98}$ $(6d\pi_{1/2u})^{1.78}$ $(6d\pi_{3/2u})^{1.79}$ $(7s\sigma_{1/2u})^{1.02}$
1_g	$(7s\sigma_{1/2g})^{1.84}$ $(6d\sigma_{1/2g})^{0.97}$ $(6d\delta_{3/2g})^{0.93}$ $(6d\pi_{1/2u})^{1.09}$ $(6d\pi_{3/2u})^{1.68}$ $(7s\sigma_{1/2u})^{0.98}$
0_g	$(7s\sigma_{1/2g})^{1.83}$ $(6d\sigma_{1/2g})^{0.87}$ $(6d\delta_{3/2g})^{0.80}$ $(6d\pi_{1/2u})^{1.18}$ $(6d\pi_{3/2u})^{1.15}$ $(7s\sigma_{1/2u})^{1.68}$
0_g	$(7s\sigma_{1/2g})^{1.83}$ $(6d\sigma_{1/2g})^{0.98}$ $(6d\delta_{3/2g})^{0.93}$ $(6d\pi_{1/2u})^{1.05}$ $(6d\pi_{3/2u})^{1.02}$ $(7s\sigma_{1/2u})^{1.71}$
0_u	$(7s\sigma_{1/2g})^{1.78}$ $(6d\sigma_{1/2g})^{1.00}$ $(6d\delta_{3/2g})^{0.25}$ $(6d\pi_{1/2u})^{1.07}$ $(6d\pi_{3/2u})^{1.76}$ $(7s\sigma_{1/2u})^{1.74}$

correlation the current picture of the electronic spectra will most likely change to comprise also states that have occupation numbers close to zero for the ($7s\sigma_{1/2u}$) spinor. The quest for the ground state of the thorium diatom thus remains a challenging task.

8.2 A Word or Two about U_2

The fundamental concept of covalent bonding, meaning electron pairing between two atoms, has been introduced by Lewis in 1916 [194]. Ever since a much discussed question in chemistry concerned the maximum multiplicity that can be achieved in a chemical bond [195–197]. In other words, "what is the maximum number of covalent chemical bonds that two atoms can share?" [196]

In 1964 Cotton and co-workers [198] published the crystal structure of $K_2[Re_2Cl_8] \cdot 2H_2O$ where they found experimental evidence for a fourfold bond formed between the two transition-metal centers. Their observation constituted a milestone – until then the limit of bonds between the same two atoms was considered to be at most three as for example in N_2 – that gave rise to a new field in inorganic transition-metal chemistry with the $[Re_2Cl_8]^{-2}$ ion as a prototype [199]. It seems appealing and quite intuitive for a chemist to describe the Re(III)-Re(III) quadruple bond in the simple picture of molecular orbital (MO) theory as a $5d\sigma^2 5d\pi^4\ 5d\delta^2$ bond assuming that each bonding orbital is always doubly occupied. This conception is, however, inappropriate since it does not account for weak bonds with a considerable participation of an antibonding orbital. Following the idea of Roos *et al.* [197] a more suitable measure of the bond multiplicity may be based on the occupation numbers of natural orbitals which can be calculated from correlated multiconfigurational wave functions. In so doing, a typically non-integer *effective bond order* (EBO) may be defined in terms of the occupation number b_i of the ith orbital and the corresponding occupation number ab_i of the antibonding orbital:

$$\mathrm{EBO} = \sum_i \frac{b_i - ab_i}{2}. \tag{8.1}$$

In order to arrive at a more realistic bond order the next integer larger than the calculated fractional EBO should be taken. According to the definition in Eq. 8.1, a bond is weakened, *e.g.* if the natural occupation number for the antibonding orbital significantly differs from zero. The advantage of using natural orbital occupation numbers as a means to measure the bond order between two atoms stems from their stability with respect to variations in the basis set and the quality of the wave function provided that it comprises the most important active orbitals [197].

Using the above relation, Roos *et al.* [200] reported an EBO of 3.20 for the $[Re_2Cl_8]^{2-}$ ion where the deviations from 4 are mainly due to the weak δ bond. The contribution

from the δ bond to the total EBO was calculated at the CASSCF level as 0.54 rather than 1. To the date, a maximum number of six covalent bonds between two atoms of the same element was found in similar studies of in particular transition-metal dimers. EBOs of 5.17 and 5.19 were computed for the Mo_2 and W_2 diatom, respectively [197]. In this context, it is natural to ask whether even higher multiple bond orders are possible? This would require the participation of the f-shell which is likely only for the actinide elements. The $4f$ shell in the lanthanides is considerably more contracted than the remaining valence $6s$ and $5d$ shells which excludes the $4f$ shell from significantly contributing to bonding. In recent works, Roos and co-workers [184] studied the early actinide dimers including U_2 [201]. The largest EBOs of 4.5 and 4.2 which indicate a quintuple bond were computed for the Pa_2 and U_2 dimer, respectively. Furthermore, they concluded from considerations of atomic promotion energies which are needed to unpair the $7s$ electrons as well as to promote electrons from the $5f$ to the $6d$ shell in the transuranium elements that it is unlikely to find higher EBOs for diatoms of these elements. Hence, the upper limit of covalent bonds between equal atoms is most probably reached with six bonds computed for the Mo_2 and W_2 diatoms.

The bonding pattern of the U_2 diatom as calculated by Roos *et al.* [184,201] seems to be unique and more complex than any other known diatomic bond. It therefore deserves closer attention. The authors claim on the basis of scalar-relativistic CASSCF calculations the following bonding situation: Three two-electron-two-center electron pair bonds are formed by hybrid orbitals of primarily $7s$ and $6d$ character ($7s\sigma_g$ and two degenerate $6d\pi_u$ orbitals). In addition, four one-electron-two-center bonds are developed composed of two singly occupied σ- and δ-type orbitals of predominantly $6d$ character ($6d\sigma_g$ and $6d\delta_g$) as well as two singly occupied δ- and π-type orbitals with distinct $5f$ character ($5f\pi_g/5f\delta_u$ respectively $5f\delta_g/5f\pi_u$). Finally, two electrons with parallel spins occupy localized $5f\phi_g$ and $5f\phi_u$ orbitals which are equally distributed over both atoms to add up to a single $5f$ orbital on each atom. The calculated bonding picture may thus be summarized as $\sigma^2\pi^4\sigma^1\delta^1\delta^1\pi^1\phi^1\phi^1$. They furthermore predicted that all unpaired electrons display parallel spins corresponding to a ferromagnetic coupling which can be attributed to favorable exchange stabilization resulting from an interaction of the localized $5f$ electrons and the $5f$ one-electron bonds. In subsequent CASPT2/RASSI-SO calculations Roos *et*

al. computed the coupling of the total orbital angular momentum ($\Lambda = 11$)[8] and the total spin ($S = 3$) which combined to an $\Omega = 8$ state of *gerade* symmetry. As the authors stated, an unambiguous determination of the ground state of U_2 was, however, impossible from their calculations including spin-orbit coupling since a second state with $\Omega = 9_g$ was found to be only 0.01 eV energetically above the suggested $\Omega = 8_g$ state.

Albeit having proven to yield very good theoretical predictions in many different cases [202] the above outlined studies on the actinide diatoms and particularly on U_2 still leave room for improvement considering the neglect of spin-orbit effects at the essential orbital optimization step[9]. This is evident from the fact that the shape of the atomic orbitals significantly depends on the coupling to the electronic spin in heavy elements as illustrated for the Bi atom in Section 6.1.

Given the presumable complexity of a multiple bond in a diatom of the heavy element uranium that includes the participation of the (partially) occupied atomic $7s6d5f$ shells, it may be desirable to examine such a particular system in a more rigorous framework where spin-orbit coupling and electron correlation are treated on an equal footing. The major objective of my present work was therefore to shed light on the bonding picture in the U_2 diatom applying a KR-MCSCF/MRCI approach where the molecular Kramers-paired spinors were optimized under full account of spin-orbit interaction.

For this purpose and for reasons of computational efficiency, I used the exact two-component Hamiltonian (X2C) scheme of Iliaš and Saue [27, 123] in the present investigation. Two-electron spin-same-orbit and spin-other-orbit contributions were included via atomic mean-field integrals obtained with the AMFI [124–126] code. Furthermore, the uncontracted basis set from Ref. [203] with $\{26s21p17d12f\}$ functions was augmented with three additional g functions[10] which proved to be of importance in a study of the UO_2 molecule [59]. A starting set of Kramers-paired spinors for the subsequent MCSCF calculations was obtained from an average-of-configurations Hartree-Fock calculation with twelve electrons distributed among 26 Kramers pairs consisting of the valence $7s$ $6d$ $5f$ shells of each uranium atom. As a first step towards the calculation of full potential energy curves I carried out single-point state-specific MCSCF calculations for the four

[8] This value is obtained by summing up the orbital angular momenta for all singly occupied orbitals.

[9] The CASSCF calculations only take into account scalar-relativistic effects.

[10] An additional h function was not included here since the AMFI program as implemented in the `DIRAC` program is limited to functions with $l \leq 4$ (s, p, d, f, g)

Table 8.6: Generalized Active Spaces (GAS) and occupation constraints for U_2 KR-MCSCF calculations in C_{2h}^* double-group symmetry. The minimum and maximum number of electrons are accumulated values, *i.e.*, by adding the number of electrons in this and all preceding GA spaces.

S6(6in12)MRSD					
GAS	Kramers pairs per irrep		Min./max. accum. el.		
	E_{1g}	E_{1u}	Min. el.	Max. el.	Shell types
I	1	2	5	6	$7s\sigma_g, 6d\pi_u(2)$
II	9	6	10	12	$6d\sigma_g, 6d\delta_g(2), 5f\pi_g(2),$ $5f\pi_g(2), 5f\delta_g(2), 5f\phi_g(2),$ $5f\pi_u(2), 5f\delta_u(2), 5f\phi_u(2)$
III	3	5	12	12	$6d\pi_g(2), 5f\sigma_g, 7s\sigma_u, 6d\sigma_u,$ $6d\delta_u(2), 5f\sigma_u$

bosonic irreps A_g, B_g, A_u and B_u of the abelian double group C_{2h}^* at an U-U interatomic distance of 2.43 Å. This value corresponds to the equilibrium bond distance of U_2 calculated by Roos *et al.* [184]. The active KR-MCSCF space is composed as given in Table 8.6. It is subdivided into three GAS spaces which were constructed taking into account the CASSCF/CASPT2 results [184] discussed above. GAS I contains the strongly bonding $7s\sigma_g$ and two $6d\pi_u$ Kramers-paired spinors[11]. The second GAS II space comprises all spinors which will partly contribute to the overall bonding. Finally, all non-bonding and anti-bonding spinors were placed in GAS III.

An MCSCF calculation with a complete valence CAS space ($7s6d5f$) distributing the 12 electrons in 26 Kramers pairs yields a configuration space of more than 10^{12} determinants which is currently not feasible. My restricted active space MCSCF calculation dubbed as S6(6in15)MRSD was thus considerably smaller and spanned a configuration space of roughly 44×10^6 determinants. Due to present technical difficulties in the MCSCF program which require further development and improvements, my results from these elaborate MCSCF calculations can only be regarded as being of qualitative nature. A detailed analysis of the final results[12] revealed that "symmetry-broken" solutions were obtained, namely spinors of different m_j quantum numbers were illicitly mixed in the course of the spinor optimization step. As it turned out, this could happen because the

[11] An approximate λ notation is used to characterize the individual spinors.

[12] The calculations were running for more than one year on a single processor.

routine that performs the orbital rotations in each macro iteration [13] did not explicitly account for a proper m_j-blocking [204] in case of double-group symmetries lower than the full linear symmetry group of the system in question. Since we have not been able to fix this issue in due time for my present thesis, new calculations could not be carried out to date. Although I refrain from further discussing any of my results, it is worthwhile to mention that my calculations seem to indicate in agreement with Reference 184 low-lying $\Omega = 9_g$ and $\Omega = 8_g$ electronic states in the U_2 diatom. This speculative statement may be justified on the basis that all occupied Kramer-paired spinors predominantly maintained a pure m_j quantum number. Future work thus comprises a programming solution to overcome the present shortcoming. By means of my parallelization of the essential inner parts of the MCSCF program which has been a main objective of my thesis, considerable savings for the time needed to accomplish new results can be expected.

[13] For an overview of the most important steps in a direct second-order-MCSCF procedure the reader is referred to Section 3.2.

Chapter 9

Concluding Remarks and Perspectives

Summarizing, this thesis combines both development and implementation works of parallel algorithms in a relativistic four-component framework and their application to a large variety of atomic and molecular heavy-element compounds in their ground and excited states. Thus, things have come full circle regarding the main topic of my thesis: parallel relativistic multiconfiguration methods – new powerful tools for heavy-element electronic-structure studies.

What are the major achievements of this work, what remains to be done, and what will the future hold?

An efficient parallel algorithm has been presented in Part II. It is in principle applicable to any large-scale eigenvalue problem in computational science that can be solved iteratively. In this work, the algorithm has been leveraged to devise a parallel scheme for the (relativistic) generalized active space configuration interaction (GASCI) method. The excellent scalability of both the parallel non- and scalar-relativistic and fully relativistic GASCI implementations `LUCITA` and `LUCIAREL`, has been demonstrated by means of large-scale test simulations for two representatives of today's most common parallel computer architectures. It was furthermore expounded how the link between the essentials of a genuine relativistic Kramers-restricted multiconfiguration self-consistent field (KR-MCSCF) method and the direct CI implementation of `LUCIAREL` facilitates a parallelization of the KR-MCSCF program.

Moreover, I have been elaborating on the implementation of a parallel CI program which allows the calculation of first-order atomic and molecular properties within the four-component relativistic framework. A first application of this versatile module, namely the determination of the total orbital angular momentum of a given electronic state, has been frequently used in the present work to precisely characterize calculated atomic and molecular electronic spectra.

The novel parallel GASCI programs have paved the way for the variety of atomic and molecular applications in Part III. These studies encompass, for example, the at present most accurate theoretical estimate for the spin-orbit splitting between the ground and first excited state of BiH and the computation of the lower electronic and vibrational spectrum of RbYb which led to a reinterpretation of the initially proposed photoassociation process [164] in the ultracold regime starting from Rb and Yb atoms. Moreover, a rigorous elucidation of electron correlation effects on the lower even-parity electronic states of the thorium atom is included.

The comparison of different relativistic methodologies aiming at a precise theoretical determination of the electronic structure of the triiodide anion (I_3^-) indicated the suitability of my parallel CI approach which is, in contrast to the coupled cluster approach that served as a reference, applicable on the whole potential energy surface of this triatomic species.

A possible non-radiative charge-transfer mechanism in the collision process of a Ba^+ ion and a Rb atom at very low temperatures yielding a Ba atom and a Rb^+ ion has been outlined qualitatively on the basis of the computed electronic excitation spectrum of the $(RbBa)^+$ molecular ion. In order to give a quantitative estimate of the charge-transfer rate in the envisaged experiments, the underlying CI implementation of the CI property code needs to be modified to enable the calculation of electronic transition dipole moments.

Upon completion of a fully parallel KR-MCSCF algorithm and overcoming of present technical issues in the implementation of the KR-MCSCF module it will be very exciting to obtain reliable predictions of the bonding picture in the uranium dimer U_2 from calculations that include all important relativistic effects, in particular spin-orbit coupling, in the orbital optimization. The major steps towards a fully parallel KR-MCSCF algorithm have been accomplished in the present thesis. What remains is to devise a parallel scheme for the basic structure of the KR-MCSCF algorithm. Here, I will greatly benefit from

my experience of the parallelization of the CI algorithms which exhibit a similar pattern. The implementation of a universal relativistic second-order Møller-Plesset perturbation theory natural orbital module (MP2-NO) which can serve as a configuration and orbital generator [205] for the ensuing MCSCF step will further enhance the applicability of the MCSCF method for molecular systems which are dominated by strong static electron correlation. An initial version of this MP2-NO method suitable for closed-shell systems has already been implemented [206].

Finally, a parallel KR-MCSCF program is also desirable particularly with regard to an extension of the novel multiconfiguration self-consistent field short-range density functional theory (MCSCF-srDFT) approach [207–210] to the four-component relativistic framework which strongly suggests an efficient and flexible KR-MCSCF component.

Appendix A

General Definitions

In the discussion of MCSCF/GASCI calculations various computational models are termed with shortcuts in this thesis. The notation will be clarified in the following appendix. Statistical measures are used in some places to quantify errors of calculations. A definition of these means is given in Appendix A.2. In Appendix A.3 I summarize briefly the Franck-Condon principle and its implication on electronic transitions in molecules.

A.1 Notation of Wave Function Models for MCSCF/ GASCI Calculations

Since the reader might not be familiar with my notation of wave function models for MCSCF/GASCI calculations employed in this thesis, it shall be introduced here with an illustrating example. A comprehensive discussion of the concept of generalized active spaces (GAS) can be found in the literature [60,211]. The majority of the MCSCF/GASCI computational models are of restricted-active-space type with a maximum number of holes in GAS I, no restrictions in GAS II, and with a maximum number of particles in GAS III. The notation follows the scheme "GAS I(GAS II)GAS III". The GAS set-up "S8(4in6)MRSD" in Table A.1, taken from Section 8.1 concerning the thorium atom may serve as a representative example: "S8(4in6)MRSD" means that at most 1 hole among the 8 electrons in 4 Kramers pairs (in this case: Th $6s6p$ spinors) is allowed, 4 electrons are distributed in 6 Kramers pairs in all possible ways ((4in6); plus of course excitations from GAS I to GAS II), and finally that all possible single and double excitations into

Table A.1: Generalized Active Space (GAS) and occupation constraints using the example of a Th ground- and excited-state calculation in C_{2h}^{*} double-group symmetry which is discussed in Section 8.1. The minimum and maximum number of electrons are accumulated values, *i.e.*, by adding the number of electrons in this and all preceding GA spaces.

S8(4in6)MRSD					
GA Space	Kramers pairs per irrep		Min./max. accum. el.		
	E_{1g}	E_{1u}	Min. el.	Max. el.	Shell types
I	1	3	7	8	$6s6p$
II	6	0	10	12	$6d7s$
III	52	62	12	12	virtual Kramers pairs

GAS III Kramers pairs are generated from the reference configurations obeying the constraints put on GAS I and GAS II (MRSD). To simplify a distinction between calculations employing different basis sets, the acronym for a given basis set is added to the notation of the wave function model. Assuming a TZ basis set the final notation would read as: "S8(4in6)MRSD/TZ".

A.2 Statistical Measures

In this thesis the following statistical measures were used to quantify the errors of the calculated spectroscopic parameters if applicable. In principle, the error of a parameter P_i^{calc} calculated with a given model and parameter set is given by:

$$\Delta_i = P_i^{\mathrm{calc}} - P_i^{\mathrm{exp}}, \tag{A.1}$$

$$\tag{A.2}$$

where P_i^{exp} denotes the measured value of the parameter. More sophisticated measures are the mean error $\bar{\Delta}$, the standard deviation Δ_{std}, the mean absolute error $\bar{\Delta}_{\mathrm{abs}}$ and

the absolute error $\Delta_{\max}$. They are defined as follows:

$$\bar{\Delta} = \frac{1}{n}\sum_{i=1}^{n}\Delta_i \tag{A.3}$$

$$\Delta_{\text{std}} = \sqrt{\frac{1}{n-1}\sum_{i=1}^{n}(\Delta_i - \bar{\Delta})^2} \tag{A.4}$$

$$\bar{\Delta}_{\text{abs}} = \frac{1}{n}\sum_{i=1}^{n}|\Delta_i| \tag{A.5}$$

$$\Delta_{\max} = \max_i |\Delta_i| \tag{A.6}$$

A.3 Franck-Condon Principle

Due to the large mass difference of the nuclei and the electrons in a molecule the components move on different timescales. Hence, the corresponding Schrödinger equation can be solved independently as a first approximation (Born-Oppenheimer approximation). The resulting wave function $\Psi(\mathbf{r})$ separates into a nuclear $\Theta(\mathbf{R})$ and an electronic part $\Psi(\mathbf{r}';\mathbf{R})$ which depends parametrically on the nuclear coordinates:

$$\Psi(\mathbf{r}) = \Theta(\mathbf{R})\Psi(\mathbf{r}';\mathbf{R}). \tag{A.7}$$

If a photon is absorbed by a molecule and an electron is extremely fast elevated in a different state the wave function of the nuclei will not change in the meantime. Thus, transitions are allowed only between those states that exhibit overlap between their nuclear wave functions. According to the Franck-Condon principle the probability of a transition scales with the degree of overlap. The dipole operator $\hat{\mu}$ in the transition matrix element p that describes the transition from the initial state $\Psi_1(\mathbf{r})$ to the final state $\Psi_2(\mathbf{r})$ is similarly split into a nuclear $\hat{\mu}_n$ and an electronic $\hat{\mu}_e$ part:

$$p = \langle\Psi_1(\mathbf{r})\,|\hat{\mu}_n + \hat{\mu}_e|\,\Psi_2(\mathbf{r})\rangle \tag{A.8}$$

$$= \langle\Theta_1(\mathbf{R})\,|\hat{\mu}_n|\,\Theta_2(\mathbf{R})\rangle\,\underbrace{\langle\Psi_1(\mathbf{r}';\mathbf{R})\mid\Psi_2(\mathbf{r}';\mathbf{R})\rangle}_{\mathsf{a}} \tag{A.9}$$

$$+ \underbrace{\langle\Psi_1(\mathbf{r}';\mathbf{R})\,|\hat{\mu}_e|\,\Psi_2(\mathbf{r}';\mathbf{R})\rangle}_{\text{TDM}}\underbrace{\langle\Theta_1(\mathbf{R})\mid\Theta_2(\mathbf{R})\rangle}_{\mathsf{b}}. \tag{A.10}$$

The scalar product a is zero because different electronic eigenstates are always orthogonal. The square of term b is called Franck-Condon factor $\text{FCF} = |\mathsf{b}|^2$. The total transition probability $\text{P} = |p|^2$ then comprises the product of the square of the electronic transition dipole moment (TDM) and the FCF.

List of Figures

List of Tables

Bibliography

[1] A. Messiah. *Quantum Mechanics*, volume 1,2. Dover Publications, Mineola, first edition edition, 1999.

[2] E. Schrödinger. An undulatory theory of the mechanics of atoms and molecules. *Phys. Rev.*, 28:1049–1070, 1926.

[3] A. Einstein. Zur Elektrodynamik bewegter Körper. *Ann. Phys.*, 17:891–921, 1905.

[4] P. A. M. Dirac. The quantum theory of the electron. *Proc. Roy. Soc.*, 117:610–624, 1928.

[5] P. A. M. Dirac. The quantum theory of the electron. Part II. *Proc. Roy. Soc.*, 118:351–361, 1928.

[6] P. A. M. Dirac. Quantum mechanics of many-electron systems. *Proc. Roy. Soc.*, 123:714–733, 1929.

[7] P. Pyykkö and J. P. Desclaux. Relativity and the periodic system of elements. *Acc. Chem. Res.*, 12:276–281, 1979.

[8] P. Pyykkö. Relativistic effects in structural chemistry. *Chem. Rev.*, 88:563, 1988.

[9] T. Fleig and C. M. Marian. Relativistic all-electron ab initio calculations on the platinum hydride molecule. *Chem. Phys. Lett.*, 222:267, 1994.

[10] DIRAC, a relativistic ab initio electronic structure program, developer version, written by L. Visscher, H. J. Aa. Jensen, and T. Saue, with new contributions from R. Bast, S. Dubillard, K. G. Dyall, U. Ekström, E. Eliav, T. Fleig, A. S. P. Gomes, T. U. Helgaker, J. Henriksson, M. Iliaš, Ch. R. Jacob, S. Knecht,

P. Norman, J. Olsen, M. Pernpointner, K. Ruud, P. Sałek, and J. Sikkema (see http://dirac.chem.sdu.dk).

[11] L. Visscher, O. Visser, .P J. C. Aerts, H. Merenga, and W. C. Nieuwpoort. MOLFDIR, A relativistic Dirac-Fock-CI program package developed at the University of Groningen, http://hydra.chem.rug.nl/ broer/molfdir/molfdir.html. *Comp. Phys. Commun.*, 81:120, 1994.

[12] E. Clementi and G. Corongiu, editors. *Methods and Techniques for Computational Chemistry, METECC-5*, pages 169 – 218. STEF, Cagliari, 1995. L. Visscher and W. A. de Jong and O. Visser and P. J. C. Aerts and H. Merenga and W. C. Nieuwpoort.

[13] T. Yanai, T. Nakajima, Y. Ishikawa, and K. Hirao. A new computational scheme for the Dirac-Hartree-Fock method employing an efficient integral algorithm. *J. Chem. Phys.*, 114:6526–6538, 2001.

[14] T. Yanai, H. Iikura, T. Nakajima, Y. Ishikawa, and K. Hirao. A new implementation of four-component relativistic density functional method for heavy-atom polyatomic systems. *J. Chem. Phys.*, 115:8267–8273, 2001.

[15] T. Yanai, T. Nakajima, Y. Ishikawa, and K. Hirao. A highly efficient algorithm for electron repulsion integrals over relativistic four-component Gaussian-type spinors. *J. Chem. Phys.*, 116:10122–10128, 2002.

[16] K. G. Dyall and K. Fægri, Jr. *Introduction to Relativistic Quantum Chemistry.* Oxford University Press, New York, 2007.

[17] M. Reiher and A. Wolf. *Relativistic Quantum Chemistry: The Fundamental Theory of Molecular Science.* Wiley-VCH, Weinheim, 2009.

[18] M. Born and R. Oppenheimer. Zur Quantentheorie der Molekeln. *Ann. Phys.*, 84:457, 1927.

[19] M. Gell-Mann. The interpretation of the new particles as displaced charged multiplets. *Nuovo Cimento Suppl.*, 4:848, 1956.

[20] T. Saue and L. Visscher. Four-component electronic structure methods for molecules. In S. Wilson and U. Kaldor, editors, *Theoretical Chemistry and Physics*

of Heavy and Superheavy Elements, pages 211–268, Dordrecht, 2003. Kluwer Academic Publishers.

[21] Y. Ishikawa, R. Baretty, and R. C. Binning, Jr. Relativistic Gaussian basis set calculations on one-electron ions with a nucleus of finite extent. *Chem. Phys. Lett.*, 121:130–133, 1985.

[22] G. Breit. The effect of retardation on the interaction of two electrons. *Phys. Rev.*, 34:553, 1929.

[23] J. A. Gaunt. The triplets of helium. *Proc. Roy. Soc.*, A 122:513–532, 1929.

[24] J. A. Gaunt. The relativistic theory of an atom with many electrons. *Proc. Roy. Soc.*, A 124:163–176, 1929.

[25] Trond Saue. *Principles and Applications of Relativistic Molecular Calculations*. Dissertation, Department of Chemistry, Faculty of Mathematics and Natural Sciences, University of Oslo, Norway, 1995.

[26] T. Saue. Spin-interactions and the non-relativistic limit of electrodynamics. *Adv. Quant. Chem.*, 48:383–405, 2005.

[27] M. Iliaš and T. Saue. An infinite-order two-component relativistic hamiltonian by a simple one-step transformation. *J. Chem. Phys.*, 126:064102, 2007.

[28] J. Sucher. Foundations of the relativistic theory of many-electron atoms. *Phys. Rev. A*, 22:348–362, 1980.

[29] G. E. Brown and D. G. Ravenhall. On the interaction of two electrons. *Proc. Roy. Soc.*, 208:552–559, 1951.

[30] T. Saue and H. J. Aa. Jensen. Quaternion symmetry in relativistic molecular calculations: The Dirac-Hartree-Fock method. *J. Chem. Phys.*, 111:6211–6222, 1999.

[31] J. D. Talman. Minimax principle for the Dirac equation. *Phys. Rev. Lett.*, 57:1091, 1986.

[32] L. Visscher. The Dirac equation in quantum chemistry: Strategies to overcome the current computational problems. *J. Comp. Chem.*, 23:759, 2002.

[33] L. Visscher and T. Saue. Approximate relativistic electronic structure methods based on the quaternion modified Dirac equation. *J. Chem. Phys.*, 113:3996, 2000.

[34] M. Dolg. Relativistic effective core potentials. In P. Schwerdtfeger, editor, *Relativistic Electronic Stucture Theory Part 1. Fundamentals*, pages 793–862, Amsterdam, 2002. Elsevier.

[35] M. Douglas and N. M. Kroll. Quantum electrodynamical corrections to the structure of helium. *Ann. Phys.*, 82:89, 1974.

[36] B. A. Heß. Applicability of the no-pair equation with free-particle projection operators to atomic and molecular structure calculations. *Phys. Rev. A*, 32:756, 1985.

[37] B. A. Heß. Relativistic electronic-structure calculations employing a two-component no-pair formalism with external field projection operators. *Phys. Rev. A*, 33:3742, 1986.

[38] E. van Lenthe, E. J. Baerends, and J. G. Snijders. Relativistic regular two-component Hamiltonians. *J. Chem. Phys.*, 99:4597–4610, 1993.

[39] E. van Lenthe, J. G. Snijders, and E. J. Baerends. The zero-order regular approximation for relativistic effects: The effect of spin-orbit coupling in closed shell molecules. *J. Chem. Phys.*, 105:6505–6516, 1996.

[40] W. Kutzelnigg. Basis set expansion of the Dirac operator without variational collapse. *Int. J. Quantum Chem.*, 25:107–129, 1984.

[41] K. G. Dyall. An exact separation of the spin-free and spin-dependent terms of the Dirac-Coulomb-Breit Hamiltonian. *J. Chem. Phys.*, 100:2118, 1994.

[42] H. A. Kramers. Théorie générale de la rotation paramagnétique dans les cristaux. *Proc. R. Acad. Amsterdam*, 33:959–972, 1930.

[43] H. J. Aa. Jensen, K. G. Dyall, T. Saue, and K. Fægri. Relativistic four-component multiconfigurational self-consistent field theory for molecules: Formalism. *J. Chem. Phys.*, 104:4083, 1996.

[44] M. Tinkham. *Group Theory and Quantum Mechanics*. McGraw-Hill, New York, 1964.

[45] E. P. Wigner. *Group Theory and its Application to the Quantum Mechanics of Atomic Spectra*. Academic Press, New York, 1959.

[46] L. Visscher. On the construction of double group molecular symmetry functions. *Chem. Phys. Lett.*, 253:20, 1996.

[47] E. P. Wigner. Über die Operation der Zeitumkehr in der Quantenmechanik. *Göttinger Nachrichten*, 31:547–559, 1932.

[48] Basis Set Exchange: A Community Database for Computational Sciences. see https://bse.pnl.gov/bse/portal.

[49] L. Visscher, P. J. C. Aerts, O. Visser, and W. C. Nieuwpoort. Kinetic balance in contracted basis sets for relativistic calculations. *Int. J. Quantum Chem. Symp.*, 25:131–139, 1991.

[50] http://dirac.chem.sdu.dk/basisarchives/dyall/index.html.

[51] R. E. Stanton and S. Havriliak. Kinetic balance: A partial solution to the problem of variational safety in Dirac calculations. *J. Chem. Phys.*, 81:1910, 1984.

[52] K. G. Dyall, I. P. Grant, and S. Wilson. Matrix representation of operator products. *J. Phys. B: At. Mol. Opt. Phys.*, 17:493–503, 1984.

[53] K. G. Dyall and Jr. K. Fægri. Kinetic balance and variational bounds failure in the solution of the Dirac equation in a finite Gaussian basis set. *Chem. Phys. Lett.*, 174:25–32, 1990.

[54] E. R. Davidson. The iterative calculation of a few of the lowest eigenvalues and corresponding eigenvectors of large real-symmetric matrices. *J. Comput. Phys.*, 17:87, 1975.

[55] J. Olsen, P. Jørgensen, and J. Simons. Passing the one-billion limit in full configuration-interaction (FCI) calculations. *Chem. Phys. Lett.*, 169:463, 1990.

[56] E. R. Davidson. Monster matrices: their eigenvalues and eigenvectors. *Computer in Physics*, 7:519–522, 1993.

[57] T. Fleig, J. Olsen, and C. M. Marian. The generalized active space concept for the relativistic treatment of electron correlation. I. Kramers-restricted two-component configuration interaction. *J. Chem. Phys.*, 114:4775, 2001.

[58] T. Fleig, J. Olsen, and L. Visscher. The generalized active space concept for the relativistic treatment of electron correlation. II. Large-scale configuration interaction implementation based on relativistic 2- and 4-spinors and its application. *J. Chem. Phys.*, 119:2963, 2003.

[59] T. Fleig, H. J. Aa. Jensen, J. Olsen, and L. Visscher. The generalized active space concept for the relativistic treatment of electron correlation. III. Large-scale configuration interaction in a four-component multi-configuration self-consistent field program and application to UO_2. *J. Chem. Phys.*, 124:104106, 2006.

[60] Timo Fleig. *Wave Function Based Multi-Reference Electron Correlation Methods for the Relativistic Computation of Atomic and Molecular Properties. Development and Application.* Habilitationsschrift, Mathematisch-Naturwissenschaftliche Fakultät, Universität Düsseldorf, 2006.

[61] J. Thyssen, T. Fleig, and H. J. Aa. Jensen. A direct relativistic four-component multi-configuration self-consistent-field method for molecules. *J. Chem. Phys.*, 129:034109, 2008.

[62] T. Fleig and L. Visscher. Large-scale electron correlation calculations in the framework of the spin-free Dirac formalism: the Au_2 molecule revisited. *Chem. Phys.*, 311:113, 2005.

[63] J. Olsen, B. O. Roos, P. Jørgensen, and H. J. Aa. Jensen. Determinant based configuration interaction algorithms for complete and restricted configuration interaction spaces. *J. Chem. Phys.*, 89:2185, 1988.

[64] B. O. Roos. The multiconfigurational (MC) self-consistent field (SCF) theory. In B. O. Roos, editor, *Lecture Notes in Quantum Chemistry*, page 177, Berlin, 1992. Springer.

[65] Jørn Thyssen. *Development and Applications of Methods for Correlated Relativistic Calculations of Molecular Properties*. Dissertation, Department of Chemistry, University of Southern Denmark, 2001.

[66] G. A. Aucar, H. J. Aa. Jensen, and J. Oddershede. Operator representations in Kramers bases. *Chem. Phys. Lett.*, 232:47, 1995.

[67] R. Fletcher. *Practical Methods of Optimization*. Wiley, Chichester, 1980.

[68] P. Jørgensen, P. Swanstrøm, and D. L. Yeager. Guaranteed convergence in ground state multiconfigurational self-consistent field calculations. *J. Chem. Phys.*, 78:347–356, 1983.

[69] H. J. Aa. Jensen and H. Ågren. A direct, restricted-step, second-order MCSCF program for large-scale *ab initio* calculations. *Chem. Phys.*, 104:229, 1986.

[70] http://wiki.chem.vu.nl/dirac/index.php/List_of_developers.

[71] T. Fleig and L. Visscher. Large-scale electron correlation calculations in the framework of the spin-free dirac formalism. The Au_2 molecule revisited. *Chem. Phys.*, 311:113, 2005.

[72] M. Iliaš, V. Kellö, T. Fleig, and M. Urban. Electric properties of the hydrogen iodide: Reexamination of correlation and relativistic effects. *Theor. Chim. Acta*, 110:176, 2003.

[73] T. Fleig. Spin-orbit resolved static polarizabilities of group 13 atoms. 4-component relativistic configuration interaction and coupled cluster calculations. *Phys. Rev. A*, 72:052506, 2005.

[74] T. Fleig, L. K. Sørensen, and J. Olsen. A relativistic 4-component general-order multi-reference coupled cluster method: Initial implementation and application to HBr. *Theor. Chem. Acc.*, 118:347, 2007.

[75] L. K. Sørensen, T. Fleig, and J. Olsen. Spectroscopic and electric properties of the LiCs molecule. A coupled cluster study including higher excitations. *J. Phys. B: At. Mol. Opt. Phys.*, 42:165102, 2009.

[76] L. K. Sørensen, T. Fleig, and J. Olsen. Relativistic 4- and 2-component generalized-active-space coupled cluster, 2009. submitted for publication.

[77] http://www.top500.org (retrieved August 27th, 2009).

[78] http://www.mpi-forum.org.

[79] M. Klene, M. A. Robb, M. J. Frisch, and P. Celani. Parallel implementation of the CI-vector evaluation in full CI/CAS-SCF. *J. Chem. Phys.*, 113:5653, 2000.

[80] Z. Gan, Y. Alexeev, M. S. Gordon, and R. A. Kendall. The parallel implementation of a full configuration interaction program. *J. Chem. Phys.*, 119:47, 2003.

[81] B. Suo, G. Zhai, Y. Wang, Z. Wen, X. Hu, and L. Li. Parallelization of MRCI based on hole-particle symmetry. *J. Comp. Chem.*, 26:88, 2005.

[82] K. Tanaka, Y. Mochizuki, T. Ishikawa, H. Terashima, and H. Tokiwa. A graphical symmetric group approach for a spin adapted full configuration interaction: partitioning of a configuration graph into sets of closed-shell and open-shell graphs. *Theor. Chem. Acc.*, 117:397, 2007.

[83] M. Kleinschmidt, C. M. Marian, M. Waletzke, and S. Grimme. Parallel multireference configuration interaction calculations on mini-β-carotenes and β-carotene. *J. Chem. Phys.*, 130:044708, 2009.

[84] T. Fleig. Relativistic string-based electron correlation methods. In M. Barysz and Y. Ishikawa, editors, *Relativistic Methods for Chemists*. Springer Verlag, Berlin, 2009.

[85] G. H. F. Diercksen, B. O. Roos, and A. Sadlej. Legitimate calculation of first-order molecular properties in the case of limited CI functions. Dipole moments. *Chem. Phys.*, 59:29–39, 1981.

[86] T. Helgaker, M. Jaszuński, and K. Ruud. Ab initio methods for the calculation of NMR shielding and indirect spin-spin coupling constants. *Chem. Rev.*, 99:293–352, 1999.

[87] T. Saue. Post Dirac-Hartree-Fock methods - properties. In P. Schwerdtfeger, editor, *Relativistic Electronic Stucture Theory Part 1. Fundamentals*, pages 332–400, Amsterdam, 2002. Elsevier.

[88] P.-O. Nerbrant, B. O. Roos, and A. Sadlej. First-order properties and the Hellmann-Feynman theorem in the case of a limited CI wave function. *Int. J. Quantum Chem.*, 15:135–145, 1979.

[89] M. Ernzerhof, C. M. Marian, and S. D. Peyerimhoff. On the calculation of first-order properties: Expectation value versus energy derivative approach. *Int. J. Quantum Chem.*, 43:659–668, 1992.

[90] W. Langenaeker, F. De Proft, and P. Geerlings. Limited configuration interaction calculations of one-electron properties: the use of a window. *J. Mol. Struct. (Theochem)*, 313:283–290, 1994.

[91] R. Polák and J. Fišer. Multireference CI calculation of nuclear quadrupole coupling constants of CN^+ and CN^-: rovibrational dependence. *Spectrochimica Acta A*, 58:2029–2041, 2002.

[92] J. Seino, Y. Honda, M. Hada, and H. Nakatsuji. SAC and SAC-CI calculations of excitation and circular dichroism spectra of straight-chain and cyclic dichalcogens. *J. Phys. Chem. A*, 110:10053–10062, 2006.

[93] J. Olsen and P. Jørgensen. Linear and non-linear response functions for an exact state and for an MCSCF state. *J. Chem. Phys.*, 82:3235, 1984.

[94] O. Christiansen, P. Jørgensen, and C. Hättig. Response functions from fourier component variational perturbation theory applied to a time-averaged quasienergy. *Int. J. Quantum Chem.*, 68:1, 1998.

[95] S. Grimme and M. Waletzke. A combination of Kohn-Sham density functional theory and multi-reference configuration interaction methods. *J. Chem. Phys.*, 111:5645–5655, 1999.

[96] http://commons.wikimedia.org/wiki/File:800px-PTable.png (retrieved July 2nd, 2009).

[97] http://www.chemie.li/pse.php (retrieved August 26th, 2009).

[98] K. Balasubramanian. Relativistic configuration interaction calculations of the low-lying states of BiH. *Chem. Phys. Lett.*, 114:201, 1985.

[99] M. Dolg, W. Küchle, H. Stoll, H. Preuss, and P. Schwerdtfeger. Ab initio pseudopotentials for Hg to Rn. II. Molecular calculations on the hydrides of Hg to At and the fluorides of Rn. *Mol. Phys.*, 74:1265, 1991.

[100] A. B. Alekseyev, R. J. Buenker, H. P. Liebermann, and G. Hirsch. Spin-orbit configuration interaction study of the potential energy curves and radiative lifetimes of the low-lying states of bismuth hydride. *J. Chem. Phys.*, 100:2989, 1994.

[101] L. Seijo. Relativistic ab initio model potential calculations including spin-orbit effects through the Wood-Boring Hamiltonian. *J. Chem. Phys.*, 102:8078, 1995.

[102] M. Dolg. Accuracy of energy-adjusted quasirelativistic pseudopotentials: a calibration study of XH and X2(X = F,Cl,Br,I,At). *Mol. Phys.*, 88:1645, 1996.

[103] G. A. DiLabio and P. A. Christiansen. Low-lying 0^+ states of bismuth hydride. *Chem. Phys. Lett.*, 277:473, 1997.

[104] S. A. Wildman, G. A. DiLabio, and P. A. Christiansen. Accurate relativistic effective potentials for the sixth-row main group elements. *J. Chem. Phys.*, 107:9975, 1997.

[105] G. A. DiLabio and P. A. Christiansen. Separability of spin-orbit and correlation energies for the sixth-row main group hydride ground states. *J. Chem. Phys.*, 108:7527, 1998.

[106] F. Rakowitz and C. M. Marian. An extrapolation scheme for spin-orbit configuration interaction energies applied to the ground and excited electronic states of thallium hydride. *Chem. Phys.*, 225:223, 1997.

[107] C. S. Nash and B. E. Bursten. Spin-orbit effects, VSEPR theory, and the electronic structures of heavy and superheavy group IVa hydrides and group VIIIa tetrafluorides. a partial role reversal for elements 114 and 118. *J. Phys. Chem. A*, 103:402, 1999.

[108] C. S. Nash and B. E. Bursten. Spin-orbit effects on the electronic structure of heavy and superheavy hydrogen halides: Prediction of an anomalously strong bond in H[117]. *J. Phys. Chem. A*, 103:632, 1999.

[109] H. Stoll, B. Metz, and M. Dolg. Relativistic energy-consistent pseudopotentials - recent developments. *J. Comp. Chem.*, 23:767, 2001.

[110] T. Saue, K. Fægri, and O. Gropen. Relativistic effects on the bonding of heavy and superheavy hydrogen halides. *Chem. Phys. Lett.*, 263:360, 1996.

[111] K. Fægri and T. Saue. Diatomic molecules between very heavy elements of group 13 and group 17: A study of relativistic effects on bonding. *J. Chem. Phys.*, 115:2456, 2001.

[112] Y. K. Han, C. Bae, S. K. Son, and Y. S. Lee. Spin-orbit effects on the transactinide p-block element monohydrides MH (M=element 113-118). *J. Chem. Phys.*, 112:2684, 1999.

[113] F. Hund. Concerning the importance of some appearences in the molecular spectra. *Z. Phys.*, 36:658, 1926.

[114] G. Herzberg. *Molecular Spectra and Molecular Structure, volume I. Spectra of Diatomic Molecules*. Van Nostrand Reinhold, 1950.

[115] G. Herzberg. *Molecular Spectra and Molecular Structure*. Krieger Publishing Company, Malabar, Florida, 1989.

[116] K. G. Dyall, I. P. Grant, C. T. Johnson, F. A. Parpia, and E. P. Plummer. GRASP: A General-purpose Relativistic Atomic Structure Program. *Comp. Phys. Comm.*, 55:425, 1989.

[117] K. G. Dyall. Relativistic Quadruple-Zeta and Revised Triple-Zeta and Double-Zeta Basis Sets for the 4p, 5p, and 6p Elements. *Theor. Chem. Acc.*, 115:441, 2006.

[118] T. H. Dunning Jr. Gaussian basis sets for use in correlated molecular calculations. I. The atoms boron through neon and hydrogen. *J. Chem. Phys.*, 90:1007, 1989.

[119] L. K. Sørensen, J. Olsen and T. Fleig. Kramers unrestricted generalized active space coupled-cluster. Implementation and application on BiH. to be submitted.

[120] A. Heimer. Über das Bandenspektrum des Wismuthydrids. *Z. Phys.*, 95:328, 1935.

[121] K. P. Huber and G. Herzberg, "Constants of Diatomic Molecules" (data prepared by J. W. Gallagher and R. D. Johnson, III) in NIST Chemistry WebBook, NIST Standard Reference Database Number 69, Eds. P. J. Linstrom and W. G. Mallard, National Institute of Standards and Technology, Gaithersburg MD, 20899, http://webbook.nist.gov, (retrieved December 10, 2008).

[122] J. E. Sansonetti, W. C. Martin and S. L. Young. Handbook of Basic Atomic Spectroscopic Data. Available: http://physics.nist.gov/PhysRefData/Handbook/index.html (retrieved July 6, 2009). National Institute of Standards and Technology, Gaithersburg, MD.

[123] M. Iliaš and H. J. Aa. Jensen. Two-component relativistic methods based on the quaternion modified dirac equation: From the Douglas-Kroll to the Barysz-Sadlej-Snijders infinite order. *private communication*, 2009.

[124] AMFI, an atomic mean-field spin-orbit integral program, 1996 and 1999. Bernd Schimmelpfennig, University of Stockholm.

[125] B. A. Hess, C. M. Marian, U. Wahlgren, and O. Gropen. A mean-field spin-orbit method applicable to correlated wavefunctions. *Chem. Phys. Lett.*, 251:365, 1996.

[126] M. Iliaš, V. Kello, L. Visscher, and B. Schimmelpfennig. Inclusion of mean-field spin-orbit effects based on all-electron two-component spinors: Pilot calculations on atomic and molecular properties. *J. Chem. Phys.*, 115:9667, 2001.

[127] M. Fushitani. Applications of pump-probe spectroscopy. *Annu. Rep. Prog. Chem., Sect. C: Phys. Chem.*, 104:272–297, 2008.

[128] U. Banin, A. Waldman, and S. Ruhman. Ultrafast photodissociation of I_3^- in solution: Direct observation of coherent product vibrations. *J. Chem. Phys.*, 96:2416–2419, 1992.

[129] U. Banin and S. Ruhman. Ultrafast photodissociation of I_3^-. coherent photochemistry in solution. *J. Chem. Phys.*, 98:4391–4403, 1993.

[130] U. Banin and S. Ruhman. Ultrafast vibrational dynamics of nascent diiodide fragments studied by femtosecond transient resonance impulsive stimulated raman scattering. *J. Chem. Phys.*, 99:9318–9321, 1993.

[131] T. Kühne and P. Vöhringer. Vibrational relaxation and geminate recombination in the femtosecond-photodissociation of triiodide in solution. *J. Chem. Phys.*, 105:10788–10802, 1996.

[132] T. Kühne, R. Küster, and P. Vöhringer. Femtosecond photodissociation of triiodide in solution: Excitation energy dependence and transition state dynamics. *Chem. Phys.*, 233:10788–10802, 1998.

[133] T. Kühne and P. Vöhringer. Transient anisotropy and fragment rotational excitation in the femtosecond photodissociation of triiodide in solution. *J. Phys. Chem. A*, 102:4177–4185, 1998.

[134] A. A. Hoops, J. R. Gascooke, A. E. Faulhaber, K. E. Kautzman, and D. M. Neumark. Two- and three-body photodissociation of gas phase I_3^-. *J. Chem. Phys.*, 120:7901–7909, 2004.

[135] M. T. Zanni, B. J. Greenblatt, A. V. Davis, and D. M. Neumark. Photodissociation of gas phase I_3^- using femtosecond photoelectron spectroscopy. *J. Chem. Phys.*, 111:2991–3003, 1999.

[136] H. Choi, R. T. Bise, A. A. Hoops, and D. M. Neumark. Photodissociation dynamics of the triiodide anion (I_3^-). *J. Chem. Phys.*, 113:2255–2262, 2000.

[137] L. Zhu, K. Takahashi, M. Saeki, T. Tsukuda, and T. Nagata. Photodissociation of gas-phase I_3^-: product branching in the visible and UV regions. *Chem. Phys. Lett.*, 350:233–239, 2001.

[138] R. Nakanishi, N. Saitou, T. Ohno, S. Kowashi, S. Yabushita, and T. Nagata. Photodissociation of gas-phase I_3^-: Comprehensive understanding of nonadiabatic dissociation dynamics. *J. Chem. Phys.*, 126:204311, 2007.

[139] J. Vala, R. Kosloff, and J. N. Harvey. Ab initio and diatomics in molecule potentials for I_2^-, I_2, I_3^- and I_3. *J. Chem. Phys.*, 114:7413–7423, 2001.

[140] E. K. U. Gross and W. Kohn. Time-dependent density-functional theory. *Adv. Quant. Chem.*, 21:255, 1990.

[141] B. O. Roos, P. R. Taylor, and P. E. M. Siegbahn. A complete active space SCF method (CASSCF) using a density matrix formulated super-CI approach. *Chem. Phys.*, 48:157–173, 1980.

[142] K. Andersson, P. Å. Malmqvist, B. O. Roos, A. J. Sadlej, and K. Wolinski. 2nd-Order Perturbation Theory with a CASSCF Reference Function. *J. Phys. Chem.*, 94:5483, 1990.

[143] P. Å. Malmqvist, B. O. Roos, and B. Schimmelpfennig. The restricted active space (RAS) state interaction approach with spin-orbit coupling. *Chem. Phys. Lett.*, 357:230, 2002.

[144] L. Visscher, E. Eliav, and U. Kaldor. Formulation and implementation of the relativistic fock-space coupled cluster method for molecules. *J. Chem. Phys.*, 115(21):9720–9726, 2001.

[145] A. Landau, E. Eliav, Y. Ishikawa, and U. Kaldor. Intermediate hamiltonian fock-space coupled-cluster method: Excitation energies of barium and radium. *J. Chem. Phys.*, 113:9905–9910, 2000.

[146] A. Landau, E. Eliav, Y. Ishikawa, and U. Kaldor. Intermediate hamiltonian fock-space coupled cluster method in the one-hole one-particle sector: Excitation energies of xenon and radon. *J. Chem. Phys.*, 115:6862–6865, 2001.

[147] T. Migchelsen and A. Vos. The crystal structure of two modifications of tetraethylammonium triiodide, $(C_2H_5)_4NI_3$. *Acta Cryst.*, 23:796–804, 1967.

[148] K. G. Dyall. Relativistic and nonrelativistic finite nucleus optimized triple-zeta basis sets for the 4p, 5p and 6p elements. *Theor. Chem. Acc.*, 108:335, 2002.

[149] T. Helgaker, P. Jørgensen, and J. Olsen. *Molecular Electronic Structure Theory.* John Wiley & Sons, LTD, Chichester, 2000.

[150] J. Doyle, B. Friedrich, R. V. Krems, and F. Masnou-Seeuws. Quo vadis, cold molecules? *Eur. Phys. J. D*, 31:149, 2004.

[151] J. J. Hudson, B. E. Sauer, M. R. Tarbutt, and E. A. Hinds. Measurement of the electron electric dipole moment using YbF molecules. *Phys. Rev. Lett.*, 89:023003, 2002.

[152] B. C. Regan, E. D. Commins, C. J. Schmidt, and D. DeMille. New limit on the electron electric dipole moment. *Phys. Rev. Lett.*, 88:071805, 2002.

[153] T. Zelevinsky, S. Kotochigova, and J. Ye. Precision test of mass-ratio variations with lattice-confined ultracold molecules. *Phys. Rev. Lett.*, 100:043201, 2008.

[154] S. Schiller and V. Korobov. Tests of time independence of the electron and nuclear masses with ultracold molecules. *Phys. Rev. A*, 71:032505, 2005.

[155] W. C. Stwalley and H. Wang. Photoassociation of ultracold atoms: A new spectroscopic technique. *J. Mol. Spectrosc.*, 195:194, 1999.

[156] J. D. Weinstein, R. deCarvalho, T. Guillet, B. Friedrich, and J. M. Doyle. Magnetic trapping of calcium monohydride molecules at millikelvin temperatures. *Nature*, 395:148, 1998.

[157] H. L. Bethlem, G. Berden, and G. Meijer. Decelerating neutral dipolar molecules. *Phys. Rev. Lett.*, 83:1558, 1999.

[158] T. Köhler, K. Góral, and P. S. Julienne. Production of cold molecules via magnetically tunable Feshbach resonances. *Mol. Phys.*, 78:1311, 2006.

[159] N. Nemitz, F. Baumer, F. Münchow, S. Tassy, and A. Görlitz. Production of ultracold heteronuclear RbYb* molecules by photoassociation, 2008. arXiv:0807.0852v1 [quant-ph].

[160] J. Hecker Denschlag. University of Innsbruck (now University of Ulm), private communication, 2009. Project BaRbIe: An ion in a sea of ultracold neutral atoms, see also http://www.uibk.ac.at/exphys/ultracold/projects/barbi/index.html.

[161] O. Dulieu, M. Raoult, and E. Tiemann. Cold Molecules; a chemistry kitchen for physicists? *J. Phys. B: At. Mol. Opt. Phys.*, 39 (19):Introductory review, 2006.

[162] A. Micheli, G. K. Brennen, and P. Zoller. A toolbox for lattice-spin models with polar molecules. *Nature*, 2:341, 2006.

[163] S. Tassy, N. Nemitz, F. Baumer, C. Höhl, Batär, and A. Görlitz. Sympathetic cooling in a mixture of diamagnetic and paramagnetic atoms, 2007. arXiv:0709.0827v1 [physics.atom-ph].

[164] Nils Nemitz. *Production and spectroscopy of ultracold YbRb* molecules.* Dissertation, Mathematisch-Naturwissenschaftliche Fakultät, Heinrich-Heine-Universität Düsseldorf, 2008.

[165] S. F. Boys and F. Bernardi. The calculation of small molecular interactions by the differences of separate total energies. some procedures with reduced errors. *Mol. Phys.*, 19:553, 1970.

[166] A. S. P. Gomes and K. G. Dyall. In preparation. Available from the Dirac web site, http://dirac.chem.sdu.dk.

[167] K. G. Dyall. *J. Phys. Chem. A*, 2009, in press. Available from the Dirac web site, http://dirac.chem.sdu.dk.

[168] Y. Ralchenko, A. E. Kramida, J. Reader, and NIST ASD Team (2008). NIST Atomic Spectra Database (version 3.1.5). Available: http://physics.nist.gov/asd3 (retrieved May 3rd, 2009). National Institute of Standards and Technology, Gaithersburg, MD.

[169] U. Gaubatz, P. Rudecki, M. Becker, S. Schiemann, M. Kulz, and K. Bergmann. Population switching between vibrational levels in molecular beams. *Chem. Phys. Lett.*, 149:463–468, 1988.

[170] U. Gaubatz, P. Rudecki, S. Schiemann, and K. Bergmann. Population transfer between molecular vibrational levels by stimulated raman scattering with partially overlapping laser fields. a new concept and experimental results. *J. Chem. Phys.*, 92:5363, 1990.

[171] R. J. Le Roy, LEVEL 8.0: *A Computer Program for Solving the Radial Schrödinger Equation for Bound and Quasibound Levels,* University of Waterloo Chemical Physics Research Report CP-663 (2007); see http://leroy.uwaterloo.ca/programs/ .

[172] Timo Fleig. RbYb potentials, Heinrich-Heine-University Düsseldorf. Private communication, April 2008.

[173] R. Coté, V. Kharchenko, and M. D. Lukin. Mesocopic molecular ions in Bose-Einstein condensates. *Phys. Rev. Lett.*, 89:093001, 2002.

[174] M. Sabidó, J. de Andrés, J. Sogas, M. Alberti, J. M. Bofill, and A. Aguilar. Inelastic electronic excitation and electron transfer processes in collisions between $Mg(3^1S_0)$ atoms and $K^+(^1S_0)$ ions studied by crossed beams in the 0.10-3.80-keV energy range. *J. Chem. Phys.*, 123:124314, 2005.

[175] M. Sabidó, J. de Andrés, J. Sogas, M. Alberti, J. M. Bofill, and A. Aguilar. Crossed ion-atom beam study of the inelastic collision processes between neutral $Mg(3^1S_0)$ atoms and $Cs^+(^1S_0)$ ions in the 0.05-4.20 keV energy range. *Phys. Chem. Chem. Phys.*, 7:310, 2005.

[176] O. P. Makarov, R. Côté, H. Michels, and W. W. Smith. Radiative charge-transfer lifetime of the excited state of $(NaCa)^+$. *Phys. Rev. A*, 67:042705, 2003.

[177] G. Karlström, R. Lindh, P.-Å. Malmqvist, B. O. Roos, U. Ryde, V. Veryazov, P.-O. Widmark, M. Cossi, B. Schimmelpfennig, P. Neogrády, and L. Seijo. MOLCAS: a program package for computational chemistry. *Comp. Mater. Scien.*, 28:222, 2003.

[178] Y. Ralchenko, A. E. Kramida, J. Reader, and NIST ASD Team (2008). NIST Atomic Spectra Database (version 3.1.5). Available: http://physics.nist.gov/asd3 (retrieved May 3rd, 2009). National Institute of Standards and Technology, Gaithersburg, MD.

[179] C. W. Bauschlicher, Jr., S. P. Walch, and H. Partridge. On correlation in the first row transition metal atoms. *J. Chem. Phys.*, 76:1033–1039, 1982.

[180] *NIST Chemistry WebBook* (version 69, 2005) National Institute of Standards and Technology, Gaithersburg, MD.

[181] L. N. Gorokhov, A. M. Emelyanov, and Y. S. Khodeev. Mass-spectroscopic investigation of stability of gaseous U_2O_2 and U_2. *High Temp.*, 12:1156–1158, 1974.

[182] J. Blaise and J.-F. Wyart. Selected constants of energy levels and atomic spectra of actinides. http://www.lac.u-psud.fr/Database/Contents.html (retrieved January 21, 2009).

[183] J.-P. Desclaux. Relativistic Dirac-Fock expectation values for atoms with Z=1 to Z=120. *Atomic Data and Nuclear Data Tables*, 12:311, 1973.

[184] B. O. Roos, P.-Å. Malmqvist, and L. Gagliardi. Exploring the actinide-actinide bond: Theoretical studies of the chemical bond in Ac_2, Th_2, Pa_2 and U_2. *J. Am. Chem. Soc.*, 128:17000–17006, 2006.

[185] K. G. Dyall. Relativistic double-zeta, triple-zeta, and quadruple-zeta basis sets for the actinides Ac-Lr. *Theor. Chim. Acta*, 117:491, 2007.

[186] T. Noro, M. Sekiya, Y. Osanai, T. Koga, and H. Matsuyama. Relativistic correlating basis sets for actinide atoms from $_{90}$Th to $_{103}$Lr. *J. Comp. Chem.*, 28:2511–2516, 2007.

[187] B. O. Roos, R. Lindh, P.-Å. Malmqvist, V. Veryazov, and P.-O. Widmark. New relativistic ANO basis sets for actinide atoms. *Chem. Phys. Lett.*, 409:295–299, 2005.

[188] J. Thyssen and H. J. Aa. Jensen, Average-of-configurations SCF manuscript, unpublished (1998).

[189] M. Dolg. Lanthanides and Actinides. In P. v. R. Schleyer, N. L. Allinger, T. Clark, J. Gasteiger, P. A. Kollmann, H. F. Schaefer III, and P. R. Schreiner, editors, *Encyclopedia of Computational Chemistry*, pages 1478–1486, Chichester, 1998. Wiley.

[190] Ivan Infante. *Computational Studies in Actinide Chemistry*. Dissertation, Faculteit der Exacte Wetenschappen, Vrije Universiteit Amsterdam, The Netherlands, 2006.

[191] P. W. Atkins and R. S. Friedman. *Molecular Quantum Mechanics*. Oxford University Press, New York, USA, 2001.

[192] E. Eliav, A. Landau, Y. Ishikawa, and U. Kaldor. Electronic structure of eka-thorium (element 122) compared with thorium. *J. Phys. B: At. Mol. Opt. Phys.*, 35:1693, 2002.

[193] B. O. Roos and P. Å. Malmqvist. Relativistic quantum chemistry: the multiconfigurational approach. *Phys. Chem. Chem. Phys.*, 6:2919–2927, 2004.

[194] N. G. Lewis. The atom and the molecule. *J. Am. Chem. Soc.*, 38:762–785, 1916.

[195] U. Radius and F. Breher. To boldly pass the metal-metal quadruple bond. *Angew. Chem. Int. Ed.*, 45:3006–3010, 2006.

[196] G. Frenking and R. Tonner. The six-bond bound. *Nature*, 446:276–277, 2007.

[197] B. O. Roos, A. C. Borin, and L. Gagliardi. Reaching the maximum multiplicity of the covalent chemical bond. *Angew. Chem.*, 119:1491–1494, 2007.

[198] F. A. Cotton, N. F. Curtis, C. B. Harris, B. F. G. Johnson, S. J. Lippard, J. T. Mague, W. R. Robinson, and J. S. Wood. Mononuclear and polynuclear chemistry of rhenium(III): its pronounced homophilicity. *Science*, 145:1305–1307, 1964.

[199] F. A. Cotton, L. A. Murrillo, and R. A. Walton. *Multiple Bonds Between Metal Atoms*. Springer, Berlin, 3rd edition, 2005.

[200] L. Gagliardi and B. O. Roos. The electronic spectrum of $Re_2Cl_8^{2-}$: A theoretical study. *Inorg. Chem.*, 42:1599–1603, 2003.

[201] L. Gagliardi and B. O. Roos. Quantum chemical calculations show that the uranium molecule U_2 has a quintuple bond. *Nature*, 433:848, 2005.

[202] B. O. Roos and P.-Å. Malmqvist. Relativistic quantum chemistry: The multiconfigurational approach. *Phys. Chem. Chem. Phys.*, 6:2919–2927, 2004.

[203] W. A. De Jong, L. Visscher, and W. C. Nieuwpoort. On the bonding and the electric field gradient of the uranyl ion. *J. Mol. Struct. THEOCHEM*, 458:41, 1999. Erratum 581:259, 2002.

[204] Hans Jørgen Aagaard Jensen. University of Southern Denmark, Odense. Private communication, 2009.

[205] H. J. Aa. Jensen, P. Jørgensen, H. Ågren, and J. Olsen. Second-order Møller-Plesset perturbation theory as a configuration and orbital generator in multiconfiguration self-consistent field calculations. *J. Chem. Phys.*, 88:3834–3839, 1988.

[206] S. Knecht, H. J. Aa. Jensen, and L. K. Sørensen. Four-component MP2 natural orbitals: An efficient way of selecting appropiate active spaces for coupled cluster and multiconfigurational self-consistent field calculations, 2009. unpublished work.

[207] J. K. Pedersen. *Description of correlation and relativistic effects in calculations of molecular properties*. Dissertation, Department of Physics and Chemistry, University of Southern Denmark, 2004.

[208] E. Fromager, J. Toulouse, and H. J. Aa. Jensen. On the universality of the long-/short-range separation in multiconfigurational density functional theory. *J. Chem. Phys.*, 126:074111, 2007.

[209] E. Fromager and H. J. Aa. Jensen. Self-consistent many-body perturbation theory in range-separated density-functional theory: A one-electron reduced-density-matrix-based formulation. *Phys. Rev. A*, 78:022504, 2008.

[210] E. Fromager, F. Réal, P. Wåhlin, U. Wahlgren, and H. J. Aa. Jensen. On the universality of the long-/short-range separation in multiconfigurational density functional theory. II. Investigating f^0 actinide species. *J. Chem. Phys.*, 131:054107, 2009.

[211] J. Olsen. The initial implementation and applications of a general active space coupled cluster method. *J. Chem. Phys.*, 113:7140, 2000.

List of Abbreviations

CAS	Complete active spaces
CASPT2	Complete active space perturbation theory to 2nd order
CASSCF	Complete active space self-consistent-field
CC	Coupled Cluster
CI	Configuration interaction
DCHF	Dirac-Coulomb Hartree-Fock
DFT	Density functional theory
FSCC	Fock-space coupled cluster
GAS	Generalized active spaces
GASCI	Generalized active spaces configuration interaction
IHFSCC	Intermediate Hamiltonian Fock-space coupled cluster
IOTC	Infinite-order two-component
KR-MCSCF	Kramers-restricted multiconfigurational self-consistent-field
MRCC	Multi-reference coupled cluster
MRCI	Multi-reference configuration interaction
SF	Spin-free
SO-CASPT2	Spin-orbit complete active space perturbation theory to 2nd order
TDDFT	Time-dependent density functional theory
X2C	Exact two-component

Paper 1

Stefan Knecht, Hans Jørgen Aagaard Jensen, and Timo Fleig

Large-scale parallel configuration interaction. I. Non-relativistic and scalar-relativistic general active space implementation with application to (Rb-Ba)$^+$.

J. Chem. Phys., **128** (2008) 014108

Large-scale parallel configuration interaction. I. Nonrelativistic and scalar-relativistic general active space implementation with application to $(Rb-Ba)^+$

Stefan Knecht[a)]
Department of Theoretical Chemistry, Heinrich Heine University Düsseldorf, Universitätsstraße 1, D-40225 Düsseldorf, Germany

Hans Jørgen Aa. Jensen[b)]
Department of Physics and Chemistry, University of Southern Denmark, DK-5230 Odense M, Denmark

Timo Fleig[c)]
Department of Theoretical Chemistry, Heinrich Heine University Düsseldorf, Universitätsstraße 1, D-40225 Düsseldorf, Germany

(Received 4 September 2007; accepted 11 October 2007; published online 7 January 2008)

We present a parallel implementation of a string-driven general active space configuration interaction program for nonrelativistic and scalar-relativistic electronic-structure calculations. The code has been modularly incorporated in the DIRAC quantum chemistry program package. The implementation is based on the message passing interface and a distributed data model in order to efficiently exploit key features of various modern computer architectures. We exemplify the nearly linear scalability of our parallel code in large-scale multireference configuration interaction (MRCI) calculations, and we discuss the parallel speedup with respect to machine-dependent aspects. The largest sample MRCI calculation includes 1.5×10^9 Slater determinants. Using the new code we determine for the first time the full short-range electronic potentials and spectroscopic constants for the ground state and for eight low-lying excited states of the weakly bound molecular system $(Rb-Ba)^+$ with the spin-orbit-free Dirac formalism and using extensive uncontracted basis sets. The time required to compute to full convergence these electronic states for $(Rb-Ba)^+$ in a single-point MRCI calculation correlating 18 electrons and using 16 cores was reduced from more than 10 days to less than 1 day. © *2008 American Institute of Physics*. [DOI: 10.1063/1.2805369]

I. INTRODUCTION

Configuration interaction (CI) theory remains a widespread method for electronic-structure studies, in particular, for the investigation of electronically excited states of atoms and molecules. This is to a large part due to its conceptual simplicity. The determination of the correlation energy in such applications usually necessitates the use of multireference (MR) CI expansions already in the treatment of molecules with light elements, but for heavy-element (nuclear charge $Z\geqslant30$) molecular studies multireference methods are of paramount importance due to the open-shell character of many such systems. The MRCI expansions, however, quickly become extremely long when one-particle basis sets of high quality are employed and the number of correlated electrons is large. This situation is generally encountered in quantum-chemical investigations of high accuracy. Thus, MRCI calculations beyond 10^9 Slater determinants are commonly needed for an adequate treatment of heavy-element systems and such applications therefore call for an efficient and general parallel implementation.

With the rapid advance of massively parallel computer architectures, a parallel MRCI implementation is an effective means of extending the applicability of the CI approach. To this day, several implementations of parallel full (F)CI/MRCI codes embedded in program packages such as GAMESS,[1] COLUMBUS,[2,3] MOLPRO,[4] and GAUSSIAN (Ref. 5) have been reported in the literature. Some recent parallel CI programs—MRCI (Ref. 6) and FCI (Ref. 7)—use configuration state functions (CSFs) rather than Slater determinants. However, almost all modern massively parallel[8] and sequential FCI algorithms are determinant based (following the footsteps of Knowles and Handy,[9] Olsen *et al.*,[10,11] Zarrabian *et al.*[12] and others), mainly because of the efficiency in computing the dominant linear transformation step of the expansion vectors.

In this paper, we present a linear-transformation driven parallel implementation of the string-based MRCI and FCI program LUCITA,[10,11,13] capable of performing MRCI expansions in a very flexible way through the general active space (GAS) approach. The central ideas ensuring efficiency are a distributed data model and a static load-balancing scheme. In addition, we have designed our parallel implementation in such a way that it can be applied effectively on supercomputers, e.g., IBM's pSeries, as well as on today's standard personal computer (PC) clusters.

Beside extensive tests of the parallel implementation on the ground state of the water molecule, we include in this

a)Electronic mail: stefan@theochem.uni-duesseldorf.de.
b)Electronic mail: hjj@ifk.sdu.dk.
c)Electronic mail: timo@theochem.uni-duesseldorf.de.

paper an initial study of the electronic structure of the $(Rb-Ba)^+$ molecular ion. This system belongs to a class of molecules which is investigated in ongoing ultracold molecule experiments[14,15] aimed at a fundamental understanding of interatomic and intermolecular interactions at extremely low temperatures. The short-range potential curves of the system are determined here for the first time and provide guiding information for further experimental and theoretical studies. Spin-orbit interaction plays a crucial role in many electronic states of heavy-element species; nevertheless, parallel spin-orbit-free CI calculations allow for a high-level study of electron correlation effects on the electronic structure. The results provide a valuable initial assessment of the systems and a guideline for further calculations including spin-orbit effects.

The paper is structured as follows: In Sec. II we commence by a review of the string-driven CI implementation on which our parallel implementation is based and a brief account of the physical framework for the approach, i.e., the applicable Hamiltonians, symmetry considerations, etc. We then describe the parallel algorithm and central features of the implementation in full detail, and we discuss its performance in large-scale test applications to the water molecule. In the third section our initial application on $(Rb-Ba)^+$ is reported. In the final section, we summarize the major conclusions and discuss prospects for future work, in particular, the parallelization of fully relativistic MRCI.

II. PARALLEL CONFIGURATION INTERACTION IMPLEMENTATION

A. Theoretical aspects

1. Hamiltonians and molecular symmetry

Our parallel CI implementation is based on the large-scale sequential string-driven program LUCITA (Ref. 13) which originated from the LUCIA code written by Olsen.[16,17] It was recently interfaced[13] to the DIRAC program package[18] which allows us to exploit the methodology implemented there. In particular, the new parallel CI can thus be used with all nonrelativistic and "scalar"-relativistic Hamiltonians implemented in DIRAC. The CI setup is based upon orthonormal molecular spin orbitals that are typically obtained from either a closed-shell or an open-shell Hartree-Fock calculation, and in the CI expansion only Slater determinants of a specified spatial symmetry and M_S value are included. The single point groups D_{2h} and its subgroups and the linear symmetries $C_{\infty v}$ and $D_{\infty h}$ have been implemented. The symmetry handling in the DIRAC program package was originally written for the use of four-component spinors in double point group symmetry, but the program does take advantage of single-point group symmetry for spin-orbit-free model Hamiltonians, a feature that is implemented in the four-component spin-orbit-free formalism[19] and the nonrelativistic Lévy-Leblond[20] scheme. The spin-orbit-free formalism in DIRAC essentially corresponds to an infinite-order Douglas-Kroll-Hess scalar-relativistic approximation. As the CI module uses integrals over molecular orbitals as input data, the parallel CI code can be used without any code changes in the CI module with the new memory-saving two-component methods under implementation in DIRAC.[21–23]

2. Orbital space definitions

For the one-particle space we employ the concept of defining electronic orbital subspaces of inactive, active, and secondary types, where the inactive orbitals are fully occupied, the active orbitals may be partially occupied, and the secondary orbitals are empty.[24] The GAS formalism is a complete generalization of the restricted active space (RAS) model[10] and it allows for an arbitrary division of orbital spaces tailored to the considered chemical or physical electronic-structure problem. In addition, arbitrary electron occupation constraints can be chosen for the resulting GA spaces. As a consequence, both the number of active spaces and their occupation limits are now redefined in general terms compared to the commonly used complete and restricted active space models (CAS, RAS). Implementations based on the GAS concept have been realized in the context of both nonrelativistic and relativistic CI methods.[16,25,26] Furthermore, multiconfiguration self-consistent-field (MCSCF) and coupled-cluster implementations based on the GAS model have also been published recently.[17,27,28]

As an example, variable occupation in four active spaces could be used to construct a typical MRCI expansion for single and double outer-core excitations (core-core and core-valence type correlations), a small CAS space, a space where the excitations are restricted up to quadruples, and a space with an occupation limitation of at most two electrons (virtual space).

The GAS concept, in particular, the resulting selection of Slater determinants that need to be included, plays an essential role for our parallel implementation. This will be described in Sec. II B as well as in Sec. II C 1.

B. Outline of the CI technique

We commence with a brief outline of the underlying CI algorithm implemented in LUCITA,[13] which comprised an excellent setout for our parallel implementation. In general, the starting point is the CI eigenvalue problem

$$\mathbf{HC} = \mathbf{CE}. \tag{1}$$

However, in large-scale CI calculations one is typically only interested in the computation of a few eigenvalues and eigenvectors of the large, real-symmetric matrix $\mathbf{H}$ such that an efficient iterative diagonalization method may be employed. In Fig. 1 an outline of the optimization algorithm which is implemented in the current sequential version of LUCITA is given. It is Olsen's generalized version[11] of the original implementation of Davidson.[29] For a thorough discussion of the complete procedure and of the basic implementation the reader is referred to References 10, 11, 13, and 26. In what follows we want to draw your attention to some essential features of the sequential setout implementation and to develop an efficient parallelization scheme by taking advantage of these.

The computationally demanding as well as the most time-consuming step in each generalized Davidson iteration is the calculation of the linearly transformed vector $\boldsymbol{\sigma}_n$,

1: Calculate diagonal matrix $\mathbf{H}_D$ with elements H_{ii}
2: Set up trial vectors building a subspace $\{\mathbf{b}_1^{(0)}, \mathbf{b}_2^{(0)}, \ldots, \mathbf{b}_M^{(0)}\}$ of dimension M
3: **while** current iteration < maximum number of iterations **do**
4: Evaluate linear transformations $\boldsymbol{\sigma}_n = \mathbf{H}\ \mathbf{b}_n$, n = 1,...,M.
5: Calculate and diagonalize the projected matrix $\tilde{\mathbf{H}} \rightarrow \lambda_k^{(M)}, \boldsymbol{\alpha}_k^{(M)}$, with $\tilde{H}_{mn} = \langle \mathbf{b}_m^{(0)} | \boldsymbol{\sigma}_n \rangle$
6: Calculate residuals $\mathbf{R}_k = \sum_{n=1}^{M} \left(\boldsymbol{\sigma}_n - \lambda_k^{(M)}\, \mathbf{b}_n \right) \alpha_{n,k}^{(M)}$, $k = 1, M$
7: **if** not converged **then**
8: Build up new reference vectors $\mathbf{b}'_n = \left(\mathbf{H_D} - \lambda_n^{(M)} \right)^{-1} \mathbf{R}_n$
9: Orthogonalize $\mathbf{b}'_n$ to previous vectors and normalize them
10: **else** {converged}
11: GOTO 14
12: **end if**
13: **end while**
14: END

FIG. 1. Flow chart of the iterative Davidson diagonalization method implemented in LUCITA.

$$\boldsymbol{\sigma}_n = \mathbf{H}\mathbf{b}_n, \tag{2}$$

where both the $\mathbf{b}_n$ and $\boldsymbol{\sigma}_n$ vectors may be written in terms of alpha strings $\mathcal{S}(I_\alpha)$ and beta strings $\mathcal{S}(I_\beta)$.[9,30] Considering only the two-electron alpha-beta part of the $\boldsymbol{\sigma}_n^{I_\alpha I_\beta}$ vector, the evaluation can be expressed as

$$\sigma_n^{I_\alpha I_\beta} = \sum_{J_\alpha J_\beta} \sum_{ijkl} \mathbf{A}_{ijkl}^{I_\alpha I_\beta, J_\alpha J_\beta} (ij|kl) \mathbf{b}_n^{J_\alpha J_\beta}, \tag{3}$$

where $\mathbf{A}_{ijkl}^{I_\alpha I_\beta, J_\alpha J_\beta} = \langle \mathcal{S}(I_\beta) | \hat{a}_{i\beta}^\dagger \hat{a}_{j\beta} | \mathcal{S}(J_\beta) \rangle \langle \mathcal{S}(I_\alpha) | \hat{a}_{k\alpha}^\dagger \hat{a}_{l\alpha} | \mathcal{S}(J_\alpha) \rangle$ is the coupling coefficient and $|\mathcal{S}(J_\alpha)\mathcal{S}(J_\beta)\rangle$ is the Slater determinant defined by strings of spin-orbital creation operators $\mathcal{S}(J_\alpha)$ and $\mathcal{S}(J_\beta)$. Furthermore, $\mathbf{b}_n^{J_\alpha J_\beta}$ denotes the expansion coefficient referring to this Slater determinant in the $\mathbf{b}_n$ vector and $(ij|kl)$ is the integral for the spin orbitals labeled with lowercase indices i, j, k, and l.

The string formulation of Slater determinants by means of ordered products of n_α and n_β creation operators comprises an excellent basis for an efficient parallel implementation. Each string, be it an α string $|\mathcal{S}(J_\alpha)\rangle$ or a β string $|\mathcal{S}(J_\beta)\rangle$, has a definite *type T* and *symmetry S*. The type of a string is determined by its GAS definition, i.e., the number of creation operators in each GA space, while its spatial symmetry follows from the symmetry of the spin orbitals occupied in the string. According to the GAS specifications the specified total spatial symmetry, restrictions on allowed combinations of alpha and beta strings that automatically lead to the picture of a CI vector forming a matrix of (occupation)-type-(occupation)-type-symmetry-symmetry (*TTSS*) blocks are imposed. Each allowed expansion coefficient $\mathbf{b}_n^{J_\alpha J_\beta}$ thus belong to a specific allowed $\mathbf{b}_n^{TTSS_j}$ block. Moreover, the resulting block partitioning is implicitly symmetric with respect to both the $\mathbf{b}_n$ and $\boldsymbol{\sigma}_n$ vector, a feature which has been extensively exploited in our parallelization algorithm. We have also made use of the previously implemented concept of batching the number of *TTSS* blocks in memory,[11] making it possible to handle CI expansions which do not fit in memory. This batching was a big advantage for the parallelization, as it made it straightforward to assign a given *TTSS* batch to a specific processor and as the code for handling the linear transformation of such a batch was already written, using lists of which other *TTSS* blocks a given *TTSS* block connects to.

This feature makes it possible for the new code to handle very long CI expansions (up to the order of 10^{10}–10^{11} with typical computer resources in a contemporary PC cluster).

We discuss the key features of our parallel implementation in the following section, in particular, the importance of an efficient parallelization scheme for the $\mathbf{Hb}_n$ task with respect to both load balancing and communication costs (Sec. II C 3). There, we also compare our string-driven implementation to other common approaches to CI parallelization.

C. Parallel implementation

1. General aspects

We first consider the general question of how to ensure the portability for a parallel implementation of a program that is embedded in a program suite, *in casu* DIRAC.[18] For this purpose, we designed the parallel algorithm by means of the standard message passing interface (MPI) since it is freely available[31,32] and generally available on most parallel computers and since it also provides library functions both for the efficient use of shared memory (one-sided communication) as well as distributed memory (point-to-point and collective communication) machines. By doing so, the migration for the end user from a sequential to a parallel executable becomes rather straightforward for many different architectures, including the modern multinode clusters of symmetric multiprocessor (SMP) machines.

A sophisticated parallel handling of extremely long CI expansions, up to 10^9 determinants, requires a careful consideration of communication, memory management, and disk storage, even in single-root computations.

Communication. In order to keep communication costs low whenever large $\mathbf{b}_n$-vector segments have to be ex-

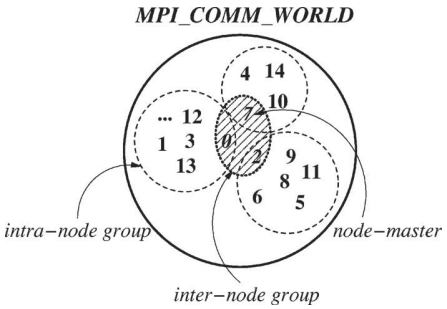

FIG. 2. Splitting scheme of processes for different communication patterns applied in the parallel implementation. Each number corresponds to a unique processor that is contained in the global group of all processors *MPI_COMM_WORLD*.

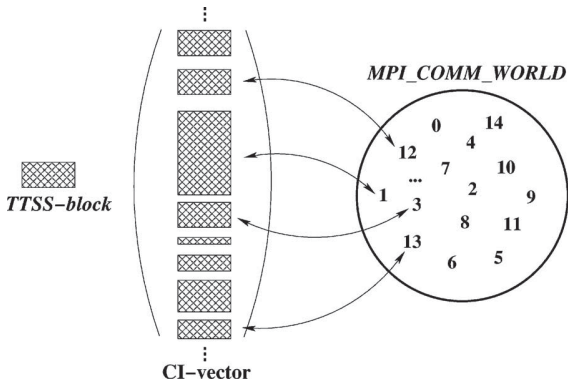

FIG. 3. *TTSS*-block distribution among all available processes used as central parallelization pattern. Each number corresponds to a unique processor that is contained in the global group of all processors *MPI_COMM_WORLD*.

changed we introduced two different communication patterns in addition to the general global *MPI_COMM_WORLD* model: "slow" *internode* communication and "fast" *intranode* communication on each node.

This is achieved by dividing (*MPI_comm_split*) the global communication group *MPI_COMM_WORLD* that consists of all processes into the corresponding subgroups according to the underlying MPI process topology. The creation of internode and intranode communication groups is visualized in Fig. 2. Thus, we assign out of each node-specific process group a master (node master) that will exclusively participate in all intense internode communication, in particular, the exchange of parts of the $\mathbf{b}_n$ vectors, which are the only CI vector segments to be communicated between nodes in our final algorithm. The overhead for the remaining low-cost communication is negligible and can therefore be carried out via global collective routines.

Memory. The maximized use of available memory on each process plays an important role for an optimal scalability of the parallel implementation. Although it may not be possible to keep two large CI vectors in memory on a single process, it often can be realized in parallel computation as the total memory normally grows linearly with the number of nodes with local memory. The key issue is the division of the CI vector into proper subelements, where all instances of this subelement are assigned to and saved on disk by one and only one process. As mentioned above, the present sequential version of LUCITA operates with a vector partitioning scheme in terms of *TTSS* blocks. This blocking can readily be adopted to obtain a balanced task distribution. Figure 3 illustrates our central idea of a fixed assignment of each nonvanishing *TTSS* block to a specific process out of *MPI_COMM_WORLD*. We will address and discuss the difficulty of load balancing, in particular, for the $\mathbf{Hb}_n$ step in Sec. II C 3. As a remark on ongoing work, the block distribution among the processors will also reduce the number of integrals that must reside in the core at any given time. This is, however, not exploited at the moment.

The *TTSS* blocks are organized in batches individually on each processor for both the $\boldsymbol{\sigma}_n$ vector and the $\mathbf{b}_n$ vector where the length of a batch corresponds to the maximum amount of memory (on a given processor) that can be allocated. We therefore generally minimize disk access, which is known to be a serious bottleneck in parallel efficiency.

Disk storage. The MPI-2 standard with its input/output (I/O) facilities provides a variety of library routines which permit an efficient individual as well as collective file handling. Our key concept for minimized I/O effort is closely related to minimized communication costs by taking into account special features of various system architectures, e.g., IBM's general parallel file system (GPFS) that provides global data access for each processor. Furthermore, to reduce intranode communication among cores on SMP machines we implemented the use of parallel access of each core to group files according to the established communication groups as depicted in Fig. 2. Because of the application of either global or local group files we accomplish a complete avoidance and a significant reduction of rather expensive communication tasks. Since all trial CI vectors $\mathbf{b}_n$ as well as $\boldsymbol{\sigma}_n$ vectors partition into *TTSS* blocks each processor only needs to store its assigned nonzero vector segments into the group file which are needed to process, e.g., all local subspace operations. This distributed storage thus entails a significant reduction of disk requirements on each node (processor group).

2. Subspace operations

Each generalized Davidson iteration mainly consists of two different parts, the subspace operations and the evaluation of the linearly transformed vector $\boldsymbol{\sigma}_n$, as shown in Fig. 1. Before turning to the parallel algorithm for the $\boldsymbol{\sigma}_n$-vector evaluation we want to discuss the parallel implementation and performance of the subspace operations. They are comprised by several vector operations such as the generation of the start vectors, determination of the residual, evaluation, orthogonalization, and renormalization of the new trial vector, and so forth. Because of the distribution scheme of the *TTSS* blocks resulting from each $\mathbf{b}_n$ and $\boldsymbol{\sigma}_n$ vector all the intense vector processing steps can be handled locally on each process since either only dot products or vector scaling or other simple vector operations are involved. Note that this applies in particular to the iterative update of the elements of the reduced Hamiltonian matrix $\tilde{\mathbf{H}}$ which is also done independently on each processor in terms of the batches of *TTSS* blocks assigned to that processor. This therefore does not require any explicit global vector-exchange communication

1: evaluate linear transformation $\boldsymbol{\sigma}_n = \mathbf{H}\,\mathbf{b}_n$
2: gather information in a block list about locally required $\mathbf{C}_j$ blocks deduced from the initially constructed $\mathbf{b}_n$-$\boldsymbol{\sigma}_n$ connection matrix
3: **if** distributed data approach **then**
4: communicate $\mathbf{b}_n^{TTSS}$ blocks among node masters using *MPI_bcast* according to the block list
5: **end if**
6: **while** current batch $\leq$ maximum number of batches (maxbat_s) of $\boldsymbol{\sigma}$ blocks **do**
7: **while** i $\leq$ number of $\boldsymbol{\sigma}$ blocks within the current batch **do**
8: calculate all contributions to $\boldsymbol{\sigma}_i$ from the various $\mathbf{C}_j$ blocks
9: **end while**
10: **if** replicated data approach **then**
11: call *MPI_reduce* respectively *MPI_allreduce* to sum up contributions to all $\boldsymbol{\sigma}_i$ from different processors on the assigned processor(s)
12: **end if**
13: **end while**

FIG. 4. Comparison of the replicated data model with the distributed data model for the $\boldsymbol{\sigma}$-vector evaluation

but global data transfer of partially updated scalar values or rather small arrays where efficient collective communication routines (*MPI_bcast, MPI_allreduce*) are employed.

3. Sigma-vector generation

We commence with a comparison of the different parallelization models for the computationally most demanding step $\mathbf{Hb}_n$. A more detailed description of how the $\boldsymbol{\sigma}_n$-vector calculation is organized in the innermost loops in LUCITA is described elsewhere.[10,11,26] Following Gan *et al.*[1] there are two obvious schemes for the implementation of the $\mathbf{Hb}_n$ step, using either a replicated or a distributed data model.

A FCI parallelization scheme based on the extensive use of the Linda model[33] has been presented by Klene *et al.*[5] Since they follow a somewhat different parallelization strategy already from the outset their work will not be subject to the following discussion. Both Tanaka *et al.*[7] and Suo *et al.*[6] realized a pure replicated data model in their parallel CI implementations where one of the main differences between their parallel approaches stems from a usage of different parallel library tools. It should be noted that such an approach lacks efficiency as soon as the partially updated $\boldsymbol{\sigma}_n$ vector cannot be kept in memory on each processor and has to be written to disk instead. In such a case, which may easily occur in large-scale CI calculations, the vector partitions need to be collected from disk subsequent to the evaluation loops. To illustrate a possible drawback of the replicated data approach, consider the lower part of the $\boldsymbol{\sigma}_n$-vector evaluation algorithm which is sketched in Fig. 4 in a pseudocode visualization. The replicated data model which, of course, depends on the chosen load-balancing algorithm, is very efficient as long as the evaluation of the $\boldsymbol{\sigma}_n$ vector requires only a single batch (maxbat_s=1) of (*TTSS*) blocks on each processor. It will, however, require costly communication (*MPI_(all)reduce*) inside the first loop of the $\mathbf{Hb}_n$ step for values of maxbat_s greater than 1 since a complete computation of a single sigma block $\boldsymbol{\sigma}_n^{TTSS_i}$ that has been explicitly assigned to a specific processor according to the scheme in Fig. 4, is made up of contributions from different $\mathbf{b}_n^{TTSS_j}$ blocks. As a general rule, communication taking place in each step of a loop is obviously equivalent to synchronization which may hamper a reasonable load balancing. Furthermore, simultaneous communication and summation of large batch chunks—in the test computations we typically deal with lengths up to 5×10^7 determinants—could easily cause program failures related to memory excess by the MPI library functions because of the tremendous communication demands. We observed this in the course of our work. Thus, full portability of our parallel code could not have been assured, but we retained an implementation of the replicated data approach for test purposes. Also, Gan *et al.* clearly demonstrated in their implementations of replicated and distributed data models[1] the superiority of the distributed model due to reduced data communication.

We shall now describe the essential features of our parallel $\boldsymbol{\sigma}_n$-vector evaluation implementation based on the idea of a distributed data model as depicted in Fig. 4. The basic concept of the distributed data model, as it is also used in the present work, is the local computation of each sigma block $\boldsymbol{\sigma}_i$ on a designated processor, which thus requires the collection of all connecting CI coefficient *TTSS* blocks beforehand, as shown in the upper part of Fig. 4. We note that this task could be performed by exploiting the facility of one-sided communication which the MPI library provides. This option has, however, not been implemented in our parallel code at the moment. Concerning further work on improving our parallel implementation such shared-memory-like communication techniques may be of particular interest, taking into account the increasing number of multicore machines that are available today and that are usually equipped with shared memory.

Based on our present distributed data approach we have chosen to emphasize the following three important features in the design of the CI coefficient gathering algorithm: file

sharing within a group, communication only among node masters, and adapted splitting of the group of node masters into communication subgroups.

The first option will accomplish input/output minimization on a node with a group of processors since it avoids multiple storing, maybe on the same disk, of the *TTSS* blocks needed by more than one processor on this node. Since all processes with an entry of zero in their block list for a given *TTSS* block drop out of the network of node masters (shaded ellipse in Fig. 2; internode group), the communication effort in each collection task (*MPI_bcast*) is greatly reduced. The associated communication overhead for the subdivision and reunification of the node-master network is thereby negligible. The increased input/output activity of all connected *TTSS* blocks within a group of processors is overcompensated by the low memory requirements for the handling of large-scale CI expansions. Details about the parallel performance with respect to memory requirements and I/O activity are discussed in Sec. II D. It is worthwhile to note that the adapted batching corresponds to maximized use of memory which has a favorable effect on the scaling of the new parallel code. Thus, e.g., for the determination of the required *TTSS* batches of the $\mathbf{b}_n$ vector on a given processor we can simply disregard all those *TTSS* blocks that are neither assigned to this processor nor connected by the Hamiltonian [see Eq. (3)].

A crucial aspect of any successful parallelization is, in general, a good load balancing. We already mentioned the idea of a static *TTSS* block assignment model in Sec. II C 1 which is used throughout the generalized Davidson algorithm. The key question of how to achieve a global, good load balancing for the essential step $\mathbf{Hb}_n$ remains. For this, we proceed as follows: Once at the outset of the iterative generalized Davidson algorithm all allowed connections from $\mathbf{b}_n^{TTSS_j}$ blocks to a given $\boldsymbol{\sigma}_n^{TTSS_i}$ block are determined. In doing so, we obtain a $\mathbf{b}_n \rightarrow \boldsymbol{\sigma}_n$ connection matrix which is used to compute the total "weight" of a *TTSS* block. This weight is a measure of the computational effort arising from a given *TTSS* block. The total weight of each *TTSS* block is generated from its count of connections multiplied by its length (number of coefficients). The block distribution is now carried out such that an even total weight is achieved for every processor. The number of *TTSS* blocks and their lengths can of course be varied by imposing extra redundant GAS constraints for a specific CI expansion, which facilitates a balanced block distribution, for example, by dividing a singles and doubles GA space into two GA spaces with half the orbitals, allowing 0, 1, or 2 electrons in both GA spaces. This partitioning freedom is in a sense similar to an introduction of task-list parameters as mentioned in the following. Furthermore, we store all individually required entries of the connection matrix which entails only an additional allocation of an INTEGER array of a length equal to the number of nonvanishing *TTSS* blocks. This array is then of particular use for the block collection task as illustrated in Fig. 4.

A number of previous parallel CI implementations employ a dynamic load balancing scheme, in particular, for the most time-consuming step, the evaluation of $\mathbf{Hb}_n$. As a basic principle they apply a task list which is designed according to their different implementation patterns, see e.g., Refs. 1, 2, 4, 6, and 7 and others. An advantage of such a procedure is that one may make use of several parameters to gain more granularity on the task division. This can be useful to achieve an optimal load balancing as well as to guarantee program portability.[1,4] However, our static approach to load balancing works very well, and we have therefore not pursued dynamic algorithms.

D. Parallel performance

We first focus on the sequential performance of our new parallelized code. The following large-scale test applications have been performed for the ground state of the water molecule (C_{2v} symmetry) at equilibrium geometry using Dunning's cc-pVDZ basis[34] in uncontracted form in the four-component spin-free Dirac-Coulomb approximation. In Table I the GAS schemes for the two test cases **A** and **B** are listed; they yield CI expansions of roughly 450×10^6 (**A**) and 1158×10^6 determinants (**B**), composed of 4708 and 5844 nonvanishing *TTSS* blocks, respectively. The timings presented in this subsection have been taken using two different system architectures. The first system is an IBM pSeries p690 cluster of 41 frames with each frame consisting of 32 Power4+ processors running at 1.7 GHz. The frames are connected with high-performance switches (bandwidth >1400 MB/s, latency <6.5 μs),[35] and each frame has access to a GPFS. Our second test system is a Linux-based cluster which is made up of 200 nodes of two Intel Woodcrest (2.66 GHz; dual core version) processors each, equipped with either 4 Gbytes (160 nodes) or 8 Gbytes (40 nodes) of shared main memory and a dual gigabit ethernet connection, respectively.[36] The nodes are interconnected by gigabit switches and provided with local disks.

Table II shows our timing data for a representative generalized Davidson iteration for both the original serial code and the new revised parallel code running on one processor and on both system architectures. The sequential efficiency is only slightly improved on the Linux cluster whereas a significant performance enhancement for test case **A** is found on the IBM cluster.[49] We attribute this observation to the optimized and reduced I/O costs of our parallel code compared to the original code on a GPFS which is known to be very sensitive to the current load caused by other users. In general, our large-scale CI implementation exhibits some I/O dependency, which is nevertheless much less pronounced than in the parallel FCI implementation reported by Ansaloni *et al.*[8]

The parallel performance and scalability of our new code was tested on up to 128 processors using both CI setups **A** and **B** (see Table I) and 1 Gbytes of core memory for each processor (required minimum: 0.5 Gbytes). We first consider the timing results for a single generalized Davidson iteration in combination with the $\boldsymbol{\sigma}$-vector generation step obtained for test case **A** on the IBM machine which are collected in Table III. The speedup $\mathcal{S}(p,N)$ in parallel calculations is generally defined as

TABLE I. General active spaces (GASs) and occupation constraints for H_2O ground state calculations **A** and **B** in C_{2v} symmetry using an uncontracted cc-pVDZ type of basis set (see text). The minimum and maximum number of electrons are accumulated values, i.e., by adding the number of electrons in this and all preceeding GA spaces. The spaces have not been constructed according to physical arguments but to mimic typical realistic calculations.

	Orbitals per irrepresentation				Minimum/maximum accumulated electrons		
GA space	A_1	B_1	B_2	A_2	Minimum electrons	Maximum electrons	Shell types
					Test case **A** 445 250 936 determinants		
I	1	0	0	0	0	2	$1s$ (O)
II	1	1	0	0	0	6	$2s$, $2p_x$ (O)
III	0	0	1	0	0	8	$2p_y$ (O)
IV	4	2	0	0	6	10	$2p_z$ (O); $1s$ (H); virtuals
V	9	7	4	2	10	10	virtuals
					Test case **B** 1 579 484 992 determinants		
I	1	0	0	0	0	2	$1s$ (O)
II	1	1	0	0	0	6	$2s$, $2p_x$ (O)
III	0	0	1	0	0	8	$2p_y$ (O)
IV	4	2	0	0	5	10	$2p_z$ (O); $1s$ (H); virtuals
V	9	7	4	2	10	10	virtuals

$$\mathcal{S}(p,N) = \frac{T(1,N)}{T(p,N)}, \tag{4}$$

where $T(p,N)$ is the required time to solve a problem of size N on p processors.

The performance test on the IBM cluster yielded a reasonable speedup for the $\mathbf{Hb}_n$ step, in particular, for 4 and 16 processors, that is 3.70 and 12.88, respectively. Nevertheless, the speedup for the total iteration drops significantly for a larger number of processors. We ascribe these performance characteristics to the increase in the GPFS disk accesses most notably in the subspace operations part of the generalized Davidson iteration. In this test calculation with almost 450×10^6 determinants, about 450×10^6 REAL*8 numbers per trial vector, corresponding to 3.4 Gbytes of disk space for each, have to be read from and written to hard disk in a subspace operation. Although we have optimized our parallel implementation with respect to the number of READ and WRITE statements by processing vector operations likewise in terms of batches of *TTSS* blocks, we may suffer from the current total disk usage on the general parallel file system during data transfer, as already indicated above. The satisfactory speedup for the $\mathbf{Hb}_n$ step, however, illustrates the effectiveness of our static load-balancing scheme.

On the Linux cluster we obtained almost perfect scalability of the $\mathbf{Hb}_n$ step and with respect to the total execution time for a generalized Davidson iteration even a superlinear speedup in test calculation **A** when running with one CPU per node, as is explicitly shown in Table V for computations using two (speedup of 2.15), four (4.32), and eight (8.47) processors. Since each node is built up of two dual core processors (in total four cores) there are obviously several ways of processing, e.g., a four-CPU parallel calculation. Therefore, we want to analyze in more detail a single-node calculation using all four cores as well as a four-node single-core computation. The excellent speedup obtained with the latter setup is mainly a direct consequence of two basic facts. On the one hand, in memory- and CPU-intense computations as, e.g., the "matrix × vector" $\mathbf{Hb}_n$ step, we may have to take possible memory access conflicts between different CPUs into account as soon as multicore processors are involved. This particular effect on the parallel efficiency has also been discussed by Tanaka *et al.* in Ref. 7. Another relevant aspect is that each multicore node in our present system has a shared hard disk, which in our algorithm is exploited to both completely avoid intranode communication with regard to a $\mathbf{b}_n$-vector coefficient gathering needed for the $\mathbf{Hb}_n$ step and to reduce disk space usage, but which may at the large scale give rise to non-negligible disk-access interference among the cores.

Since we make use of exactly the same load-balancing scheme in both varieties of allocating processors we are able

TABLE II. Timing tests (wall time) of single CPU calculations on two different system architectures (see text for more details) for test case **A** (445 250 936 determinants) and test case **B** (1 579 484 992 determinants).

	Time per iteration (s)—Linux cluster			Time per iteration (s)—IBM cluster		
Test case	Original code	New code	Efficiency	Original code	New code	Efficiency
A	15 508	14 280	1.09	31 740	18 711	1.70
B	65 224	58 177	1.12	⋯	⋯	

TABLE III. Parallel performance calculations on the ground state of H_2O for test case **A** (445 250 936 determinants) running on the IBM cluster. The measured timings are wall times exclusively.

NProc	$\mathbf{Hb}_n$ Computation (s)	Speedup	Time per iteration (s)	Speedup
1	10 550	1.00	18 711	1.00
4	2 851	3.70	5 036	3.72
8	1 843	5.72	3 639	5.14
16	819	12.88	2 358	7.94
32	525	20.10	1 881	9.95

to draw a direct comparison for the evaluation of a representative batch of $\boldsymbol{\sigma}$-*TTSS* blocks on a given CPU. The timing data for test cases **A** and **B** is compiled in Table IV. It should be noted that we have to introduce additional communication with the *four nodes with one core each* scheme in order to gather the required $\mathbf{b}_n$ coefficients on each core. However, this little extra work only takes about 150 s for test case **A** out of 2608 s to complete the entire $\mathbf{Hb}_n$ step. Comparing the columns labeled *one node with four cores* and *four nodes with one core each* clearly reveals differences in the time taken to read the required $\mathbf{b}_n$ coefficients into core memory and considerable discrepancies in the $\boldsymbol{\sigma}$-*TTSS* block computing time which mainly consists of all matrix-vector operations. There are basically two sources for the deviations: in the *four nodes with one core each* computing scheme no memory-access conflicts can hamper the matrix-vector operations and, in addition, the heavy disk I/O is implicitly "parallelized." This intrinsic "coarse-grain" disk I/O parallelization becomes even more pronounced for all subspace operations as illustrated by the overall speedup in Table V for test case **A** and, in particular, in Table VI for test case **B**. As an example, one may find an excellent total speedup for eight processors following an *eight nodes with one core on each* scheme (test case **B**) that even slightly increases from 7.36 for the $\mathbf{Hb}_n$ step to 7.73 for the complete iteration. In contrast, the overall speedup obtained with eight cores running on two nodes is reduced considerably from 4.31 ($\mathbf{Hb}_n$ step) to 2.74.

TABLE IV. Timing data for computing a typical batch of $\boldsymbol{\sigma}$-*TTSS* blocks for test cases **A** (445 250 936 determinants) and **B** (1 579 484 992 determinants) on a given CPU comparing different setups either using four cores on a single node or one core each on four nodes.

	One node with four cores Time spent (s)	Four nodes with one core each Time spent (s)
	Test case **A**	
READING $\mathbf{b}_n$ coefficient	45	3
Computing $\boldsymbol{\sigma}$ blocks	1399	953
Total batch time	1445	957
	Test case **B**	
	one node with four cores	four nodes with one core each
READING $\mathbf{b}_n$ coefficient	602	101
Computing $\boldsymbol{\sigma}$ blocks	2487	1572
Total batch time	3092	1674

TABLE V. Parallel performance calculations on the ground state of H_2O for test case **A** (445 250 936 determinants) running on the Linux cluster with four cores on each node, e.g., 32 processors=8(nodes)×4(cores). The measured timings are wall times exclusively.

NProc	$\mathbf{Hb}_n$ Computation (s)	Speedup	Time per iteration (s)	Speedup
1	10 114	1.00	14 250	1.00
2	5 273	1.92	10 303	1.38
2[a]	5 034	2.01	6 637	2.15
4	4 343	2.32	9 949	1.43
4[b]	2 608	3.88	3 299	4.32
8	2 293	4.41	4 602	3.10
8[c]	1 352	7.48	1 682	8.47
16	1 202	8.41	2 051	6.95
16[d]	713	14.19	941	15.14
32	740	13.67	1 025	13.90
64	524	19.30	633	22.51
128	292	34.64	345	41.30

[a]Calculation on two nodes using one core each.
[b]Calculation on four nodes using one core each.
[c]Calculation on eight nodes using one core each.
[d]Calculation on 16 nodes using one core each.

Finally, we should comment more explicitly on the speedups going from 4 to 128 processors for test cases **A** as well as for **B** within the *one node with four cores* scheme which are also listed in Tables V and VI. Starting from a speedup value of 1.43 for **A** and 1.09 for **B**, which may serve as a "reference," the speedup is nearly doubled by increasing the number of nodes by a factor of 2. Considering the performance enhancement for a large number of processors, for example, 128 processors in test case **B**, a full doubling is not accomplished anymore. In this case this is due to the fact that the time spent in the algorithm to gather the $\mathbf{b}_n$ coefficients among the node masters (see also Fig. 4) is in the same order of magnitude (725 s) as the time needed to compute the partial $\boldsymbol{\sigma}$ vector on each CPU (about 690 s). We thus reason that even though we optimized this step with respect to the use of two-sided communication MPI library functions, we may get

TABLE VI. Parallel performance on the ground state of H_2O for test case **B** (1 579 484 992 determinants) running on the Linux cluster with four cores on each node, e.g., 32 processors=8(nodes)×4(cores). The measured timings are wall times exclusively.

NProc	$\mathbf{Hb}_n$ computation (s)	Speedup	Time per iteration (s)	Speedup
1	42 888	1.00	58 177	1.00
2	24 295	1.77	45 660	1.27
2[a]	22 047	1.95	29 305	1.99
4	21 575	1.99	53 629	1.09
4[b]	11 264	3.81	15 041	3.88
8	9 950	4.31	21 220	2.74
8[c]	5 830	7.36	7 531	7.73
16	5 259	8.16	10 847	5.36
16[d]	3 238	13.25	4 104	14.18
32	2 809	15.26	5 110	11.39
64	1 745	24.58	2 586	22.50
128	1 368	31.35	1 691	34.40

[a]Calculation on two nodes using one core each.
[b]Calculation on four nodes using one core each.
[c]Calculation on eight nodes using one core each.
[d]Calculation on 16 nodes using one core each.

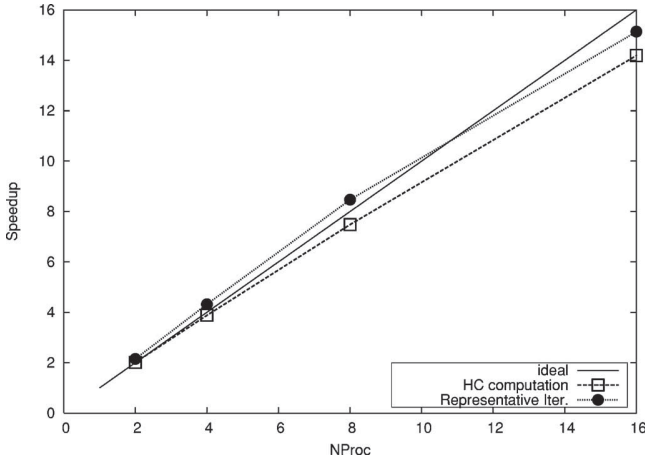

FIG. 5. Parallel performance of the parallel LUCITA code in a calculation on the ground state of H_2O running on a Linux cluster. The CI expansion spans 445 250 936 determinants.

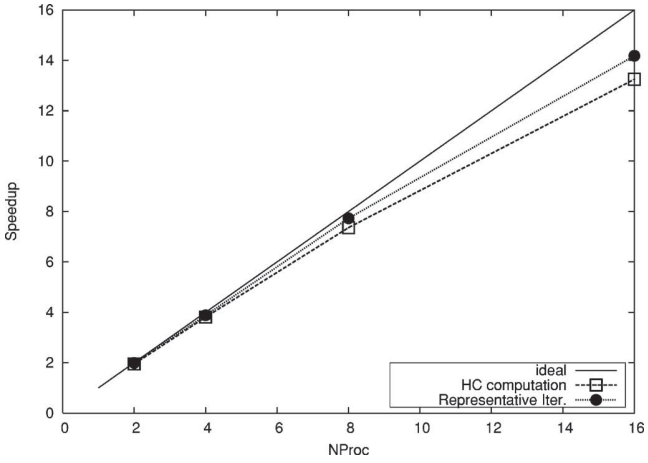

FIG. 6. Parallel performance of the parallel LUCITA code in a calculation on the ground state of H_2O running on a Linux cluster. The CI expansion spans 1 579 484 992 determinants.

close to the gigabit network performance limit of our cluster. At present, we are also investigating the implementation of one-sided communication routines which may help improve the parallel efficiency in the future. As a further remark on ongoing work, *TTSS* blocks of $\mathbf{b}_n$ may contain substantial amounts of coefficients which are of little importance (e.g., coefficients $<10^{-10}$) as discussed by others and thus allow for an effective vector screening as well as vector compressing. By keeping only $\mathbf{b}_n$ coefficients that are above a given threshold and using compression techniques for both $\mathbf{b}_n$ and $\boldsymbol{\sigma}_n$ based on the required numerical accuracy (e.g., $<10^{-14}$), we should benefit from a reduced I/O activity, in particular, in the I/O intense subspace operation parts of a generalized Davidson iteration. In doing so, we can expect a significant improvement for the parallel efficiency in case of both multicore systems and system architectures using a general parallel file system.

Taking all aspects of our extensive timing results into account, the good performance of the new parallel implementation presented here is underlined. We demonstrate the parallel efficiency on the Linux cluster for calculation types **A** (445 250 936 determinants) and **B** (1 579 484 992 determinants) in Figs. 5 and 6, respectively. For both test calculations an excellent parallel scaling is obtained. The speedup for each of the test cases on 16 nodes using a single core on each node is 15.1 and 14.2, respectively, for the large benchmark calculation. The lower speedup of the $\mathbf{Hb}_n$ step as compared to the entire generalized Davidson iteration (see Figs. 5 and 6) is explained by the inevitable increase in communication in the $\mathbf{Hb}_n$ step, since every core now collects its required $\mathbf{b}_n$ coefficients. In addition, the overall speedup notably benefits from the simultaneously "parallelized" I/O load in all subspace operations because each core has access to its own hard disk. The latter issue may, in particular, be the reason why a slightly superlinear speedup was observed when running test case **A** on up to eight processors.

III. APPLICATION TO THE $(Rb-Ba)^+$ MOLECULAR ION

Investigations on the collision kinetics of heavy ionic and neutral main-group atoms at ultracold temperatures ($\leqslant 1$ mK) is a field of growing interest in experimental physics. These studies aim at a profound understanding of the collision processes and products and ultimately at a controlled chemistry at the quantum level[37] and the possibility of testing fundamental symmetries in nature.[38,39] Current experiments involve translational sympathetic cooling of atomic ions by laser-cooled neutrals (Rb) for arbitrary atomic ions, e.g., Rb^+, Cs^+, Sr^+, or Na^+.[40] In particular, the collision kinetics and the short-range electronic potential energy curves (PEC) of the benchmark system $(Rb-Ba)^+$ are of great interest. This system has not been investigated theoretically before, as far as we know. It is valence isoelectronic with the $(Ca-Na)^+$ system which has been studied earlier.[41] Here, the lowest-lying electronic states are Σ states which are quite accurately described without spin-orbit interaction. The goal of our present study is to provide a survey of the short-range potentials for the lowest electronic states at a high level of accuracy with respect to the treatment of dynamic electron correlation.

A. Qualitative molecular electronic spectrum

In Table VII the atomic configurations and terms as well as their corresponding molecular states that are expected to form the lower part of the electronic spectrum are reported. These also include the Σ states correlated with the charge-exchange channel leading to ionized barium and neutral rubidium atoms. The presence of a Ba $4d$ shell close in energy to the valence-electronic $5s$ and $5p$ shells suggests an increased manifold of low-lying excited states with angular momentum projection greater than zero compared to the

TABLE VII. Molecular electronic states of $(Rb-Ba)^+$ in the $\Lambda-S$ coupling picture [Hund's case (a)] and associated atomic fragments.

Atomic configurations and states $^{(2S+1)}L_J$	Molecular $^{(2S+1)}\Lambda_\Omega$ states
$Rb^+_{5s^0}(^1S_0)+Ba_{6s^2}(^1S_0)$	$^1\Sigma^+_0$
$Rb_{5s^1}(^2S_{1/2})+Ba^+_{6s^1}(^2S_{1/2})$	$^3\Sigma^+_{1,0}$, $^1\Sigma^+_0$
$Rb^+_{5s^0}(^1S_0)+Ba_{6s^15d^1}(^3D_{3,2,1})$	$^3\Delta_{3,2,1}$, $^3\Pi_{2,1,0}$, $^+\Sigma^+_{1,0}$
$Rb^+_{5s^0}(^1S_0)+Ba_{6s^15d^1}(^1D_2)$	$^1\Delta_2$, $^1\Pi_1$, $^1\Sigma^+_0$

TABLE VIII. General active spaces (GASs) and occupation constraints for $(Rb-Ba)^+$ ground and excited states for both calculations MR(2in7)CISD18 and MR(2in6)CISD38 in C_{2v} symmetry. The minimum and maximum numbers of electrons are accumulated values, i.e., by adding the number of electrons in this and all preceeding GA spaces.

	Orbitals per irrepresentation				Minimum/maximum accumulated electrons		
GA space	A_1	B_1	B_2	A_2	Minimum electrons	Maximum electrons	Shell types
				MR(2in7)CISD18			
I	4	2	2	0	14	16	5*s*, 5*p* (Ba); 4 *s*, 4*p* (Rb)
II	4	1	1	1	16	18	6*s*, 5*d* (Ba); 5*s* (Rb)
III	20	20	20	6	16	18	virtuals
IV	26	10	10	7	18	18	virtuals
				MR(2in6)CISD38			
I	8	4	4	2	34	36	4*d*, 5 *s*, 5*p* (Ba); 3*d*, 4*s*, 4*p* (Rb)
II	3	1	1	1	36	38	6*s*, 5*d*[a] (Ba); 5*s* (Rb)
III	19	12	12	5	36	38	virtuals
IV	19	12	12	5	36	38	virtuals
V	19	12	12	6	38	38	virtuals

[a] $\sigma_{5d_{z^2}}$ was not included in the active space for technical reasons.

lighter valence-isoelectronic species $(Ca-Na)^+$. As these states are affected by spin-orbit interaction to first order in a perturbation theory sense and as barium is a heavy atom, the corresponding splittings and mixings are expected to be sizeable. Hence, we will restrict our study of the short-range electronic potentials to the ground state and a selected set of lowest-lying excited states.

B. Physical framework and basis sets

We have computed electronic adiabatic potential curves for a set of low-lying electronic states of $(Rb-Ba)^+$ using the spin-orbit free Dirac-Coulomb Hamiltonian. In this approach, the so-called "scalar-relativistic" effects are taken into account fully and spin-orbit interaction is neglected. The calculations have been performed in C_{2v} symmetry using the extensive uncontracted ANO-RCC basis set (from the MOLCAS6 package[42]) for both atoms Rb and Ba. These basis sets which are near quadruple zeta quality include $\{23s19p11d4f\}$ primitive Gaussian functions for Rb and $\{26s22p15d4f\}$ functions for Ba. Thus, all-electron calculations are performed which provide a higher accuracy for the short-range potentials than studies based on effective core potentials. In the correlated calculations the virtual space is truncated such that the energetically higher-lying virtual orbitals are discarded which is a standard procedure in relativistic calculations with uncontracted basis sets.[43] The truncation thresholds are chosen to lie in large energy gaps (3–10 a.u.) in the virtual space and at high values depending on the number of correlated electrons (details are given in the subsections below). It is therefore ensured that the truncation errors are negligibly small and that the potential energy curves are smooth, i.e., they do not suffer from discontinuities.

The initial set of starting orbitals for the correlated calculations was obtained from a spin-free all-electron Dirac-Coulomb Hartree-Fock (HF) calculation with an open-shell state averaging over all electronic configurations with two electrons distributed among seven orbitals (2in7). The resulting space is composed of the σ_{6s5s} (A_1 symmetry), $\sigma^*_{6s5s}(A_1)$, $\pi_{5d_{yz}}(B_2)$, $\pi_{5d_{xz}}(B_1)$, $\sigma_{5d_{x^2-y^2}}(A_1)$, $\delta_{5d_{xy}}(A_2)$, and $\sigma_{5d_{z^2}}(A_1)$ orbitals, which ensures a balanced description of ground and excited states with variable *s* and *d* occupations. All Hartree-Fock calculations converge very smoothly at the various internuclear distances.

C. Active space considerations

A proper description of bond formation and dissociation of the molecular system considering also charge-exchange processes necessitates a correlation treatment with a multireference space. The choices of generalized active spaces for the ensuing MR treatments are shown in Table VIII. Our first set of MRCI calculations includes 18 active electrons where the remaining electrons form a frozen core. The first active space (GAS I) is composed of the essentially atomic 5*s* and 5*p* orbitals of Ba and 4*s* and 4*p* orbitals of Rb (subvalence orbitals). The valence active space (GAS II) comprises the seven orbitals given above representing the state-averaging space at the uncorrelated HF level. All following active spaces contain the virtual orbitals. Because of the use of uncontracted basis sets we find a large number of core-localized orbitals with high energies. Since in this case we consider only valence and subvalence correlation we truncate the virtual space at 5 a.u. leaving 119 orbitals active. Accordingly, this level of calculation is dubbed MR(2in7)CISD18.

In a further step we enlarge the first active space (GAS I) by adding outer-core electrons from the 4*d* shell of Ba as well as the 3*d* shell of Rb. GAS I now contains 36 electrons. We consistently adapt the cutoff threshold for the virtual space to 10 a.u. (GAS III, GAS IV, and GAS V, respectively) leading to a secondary space comprised by 145 virtual orbitals. For computational reasons we use a slightly reduced valence active space (GAS II) for this investigation where the $\sigma_{5d_{z^2}}$ orbital is not included. This level of calculation is dubbed MR(2in6)CISD38.

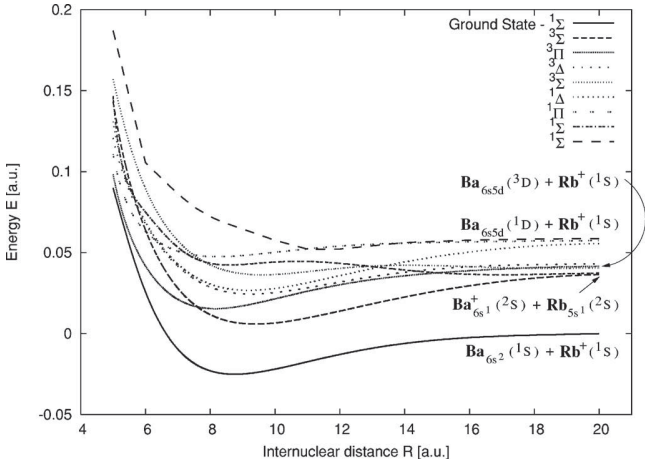

FIG. 7. Potential curves of the seven lowest-lying electronic molecular states of the $(Rb-Ba)^+$ molecular ion. Atomic dissociation channels for all states of various axial symmetry are shown. The computational level is MR(2in7)CISD18 (see text).

D. PECs of the lowest-lying molecular electronic states

1. Calculation of PECs including subvalence correlation

The following results have been obtained by multireference calculations using the CI space MR(2in7)CISD18. Table VIII displays how to benefit from the general active space concept in constructing suitable configuration spaces. The minimum electron occupation number stands for a maximum of two holes in the first active space (GAS I). Our valence space (GAS II) adds two electrons which are allowed to occupy all seven orbitals in accordance with the symmetry constraint. From the combined spaces I and II at most single and double excitations into the virtual space (GAS III and GAS IV, respectively) are allowed. We split the purely virtual space into two GA spaces in order to save computational resources (memory) since more and smaller *TTSS* blocks are obtained in this fashion. In addition to all single and double excitations, this excitation scheme also takes important quadruple excitations into account, i.e., we also allow for combined double excitations within orbitals in the valence space and from inner valence shells into virtual orbitals. This ensures a balanced correlation treatment of all considered electronic states and proper dissociation. We obtain a maximum expansion length of about 26.4×10^6 determinants in the A_1 symmetry representation.

In Fig. 7 we show the computed short-range potentials for the nine lowest electronic states of the ionic molecular system. We also show the correlation of the molecular states with corresponding atomic configurations at the dissociation limit. All curves have been obtained from single-point energy calculations in the range of internuclear distances from 5.0 to 20.0 Bohr. A polynomial fitting procedure is used to fit our potentials for all electronic states save for the highest $^1\Sigma^+$ state which yielded poor fits. Based on the fitted potentials spectral constants have been determined by solving a one-dimensional Schrödinger equation of nuclear motion. The spectroscopic constants for all nine states are compiled in Table IX. For a better comparison with our more extensive MR(2in6)CISD38 study we also report in Table IX state-specific spectroscopic data at the MR(2in6)CISD18 computational level. There is neither experimental nor other theoretical molecular data available at present.

The $(Rb-Ba)^+$ ion is found to form a weakly bound molecular system at an equilibrium bond length of 4.631 Å exhibiting a $X\,^1\Sigma^+$ ground state configuration. The first bounded excited state $a\,^3\Sigma^+$ resembles the state ordering obtained in the study of the valence-isoelectronic $(Ca-Na)^+$ system. This $a\,^3\Sigma^+$ state, however, crosses another weakly bound state $b\,^3\Pi$ at short internuclear distances. Two additional excited states of Δ symmetry (triplet and singlet) as well as a singlet $B\,^1\Pi$, two $^1\Sigma^+$, and another $d\,^3\Sigma^+$ state complete the picture of the lowest-lying molecular states of $(Rb-Ba)^+$. Our findings within the spin-free approach support the expectations arising from the qualitative molecular spectrum given in Table VII.

The results from the molecular calculations at the dissociation limit as indicated in Fig. 8 are in good agreement with available experimental atomic spectra of both atoms.[44] The computed quasimolecular atomic excitation energies are listed in Table X in comparison with the corresponding experimental values for the atomic excitation energies. Our cal-

TABLE IX. Spectroscopic constants for the ground and low-lying excited states of $(Rb-Ba)^+$.

	Method	$X\,^1\Sigma^+$	$a\,^3\Sigma^+$	$b\,^3\Pi$	$d\,^3\Delta$	$A\,^1\Delta$	$d\,^3\Sigma^+$	$B\,^1\Pi$	$C\,^1\Sigma^+$	$D\,^1\Sigma^+$
R_e (Å)	MR(2in7)CISD18	4.631	4.970	4.315	4.904	4.858	5.077	4.362	⋯	⋯
	MR(2in6)CISD18	4.662	4.943	4.323	4.861	4.861		4.467	⋯	
	MR(2in6)CISD38	4.684	4.964						⋯	
ω_e (cm^{-1})	MR(2in7)CISD18	54.3	46.2	55.7	44.6	46.2	39.6	39.4	⋯	⋯
	MR(2in6)CISD18	55.1	47.9	55.4	44.4	46.5		36.1	⋯	
	MR(2in6)CISD38	55.2	48.0						⋯	
T_e (eV)	MR(2in7)CISD18		0.843	1.102	1.347	1.410	1.671	1.975	⋯	⋯
	MR(2in6)CISD18		0.844	1.095	1.336	1.398		1.972	⋯	
	MR(2in6)CISD38		0.844						⋯	
T_v (eV)	MR(2in7)CISD18		0.871	1.127	1.363	1.421	1.709	1.985	1.839	2.486
	MR(2in6)CISD18		0.864	1.123	1.349	1.407		1.977	2.054	
	MR(2in6)CISD38		0.864						2.133	

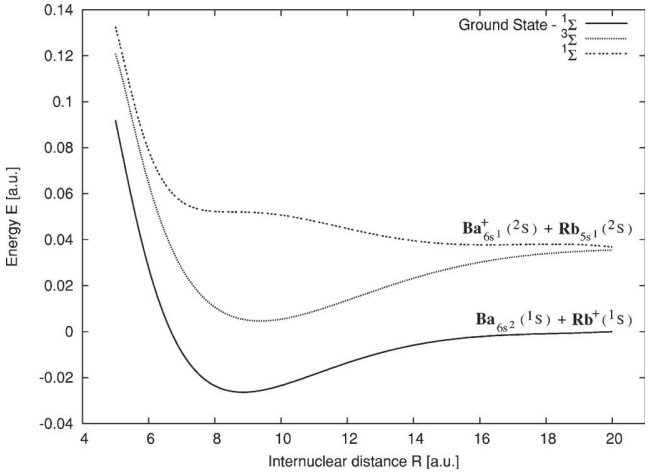

FIG. 8. Potential curves for selected Σ states of the $(Rb-Ba)^+$ molecular ion. Atomic dissociation channels for the molecular states are indicated. The computational level is MR(2in6)CISD38 (see text).

culated value of 9109 cm^{-1} for the Ba_{6s5d} configuration (^3D) is in very good agreement with the experimental value of 9216 cm^{-1} [deduced from the ^3D ($J=2$) term at the center of the Landé intervals].[45] The computed excitation energy for the Ba ^1D term is about 1200 cm^{-1} too high in energy. Because of the neglect of spin-orbit coupling we do not allow an obviously important coupling between the ^1D term and the ^3P terms arising from a $6s6p$ configuration in the Ba atom. At the full four-component MRCI computational level we expect the ^1D term to shift towards lower energy due to the mixing with the $J=2$ component of the close-lying ^3P state. Furthermore, the explicit treatment of spin-orbit interaction will give rise to a first-order splitting of all electronic states with $\Lambda>0$ and, in particular, states with equal Ω components, e.g., $^3\Delta_2$ and $^3\Pi_2$, will mix considerably due to their energetic vicinity. This could result in a breakdown of the $\Lambda-S$ coupling picture. Thus, it is mandatory to further extend the investigation of the lowest-lying electronic states of $(Rb-Ba)^+$ to a rigorous treatment of spin-orbit interaction and electron correlation which is the focus of an ongoing study.[46]

2. Investigation of the lowest Σ states including core-core and core-valence correlation

In addition to our comprehensive survey of the short-range potentials for the nine lowest-lying electronic states of $(Rb-Ba)^+$ in the spin-free approach we carried out more extensive calculations to determine the short-range potentials of the three lowest molecular electronic states of axial Σ symmetry. The goal of these high-level computations was to study, in particular, the influence of explicit core-core and core-valence correlation on the shape of the potentials and the resulting spectroscopic constants. Within the MR(2in6)CISD38 excitation scheme (lower part of Table VIII) we generate an expansion length of about 145×10^6 determinants with 38 electrons correlated.

The fitted potential energy curves are depicted in Fig. 8, and the available spectroscopic constants are listed in Table IX. The curves closely resemble those obtained at the MR(2in7)CISD18 level but with a slightly increased ground-state equilibrium bond length of 4.684 Å. Beside a small decrease of R_e for the $a\ ^3\Sigma^+$ state amounting to only 0.006 Å, the inclusion of core-core and core-valence correlation also yields slightly higher values of the harmonic frequency ω_e for both states $X\ ^1\Sigma^+$ and $a\ ^3\Sigma^+$. Particularly important for ultracold molecular experiments are the vertical and adiabatic excitation energies (see Table X). The inclusion of outer-core correlation is seen to lead only to very small corrections here. A full configuration averaging in the valence space plays a greater role in the calculation of excitation energies here than an extension of the correlated shells into the atomic cores. We therefore consider this initial assessment of the electronic structure of $(Rb-Ba)^+$ as a valuable guideline for further theoretical and experimental studies.

IV. SUMMARY AND PROSPECTS

We have reported the parallel implementation of a large-scale configuration interaction electronic-structure program applicable with any nonrelativistic or "scalar"-relativistic Hamiltonian operator. The implementation is based on the flexible general active space (GAS) concept, allowing calculations spanning from configuration interaction singles (CIS) to FCI. The parallel implementation is based on a string-driven GAS algorithm, and the use of an efficient static load-balancing strategy has been discussed and implemented. We have put particular emphasis on central features of any parallel large-scale CI implementation, which are input/output activity, memory demand, and communication costs. Key aspects of the employed message passing model are discussed with respect to various modern computer architectures.

Extensive parallel performance studies of the new code were carried out on a massively parallel architecture (IBM pSeries machine) as well as on a Linux cluster equipped with multicore nodes. A satisfactory scaling performance is achieved on the IBM machine while high computational performance can be reached on the Linux cluster. We thus significantly improve the applicability of parallel large-scale CI

TABLE X. Comparison of computed quasimolecular with experimental atomic excitation energies at the dissociation limit of $(Rb-Ba)^+$. Values are given in cm^{-1}.

Dissociation channel	MR(2in7)CISD18	MR(2in6)CISD18	MR(2in6)CISD38	Experiment
$Ba^+_{6s^1}(^2S)+Rb_{5s^1}(^2S)$	8 006	8 116	8065	8 824[a]
$Ba_{6s^15d^1}(^3D)+Rb^+_{5s^0}(^1S)$	9 109	9 222	9223	9 216[b]
$Ba_{6s^15d^1}(^1D)+Rb^+_{5s^0}(^1S)$	12 604	12 724		11 395

[a]Value obtained from ΔIP(Ba,Rb) (Ref. 45).
[b]^3D ($J=2$) (Ref. 44).

calculations in the nonrelativistic regime as well as the spin-free Dirac formalism, exploiting the full power of modern computer architectures.

As an initial application of our new parallel code we present for the first time a comprehensive study of the nine lowest-lying electronic short-range potentials of the $(Rb-Ba)^+$ molecule ion, which hardly would have been feasible in an acceptable time frame with a serial code. We find a $^1\Sigma^+$ molecular ground state with a Rb–Ba bond length of $R_e=4.631$ Å at the MR(2in7)CISD18 computational level. Moreover, we obtain an excellent agreement between our calculated atomic configurations and the available corresponding experimental atomic spectra of each atom at the dissociation limit. In a benchmark study of the lower Σ states where 38 electrons are correlated we find only minute changes of spectral constants as compared to the calculations where only 18 electrons are correlated (valence and subvalence correlation).

We are proceeding with work on improving the parallel efficiency. The implementation of one-sided communication routines to possibly reduce the communication costs as well as a suited vector compressing scheme are expected to be advantageous. Furthermore, we are extending the parallelization work to a four-component relativistic direct Kramers-restricted (KR)-MCSCF/GASCI/FCI program system[26,27,47,48] where spin-orbit interaction is included. In our forthcoming publication[46] the fully relativistic potential energy curves of $(Rb-Ba)^+$ will be presented including a rigorous and simultaneous treatment of electron correlation and spin-orbit coupling, shedding further light on the lower part of the electronic spectrum in this weakly bound molecular system. The first-order splittings and second-order mixings of the Δ and Π electronic states will be of particular importance here. Moreover, the knowledge gained in the course of the present studies will be exploited in investigations of other "ultracold" molecular species with similar electronic structures such as $(Rb-Cs)^+$ and RbYb which are studied in ongoing collision experiments in the ultracold regime.

ACKNOWLEDGMENTS

This work has received support from the Sixth Framework Programme Marie Curie Research Training Network "NANOQUANT" under Contract No. MRTN-CT-2003-506842 and the Danish Natural Science Resarch Council Grant No. 272-05-0469. S.K. and T.F. also thank the Collaborative Research Center SFB663 in Düsseldorf for financial support and the University of Southern Denmark (Odense) for hospitality. A generous allotment of computing time from the Danish Center for Scientific Computing and a grant for computing time at the John von Neumann Institute for Scientific Computing (NIC), Forschungszentrum Jülich (Germany), are gratefully acknowledged.

[1] Z. Gan, Y. Alexeev, M. S. Gordon, and R. A. Kendall, J. Chem. Phys. **119**, 47 (2003).
[2] H. Dachsel, H. Lischka, R. Shepard, J. Nieplocha, and R. J. Harrison, J. Comput. Chem. **18**, 430 (1997).
[3] H. Dachsel, R. J. Harrison, and D. A. Dixon, J. Phys. Chem. A **103**, 152 (1999).
[4] A. J. Dobbyn, P. J. Knowles, and R. J. Harrison, J. Comput. Chem. **19**, 1215 (1998).
[5] M. Klene, M. A. Robb, M. J. Frisch, and P. Celani, J. Chem. Phys. **113**, 5653 (2000).
[6] B. Suo, G. Zhai, Y. Wang, Z. Wen, X. Hu, and L. Li, J. Comput. Chem. **26**, 88 (2005).
[7] K. Tanaka, Y. Mochizuki, T. Ishikawa, H. Terashima, and H. Tokiwa, Theor. Chim. Acta **117**, 397 (2007).
[8] R. Ansaloni, G. L. Bendazzoli, S. Evangelisti, and E. Rossi, Comput. Phys. Commun. **128**, 496 (2000).
[9] P. J. Knowles and N. C. Handy, Chem. Phys. Lett. **111**, 315 (1984).
[10] J. Olsen, B. O. Roos, P. Jørgensen, and H. J. Aa. Jensen, J. Chem. Phys. **89**, 2185 (1988).
[11] J. Olsen, P. Jørgensen, and J. Simons, Chem. Phys. Lett. **169**, 463 (1990).
[12] S. Zarrabian, C. R. Sarma, and J. Paldus, Chem. Phys. Lett. **155**, 183 (1989).
[13] T. Fleig and L. Visscher, Chem. Phys. **311**, 113 (2005).
[14] A. Ostendorf, C. B. Zhang, M. A. Wilson, D. Offenberg, B. Roth, and S. Schiller, Phys. Rev. Lett. **97**, 243005 (2006).
[15] B. Roth, A. Ostendorf, H. Wenz, and S. Schiller, J. Phys. B **38**, 3673 (2005).
[16] LUCIA, a general CI and CC code written by J. Olsen, University of Aarhus.
[17] J. Olsen, J. Chem. Phys. **113**, 7140 (2000).
[18] "DIRAC, a relativistic *ab initio* electronic structure program, developer version," written by H. J. Aa. Jensen, T. Saue, and L. Visscher with contributions from V. Bakken, E. Eliav, T. Enevoldsen, T. Fleig, O. Fossgaard, T. Helgaker, J. Laerdahl, C. V. Larsen, P. Norman, J. Olsen, M. Pernpointner, J. K. Pedersen, K. Ruud, P. Salek, J. N. P. van Stralen, J. Thyssen, O. Visser, and T. Winther (http://dirac.chem.sdu.dk).
[19] K. G. Dyall, J. Chem. Phys. **100**, 2118 (1994).
[20] J. M. Lévy-Leblond, Commun. Math. Phys. **6**, 286 (1967).
[21] M. Iliaš, H. J. Aa. Jensen, V. Kellö, B. O. Roos, and M. Urban, Chem. Phys. Lett. **408**, 210 (2005).
[22] M. Iliaš and T. Saue, J. Chem. Phys. **126**, 064102 (2007).
[23] H. J. Aa. Jensen and M. Iliaš (unpublished).
[24] B. Roos, *Ab initio Methods in Quantum Chemistry-II*, edited by K. P. Lawley (Wiley, New York, 1987), p. 399.
[25] T. Fleig, J. Olsen, and L. Visscher, J. Chem. Phys. **119**, 2963 (2003).
[26] T. Fleig, J. Olsen, and C. M. Marian, J. Chem. Phys. **114**, 4775 (2001).
[27] T. Fleig, H. J. Aa. Jensen, J. Olsen, and L. Visscher, J. Chem. Phys. **124**, 104106 (2006).
[28] T. Fleig, L. K. Sørensen, and J. Olsen, Theor. Chem. Acc. **118**, 347 (2007).
[29] E. R. Davidson, J. Comput. Phys. **17**, 87 (1975).
[30] N. C. Handy, Chem. Phys. Lett. **74**, 280 (1980).
[31] E. Gabriel, G. E. Fagg, G. Bosilca, T. Angskun, J. J. Dongarra, J. M. Squyres, V. Sahay, P. Kambadur, B. Barrett, A. Lumsdaine, R. H. Castain, D. J. Daniel, R. L. Graham, and T. S. Woodall, *Proceedings of the 11th European PVM/MPI Users' Group Meeting*, Budapest, Hungary, September 2004, pp. 97–104.
[32] W. Gropp, *Proceedings of the Ninth European PVM/MPI Users' Group Meeting on Recent Advances in Parallel Virtual Machine and Message Passing Interface*, London, UK, 2002 (Springer-Verlag, Berlin, 2002), p. 7.
[33] *Linda, User's guide & Reference Manual*, Version 3.0, Scientific Computing Associates 1995.
[34] T. H. Dunning, Jr., J. Chem. Phys. **90**, 1007 (1989).
[35] Juelich Multiprocessor (JUMP), Jülich Supercomputing Centre, Forschungszentrum Jülich GmbH.
[36] Horseshoe, Super Computer of the Danish Center for Scientific Computing at the University of Southern Denmark.
[37] J. Doyle, B. Friedrich, R. V. Krems, and F. Masnou-Seeuws, Eur. Phys. J. D **31**, 149 (2004).
[38] J. J. Hudson, B. E. Sauer, M. R. Tarbutt, and E. A. Hinds, Phys. Rev. Lett. **89**, 023003 (2002).
[39] B. C. Regan, E. D. Commins, C. J. Schmidt, and D. DeMille, Phys. Rev. Lett. **88**, 071805 (2002).
[40] S. Schiller (Düsseldorf) (private communication).
[41] O. P. Makarov, R. Côté, H. Michels, and W. W. Smith, Phys. Rev. A **67**, 042705 (2003).
[42] G. Karlström, R. Lindh, P.-Å. Malmqvist, B. O. Roos, U. Ryde, V. Veryazov, P.-O. Widmark, M. Cossi, B. Schimmelpfennig, P. Neogrády and L. Seijo, Comput. Mater. Sci. **28**, 222 (2003).

[43] L. Visscher, in *Relativistic Electronic Structure Theory*, edited by P. Schwerdtfeger, (Elsevier, Amsterdam, 2002), Vol. 1, Chap. 6, p. 291.
[44] Yu. Ralchenko, F.-C. Jou, D. E. Kelleher, A. E. Kramida, A. Musgrove, J. Reader, W. L. Wiese, and K. Olsen, *NIST Atomic Spectra Database* (version 3.1.1) National Institute of Standards and Technology, Gaithersburg, MD, 2007.
[45] *NIST Chemistry WebBook* (version 69, 2005) National Institute of Standards and Technology, Gaithersburg, MD.
[46] S. Knecht, H. J. Aa. Jensen, and T. Fleig (unpublished).
[47] J. Thyssen, H. J. Aa. Jensen, and T. Fleig, "A direct relativistic four-component multi-configuration self-consistent-field method for molecules," J. Chem. Phys. (submitted).
[48] H. J. Aa. Jensen, K. G. Dyall, T. Saue, and K. Fægri, J. Chem. Phys. **104**, 4083 (1996).
[49] Required time for a representative generalized Davidson iteration for test case **B** is beyond the 24 h queue limit on this supercomputer.

Paper 2

Stefan Knecht, Hans Jørgen Aagaard Jensen, and Timo Fleig

Large-scale parallel configuration interaction. II. Two- and four-component double-group general active space implementation with application to BiH.

submitted to J. Chem. Phys..

Large-Scale Parallel Configuration Interaction. II. Two- and Four-Component Double-Group General Active Space Implementation with Application to BiH

Stefan Knecht*

Department of Theoretical Chemistry,

Heinrich Heine University Düsseldorf,

Universitätsstraße 1, D-40225 Düsseldorf, Germany

Hans Jørgen Aa. Jensen†

Department of Physics and Chemistry,

University of Southern Denmark,

DK-5230 Odense M, Denmark

Timo Fleig‡

Laboratoire de Chimie et Physique Quantiques,

I.R.S.A.M.C., Université Paul Sabatier, Toulouse III,

route de Narbonne 118, 31062 Toulouse Cedex 04, France

(Dated: September 21, 2009)

Abstract

We present a parallel implementation of a large-scale relativistic double-group configuration interaction (CI) program. It is applicable with a large variety of two- and four-component Hamiltonians. The parallel algorithm is based on a distributed data model in combination with a static load balancing scheme. The excellent scalability of our parallelization scheme is demonstrated in large-scale four-component multi-reference CI (MRCI) benchmark tests on various modern computer architectures, and we also discuss hardware-dependent aspects with respect to possible speedup limitations. As an illustration of the potential of our new parallel code, we have calculated spectroscopic properties for the BiH molecule at various excitation levels using extensive basis sets. We focus in particular on an accurate description of the splitting of the ground state and the first excited state which is caused by spin-orbit coupling. Our largest parallel MRCI calculation thereby comprised an expansion length of 2.7×10^9 Slater determinants.

PACS numbers: 31.15.ae, 31.15.aj, 31.15.am, 31.15.vn, 33.15.Dj, 31.15.ag

Keywords: Configuration Interaction, Relativistic Quantum Chemistry, Parallel Algorithm, Four-Component, Spin-Orbit Coupling, Diatomics, Excited States

*Electronic address: stefan@theochem.uni-duesseldorf.de

†Electronic address: hjj@ifk.sdu.dk

‡Electronic address: timo.fleig@irsamc.ups-tlse.fr

Contents

I. INTRODUCTION

An accurate description of the electronic structure and properties of atoms or molecules containing heavy elements generally requires an adequate description of both electron correlation and relativistic effects [1]. Due to the reduction of non-relativistic (spin and spatial) symmetries caused by magnetic couplings - the most important of which is the spin-orbit interaction - it becomes significantly more difficult to devise electron correlation methods accounting for these effects in an efficient manner. Moreover, accurate electronic-structure methods for heavy-element systems face two major problems: Many electrons per atom have to be correlated, and often a large number of valence electrons are unpaired. Efficient multi-reference approaches of general applicability are therefore required. The relativistic configuration interaction (CI) method meets the requirement of general applicability, since wave function expansions representing any open-shell or multi-reference problem are straightforwardly accessible [2]. The question of efficiency plays a key role for the advance of CI-based methods in the heavy-element regime and comprises the central motivation for the work presented here.

Many wave-function based approaches to heavy-element electronic structure do not treat spin-orbit coupling *a priori* but include it at a later stage of the calculation, see e.g. [3–7]. These approaches are based on assumptions of additivity of electron correlation and spin-orbit effects to a larger or smaller degree, or a weak polarization of orbitals due to spin-orbit interaction, or both. Whereas this is often reasonable, many cases are known where the application of more rigorous methods becomes imperative, e.g. [8, 9]. Our strategy is to approach the electronic-structure problem in heavy elements by commencing in a more rigorous fashion, i.e. not to separate spin-orbit coupling at all from orbital optimization or

electron correlation treatments. This comes with the price of having to deal with complex two-component (2c) or 4c orbitals and with rather large matrix eigenvalue problems in general [10] - very often hundreds of millions or several billions of Slater determinants - and a complex-valued formalism when molecular symmetry is low [11]. For such rigorous approaches, we must strive for a large-scale implementation which necessitates an efficient parallelization for modern computer architectures.

In this paper we report a new parallel implementation of the relativistic string-driven double group multi-reference configuration interaction (MRCI) and full configuration interaction (FCI) method `LUCIAREL` [10, 12, 13] that is available in a local version of the `DIRAC08` program package [14]. It represents the continuation of our parallelization work on non-relativistic large-scale electron correlation methods. In Ref. 15 we discussed in detail the linear-transformation driven parallel implementation of a string-based non-relativistic and scalar-relativistic MRCI and FCI method [16–18] which is available in the release version of the `DIRAC08` program package [14]. Some of the key features of this parallel implementation, including the static load balancing model which we found to yield very good performance on various system architectures, are also exploited in the present work. One would expect that this performance is even surpassed in the present (fully) relativistic case: Since the Hamiltonian matrix is less sparse when spin-orbit coupling is included, the parallelism of the linear-transformation step becomes more dominant than in the non-relativistic case.

In addition to comprehensive performance tests on the electronic ground state of the bismuth monohydride molecule, we will consider a systematic theoretical determination of the ground state spin-orbit splitting which is experimentally well-known. Since our MRCI study represents to the best of our knowledge the first work on the ground-state splitting of BiH where spin-orbit coupling and electron correlation are treated on the same footing, we

will compare our results to previous theoretical studies where spin-orbit effects are introduced *a posteriori* in various approaches.

The paper is organized as follows: In Section II we give a short review of the string-driven CI algorithm on which our parallel implementation is based. In this context, we discuss essential consequences for our parallel algorithm resulting from a fully relativistic double group framework which had not to be taken into consideration in our previous non-relativistic and scalar-relativistic implementation. We then describe the details of our parallelization scheme with regard to the sigma-vector generation, followed by performance studies of the new parallel code for large-scale test applications to the BiH molecule where strengths and weaknesses of the parallel algorithms are examined in more detail. The third section comprises the results of our study of the ground state and lowest excited state (in the relativistic picture) of bismuth monohydride. We finally give a summary of our work and draw conclusions for future work.

II. PARALLEL RELATIVISTIC CONFIGURATION INTERACTION IMPLEMENTATION

The parallel CI implementation presented in this paper is based on the relativistic double group CI program `LUCIAREL` [10, 12, 13] that is available in a local version of the `DIRAC08` program package [14]. In the following subsections we give a brief overview of the relativistic CI technique as implemented in `LUCIAREL` and focus in more detail on key aspects of our parallel algorithm with respect to essential parts of the CI optimization scheme. The section concludes with a discussion of the parallel performance in large-scale benchmark studies for two of the most common computer architectures.

A. Relativistic Configuration Interaction Theory

The relativistic double group program LUCIAREL fully exploits the advantages of a genuine string-based implementation where explicit comparisons of configurations in the determination of coupling coefficients are avoided. This guarantees efficiency even when higher-order excitations are taken into account. In non- or scalar-relativistic CI a determinant is the product of an α-string and a β-string, and has a specific M_S value [16]. In our relativistic implementation, the two strings are replaced by a $\mathcal{P}$-string of j Kramers spinors $\{\varphi_I\}$ and a $\bar{\mathcal{Q}}$-string of $N-j$ Kramers (time-reversal) partners $\{\varphi_{\bar{I}}\}$:

$$\begin{aligned} \hat{\mathcal{P}}^\dagger|vac> &= \hat{a}^\dagger_{P_1}\hat{a}^\dagger_{P_2}\ldots\hat{a}^\dagger_{P_j}|vac> \\ \hat{\bar{\mathcal{Q}}}^\dagger|vac> &= \hat{a}^\dagger_{\bar{Q}_1}\hat{a}^\dagger_{\bar{Q}_2}\ldots\hat{a}^\dagger_{\bar{Q}_{N-j}}|vac>, \end{aligned} \tag{1}$$

where N is the total number of electrons. A general Slater determinant $|\mathcal{P}\bar{\mathcal{Q}}\rangle$ can then be written in terms of these strings according to

$$|\mathcal{P}\bar{\mathcal{Q}}\rangle = \hat{\mathcal{P}}^\dagger\hat{\bar{\mathcal{Q}}}^\dagger|vac> . \tag{2}$$

Next, we may introduce an auxiliary bookkeeping number M_K (Kramers projection value),

$$M_K = \frac{n_{\text{unbarred}} - n_{\text{barred}}}{2} = \frac{j-(N-j)}{2} = j - N/2. \tag{3}$$

This implies that all possible determinants which may be built from an initial set of Kramers pairs can be arranged in individual subsets each with a characteristic M_K value. It should be noted that M_K is *not* a quantum number, not even when used with a scalar-relativistic Hamiltonian (for example, in the double group C_2^* the unbarred (fermion symmetry E_1) spinorbitals of a symmetry would have α-spin while the unbarred (fermion symmetry E_1) spinorbitals of b symmetry would have β-spin) [19]. One can of course choose to decouple the spatial and spin symmetries as done in non-relativistic codes, and then choose $M_K = M_S$.

The central part of any direct CI algorithm is the computation of the linear transformation of the current trial vector $\mathbf{b}_n$

$$\boldsymbol{\sigma}_n \;=\; \mathbf{H}\mathbf{b}_n, \tag{4}$$

where in this case $\mathbf{H}$ is the CI Hamiltonian matrix calculated with the relativistic Hamiltonian [12, 20]

$$\begin{aligned}\hat{H} \;=\; & \sum_{IJ}\left[h_{IJ}\hat{X}^{+}_{IJ} + \frac{1}{2}\left(h_{\bar{I}J}\hat{X}^{+}_{\bar{I}J} + h_{I\bar{J}}\hat{X}^{+}_{I\bar{J}}\right)\right] \\ & + \frac{1}{2}\sum_{KLMN}\left[(KL|MN)\,\hat{x}^{++}_{KLMN} + \left(\bar{K}L|MN\right)\hat{x}^{++}_{\bar{K}LMN} + \left(K\bar{L}|MN\right)\hat{x}^{++}_{K\bar{L}MN}\right] \\ & + \frac{1}{4}\sum_{KLMN}\left(\bar{K}L|M\bar{N}\right)\hat{x}^{++}_{\bar{K}LM\bar{N}} \\ & + \frac{1}{8}\sum_{KLMN}\left[\left(\bar{K}L|\bar{M}N\right)\hat{x}^{++}_{\bar{K}L\bar{M}N} + \left(K\bar{L}|M\bar{N}\right)\hat{x}^{++}_{K\bar{L}M\bar{N}}\right],\end{aligned} \tag{5}$$

expressed in terms of Kramers-paired spinors. Note that each term in the Hamiltonian only contributes for a specific ΔM_K value, either -2, -1, 0, +1, or +2.

To illustrate the computation of the linear transformation in Eq. (4), consider the part of the relativistic Hamiltonian given in Eq. (5) that changes the M_K-value by a single unit $\Delta M_K = +1$:

$$\hat{H}_{\Delta M_K=+1} = \sum_{IJ}\frac{1}{2}h_{I\bar{J}}\hat{X}^{+}_{I\bar{J}} + \sum_{KLMN}\frac{1}{2}\left(K\bar{L}|MN\right)\hat{x}^{++}_{K\bar{L}MN}. \tag{6}$$

Taking only the first term (given in bold face) for the Kramers replacement operator

$$\hat{x}^{++}_{K\bar{L}MN} = \mathbf{\hat{a}^{\dagger}_{K}\hat{a}^{\dagger}_{M}\hat{a}_{N}\hat{a}_{\bar{L}}} - \hat{a}^{\dagger}_{L}\hat{a}^{\dagger}_{M}\hat{a}_{N}\hat{a}_{\bar{K}} + \hat{a}^{\dagger}_{K}\hat{a}^{\dagger}_{\bar{N}}\hat{a}_{\bar{M}}\hat{a}_{\bar{L}} - \hat{a}^{\dagger}_{L}\hat{a}^{\dagger}_{\bar{N}}\hat{a}_{\bar{M}}\hat{a}_{\bar{K}}, \tag{7}$$

into consideration, the real part of this sigma-vector fragment (real r; imaginary $\imath$) reads as

$$\sigma_{\Delta M_K=+1}r(\mathcal{P}\bar{\mathcal{Q}}) = \sum_{KLMN}\sum_{\mathcal{R}\bar{\mathcal{S}}}\left\{\left(K\bar{L}|MN\right)^{r}A^{\mathcal{P}\bar{\mathcal{Q}},\mathcal{R}\bar{\mathcal{S}}}_{K\bar{L}MN}b^{r}_{\mathcal{R}\bar{\mathcal{S}}} + \left(K\bar{L}|MN\right)^{\imath}A^{\mathcal{P}\bar{\mathcal{Q}},\mathcal{R}\bar{\mathcal{S}}}_{K\bar{L}MN}b^{\imath}_{\mathcal{R}\bar{\mathcal{S}}}\right\} \tag{8}$$

where $A^{\mathcal{P}\bar{\mathcal{Q}},\mathcal{R}\bar{\mathcal{S}}}_{K\bar{L}MN} = \langle\mathcal{P}\bar{\mathcal{Q}}|\hat{a}^{\dagger}_{K}\hat{a}^{\dagger}_{M}\hat{a}_{N}\hat{a}_{\bar{L}}|\mathcal{R}\bar{\mathcal{S}}\rangle$ is the coupling coefficient for the complex integral $\left(K\bar{L}|MN\right)$ between the Slater determinants $|\mathcal{P}\bar{\mathcal{Q}}\rangle$ and $|\mathcal{R}\bar{\mathcal{S}}\rangle$. It is contracted with the complex CI expansion coefficient $b_{\mathcal{R}\bar{\mathcal{S}}}$ for this particular determinant and the integral.

The definition of orbital spaces in LUCIAREL takes advantage of the concept of general active spaces (GAS) [12]. The wave function may be specified by an arbitrary number of active orbital spaces with arbitrary electron occupation constraints thus providing maximum flexibility for the envisaged electronic-structure problem. The GAS partitioning is, furthermore, exploited to create an implicit blocking of the Slater determinants that are included in the CI expansion. In addition to its M_K value, any determinant $|\Phi_\nu\rangle = |\mathcal{P}_\nu \bar{\mathcal{Q}}_\nu\rangle$ can also be classified according to the occupation type (T) in the various active orbital spaces and point group symmetry (S) of its creator string for the occupied unbarred Kramers spinors $\hat{\mathcal{P}}^\dagger$ and the corresponding creator string for the occupied barred Kramers spinors $\hat{\bar{\mathcal{Q}}}^\dagger$. A given block of determinants of the complete CI vector is thus characterized by the occupation types and symmetries of its unbarred and barred string components, and the Kramers projection M_K. In analogy to our preceding scalar-relativistic parallel CI implementation [15] we refer to such a group of determinants as (occupation)-type-(occupation)-type-symmetry-symmetry (*TTSS*) block. This block partitioning is the same for both the sigma vector $\boldsymbol{\sigma}_n$ and the current trial vector $\mathbf{b}_n$, as the Hamiltonian and thus the CI-matrix $\mathbf{H}$ in Eq. (4) are totally symmetric. The *TTSS* blocking is used in the algorithm to skip all the coupling coefficients which are zero because the type-type of the $\boldsymbol{\sigma}_n$-block differ by more than two electrons from the type-type of the $\mathbf{b}_n$-block or because the two blocks have different symmetries. Because of this feature, these *TTSS*-blocks also form efficient building blocks for the static load balancing scheme, to be discussed in the next subsection.

Furthermore, the Dirac program package provides a large variety of two- [21] and four-component Hamiltonians which may be used with the new parallel LUCIAREL MRCI module. In the application section we use both the four-component Dirac-Coulomb Hamiltonian and the exact two-component Hamiltonian (X2C) scheme of Ilias and Saue [22, 23] where

two-electron spin same-orbit (SSO) and spin-other orbit (SOO) contributions are included via atomic mean-field integrals generated with the AMFI [24–26] code. An orthonormal molecular Kramers-paired spinor basis upon which the CI is set up can then typically be obtained from either a closed-shell or open-shell Hartree-Fock, KR-MCSCF [27] or MP2 natural spinor calculation [28].

As noted above, our relativistic MRCI implementation operates within the framework of double point group symmetry. This is essential for a consistent treatment of spin-dependent many-electron problems as neither M_S nor S^2 are good quantum numbers when spin-orbit coupling is included. For this purpose, the real-valued matrix double groups D_{2h}^*, C_{2v}^* and D_2^*, and the complex-valued matrix double groups C_{2h}^*, C_2^* and C_s^* are available for molecular calculations with the present parallel `LUCIAREL` program version. Since full linear symmetry is not implemented, we have written a parallel general-purpose CI module [29] which allows us to compute the expectation value for any one-electron operator. By using this module for the $\hat{j}_z$ operator defined as

$$\hat{j}_z \;=\; \hat{s}_z + \hat{l}_z, \tag{9}$$

it is easily possible to determine the Ω quantum number for any given electronic state at the cost of an additional sigma vector calculation where, however, only one-electron terms need to be taken into account.

B. Parallel implementation

In this section we consider characteristic features of our new parallel implementation of the relativistic MRCI code `LUCIAREL` that uses Olsen's generalized version [17] of Davidson's original iterative optimization algorithm [30]. For a detailed description of our fundamental

parallelization idea, which is also applied in the present work, the reader is referred to Ref. [15].

As the most used computer architectures for scientific computing change every few years (one example: single core → dual core → quad core → etc.), it has been a major design goal for us that the algorithm must be flexible and adaptable, such that it will be able to run efficiently on all the most used computer architectures. We have achieved this design goal by using a dual-level structure. The typical computer architecture fits into the template n nodes with m cores, where a node is defined as a (sub)system with shared memory and shared disks. Typically the bandwidth for "internode" communication is much slower than for "intranode" communication. A parallel calculation with, say, 32 tasks on a true shared memory machine would then correspond to $n = 1, m = 32$, while the same job on a Linux cluster with quad cores would correspond to $n = 8, m = 4$.

For the communication tasks we use MPI, because it is general, generally available, and under active development. In contrast to the parallel implementation described in Ref. [15] the parallelization algorithm sketched in the following also takes advantage of some of the new functionalities for one-sided communication in the MPI 2.1 message passing interface [31]. This strategy does not only allow for completely retaining the efficiency of the sequential precursor method (for a given process) but, in addition, facilitates further algorithmic improvements in the future.

1. General Considerations

The central idea of the algorithm is that in order to minimize time-consuming communication tasks, each core p is statically assigned all coefficients related to a specific subset of all the Slater determinants, $\mathbf{b}_n(p)$ for all $\mathbf{b}_n$ vectors as well as $\boldsymbol{\sigma}_n(p)$ for all $\boldsymbol{\sigma}_n$ vectors.

Each generalized Davidson iteration, sketched in a flow chart diagram in Fig. 2, consists of two distinct parts each with different requirements. The parallelization of the computationally most demanding step, the $\boldsymbol{\sigma}_n$-vector step (black box in Fig. 2), will be discussed in more detail in Sec. II B 2. The second main part is comprised by the subspace operations such as the determination of the current residual (see Fig. 2). Two of the computationally most expensive subspace tasks are

$$\tilde{H}_{kl} = \boldsymbol{\sigma}_k^\dagger \mathbf{b}_l = \sum_p^{N_{proc}} \boldsymbol{\sigma}_k^\dagger(p)\mathbf{b}_l(p) = \sum_p^{N_{proc}} \tilde{H}_{kl}(p) \tag{10}$$

$$\tilde{S'}_{kn} = \mathbf{b}_k^\dagger \mathbf{b'}_n = \sum_p^{N_{proc}} \mathbf{b}_k^\dagger(p)\mathbf{b'}_n(p) = \sum_p^{N_{proc}} \tilde{S'}_{kn}(p) \tag{11}$$

which are needed, respectively, for the subspace eigenvalue problem and for the Gram-Schmidt orthogonalization of a new trial vector $\mathbf{b'}_n$ to previous trial vectors. Since the computations of $\tilde{H}_{kl}(p)$ and $\tilde{S'}_{kn}(p)$ can be carried out locally on each process, with this design no long vectors but only scalars as $\tilde{H}_{kl}(p)$ and $\tilde{S}_{kn}(p)$ need to be communicated for the subspace tasks by means of fast global reduction operations (MPI_allreduce). This is described in more detail in Ref. 15. The only real difference to the non- or scalar-relativistic case described there is that the vectors and scalars now generally are complex-valued.

Overall good load balancing is a major concern for any parallel implementation. Hence, particular care must be taken when choosing the parameters to control load balancing. For our parallel LUCIAREL implementation, the *TTSS* blocking of the vectors $\mathbf{b}_n$ and $\boldsymbol{\sigma}_n$ as introduced in Sec. II A plays an essential role for this. From the discussion above in this subsection it is clear that our design implies that we cannot use a *dynamic* load balancing; changing the assignments to each processor would require expensive shuffling of long vectors between processors. It is therefore essential for good performance to be able to predict well *a priori* the computational load for each *TTSS* block, in order to create a close to optimal

static block distribution as depicted in Fig. 1 by using the *TTSS* blocks as units. At the outset of a calculation each *TTSS* block of nonzero length is assigned to a specific process taking account of a block-"weight" criterion. This individual block-"weight" criterion is calculated from an estimation of the respective computational load in the dominating linear transformation step $(60 - 80\%)$ of a Davidson iteration and the number of determinants in a given *TTSS* block. Achieving an even "weight" distribution of the *TTSS* blocks among all processes is thus expected to ensure a decent static load balancing. We demonstrate the performance of this approach in Sec. II C on the basis of comprehensive parallel test simulations.

Moreover, we took advantage of the batching concept of *TTSS* blocks that was already introduced in the sequential algorithm. In this context, a batch is defined as the maximum sum of *TTSS* blocks that fits into memory. By means of batches of *TTSS* blocks large-scale computations become feasible even on a contemporary single-core CPU where limited hardware may otherwise prohibit a complete storage of two CI vector segments in core memory. For the parallel algorithm described here, the individual number of batches on a given process decreases significantly as the total number of processes increases. This reduction is achieved by explicitly setting the length of all *TTSS* blocks to zero that are not assigned to a given process. The total input/output (I/O) cost for each process is thereby greatly lowered, in particular for the subspace operations as these local steps are typically processed in terms of batches.

It is worthwhile to mention that as a natural consequence of our static *TTSS* block distribution the number of integrals that have to reside in core memory of a given process can also be minimized. We have exploited this feature in our new parallel algorithm since the total number of trivially nonzero integrals rapidly increases in a spinor-based approach

compared to a spinorbital-based implementation. In contrast to the latter approach two-electron integrals of the type $(K\bar{L}|MN)$ which are, *e.g.* present in the expression for the $\Delta M_K = +1$ contribution (see Eq. (6)), do not vanish for all point groups.

In order to make full use of individual particularities of various system architectures, e.g., (true) shared memory systems, communication, memory usage and I/O are organized in complete accordance with both the present process topology and the system resources. As today's standard compute clusters generally are equipped with n interconnected nodes consisting each of m CPU cores we have implemented a basic division of the global group of all processes (*MPI_COMM_WORLD*) into distinct communication subgroups, namely *intranode* and *internode*, as introduced in Ref. 15. A node master is then chosen for each set of m cores that will exclusively take care of the expensive communication in each linear transformation step of $\mathbf{b}_n$ blocks to all of the n nodes needing this *TTSS* block (see also Sec. II B 2). In addition, file sharing based on the established *intranode* group can be enabled among the m cores minimizing the internal I/O load. If, on the other hand, a global file system is provided it may be utilized for a full file-sharing model among all processes by use of MPI file-I/O techniques. A shareable file which contains all $\mathbf{b}_n$-*TTSS* blocks is of particular use in the $\boldsymbol{\sigma}_n$ vector computation since costly *internode* communication (see Sec. II B 2 for more details) can be avoided.

Since the m cores of a single node share core memory (but often not memory cache) one could also take into account shared-memory like access algorithms based on MPI-2 one-sided communication routines (MPI_get, MPI_accumulate) for memory demanding quantities such as the two-electron integrals and the required blocks of the $\mathbf{b}_n$ vector. To ensure in general high efficiency a passive target communication model (MPI_win_lock(MPI_lock_shared)) has been implemented as visualized by the one-directional arrows in Fig. 3. The usefulness of this

functionality will obviously depend strongly on a high memory bandwidth as well as cache performance per process. Preliminary benchmark tests where the two-electron integrals and $\mathbf{b}_n$ coefficients were kept in shared main memory basically did not reveal significant communication overhead on true shared-memory systems. On cache-based multi-core systems the additional costs have, however, been noticeable. More thorough test studies on the latter, today's most common system architecture, are required and are currently being carried out. They will be part of our forthcoming publication on a parallel KR-MCSCF implementation where we will employ a one-sided communication model.

2. Sigma-vector evaluation

We shall now elaborate on our basic idea for the parallel evaluation of a sigma vector $\boldsymbol{\sigma}_n$. In our preceding publication [15], we discussed at length various recent approaches [32–35] to an efficient parallelization scheme for the $\boldsymbol{\sigma}_n$ task and concluded on the superiority of a distributed data model in agreement with Gan *et al.* [33]. We will thus briefly outline the central aspects of our distributed data approach.

In Fig. 4, we sketch the calculation of a sigma-vector $\boldsymbol{\sigma}_n$ in the present `LUCIAREL` algorithm. Each segment, here a *TTSS* block, of the complete sigma vector $\boldsymbol{\sigma}_n$ is coupled through the Hamiltonian matrix (cf Eq. 8) to the same *TTSS* block of $\mathbf{b}_n$, but also to specific other $\mathbf{b}_n$-*TTSS* blocks. To compute a full sigma-vector *TTSS* block locally on its statically designated process (see Fig. 1) therefore necessitates for each process the collection of all those $\mathbf{b}_n$-*TTSS* blocks that couple to the $\boldsymbol{\sigma}_n$-*TTSS* blocks assigned to this process, prior to the actual "matrix × vector" contraction (code line 33 in Fig. 4). For this purpose, we introduce a global communication step among all node masters at the beginning of each sigma-vector evaluation (in red in on-line version of Fig. 4) where we make use of lists of

required $\mathbf{b}_n$-*TTSS* blocks for each partial *intranode* linear transformation. These `INTEGER` lists, which are of dimension [number of *TTSS* blocks] are constructed at the outset of the diagonalization procedure and kept in main memory.

The essential gathering step can efficiently be carried out using either a collective communication (MPI_bcast) or one-sided communication (MPI_get) approach, the latter of which is currently under development by us. The present collection algorithm is designed such that the *internode* communication is minimized. For example, the communication group consisting of all node masters is further split (MPI_comm_split) whenever a *TTSS* block is not required for the sigma-vector evaluation of a given *intranode* group. The actually communicated $\mathbf{b}_n$-*TTSS* blocks are stored for each *intranode* group in a shared coefficient file `BBLOCKS` that is accessible by all the individual processes on this node via MPI file-I/O routines.

A major advantage of this strategy is that we avoid costly global communication inside the sigma-vector loop structure (see Fig. 4). Global (blocking) communication would lead to an intrinsic barrier and therefore in general to idling times and considerable performance loss. Fig. 4 also displays our shared-memory like *intranode*-access strategy for the two-electron integrals. This approach aims at a further reduction of the total memory requirements for a given calculation type by avoiding redundant subsets of integrals within a node. We thereby exploit the splitting of the integral set into subsets with respect to T_H excitation types (see Fig. 4) which enables a block-wise access to the *intranode*-shared integral set.

Finally, note that the alternative algorithm where each process computes all $\boldsymbol{\sigma}_n$ contributions from *its* $\mathbf{b}_n$-*TTSS* blocks is inferior on at least two accounts. First, unless all active $\boldsymbol{\sigma}_n$-*TTSS* blocks fit into memory on all nodes, the $\boldsymbol{\sigma}_n$-*TTSS* blocks must be added up with an MPI_reduce at the end of each $\boldsymbol{\sigma}$-batch (after code line 39 in Fig. 4) which would become

a barrier and cause idling time. Second, because of the required addition, it cannot be done with the new efficient one-sided communication calls.

C. Parallel performance

In this section we discuss the performance of our new parallel `LUCIAREL` implementation on the basis of two representative large-scale test applications. The two performance test applications consist of one CI iteration from MRCI calculations on the ground state of the bismuth monohydride molecule (using C_{2v}^* double group symmetry) at the equilibrium distance of 1.805 Å [36], based on the four-component Dirac-Coulomb Hamiltonian, and using basis sets of triple-ζ quality for both atoms (see Sec. III for further details). The simplified GAS schemes for the test cases **A** and **B** are compiled in Table I; the CI expansion in case **A** spans approximately 238×10^6 determinants and in case **B** approximately 428×10^6 determinants. The number of non-vanishing *TTSS* blocks, which are the fundamental components of our even "weight" distribution scheme in the static load balancing model, adds up to 848 (**A**) and 1788 (**B**). The performance tests were run on two computer systems representing different system architectures. The first system is a Linux-based cluster made up of 200 nodes of two Intel Woodcrest (2.66 GHz; dual core version) processors each, equipped with either 4GB (160 nodes) or 8 Gbytes (40 nodes) of shared main memory and a dual Gigabit ethernet connection. Each node is provided with a local scratch disk and a connection to Gigabit switches for internode communication. The second system is an IBM p6 575 cluster of 14 symmetric multiprocessor (SMP) nodes with each node holding 32 simultaneous multithreaded (SMT) Power6 processors running at 4.7 GHz. Each node has a ten Gigabit ethernet access to a general parallel file system (GPFS) and is equipped with 128 Gbytes main memory. Moreover, the nodes are interconnected by an InfiniBand

connection for MPI communication.

The speedup $\mathcal{S}(p, N)$ of a representative generalized Davidson iteration is defined as

$$\mathcal{S}(p, N) = \frac{T(1, N)}{T(p, N)}, \tag{12}$$

where $T(p, N)$ is the time required to perform one CI iteration (Eq. (4)) of size N on p processes. On the basis of $\mathcal{S}(p, N)$ we compare in the following the performance of our parallel algorithm on the two system architectures. Tests were run on up to 128 processors and 1.75 Gbytes of core memory per processor.

In Tables II and III we present the timing and scaling results on the IBM Power6 cluster for test cases **A** and **B**. In these timing tables the wall times (measured in seconds) are compiled for the $\boldsymbol{\sigma}$-vector evaluation as well as for the corresponding complete generalized Davidson iteration. We obtain in both cases a very good speedup for up to 64 processors (on 2 nodes) for the $\boldsymbol{\sigma}$-vector step, namely 56.17 (**A**) and 62.38 (**B**) for 64 CPUs. As it is also illustrated for test case **B** in Fig. 5 we observe, however, a drop in the speedup with regard to a total iteration, in particular for a larger number of processors, that is 46.24 (case **A**, 64 CPUs) and 51.30 (case **B**, 64 CPUs), respectively. Following the line of argument of our preceding publication [15] on a parallel implementation of a non- and scalar-relativistic FCI/MRCI program, these findings may partly be ascribed to the increasing GPFS load, most notably in the Davidson subspace operation parts where large chunks of *TTSS* blocks are read in and written almost simultaneously by all processes. In this context, it is worthwhile to mention that compared to our earlier work, a new GPFS has been installed in the meantime which exhibits an improved performance. In Reference [15] we reported for the scalar-relativistic FCI/MRCI code a speedup of 9.95 on 32 CPUs whereas with the new GPFS we obtain for the same benchmark a considerably better speedup of 18.22.

Summarizing, the overall performance of our new `LUCIAREL` implementation using a static

load balancing scheme is very satisfactory on this system architecture, *i.e.*, we find a final speedup of 28.62 for the more demanding test case **B** running on 32 processors (on a single node).

We now focus on the performance and scalability of our parallel algorithm on a standard Linux cluster. The complete results of our test calculations are compiled in Table IV (test case **A**) and Table V (test case **B**). We report on two different strategies (on up to 16 processors) to perform the benchmark calculations on n nodes with m cores:

- *n nodes using* $m = 1$ *core on each node*
- *n nodes using* $m = 4$ *cores on each node*

These two distinct allocation schemes turned out to be useful to detect and further analyze possible bottlenecks in a parallel large-scale FCI/MRCI implementation [15]. For $m = 1$ and both test sets **A** or **B** we find an excellent scalability (depicted in Fig. 6) with regard to a total Davidson iteration running on two (speedup of 1.99 resp. 2.00), four (4.05 resp. 3.96), eight (7.95 resp. 7.85) and 16 processors (15.43 resp. 15.56). Contrary to *n nodes using* $m = 1$ *core on each node*, the overall picture changes for the *n nodes using* $m = 4$ *cores on each node* scheme as can be seen for example for benchmark case **B** in Table V. We still obtain a speedup of almost a factor of two each time the number of nodes is doubled when going from four (speedup of 2.58) to 32 CPUs ($19.52 = 7.57 \times 2.58$) which supports that our static load balancing scheme operates properly. However, for the largest number of CPUs tested, 128 CPUs, a full doubling is no longer obtained. Besides arising load balancing issues with idling times on the order of 10% of the $\boldsymbol{\sigma}$-vector computation time, we partly assign this behavior to an unfavorable $\boldsymbol{\sigma}$-vector computation to $\mathbf{b}_n$-blocks communication ratio of 303 s to 288 s in accordance with our previous findings [15]. A considerable performance enhancement is

therefore expected with an internode communication beyond a Gigabit Ethernet, *e.g.* an InfiniBand network, which will be fully available in the next generation of the cluster.

What about the unsatisfactory *intranode* speedup that we observe in going from two (speedup for test case **B**: 1.90) to four (2.58) processor cores on the same node but not in the corresponding *internode* case (*n nodes using* $m = 1$ *core on each node*; speedup of 2.00 and 3.96)? These findings can essentially be explained by two facts as we also concluded in our preceding work [15]. Although the parallel algorithm has been optimized for avoiding redundant I/O activity in the *intranode* case, the disk-access overhead introduced by the additional two processors leads, in particular at the large-scale, to non-negligible disk-access conflicts and, subsequently, to a performance loss. On the contrary, the *n nodes using* $m = 1$ *core on each node* scheme greatly benefits from the intrinsic coarse-grain disk I/O parallelization. Moreover, memory bandwidth saturation obviously gains influence on the scaling of parallel applications on multi-core systems. E.g., in the $\boldsymbol{\sigma}$-vector step, a large number of matrix-matrix multiplications ($\mathbf{H} \times \mathbf{b}_n$) is carried out by each process where the corresponding components, namely integrals and vector coefficients, are kept in core memory as their number by far exceeds the individual process cache size (in our case 2 Mbytes Level 2 cache). Memory access interferences then arise due to the shared physical access to the core memory among all processes.

It should be noted that this characteristic observation has recently been discussed for the parallel MRCI implementations by Tanaka *et al.* [35] and by Kleinschmidt and coworkers [37], and also for a parallel density matrix renormalization group program by Kurashige *et al.* [38]. In Ref. 37 the authors report interestingly an *intranode* study where the cores, that were not used in the MRCI benchmark, performed unrelated direct SCF calculations. In this case no significant deterioration of the parallel performance was observed. Furthermore, in recent

benchmark calculations running their parallel spin-orbit MRCI program [37] on a Linux cluster composed of AMD Opteron nodes ("Barcelona", 2× quadcore CPUs), Kleinschmidt *et al.* find a remarkably improved *intranode* performance yielding a speedup of up to 7.0 for eight processors [39] in comparison to a speedup of 2.86 on an Intel Xeon node ("Clovertown", 2× quadcore CPUs, value taken from Reference 37). A possible explanation for the observed discrepancy could be related to the different memory access models: on an Opteron node each processor is equipped with an individual, integrated memory controller to access the main memory. By contrast, on the mentioned type of Xeon node the memory access of all processors is organized externally on the chipset ("northbridge"). In ongoing work, we currently further investigate this issue with regard to the performance of *intranode* one-sided MPI communication.

By means of comprehensive timing results we have here demonstrated the excellent performance of our new parallel implementation of a relativistic FCI/MRCI program for two of the most wide-spread types of system architectures, based on the idea of a distributed data model combined with a static load balancing scheme. An almost perfect parallel scaling is found on the Linux cluster both for benchmark test set **A** (239 472 310 determinants) and **B** (428 014 958 determinants) as illustrated in Fig. 6 for the latter case. In addition, a reasonable speedup of 51.30 for 64 processors running test case **B** on the IBM p6 575 cluster (see also Fig. 5) underlines the proper functionality of our parallel algorithm on such high-performance computing architectures. Our timing results indicate that future optimization work should in particular focus on further improvements of the *intranode* performance on multi-core machines.

III. APPLICATION TO BISMUTH MONOHYDRIDE

The electronic and vibrational spectra of the bismuth monohydride (BiH) molecule have been studied extensively both by experiment [40–46] and theory [47–52] in the past. Here we turn our attention to a characteristic feature of the lower electronic spectrum of BiH, namely the spin-orbit splitting between the ground state and the first excited state. These two states are characterized by different occupations of the valence $\pi_{1/2}$ and $\pi_{3/2}$ Kramers pairs. An accurate description of the electronic structure of this molecule consequently necessitates a consistent treatment of both electron correlation and relativistic effects. The deviations of the previous calculations from the experimental splitting also suggest that spin-orbit interaction should be included in the Hartree-Fock step, which has not been the case in most of the earlier studies [47–50, 52] (the last study [51] was a 2c relativistic effective core potential study, but as the authors write themselves, with a too small basis set for accurate numbers).

The valence electronic configuration of the scalar-relativistic approximate $^3\Sigma^-$ ground state of BiH can be written in terms of scalar-relativistic orbitals as $\sigma^2\pi^2$. Because of the strong spin-orbit coupling the Λ-S coupling picture is less appropriate, and following Hund's coupling case (c) the $^3\Sigma^-$ state splits into two components: X 0^+ and A 1. The remarkably large separation of these two states amounts to $T_e = 4923$ cm^{-1}[53]. In the approximate $\lambda\omega$-projection notation the configurations of these states are given by $\sigma^2_{1/2}\pi^2_{1/2}\pi^0_{3/2}$ and $\sigma^2_{1/2}\pi^1_{1/2}\pi^1_{3/2}$ occupation patterns, respectively.

We have performed four-component MRCI calculations based on the Dirac-Coulomb Hamiltonian at various CI excitation levels where we aim at a precise theoretical determination of T_e as well as other spectroscopic data for X 0^+ and A 1. The results are

compared to previous theoretical work as well as to experimental measurements. The effect of the spin-other-orbit interaction has in addition been estimated by comparing with a two-component Hamiltonian (X2C) (see Sec. II A) which includes these terms in the atomic mean-field approximation [24–26].

A. Computational Details

All calculations were performed in C_{2v}^{*} double group symmetry. For Bi we used Dyall's triple-ζ and quadruple-ζ basis sets [54–56] in uncontracted form. We also included the listed valence- and core-correlating functions for the Bi $5d$, $6s$ and $6p$ shells. For hydrogen we employed Dunning's cc-pVTZ and cc-pVQZ basis sets [57] in uncontracted form.

Kramers-paired spinors for the subsequent MRCI correlation calculations were obtained from all-electron average-of-configuration (four- or two-component) Hartree-Fock (HF) calculations. An open-shell state-averaging over all electronic configurations with two electrons distributed among two Kramers pairs (2in2) ensures a balanced description of all electronic states arising from the $\pi_{1/2}\pi_{3/2}$ occupation manifold that includes the states of interest X 0^+ and A 1.

The GAS setups for the MRCI studies are discussed in the following section III B and compiled in Table VI. Two active space schemes were taken into consideration, both of restricted-active-space type with a maximum number of holes in GAS I, no restrictions in GAS II, and with a maximum number of holes in GAS III. Our notation follows the scheme "GAS I(GAS II)GAS III" and is most easily explained with an example: "SD10(6in5)MRSD" would mean max 2 holes in 5 Kramers pairs, a reference complete-active-space of 6 electrons in 5 Kramers pairs (plus of course excitations from GAS I and excitations to GAS III), and finally all possible singles and doubles excitations into the GAS III Kramers pairs from all the

reference configurations formed by the restrictions on GAS I and GAS II. In the first scheme the Bi $6s_{1/2}$, $\sigma_{1/2}$, $\pi_{1/2}$ and $\pi_{3/2}$ as well as the antibonding $\sigma^*_{1/2}$ were placed in a Complete-Active-Space (GAS II) yielding a distribution of six electrons in five Kramers pairs (6in5). Core-valence and core-core correlation were included by allowing up to two holes in the Bi $5d$ Kramers pairs (GAS I). Furthermore, singles and doubles as well as combined triples and quadruples excitations from the combined spaces GAS I and GAS II into the virtual spinor space make it possible to recover essential parts of dynamic correlation. In the correlation step we limited the active virtual spinor space (GAS III) to an energy threshold of 5 E_h and 18 E_h, respectively, which is a routinely performed procedure when uncontracted basis sets are used [9]. We have nevertheless tested the ensuing errors that may be introduced in the present case (see Sec. III B for more details).

The second active space scheme listed in Table VI was primarily chosen for benchmark and calibration purposes. It gives a reasonable description of the molecule only close to the equilibrium bond distance. The minimal second CAS-like GA space (GAS II) comprised the two Kramers pairs $\pi_{1/2}$ and $\pi_{3/2}$. Core-valence correlation was taken into account by allowing up to two holes in the Bi $6s_{1/2}$, $\sigma_{1/2}$ (SD4(2in2)MRSD) and, in addition, Bi $5d$ Kramers pairs (SD14(2in2)MRSD).

We have performed single-point energy calculations at various internuclear distances close to the experimentally known equilibrium both of the ground and the first excited state, as the main objective is a theoretical estimate of the X 0^+-A 1 spin-orbit splitting. A polynomial fitting procedure was used to fit the electronic potentials. Spectral constants were determined by solving a one-dimensional Schrödinger equation of nuclear motion based on the fitted potentials. The resulting spectroscopic constants for both states, X 0^+ and A 1, are compiled in Table VII.

B. Spectroscopic constants for the X 0^+ and A 1 states

We begin our discussion with the large-core SD4(2in2)MRSD calculations where the Bi $5d$ Kramers pairs were kept in the frozen core, *i.e.*, always remaining doubly occupied. At this computational level the determined equilibrium distance (R_e) and harmonic frequency (ω_e) using a triple-ζ basis set (TZ) are in good agreement with the respective quadruple-ζ (QZ) values. In comparison with experiment these calculations tend to slightly overestimate R_e by up to 0.09 Å and ω_e by 20-80 cm^{-1}. Using the smaller TZ basis set, the adiabatic excitation energy T_e for the spin-orbit split X 0^+ and A 1 states is, on the other hand, underestimated by more than 300 cm^{-1} with regard to the experimental data. In the following we investigate in more detail various contributions that may improve our theoretical predictions, in particular for T_e.

As a first step we added the ten $5d$ outer-core electrons to the correlation treatment (SD14(2in2)MRSD computational scheme). In both cases, TZ and QZ, the explicit correlation of the $5d$ Kramers pairs leads to a significant bond contraction of about 0.03-0.04 Å. The effect on T_e is inconsistent. The spin-orbit splitting decreases with the TZ basis set while it increases with the QZ set. This reverse effect may partially be explained with a too low energy threshold for the deletion of virtual spinors: Raising the cutoff limit to energies higher than 18 E_h effectively yields a considerable correction for T_e of $\approx$ 100 cm^{-1}. The effects on bond length and harmonic frequency are, however, comparatively small. With the QZ set, on the other hand, vertical ($T_v^{1.805}$) and adiabatic excitation energies increase at the higher cutoff threshold in general only slightly by 34-60 cm^{-1} and 29-47 cm^{-1}, respectively. Summarizing, the differences in particular for the excitation energies reveal that with the triple-ζ basis sets and the lower truncation threshold one does not yet come close enough to

basis set saturation for the Bi $5d$ shell. We have confirmed this by analyzing the functions and their correlating character included in the respective virtual spaces.

We also examined the effect of higher excitations (SD14(2in2)MRSDTQ). At this level up to four particles in GAS III are taken into consideration which in particular allows for important quadruple excitations with respect to the reference space. These higher-order contributions have a great effect on T_e, yielding an increase of 166 cm^{-1} for the TZ basis. Since we have not been able to compute T_e for the QZ set at this level due to limited computational resources, we instead compare the vertical excitation energy $T_v^{1.805} = 4923$ cm^{-1} with its corresponding value of $T_v^{1.805} = 4723$ cm^{-1} at the SD14(2in2)MRSD level. The substantial increase of $T_v^{1.805}$ points to the importance of higher excitations for an adequate description both of the shape and relative position of the respective electronic potentials wells.

Let us now consider the larger (6in5) active-space calculations that by definition include some of the higher excitations mentioned above. In these large-space calculations (S10(6in5)MRSD and SD10(6in5)MRSD; high cutoff threshold of 18 E_h) deviations from the experimental data are significantly reduced to 0.008 - 0.015 Å and $\approx$ 20 cm^{-1} for the bond length and harmonic frequency, respectively. We thereby find a considerably large bond elongation of up to 0.02 Å (TZ basis) compared to the previously discussed (2in2) model. Likewise, the computed spin-orbit splitting $X\ 0^+$ - $A\ 1$ increases by about 50-80 cm^{-1} for both basis sets. Taking the SD10(6in5)MRSD/QZ calculation as a reference we get as close as $\approx$ 143 cm^{-1} to the experimental value of 4923.2 cm^{-1} [53] for the spin-orbit splitting. A direct comparison of our S10(6in5)MRSD/QZ with the SD10(6in5)MRSD/QZ results furthermore indicates that core-valence correlation (S10(6in5)MRSD) accounts for the largest corrections to all spectroscopic constants (R_e, ω_e and T_e) determined from the

corresponding valence CI (SD4(2in2)MRSD/QZ) calculation.

Finally, we comment in more detail on how our present results compare to earlier theoretical studies on BiH. At the SD10(6in5)MRSD/TZ and SD10(6in5)MRSD/QZ levels (high cutoff threshold of 18 E_h each), our computed bond lengths and harmonic frequencies for the ground- X 0^+ and first excited state A 1 are in good agreement with the corresponding data reported by Stoll *et al.* [52]. They used relativistic energy-consistent pseudopotentials in a combined two-component MRCIS/one-component CCSD(T) approach to compute the spectroscopic constants. Our present calculations achieve this in a rigorous "one-step" manner where electron correlation and relativistic effects are treated on the same footing. Our new MRCI data clearly outperform those from other previous theoretical works [48–50] as can be seen from Table VII.

In these studies in particular the theoretical prediction of the spin-orbit splitting suffered from a distinct underestimation. Alekseyev *et al.* [49] calculated a splitting of 4303 cm^{-1} using a spin-orbit MRCISD method based on spin orbitals. In their approach spin-orbit effects are introduced *a posteriori* in a perturbative fashion. In the relativistic two-component MRCIS calculations of Stoll *et al.* [52] spin-free state shifts obtained from one-component CCSD(T) calculations are added to the reference space. They report values for the splitting with deviations in the range of 300-600 cm^{-1} from the experimental value of 4923 cm^{-1} [53] where the respective magnitude of the splitting varies substantially with the number of state shifts added.

Comparing with these earlier studies our computed spin-orbit splitting of 4780 cm^{-1} represents the best theoretical estimate. As shown by our benchmark SD14(2in2)MRSDTQ calculations, we may expect the splitting to increase through the inclusion of higher excitations. On the other hand, taking into account spin-other orbit effects will give a negative

contribution on the order of ca. 60 cm^{-1} to the $X\ 0^+$ - $A\ 1$ splitting as can be estimated from our X2C-Gaunt SD14(2in2)MRSD calculations. To summarize, a consistent theoretical prediction of the experimentally known splitting between the $X\ 0^+$ and $A\ 1$ states of BiH necessitates an extensive and simultaneous treatment of electron correlation and relativistic effects.

In this context, it is worthwhile to mention that Sørensen and co-workers [58] calculated in a very recent work ground-state spectroscopic constants for BiH using a four-component multi-reference coupled cluster (CC) ansatz. As they use the identical TZ basis with a slightly higher energy cutoff for the virtual spinor space of 27 E_h we can compare to our computed data. They obtain a bond length of $R_e = 1.8030$ Å and a harmonic frequency of $\omega_e = 1694.599\ cm^{-1}$ at the CCSD(T) level correlating 16 electrons. Their findings agree very well with our (high cutoff threshold) SD10(6in5)MRSD/TZ and SD10(6in5)MRSD/QZ results, confirming the good quality of our present MRCI calculations.

IV. SUMMARY AND PROSPECTS

In this paper we present the parallel implementation of the relativistic large-scale configuration interaction program `LUCIAREL`. It is general in the sense that it is applicable with any one-, two-, or four-component Hamiltonian available in the `DIRAC08` program package [14] and also any Hamiltonian added to the program in the future. The implementation takes advantage of the general active space (GAS) concept for the definition of excitation schemes, thereby allowing calculations from configuration interaction singles up to Full CI. We have outlined central aspects of our parallel implementation based on a static load balancing scheme integrated in a distributed data model.

The performance of the new parallel code has been evaluated in extensive benchmark

studies on two different system architectures: a massively parallel IBM p6 system and a standard Linux-based cluster. An excellent parallel performance is achieved on both systems with up to 16 processors. A good scaling is also found on the IBM system for a larger number of CPUs. With the present work we have therefore substantially extended the applicability of parallel relativistic four- and two-component large-scale CI calculations on modern computer architectures.

The new parallel multireference CI (MRCI) program has been employed in a study of the ground and first excited states of the bismuth monohydride molecule, $X\ 0^+$ and $A\ 1$. The investigation includes an assessment of basis set dependencies as well as correlation and relativistic effects on the spectroscopic constants of the two states. We demonstrate the applicability of our new parallel code by means of employing reasonably large basis sets in connection with specially tailored active spaces. The computed bond lengths and harmonic frequencies are in good agreement with available experimental and theoretical data. The spin-orbit splitting between the ground- and excited state is underestimated by $\approx 140\ \mathrm{cm}^{-1}$. Nevertheless, our value is at present, to the best of our knowledge, the most accurate theoretical estimate.

As the completion of our parallelization work for configuration interaction we currently work on a complete parallel implementation of the recently presented four-component Kramers-restricted multiconfiguration self-consistent-field (KR-MCSCF) module [20, 27]. In this ongoing work, we exploit in particular the close resemblance of $\boldsymbol{\sigma}$-vector and one- and two-particle density computations within the excitation class formalism implemented in `LUCIAREL`. In addition, a thorough investigation of the performance of, properly leveraged, one-sided communication routines will be included with regard to the parallel efficiency of our completed parallel MRCI/KR-MCSCF program package. Furthermore, we work at

present on an appropriate vector compressing scheme following the idea of Ansaloni *et al.* [59]. A suitable packing procedure is expected to yield an effective reduction of the disk load in large-scale applications.

Acknowledgments

The authors are grateful to Dr. Martin Kleinschmidt for providing his parallel performance MRCI results on an AMD Opteron cluster. SK wishes to thank Lasse Kragh Sørensen for providing his four-component multi-reference coupled cluster results for BiH prior to publication as well as very stimulating discussions. Financial support (SK) of this project by the Deutsche Forschungsgemeinschaft (reference number FL 256/5-1) is gratefully acknowledged. SK and TF also thank the University of Southern Denmark (Odense) for hospitality. A generous allotment of computing time from the Danish Center for Scientific Computing and a grant for computing time at the John von Neumann Institute for Scientific Computing (NIC), Forschungszentrum Jülich (Germany), are gratefully acknowledged. We also thank the Zentrum für Informations- und Medientechnologie (ZIM) at the Heinrich Heine University Düsseldorf (Germany) for providing computation time.

TABLE I: General Active Spaces (GAS) and occupation constraints for BiH ground state calculations in C_{2v}^* double-group symmetry (applied subgroup: C_2^*) using uncontracted triple-ζ type of basis sets (see text). The minimum and maximum number of electrons are accumulated values, *i.e.*, by adding the number of electrons in this and all preceding GA spaces. The active spaces for these benchmark studies have not been constructed according to physical arguments but to mimic typical realistic large-scale calculations.

Parallel Performance Calculations A

GA Space	Kramers pairs per irrep	Min./max. accum. el.		
	$E_{1/2}$	Min. el.	Max. el.	Shell types
I	5	8	10	$5d$
II	6	14	16	$6s_{1/2}$, $\sigma_{1/2}$, $\sigma^*_{1/2}$; $\pi_{1/2}$, $\pi_{3/2}$ + 1 virt.
III	69	16	16	virtual Kramers pairs

Parallel Performance Calculations B

GA Space	Kramers pairs per irrep	Min./max. accum. el.		
	$E_{1/2}$	Min. el.	Max. el.	Shell types
I	6	10	12	$5d$, $6s_{1/2}$
II	4	13	16	$\sigma_{1/2}$, $\sigma^*_{1/2}$; $\pi_{1/2}$, $\pi_{3/2}$
III	54	16	16	virtual Kramers pairs

TABLE II: Parallel performance calculations (test case **A**) on the ground state of BiH (239 472 310 determinants) running on the IBM AIX-Power6 cluster with 32 SMT on each SMP node. The measured timings are wall times exclusively.

NProc	$\mathbf{H}\,\mathbf{b}_n$ computation [s]	*speedup*	Time per iteration [s]	*speedup*
1	17636	*1.00*	17940	*1.00*
2	8496	*2.08*	8773	*2.05*
4	4320	*4.08*	4608	*3.89*
8	2186	*8.06*	2354	*7.62*
16	1128	*15.63*	1217	*14.74*
32	554	*31.83*	659	*27.22*
64	314	*56.17*	388	*46.24*

TABLE III: Parallel performance calculations (test case **B**) on the ground state of BiH (428 014 958 determinants) running on the IBM AIX-Power6 cluster with 32 SMT on each SMP node. The measured timings are wall times exclusively.

NProc	$\mathbf{H}\,\mathbf{b}_n$ computation [s]	*speedup*	Time per iteration [s]	*speedup*
1	42105	*1.00*	43099	*1.00*
2	21087	*2.00*	21940	*1.96*
4	10924	*3.85*	11264	*3.83*
8	5309	*7.93*	5566	*7.74*
16	2713	*15.52*	2848	*15.13*
32	1385	*30.40*	1506	*28.62*
64	675	*62.38*	840	*51.30*

TABLE IV: Parallel performance calculations (test case **A**) on the ground state of BiH (239 472 310 determinants) running on the Linux cluster with 4 cores on each node, *e.g.* 32 processors = 8 (nodes) × 4 (cores). The measured timings are wall times exclusively.

NProc	$\mathbf{H}\,\mathbf{b}_n$ computation [s]	*speedup*	Time per iteration [s]	*speedup*
1	19050	*1.00*	19914	*1.00*
2	9683	*1.97*	11011	*1.81*
2[a]	9578	*1.99*	9997	*1.99*
4	6595	*2.89*	8069	*2.47*
4[b]	4850	*3.93*	4922	*4.05*
8	3529	*5.40*	4057	*4.91*
8[c]	2486	*7.66*	2504	*7.95*
16	1836	*10.38*	2040	*9.77*
16[d]	1283	*14.85*	1291	*15.43*
32	934	*20.40*	1038	*19.19*
64	549	*34.70*	609	*32.70*
128	323	*58.98*	378	*52.68*

[a] calculation on 2 nodes using one core on each node.

[b] calculation on 4 nodes using one core on each node.

[c] calculation on 8 nodes using one core on each node.

[d] calculation on 16 nodes using one core on each node.

TABLE V: Parallel performance calculations (test case **B**) on the ground state of BiH (428 014 958 determinants) running on the Linux cluster with 4 cores on each node, *e.g.* 32 processors = 8 (nodes) × 4 (cores). The measured timings are wall times exclusively.

NProc	$\mathbf{H}\,\mathbf{b}_n$ computation [s]	*speedup*	Time per iteration [s]	*speedup*
1	39683	*1.00*	40820	*1.00*
2	19864	*2.00*	21541	*1.90*
2[a]	19821	*2.00*	20366	*2.00*
4	14010	*2.83*	15834	*2.58*
4[b]	10143	*3.91*	10322	*3.96*
8	7126	*5.67*	7970	*5.12*
8[c]	5084	*7.81*	5198	*7.85*
16	3723	*10.66*	4013	*10.17*
16[d]	2595	*15.29*	2623	*15.56*
32	1940	*20.46*	2091	*19.52*
64	1266	*31.35*	1299	*31.42*
128	748	*53.05*	843	*48.42*

[a] calculation on 2 nodes using one core on each node.

[b] calculation on 4 nodes using one core on each node.

[c] calculation on 8 nodes using one core on each node.

[d] calculation on 16 nodes using one core on each node.

TABLE VI: General Active Spaces (GAS) and occupation constraints for BiH ground- and excited-state calculations in C_{2v}^* double-group symmetry (applied subgroup: C_2^*) using uncontracted triple-ζ and quadruple-ζ type of basis sets (see text), respectively. The minimum and maximum number of electrons are accumulated values, *i.e.*, by adding the number of electrons in this and all preceding GA spaces.

(6in5)MRCI Calculations

GA Space	Kramers pairs per irrep	Min./max. accum. el.		
	$E_{1/2}$	Min. el.	Max. el.	Shell types
I	5	8[a]	10	$5d$
II	5	14	16	$6s_{1/2}$, $\sigma_{1/2}$, $\pi_{1/2}$, $\pi_{3/2}$, $\sigma^*_{1/2}$
III	X[b,c]	16	16	virtual Kramers pairs

(2in2)MRCI Calculations

GA Space	Kramers pairs per irrep	Min./max. accum. el.		
	$E_{1/2}$	Min. el.	Max. el.	Shell types
I	7	12	14	$5d^d$, $6s_{1/2}$, $\sigma_{1/2}$
II	2	14[e]	16	$\pi_{1/2}$, $\pi_{3/2}$
III	X[b,c]	16	16	$\sigma^*_{1/2}$, virtual Kramers pairs

[a] in all S10(6in5)MRSD calculations the minimum accumulated number of electrons in this GA space is nine.

[b] triple-ζ basis set combination: X = 55 (5 E_h threshold) and 81 (18 E_h threshold).

[c] quadruple-ζ basis set combination: X = 96 (5 E_h threshold) and 154 (18 E_h threshold).

[d] the $5d$ Kramers pairs are always doubly occupied in the (2in2)MRSD computations.

[e] in all SD14(2in2)MRSDTQ calculations the minimum accumulated number of electrons in this GA space is 12.

TABLE VII: Spectral constants for $^{209}Bi^{1}H$ - ground and excited states from the present MRCI study in comparison with previous theoretical calculations and experimental data. For details on the basis sets and excitation schemes used in the computations the reader is referred to the text.

Active	Method/basis set	$X\ 0^+$		$A\ 1$		$T_v^{1.805}$ [cm^{-1}]	T_e [cm^{-1}]
electrons		R_e [Å]	ω_e [cm^{-1}]	R_e [Å]	ω_e [cm^{-1}]		
	This work:						
6	SD4(2in2)MRSD/TZ	1.8172	1713.104	1.8038	1752.954	4585	4591
6	SD4(2in2)MRSD/QZ	1.8199	1707.807	1.8061	1748.966	4646	4655
16	SD14(2in2)MRSD/TZ	1.7763	1803.138	1.7628	1853.459	4514	4467
16	SD14(2in2)MRSD/QZ	1.7893	1782.391	1.7744	1835.804	4723	4689
16	X2C-G SD14(2in2)MRSD/TZ[a]	1.7763	1804.416	1.7631	1854.025	4454	4407
16	SD14(2in2)MRSD/aTZ[b]	1.7770	1797.993	1.7633	1849.860	4519	4472
16	SD14(2in2)MRSD/TZ[c]	1.7815	1805.579	1.7672	1858.660	4611	4568
16	SD14(2in2)MRSD/QZ[c]	1.7800	1817.967	1.7653	1873.410	4750	4702
16	SD14(2in2)MRSDTQ/TZ	1.7773	1795.835	1.7629	1850.283	4683	4633
16	SD14(2in2)MRSDTQ/QZ					4923	
16	SD10(6in5)MRSD/TZ	1.7942	1706.301	1.7810	1746.107	4530	4509
16	SD10(6in5)MRSD/TZ[c]	1.8011	1700.410	1.7871	1741.892	4631	4617
16	S10(6in5)MRSD/QZ	1.7980	1662.823	1.7832	1706.307	4791	4773
16	SD10(6in5)MRSD/QZ	1.8013	1665.429	1.7855	1713.253	4777	4761
16	S10(6in5)MRSD/QZ[c]	1.7877	1688.046	1.7730	1733.506	4851	4820
16	SD10(6in5)MRSD/QZ[c]	1.7903	1701.469	1.7747	1753.848	4811	4780
	Previous work:						
16	CCSD(T) (TZ) [58]	1.8030	1694.599				
24/6	CCSD(T)/MRCIS [52]	1.800	1716	1.790	1741		4328
6	CISD [48]	1.90	1619				
6	MRD-CI [49]	1.867	1632	1.854	1618		4303
6	SICCI [50]	1.868	1584				
	experiment [53]	1.809	1698.9	1.788	1734.4		4923.2
	experiment [36]	1.805	1636	1.791	1669		4917

[a] Exact-Two-Component Hamiltonian including Gaunt corrections.

[b] augmented basis sets for Bi and H have been applied in these calculations.

[c] a higher cutoff in the virtual space of 18 E_h has been used.

Figure captions

Figure 1: Static *TTSS*-block assignment among all available processes as the central parallelization pattern. Each number corresponds to a unique process contained in the global group of all processes *MPI_COMM_WORLD*. The process holding the real *TTSS* block also treats the corresponding non-zero imaginary part if applicable (complex matrix double groups).

Figure 2: Iterative generalized Davidson diagonalization method flow chart as implemented in `LUCIAREL`.

Figure 3: Shared-memory access pattern for memory demanding quantities. Each number corresponds to a unique process that is contained in each *intra-node* group.

Figure 4: Pseudo-code visualization of the evaluation of the linear transformation $\boldsymbol{\sigma}_n = \mathbf{H}\,\mathbf{b}_n$, as implemented in `LUCIAREL`. All global communications are in red in the on-line version.

Figure 5: Parallel performance of the parallel `LUCIAREL` code in a calculation on the ground state of BiH running on an IBM p6 575 cluster. The CI expansion spans 428 014 958 determinants.

Figure 6: Parallel performance of the parallel `LUCIAREL` code in a calculation on the ground state of BiH running on a Linux cluster. The CI expansion spans 428 014 958 determinants.

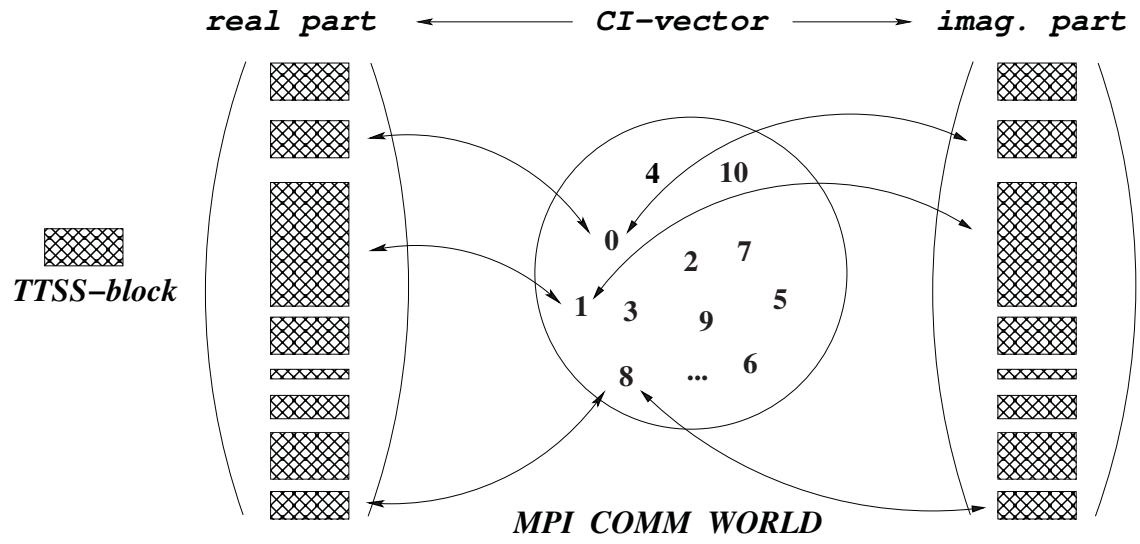

Figure 1, Knecht *et al.*, Journal of Chemical Physics

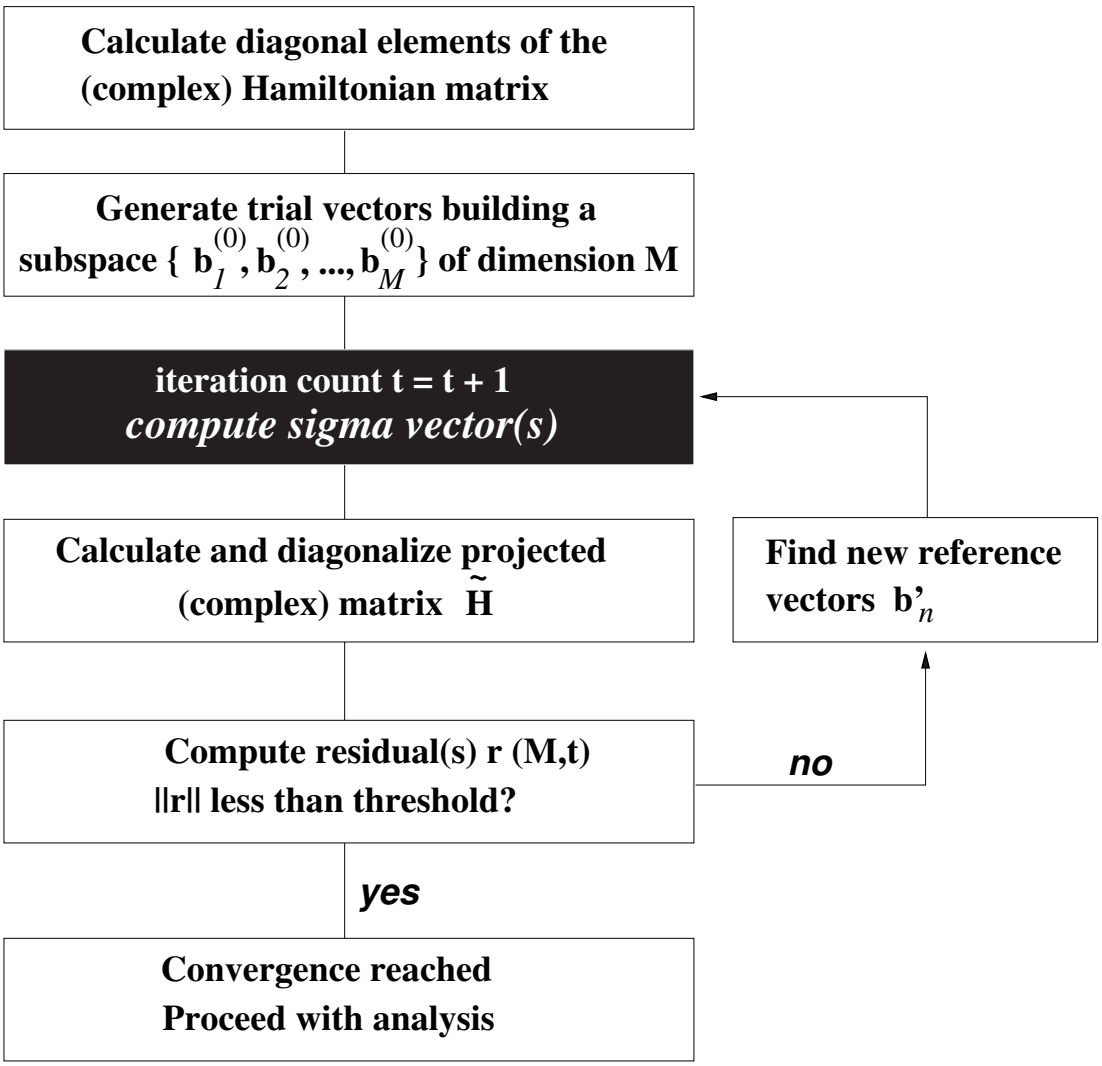

Figure 2, Knecht *et al.*, Journal of Chemical Physics

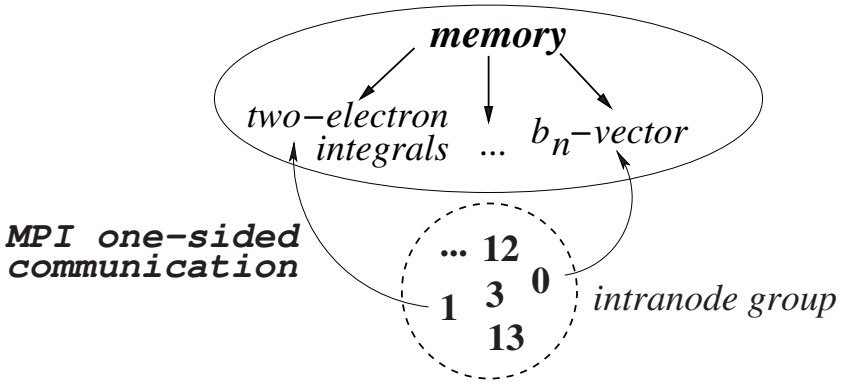

Figure 3, Knecht *et al.*, Journal of Chemical Physics

```
For each process (which is assigned a specific subset of all TTSS blocks):
loop {TTSS blocks}
  if global file system then
    if my b_n-TTSS block then
      store block into the globally accessible file BBLOCKS
    end if
  else
    if my process is node master then
      if this b_n-TTSS block is on my node then
        scatter this block to relevant node masters with MPI_bcast
        (unless one-sided communication is used)
      else if this block is needed for my node then
        gather this b_n-TTSS block from another node master
        using either MPI_bcast or MPI_get
        store block into the intranode specific file BBLOCKS
      end if
    end if
  end if
end loop[TTSS blocks]
loop {my M_K values in σ_n vector}
  loop {my σ-batches of σ_n-TTSS blocks}
    loop {my ΔM_K = −2, −1, ..., +2 values in b_n vector}
      loop {my b-batches of b_n-TTSS blocks}
        read this b-batch from the BBLOCKS file
        loop {all my connecting b_n-TTSS blocks in current b-batch}
          loop {my σ_n-TTSS blocks in current σ-batch}
            loop {excitation types T_H for a given Hamiltonian}
              if σ_n-TTSS block connects to b_n-TTSS block for this T_H type then
                fetch T_H-type specific integral block
                if shared-memory mode then
                  fetch integral block from shared intranode memory using MPI_get
                else
                  fetch integral block from local main memory
                end if
                add contribution to current σ_n-vector TTSS block
              end if
            end loop[excitation types T_H for a given Hamiltonian]
          end loop[my σ_n-TTSS blocks in current σ-batch]
        end loop[all my connecting b_n-TTSS blocks in current b-batch]
      end loop[my b-batches of b_n-TTSS blocks]
    end loop[my ΔM_K values in b_n vector]
  end loop[my σ-batches of σ_n-TTSS blocks]
end loop[my M_K values in σ_n vector]
```


Figure 4, Knecht *et al.*, Journal of Chemical Physics

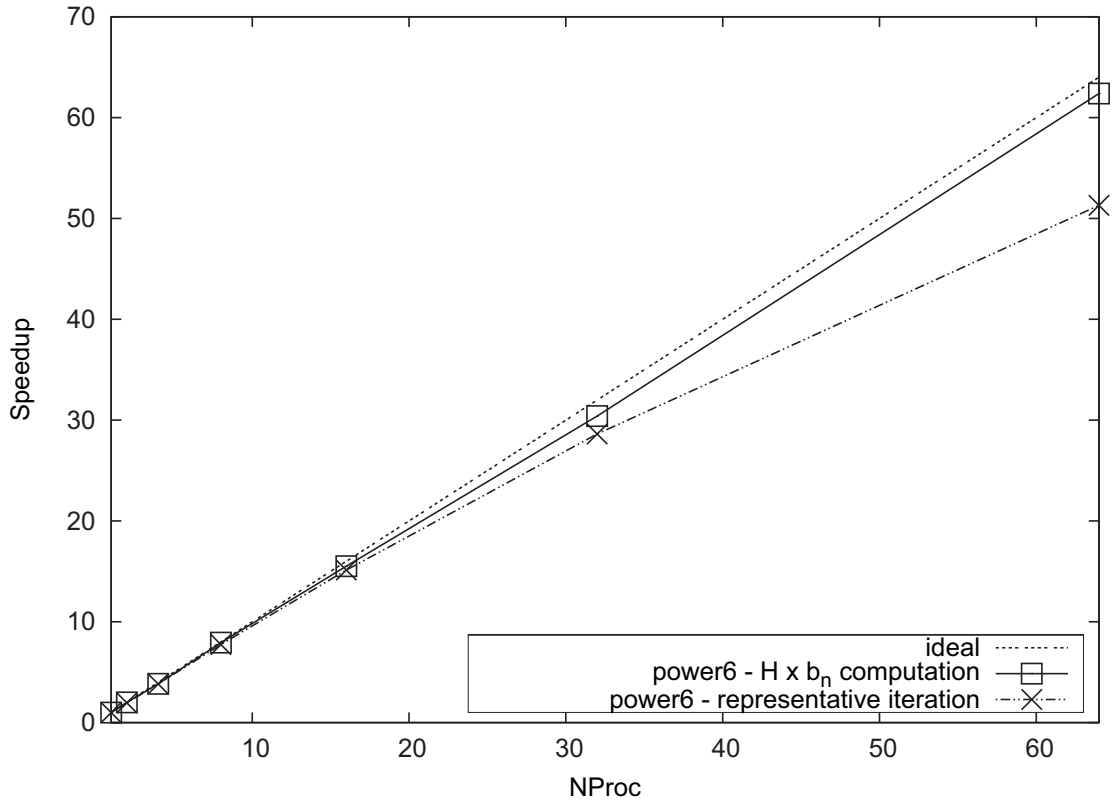

Figure 5, Knecht *et al.*, Journal of Chemical Physics

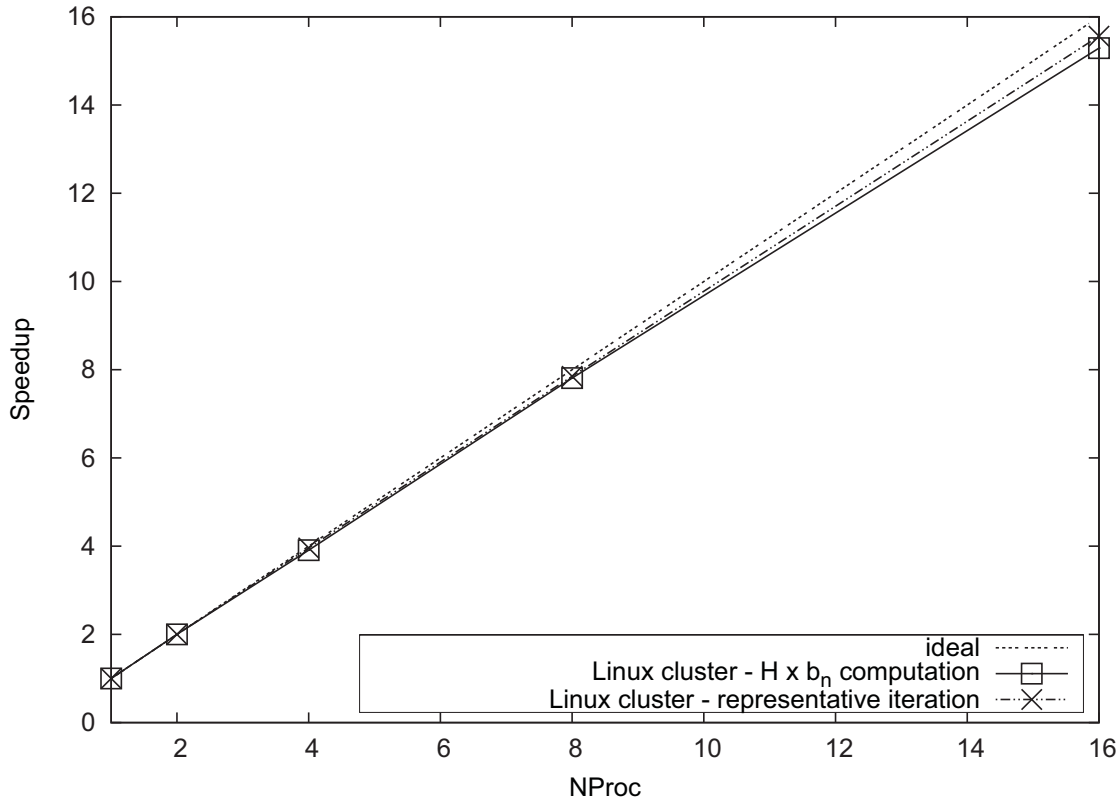

Figure 6, Knecht *et al.*, Journal of Chemical Physics

[1] B. A. Hess and C. M. Marian. In P. Jensen and P. R. Buenker, editors, *Computational Molecular Spectroscopy*, Sussex, 1999. John Wiley & Sons Ltd.

[2] T. Fleig. Relativistic string-based electron correlation methods. In M. Barysz and Y. Ishikawa, editors, *Relativistic Methods for Chemists*. Springer Verlag, Berlin, 2009.

[3] C. M. Marian. Spin-orbit coupling in molecules. In K. Lipkowitz and D. Boyd, editors, *Reviews in Computational Chemistry*, volume 17, page 99. Wiley-VCH, Weinheim, 2001.

[4] S. Yabushita, Z. Zhang, and R. M. Pitzer. Spin-orbit configuration interaction using the graphical unitary group approach and relativistic core potential and spin-orbit operators. *J. Phys. Chem.*, 103:5791, 1999.

[5] V. Vallet, L. Maron, C. Teichteil, and J. P. Flament. A two-step uncontracted determinantal effective Hamiltonian-based SO-CI method. *J. Chem. Phys.*, 113:1391, 2000.

[6] B. O. Roos and P.-Å. Malmqvist. Relativistic quantum chemistry: the multiconfigurational approach. *Phys. Chem. Chem. Phys.*, 6:2919, 2004.

[7] M. Kleinschmidt, J. Tatchen, and C. M. Marian. Spock.CI: A multireference spin-orbit configuration interaction method for large molecules. *J. Chem. Phys.*, 124:124101, 2006.

[8] H.-S. Lee, Y.-K. Han, M. C. Kim, C. Bae, and Y. S. Lee. Spin-orbit effects calculated by two-component coupled-cluster methods: test calculations on AuH, Au_2, TlH and Tl_2. *Chem. Phys. Lett.*, 293:97, 1998.

[9] T. Fleig. Spin-orbit resolved static polarizabilities of group 13 atoms. 4-component relativistic configuration interaction and coupled cluster calculations. *Phys. Rev. A*, 72:052506, 2005.

[10] T. Fleig, H. J. Aa. Jensen, J. Olsen, and L. Visscher. The generalized active space concept

for the relativistic treatment of electron correlation. III. Large-scale configuration interaction in a four-component multi-configuration self-consistent field program and application to UO_2. *J. Chem. Phys.*, 124:104106, 2006.

[11] L. Visscher and T. Saue. Approximate relativistic electronic structure methods based on the quaternion modified Dirac equation. *J. Chem. Phys.*, 113:3996, 2000.

[12] T. Fleig, J. Olsen, and C. M. Marian. The generalized active space concept for the relativistic treatment of electron correlation. I. Kramers-restricted two-component configuration interaction. *J. Chem. Phys.*, 114:4775, 2001.

[13] T. Fleig, J. Olsen, and L. Visscher. The generalized active space concept for the relativistic treatment of electron correlation. II. Large-scale configuration interaction implementation based on relativistic 2- and 4-spinors and its application. *J. Chem. Phys.*, 119:2963, 2003.

[14] DIRAC, a relativistic ab initio electronic structure program, Release DIRAC08 (2008), written by L. Visscher, H. J. Aa. Jensen, and T. Saue, with new contributions from R. Bast, S. Dubillard, K. G. Dyall, U. Ekström, E. Eliav, T. Fleig, A. S. P. Gomes, T. U. Helgaker, J. Henriksson, M. Iliaš, Ch. R. Jacob, S. Knecht, P. Norman, J. Olsen, M. Pernpointner, K. Ruud, P. Sałek, and J. Sikkema (see http://dirac.chem.sdu.dk).

[15] S. Knecht, H. J. Aa. Jensen, and T. Fleig. Large-scale parallel configuration interaction. I. non-relativistic and scalar-relativistic general active space implementation with application to $(Rb\text{-}Ba)^+$. *J. Chem. Phys.*, 128:014108, 2008.

[16] J. Olsen, B. O. Roos, P. Jørgensen, and H. J. Aa. Jensen. Determinant based configuration interaction algorithms for complete and restricted configuration interaction spaces. *J. Chem. Phys.*, 89:2185, 1988.

[17] J. Olsen, P. Jørgensen, and J. Simons. Passing the one-billion limit in full configuration-

interaction (FCI) calculations. *Chem. Phys. Lett.*, 169:463, 1990.

[18] T. Fleig and L. Visscher. Large-scale electron correlation calculations in the framework of the spin-free dirac formalism: the Au_2 molecule revisited. *Chem. Phys.*, 311:113, 2005.

[19] G F Koster, J O Dimmock, R G Wheeler, and H Statz. *Properties of the Thirty-Two Point Groups*. Massachusetts Institute of Technology, Cambridge, Massachusetts, 1963.

[20] H. J. Aa. Jensen, K. G. Dyall, T. Saue, and K. Fægri. Relativistic four-component multiconfigurational self-consistent field theory for molecules: Formalism. *J. Chem. Phys.*, 104:4083, 1996.

[21] M. Iliaš, H. J. Aa. Jensen, V. Kellö, B. O. Roos, and M. Urban. Theoretical study of PbO and the PbO anion. *Chem. Phys. Lett.*, 408:210, 2005.

[22] M. Iliaš and T. Saue. An infinite-order two-component relativistic hamiltonian by a simple one-step transformation. *J. Chem. Phys.*, 126:064102, 2007.

[23] M. Iliaš and H. J. Aa Jensen. Two-component relativistic methods based on the quaternion modified dirac equation: From the Douglas-Kroll to the Barysz-Sadlej-Snijders infinite order. *private communication*, 2009.

[24] B. Schimmelpfennig, program AMFI, Stockholm University, Sweden, 1996.

[25] B. A. Hess, C. M. Marian, U. Wahlgren, and O. Gropen. A mean-field spin-orbit method applicable to correlated wavefunctions. *Chem. Phys. Lett.*, 251:365, 1996.

[26] M. Iliaš, V. Kello, L. Visscher, and B. Schimmelpfennig. Inclusion of mean-field spin-orbit effects based on all-electron two-component spinors: Pilot calculations on atomic and molecular properties. *J. Chem. Phys.*, 115:9667, 2001.

[27] J. Thyssen, T. Fleig, and H. J. Aa. Jensen. A direct relativistic four-component multiconfiguration self-consistent-field method for molecules. *J. Chem. Phys.*, 129:034109, 2008.

[28] S. Knecht, H. J. Aa Jensen, and L. K. Sørensen. Four-component MP2 natural orbitals: An efficient way of selecting appropiate active spaces for coupled cluster and multiconfigurational self-consistent field calculations, 2009. unpublished work.

[29] S. Knecht and H. J. Aa Jensen. A general-purpose parallel four-component Kramers-restricted CI property module. unpublished work.

[30] E. R. Davidson. The iterative calculation of a few of the lowest eigenvalues and corresponding eigenvectors of large real-symmetric matrices. *J. Comput. Phys.*, 17:87, 1975.

[31] http://www.mpi-forum.org.

[32] M. Klene, M. A. Robb, M. J. Frisch, and P. Celani. Parallel implementation of the CI-vector evaluation in full CI/CAS-SCF. *J. Chem. Phys.*, 113:5653, 2000.

[33] Z. Gan, Y. Alexeev, M. S. Gordon, and R. A. Kendall. The parallel implementation of a full configuration interaction program. *J. Chem. Phys.*, 119:47, 2003.

[34] B. Suo, G. Zhai, Y. Wang, Z. Wen, X. Hu, and L. Li. Parallelization of MRCI based on hole-particle symmetry. *J. Comp. Chem.*, 26:88, 2005.

[35] K. Tanaka, Y. Mochizuki, T. Ishikawa, H. Terashima, and H. Tokiwa. A graphical symmetric group approach for a spin adapted full configuration interaction: partitioning of a configuration graph into sets of closed-shell and open-shell graphs. *Theor. Chem. Acc.*, 117:397, 2007.

[36] K. P. Huber and G. Herzberg, "Constants of Diatomic Molecules" (data prepared by J. W. Gallagher and R. D. Johnson, III) in *NIST Chemistry WebBook*, NIST Standard Reference Database Number 69, Eds. P. J. Linstrom and W. G. Mallard, National Institute of Standards and Technology, Gaithersburg MD, 20899, http://webbook.nist.gov, (retrieved December 10, 2008).

[37] M. Kleinschmidt, C. M. Marian, M. Waletzke, and S. Grimme. Parallel multireference con-

figuration interaction calculations on mini-β-carotenes and β-carotene. *J. Chem. Phys.*, 130:044708, 2009.

[38] Y. Kurashige and T. Yanai. High-performance ab initio density matrix renormalization group method: Applicability to large-scale multireference problems for metal compounds. *J. Chem. Phys.*, 130:234114, 2009.

[39] Dr. Martin Kleinschmidt. Düsseldorf 2009, private communication.

[40] A. Heimer. Über das Bandenspektrum des Wismuthydrids. *Z. Phys.*, 95:328, 1935.

[41] A. Heimer and E. Hulthén. Band spectrum of bismuth hydride. *Nature*, 127:557, 1931.

[42] E. Hulthén and A. Heimer. Spectrum of bismuth hydride. *Nature*, 129:399, 1932.

[43] B. Lindgren and Ch. Nilsson. On the spectra of BiH and BiD. *J. Mol. Spectrosc.*, 55:407, 1975.

[44] H. G. Hedderich and P. F. Bernath. Infrared emission spectroscopy of bismuth monohydride and bismuth monodeuteride. *J. Mol. Spectrosc.*, 158:170, 1993.

[45] R. D. Urban, P. Polomsky, and H. Jones. A reassessment of the ground-state infrared spectrum of BiH and BiD. *Chem. Phys. Lett.*, 181:485, 1991.

[46] A. M. R. P. Bopegedera, C. R. Brazier, and P. F. Bernath. Diode laser spectroscopy of BiH and BiD. *Chem. Phys. Lett.*, 162:301, 1989.

[47] K. Balasubramanian. Relativistic configuration interaction calculations of the low-lying states of BiH. *Chem. Phys. Lett.*, 114:201, 1985.

[48] K. Balasubramanian. Relativistic quantum calculations of spectroscopic properties of BiH. *J. Mol. Spectrosc.*, 115:258, 1986.

[49] A. B. Alekseyev, R. J. Buenker, H. P. Liebermann, and G. Hirsch. Spin-orbit configuration interaction study of the potential energy curves and radiative lifetimes of the low-lying states

of bismuth hydride. *J. Chem. Phys.*, 100:2989, 1994.

[50] G. A. DiLabio and P. A. Christiansen. Low-lying 0^+ states of bismuth hydride. *Chem. Phys. Lett.*, 277:473, 1997.

[51] Y. K. Han, C. Bae, S. K. Son, and Y. S. Lee. Spin-orbit effects on the transactinide p-block element monohydrides MH (M=element 113–118). *J. Chem. Phys.*, 112:2684, 1999.

[52] H. Stoll, B. Metz, and M. Dolg. Relativistic energy-consistent pseudopotentials - recent developments. *J. Comp. Chem.*, 23:767, 2001.

[53] G. Herzberg. *Molecular Spectra and Molecular Structure*. Krieger Publishing Company, Malabar, Florida, 1989.

[54] K. G. Dyall. Relativistic and nonrelativistic finite nucleus optimized triple-zeta basis sets for the 4p, 5p and 6p elements. *Theor. Chem. Acc.*, 108:335, 2002.

[55] K. G. Dyall. Relativistic and nonrelativistic finite nucleus optimized triple zeta basis sets for the 4p, 5p and 6p elements. *Theor. Chem. Acc.*, 109:284, 2003.

[56] K. G. Dyall. Relativistic Quadruple-Zeta and Revised Triple-Zeta and Double-Zeta Basis Sets for the 4p, 5p, and 6p Elements. *Theor. Chem. Acc.*, 115:441, 2006.

[57] T. H. Dunning Jr. Gaussian basis sets for use in correlated molecular calculations. I. The atoms boron through neon and hydrogen. *J. Chem. Phys.*, 90:1007, 1989.

[58] L. K. Sørensen, J. Olsen and T. Fleig. Kramers unrestricted generalized active space coupled-cluster. Implementation and application to BiH. to be submitted.

[59] R. Ansaloni, G. L. Bendazzoli, S. Evangelisti, and E. Rossi. A parallel Full-CI algorithm. *Comput. Phys. Commun.*, 128:496, 2000.

Paper 3

Lasse Kragh Sørensen, Stefan Knecht, Timo Fleig, and Christel M. Marian

Four-component relativistic coupled cluster and configuration interaction calculations on the ground and excited states of the RbYb molecule.

J. Phys. Chem **A**, Publication Date (Web): August 18, 2009, DOI: 10.1021/jp904914m

Four-Component Relativistic Coupled Cluster and Configuration Interaction Calculations on the Ground and Excited States of the RbYb Molecule†

Lasse Kragh Sørensen,‡ Stefan Knecht,† Timo Fleig,*,‡,§ and Christel M. Marian*,‡

Institute of Theoretical and Computational Chemistry, Heinrich Heine University Düsseldorf, Düsseldorf, Germany

Received: May 26, 2009; Revised Manuscript Received: July 29, 2009

We present high-level four-component coupled cluster and multireference configuration interaction calculations of potential energy curves, dipole moment, Franck−Condon factors and spectroscopic constants of the newly formed RbYb molecule. From finite-field calculations we obtain an electric dipole moment for RbYb of almost 1 D. In combination with its magnetic dipole moment this makes RbYb an excellent candidate for trapping and for studying dipolar interaction in the ultracold regime. Significant Franck−Condon factors are found between the rovibronic ground state and the lowest rovibrational levels of the first excited $^2\Sigma^+_{1/2}$ state but also between a broad range of rovibrational levels of the $^2\Pi_{1/2}$ and $^2\Pi_{3/2}$ states. This allows for several two-step approaches to reach the rovibronic ground state after initial photoassociation.

1. Introduction

A number of groundbreaking achievements has been reported from the field of cold and ultracold molecules, and ongoing investigations bear the potential for yet further findings of fundamental importance.[1] These range from the production of Bose−Einstein condensates (BECs)[2] to the striving for a controlled chemistry at the quantum level[3] and the possibility of testing, e.g., fundamental symmetries in nature through measurements of a postulated electric dipole moment (EDM) of an electron[4,5] or the space−time variation of fundamental constants such as the fine-structure constant α.[6,7] The experimental work for producing (ultra)cold molecules has to the date been conducted in a variety of ways, such as photoassociation (PA),[8] buffer gas cooling (sympathetic cooling),[9] Stark deceleration of polar molecules via time-modulated electric fields,[10] and magnetically tunable Feshbach resonances.[11]

Theoretical contributions to the field of (ultra)cold molecules are of value in many different respects. Among the most important is the determination of accurate molecular potential energy curves (PECs) of ground and relevant electronically excited states. These potentials are often required to be known at both short and long range.[8] At long-range, atom−atom interactions are typically evaluated by perturbation theory, whereas at short range advanced methods of molecular electronic structure theory come into play. In addition to the spectral constants which may be extracted directly from the short-range potentials (equilibrium bond lengths, harmonic vibrational frequencies, dissociation, and excitation energies),[12−14] vibrational states and Franck−Condon factors (FCFs),[15] molecule formation rates,[16] and electric properties such as permanent EDM,[17,18] transition dipole moments,[19] and static polarizabilities are of interest and have been determined by theoretical methods.

A large fraction of investigated systems in the (ultra)cold molecular sciences is composed of alkali metal diatomics. The RbYb molecule belongs to a new class of heteronuclear diatomics that due to their unpaired electron(s) may be trapped and manipulated using magnetic fields.[20] They are, for example, promising candidates for an experimental search for a permanent electric dipole moment of the electron or for producing lattice-spin models[21] for quantum computing. Recently, the thermalization of various bosonic and fermionic Yb isotopes through collisions with ultracold Rb has been shown, giving first insights into the long-range behavior of the RbYb potential.[22] On the basis of this work, the controlled production of electronically excited RbYb* molecules by single-photon photoassociation techniques has been demonstrated,[20] and continued efforts include the conservative trapping of the Rb−Yb mixture. Ultimately, the investigations aim at a molecular BEC with adjustable dipolar interaction and a new approach to measuring the electron EDM. The prospects have motivated us to explore the electronic structure of the RbYb molecule with reliable and accurate relativistic electronic structure methods.

In this paper we present, to the best of our knowledge, the first theoretical investigation of the RbYb molecule. The focus of this investigation has been on a simultaneously accurate description of the ground and lowest electronically excited states and to propose possible ways for a photoassociation process leading to the rovibronic ground state. Since two heavy atoms are involved, we apply quantum-chemical methods that treat electron correlation and relativistic effects on the same footing. Relativistic coupled cluster and configuration interaction approaches are used in a complementary fashion, the details of which are described in the following section. In the main body of the paper (section 3) we outline a way of achieving high accuracy by first a systematic study of the ground and excited states of the atoms and, in addition, of the electronic ground state of the molecule. Based on these results, a final multireference (MR) CI model expansion is chosen that can deliver accurate spectroscopic values for the states in question. We present and discuss electronic molecular potentials obtained with this MRCI model and point to possible pathways to the rovibronic ground state based on the derived FCFs. We furthermore present the computed dipole moment function of the ground state showing that RbYb also possesses a substantial

† Part of the "Russell M. Pitzer Festschrift".

* E-mail: timo.fleig@irsamc.ups-tlse.fr; Christel.Marian@uni-duesseldorf.de.

‡ HHU Düsseldorf.

§ Permanent address: Laboratoire de Chimie et Physique Quantiques, I.R.S.A.M.C., Université Paul Sabatier, Toulouse, France.

10.1021/jp904914m CCC: $40.75

electric dipole moment along with a magnetic dipole moment due to the unpaired electron. In the final section we summarize and draw conclusions.

2. Theory and Computational Details

2.1. Hamiltonian Operators. The spectroscopic properties of RbYb are expected to be significantly influenced by relativistic effects and electron correlation. For the ground state $^2\Sigma^+_{1/2}$ scalar-relativistic effects cause a large contraction and stabilization of the 6s spinors on Yb and a smaller one of the 5s spinors on Rb. For the lowest excited states we expect a significant spin−orbit splitting for $Rb_{5p^1}(^2P_{3/2,1/2})$ and a large spin−orbit coupling (SOC) for $Yb_{6s^16p^1}(^3P_{2,1,0})$ and $Yb_{6s^16p^1}(^1P_1)$. We have therefore decided to carry out this theoretical investigation in the more rigorous 4-component framework using the Dirac−Coulomb (DC) Hamiltonian for calculations including excited states and Dyall's spinfree Hamiltonian[23] for ground-state-only calculations. To correctly describe the SOC of the excited states, the DC Hamiltonian suffices since it contains the leading spin−orbit terms for heavy elements, namely the one-electron spin−orbit and the two-electron spin−same-orbit terms. The effect of the spin−other-orbit term, which is derived from the Gaunt operator and is therefore not included in the DC Hamiltonian, has been examined at the SCF level. It was found that the change in the splitting of the $Rb_{5p}(P_{3/2,1/2})$ and $Yb_{6p}(P_{3/2,1/2})$ levels decreased by 0.72 and 19.8 cm^{-1}, respectively. This reduction amounts to a change for $Rb_{5p}(P_{3/2,1/2})$ of 1.7% and for $Yb_{6p}(P_{3/2,1/2})$ of 1%, which is still below the accuracy we can typically achieve for relative energies. Including the full Breit interaction has been shown to have only little influence on the excitation energies of Yb[24] and on the alkali metal atoms in general.[25]

2.2. Correlation Methods and Setup. For the study of ground-state spectroscopic and electric properties we employed the RELCCSD module[26,27] in the DIRAC quantum chemistry program package,[28] which can perform CCSD and CCSD(T) calculations. The dominant relativistic contributions to the ground state are scalar relativistic. We therefore applied Dyall's spinfree Hamiltonian[23] in the coupled cluster calculations. Dirac−Coulomb Hartree−Fock (DCHF) calculations were performed with an averaging of three electrons in two Kramers pairs (3in2) consisting of the Rb 5s and Yb 6s spinors. Additional test calculations were carried out in a spin-dependent framework employing either a (3in2) or (3in5) averaging. In the latter DCHF setup three electrons were distributed among five Kramers pairs consisting of the Rb 5s and Yb 6s6p spinors. These ground-state coupled cluster calculations served as a benchmark for the corresponding MRCI calculations.

The calculation of excited-state wave functions and vertical as well as adiabatic excitation energies has been performed with the relativistic large-scale MRCI program LUCIAREL.[29−31] Like in the CIDBG[32] and SOCI[33] in the COLUMBUS code, double group symmetry is used. The recent parallel implementation[34] of LUCIAREL has opened for the possibility to treat larger CI expansions (>10^8 determinants) within a reasonable time frame on standard Linux-based clusters which has also been demonstrated for the SOCI program.[35]

The CI program LUCIAREL operates on the basis of a fully variational treatment of any spin-dependent two- or four-component Hamiltonian that is available in the present developer version of the DIRAC package.[28] It furthermore takes advantage of the concept of generalized active spaces (GAS)[29] to define suitable orbital spaces thereby allowing for arbitrary occupation constraints. Molecular spinors based on a true two- or four-component framework can be obtained from all-electron self-consistent field (SCF), Kramers-restricted multiconfigurational self-consistent field (KR-MCSCF),[36] or natural MP2 spinor[37] calculations. The string-driven MRCI[29−31,38] as well as the MRCC[17,39−42] methods are an alternative to the Tensor Contraction Engine[43] in generation of higher-order methods or code for more complex calculations.

To obtain accurate excitation energies, the initial DCHF step was performed with a (3in5) averaging of states. A (3in8) averaging, where the Rb 5p spinors are included, was not possible along the entire potential energy curve due to strong mixing with the Yb 5d spinors. The Rb 5p spinors were, however, included in the correlation step in a (3in8) MRCI excitation scheme that is in the following dubbed as S6_(3in8)_SD. Our notation follows the scheme "GAS I_(GAS II)_GAS III" and is most easily explained by an example: "S6_(3in8)_SD" means that at most 1 hole among the 6 electrons in 3 Kramers pairs (in this case: Rb 4p spinors) is allowed, 3 electrons are distributed in 8 Kramers pairs in all possible ways (plus of course excitations from GAS I to GAS II), and finally that all possible single and double excitations into GAS III Kramers pairs are generated from the reference configurations obeying the constraints put on GAS I and GAS II. As discussed in more detail in section 3.1, the inclusion of the Rb 4p spinors is required in the correlation step to obtain a good description of the lowest three atomic channels.

In addition to our thorough investigation of the four lowest molecular electronic states of RbYb, we show in Figure 1 a qualitative picture of the low-lying molecular electronic spectrum including respective atomic dissociation channels. In these calculations, denoted as SDT3 which corresponds to a Full CI calculation with three electrons, we truncated the space of virtual spinors at 2.0 E_h. It should be noted that the $Rb_{4d^1}(^2D_{5/2,3/2})$ states should be below the $Yb_{6s^16p^1}(^3P_2)$ states in the atomic limit which is not the case here due to the choice of DCHF averaging.

As full linear symmetry is not available yet in the present LUCIAREL implementation the calculations, have been carried out in the Abelian sub double group C_2^*. The assignment of the Ω quantum number for each individual electronic state has been accomplished by means of calculating the expectation value for the one-electron operator $\hat{j}_z = \hat{l}_z + \hat{s}_z$. This option has become available with the very recent implementation of a general CI property module[44] capable of treating basically any one-electron operator that is implemented in the program package.[28]

2.3. Basis Sets and Number of Correlated Electrons. All calculations were performed using uncontracted basis sets. For the ground-state coupled cluster calculations the aug-cc-pVTZ basis set for Yb (30s24p16d13f4g2h)[45] from Gomes and Dyall was chosen. It includes correlating functions for outer- and inner-valence shells down to the Yb 4f and polarizing functions for these. For Rb (29s21p15d2f)[46] Dyall's aug-cc-pVTZ basis set, which includes correlating and polarizing functions down to Rb 4s4p, was used. For a description of the general procedure of how to derive these functions see for example ref 47. In the following this basis set will be referred to as (ext_bas).

The effect of changing the number of correlated electrons has been examined at the CCSD and CCSD(T) levels. Either nine electrons from the Rb 4p5s and Yb 6s spinors were treated explicitly in the correlation step or 23 electrons were used, where the Yb 4f spinors were then included in addition. As shown in sections 3.1 and 3.2, the differential effects of correlating the Yb 4f electrons were found to be minor. In contrast, the correlation of the Rb 4p electrons had significant impact on the energy separation of the atomic levels and on the equilibrium

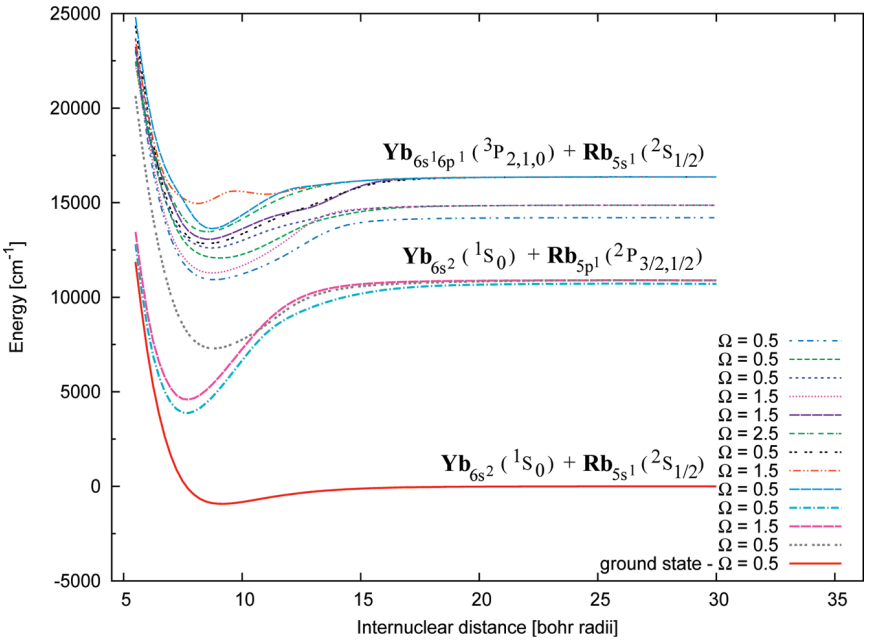

Figure 1. Qualitative picture of the potential energy curves of the molecular electronic states constituting the lower electronic spectrum of RbYb. Correlating atomic dissociation channels for the states are labeled. The computational level is CI SDT3 (see text for more details).

distance of the molecular ground state. We therefore decided to correlate nine electrons (Rb 4p5s and Yb 6s) in the MRCI calculations.

For the MRCI calculations the core-polarizing functions for both atoms were omitted since no electric properties were calculated. This reduced the size of the basis set (min_bas) to (30s24p16d13f3g1h) for Yb and (28s20p14d1f) for Rb. The truncation value for the virtual spinors in all correlated calculations was kept at 7.8 E_h since this threshold includes all polarizing functions and, in addition, was still tractable for the MRCI calculations. Spinors above this threshold are primarily core-correlating and will therefore only give minor contributions to valence spectroscopic values and electric properties.

2.4. Finite-Field Dipole Moment. The response of a molecular system to a weak external electric field ε can be treated as a perturbation to the field-free case. If the energy is expanded in a Taylor series around the field-free case

$$E(\varepsilon) = E(\varepsilon = 0) + \left.\frac{dE}{d\varepsilon}\right|_{\varepsilon=0} \varepsilon + \frac{1}{2}\left.\frac{d^2E}{d\varepsilon^2}\right|_{\varepsilon=0} \varepsilon^2 + \ldots \quad (1)$$

the first derivative of the energy E with respect to the external electric field ε taken at $\varepsilon = 0$ is the static dipole moment of the molecule. Likewise the second derivative can be related to the static polarizabilty and higher derivatives to higher-order (hyper)polarizabilities.

With the finite-field technique these analytical derivatives are approximated by a numerical derivative. To this end a small external electric field of varying field strength is applied and then a series of energy calculations is performed with these fields. By applying fields in various directions, we can also determine higher-order numerical derivatives, though these are not as accurate as the analytical ones.

The ground-state dipole moment was calculated by applying a finite electric field of varying strength along the bond axis (chosen as z). The field strengths considered here were ± 0.0001, ± 0.0002, and ± 0.0004 E_h e^{-1} $bohr^{-1}$. From these seven points a polynomial fit to the total field-dependent energy was made to find the numerical derivative and thereby also the dipole moment at a given internuclear distance. This was done at the CCSD and CCSD(T) levels of theory with 23 explicitly correlated electrons.

The advantage of the derivative technique is that it holds also for approximate wave functions, which are typically dealt with in quantum chemistry, unlike the evaluation of properties by calculating expectation values in the Hellmann−Feynman theorem, which differ from the correct value by the *wave function force*.[48]

2.5. Spectroscopic Values and Franck−Condon Factors. A polynomial fitting procedure with exponents ranging from −1 to +4 was used to fit the electronic ground- and excited-state potentials around their respective minima. Spectroscopic constants have then been determined by solving a one-dimensional Schrödinger equation of nuclear motion using a reduced mass calculated from isotopic abundance.[49] The harmonic frequency has been calculated from the second derivative at the minimum. Vibrational wave function, eigenvalues, and FCFs have been computed with the program LEVEL 8.0 by LeRoy.[15]

2.6. Counterpoise Correction. As RbYb is a van der Waals complex and therefore the ground state is very weakly bound by dispersion forces, the basis set superposition error (BSSE) may play a significant role in determining spectroscopic values even in large and balanced basis sets[50,51] due to the slow convergence toward basis set saturation. This artifact has been examined by a counterpoise (CP) correction, as suggested by Boys and Bernardi[52] for both ground and excited states, which is the correct way of evaluating differential quantities.[51,53,54] The BSSE is defined in the usual manner

$$\mathrm{BSSE}(R) = E^{A(AB)}(R) + E^{B(AB)}(R) - E^{A} - E^{B} \quad (2)$$

where $E^{A(AB)}(R)$ and $E^{B(AB)}(R)$ are the monomer energies obtained in the full dimer basis (AB) at a given distance (R) and E^A and E^B are the monomer energies in their respective basis. Every point on the potential energy curve is thereby CP corrected. The CP correction has been shown to be a very good estimate for the BSSE in medium to large basis sets and to

TABLE 1: Selection of Molecular Electronic States in the Λ−S Coupling Picture and Associated Atomic Dissociation Channels in an Energy Range of ≈25 000 cm^{-1} [a]

atomic $^{(2S+1)}L_J$	molecular $^{(2S+1)}\Lambda_\Omega$
$Rb_{5s^1}(^2S_{1/2}) + Yb_{6s^2}(^1S_0)$	$^2\Sigma^+_{1/2}$
$Rb_{5p^1}(^2P_{3/2,1/2}) + Yb_{6s^2}(^1S_0)$	$^2\Pi_{3/2,1/2}$, $^2\Sigma^+_{1/2}$
$Rb_{5s^1}(^2S_{1/2}) + Yb_{6s^16p^1}(^3P_{2,1,0})$	$^4\Pi_{5/2,3/2,1/2,-1/2}$, $^2\Pi_{3/2,1/2}$, $^4\Sigma^+_{3/2,1/2}$, $^2\Sigma^+_{1/2}$
$Rb_{4d^1}(^2D_{5/2,3/2}) + Yb_{6s^2}(^1S_0)$	$^2\Delta_{5/2,3/2}$, $^2\Pi_{3/2,1/2}$, $^2\Sigma^+_{1/2}$
$Rb_{6s^1}(^2S_{1/2}) + Yb_{6s^2}(^1S_0)$	$^2\Sigma^+_{1/2}$
$Rb_{5s^1}(^2S_{1/2}) + Yb_{6s^15d^1}(^3D_{3,2,1})$	$^4\Delta_{7/2,5/2,3/2,1/2}$, $^2\Delta_{5/2,3/2}$, $^4\Pi_{5/2,3/2,1/2,-1/2}$, $^2\Pi_{3/2,1/2}$, $^4\Sigma^+_{3/2,1/2}$, $^2\Sigma^+_{1/2}$
$Rb_{6p^1}(^2P_{3/2,1/2}) + Yb_{6s^2}(^1S_0)$	$^2\Pi_{3/2,1/2}$, $^2\Sigma^+_{1/2}$
$Rb_{5s^1}(^2S_{1/2}) + Yb_{6s^16p^1}(^1P_1)$	$^2\Pi_{3/2,1/2}$, $^2\Sigma^+_{1/2}$

[a] Molecular electronic states correlating to atomic channels with intra-atomic Yb f−d excitations, e.g., $Yb_{4f^{13}5d^16s^2}$ are not considered.

provide a smooth convergence of properties to the complete basis set limit.[55,56] Despite the apparent ease to eliminate a basis set incompleteness artifact one should, however, be careful in relying on this form of error compensation since a CP correction will not improve the overall basis.

3. Results and Discussion

3.1. Qualitative Molecular Electronic Spectrum and Atomic Calculations. Table 1 gives an overview over the atomic configurations and terms as well as the associated molecular states in the Λ−S coupling picture that are expected to form the lower part of the electronic spectrum of RbYb. The energetically close-lying valence-electronic Yb 6s and 6p shells as well as the valence-electronic Rb 5s and low-lying Rb 5p, 4d, 6s, and 6p shells suggest a large variety of excited states with angular momentum projection greater than zero within an energetic range of ≈25 000 cm^{-1}. As these states are affected by spin−orbit interaction to first order in a perturbation theory sense and as ytterbium is a heavy atom, the corresponding splittings and mixings are expected to be sizable. We provide in Figure 1 a qualitative survey of all molecular states correlating to the three lowest atomic channels listed in Table 1. Comparing the atomic-like excitation energies, computed at the CI SDT3 level of theory, with the experimentally available data, we find a large deviation of ≈2000−3000 cm^{-1} for the lowest P channels of both Rb and Yb. In contrast, the splitting among the various *J*-states is reproduced rather well. These results indicate that spin-dependent effects are taken into account properly whereas significant parts of the differential electron correlation are missing at this level of calculation. As we in the present study turn our main attention to the ground and three lowest excited states of RbYb, which are of particular importance for the experimental PA process,[20] we further investigated the effect of correlating the outer-core Rb 4p shell on the excitation energies. Since alkali atoms are known to have easily polarizable cores, we expect a considerable influence here.

Our calculated atomic and atomic-like excitation energies T_e for the lowest Rb 5s−5p transitions are compiled in Table 2 and atomic Yb 6s−6p transitions in Table 3. If core−valence polarization from the Rb 4p shell is neglected in the calculation of the lowest Rb 5s−5p transition, not only a considerable underestimation of the excitation energies of almost 2000 cm^{-1} is found, as indicated in Table 2 for the atomic S1 (one electron CI) and quasi-molecular SDT3 calculations, but also a too small fine-structure splitting of the ($^2P_{3/2,1/2}$) state of 183(2) cm^{-1} in comparison with the measured splitting of 237.6 cm^{-1}. However, taking into account single excitations from the outer-core Rb 4p shell (S6_(1in4)_SD) results in a significant improvement

TABLE 2: Atomic and Atomic-Like (Values Taken at R = 30 bohr) Excitation Energies T_e in cm^{-1} for the Lowest $Rb_{5s^1}(^2S_{1/2}) \rightarrow Rb_{5p^1}(^2P_{3/2,1/2})$ Transitions Calculated at the MRCI S1, S6_(1in4)_SD, SDT3, and S6_(3in8)_SD Levels, Respectively[a]

method/T_e (cm^{-1})	$J = 0.5$	$J = 0.5$	$J = 1.5$	
	$\Omega = 0.5$	$\Omega = 0.5$	$\Omega = 1.5$	$\Omega = 0.5$
S1	0	10692	10875	10875
S6_(1in4)_SD	0	12636	12857	12857
SDT3	0	10708	10890	10892
S6_(3in8)_SD	0	12662	12879	12883
experiment[59]	0	12578.95	12816.55	12816.55

[a] Details on the computational levels are given in the text.

TABLE 3: Atomic Excitation Energies T_e in cm^{-1} for the Lowest $Yb_{6s^2}(^0S_0) \rightarrow Yb_{6s^16p^1}(^3P_{2,1,0})$ Transitions Calculated at the MRCI S2, S14_(2in4)_SD, S20_(2in4)_SD and S20_(2in9)_SD Levels, Respectively[a]

method/T_e (cm^{-1})	$J = 0$	$J = 0$	$J = 1$	$J = 2$
S2	0	14209	14865	16362
S14_(2in4)_SD	0	15497	16164	17734
S20_(2in4)_SD	0	17233	17931	19611
S20_(2in9)_SD	0	17346	18034	19722
experiment[59]	0	17288.44	17992.01	19710.39

[a] Details on the computational levels are given in the text.

toward the experimental values. Excitation energies and the fine-structure splitting differ from the experimental data by about 40−60 cm^{-1} and 15 cm^{-1}, respectively.

What about T_e for the Rb 5p excitation computed at the quasi-atomic limit (R = 30 bohr) applying our MRCI S6_(3in8)_SD model? It can be seen from Table 2 that in the atomic limit the excitation energies are slightly shifted to higher energies by about 22−26 cm^{-1} yet yielding an excellent spin−orbit splitting of 218 cm^{-1}. The excitation energies are in very good agreement with the experimental data, exhibiting a maximum deviation of 83 cm^{-1} for the lower 2 0.5 state, and compare well to the two-component MRCI results of Lim et al.[57] using energy-consistent pseudopotentials. Furthermore, the energetic difference of only 4 cm^{-1} between the sublevels of the J = 1.5 atomic channel indicates that we are almost in the atomic limit at an internuclear distance of 30 bohr.

As a prospect for future studies on this system, we show our atomic MRCI calculations on the Yb atom where we studied the relevance of taking into account core−valence polarization from the Yb 4f and 5p shells. If only the two Yb 6s valence electrons are correlated (denoted as S2), transition energies for the respective Yb 6s−6p excitation are consistently too low by around 18%. The inclusion of the Yb 4f electrons in the correlation step (S14_(2in4)_SD) yields some improvement. However, only upon explicitly treating core−valence polarization from the Yb 5p shell (S20_(2in4)_SD) do we obtain excitation energies that are in good agreement with the experimental data. A further improvement is achieved by extending the active space to comprise the Yb 6s, 6p, and 5d shells (S20_(2in9)_SD). In this case, the deviations from the experimental values are less than 60 cm^{-1}, and the fine-structure splitting is very well reproduced.

Summarizing, the SDT3 level is insufficient for an accurate description even of the four lowest-lying dissociation channels (Rb 5s^1 + Yb 6s^2 and Rb 5p^1 + Yb 6s^2). It may thus be used only for obtaining a qualitative overview. In contrast, the S6_(3in8)_SD scheme reproduces the energetic splitting of these levels very well. Yb excitations do not play a major role in the

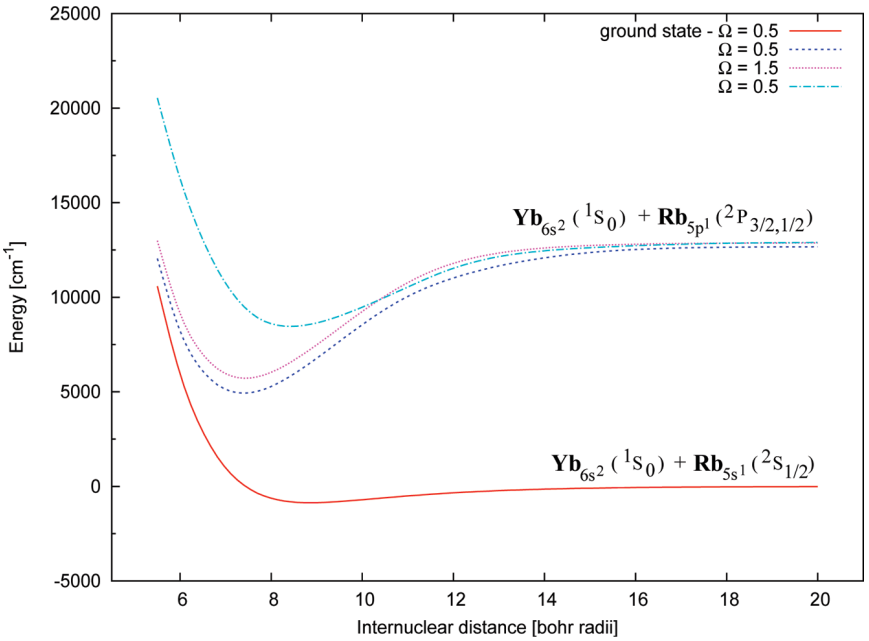

Figure 2. Potential energy curves of the four lowest-lying molecular electronic states of RbYb. Atomic dissociation channels for the states are shown. The computational level is S6_(3in8)_SD (see text for more details).

atomic channels that correlate with the four lowest-lying molecular states relevant for the PA process. We thus conclude that our chosen MRCI S6_(3in8)_SD model should provide a reliable description of the long-range behavior of these states in the RbYb molecule.

3.2. Ground-State Potential. The electronic ground state of RbYb exhibits a shallow potential shape (see Figure 2) that is a characteristic feature of a van der Waals molecule. Since the ground state is very sensitive to the DCHF averaging of the spinors and to the level of electron correlation, the simultaneously correct description of both ground and excited states becomes a complicated matter. Changes in the DCHF averaging or the correlation treatment can lead to large variations of the spectroscopic constants, here, in particular, the equilibrium bond distance. These differences may result in a substantial change of FCFs between ground and excited states.

We therefore first examined the ground state of RbYb with the coupled cluster method to provide a benchmark for the MRCI calculations. The aim here was to find the effect of outer-core polarization/correlation of the Yb 4f and Rb 4p. This has been done by varying the number of explicitly correlated electrons from 3 to 9 and to 23. Results of these calibration calculations are compiled in Table 4. Comparing those results, one sees that after a CP correction the effect of including the Rb 4p electrons on the bond length is more than 1 magnitude larger than including Yb 4f as the bond contracts from 9.18 bohr (CP-CCSD(T), 3 electrons correlated) to 8.94 bohr (CP-CCSD(T), 9 electrons correlated) and 8.93 bohr (CP-CCSD(T), 23 electrons correlated). The correlation of the Yb 4f electrons does, nevertheless, have an effect comparable to the inclusion of the Rb 4p electrons on the harmonic frequency and the dissociation energy in reducing both. These changes are, however, of little importance for the present investigation and, furthermore, the polarization of Yb 4f plays a minor role in the lowest-lying excited states for the molecule (see section 3.1). Therefore, we decided not to include the Yb 4f in the MRCI calculations. Another reason to omit the Yb 4f is the large CP correction, which shows that with this particular basis set and truncation of virtuals we did not yet come close enough to basis set saturation for the Yb 4f shell. The otherwise minor CP correction for the 3 and 9 electron CCSD and CCSD(T) calculations indicates that we have a balanced basis set.

TABLE 4: Spectroscopic Values for the 1 0.5 Ground State Calculated at the CCSD and CCSD(T) Level with 3, 9, and 23 Explicitly Correlated Electrons and with CP Corrected Values

method	corr el	R_e (bohr)	ω_e (cm^{-1})	D_e (cm^{-1})
CCSD-SF	3	9.30	26.278	606
CP-CCSD-SF	3	9.30	26.257	605
CCSD(T)-SF	3	9.18	28.941	818
CP-CCSD(T)-SF	3	9.18	28.923	816
CCSD-SF	9	9.20	24.814	600
CP-CCSD-SF	9	9.22	24.554	588
CCSD(T)-SF	9	8.93	29.724	820
CP-CCSD(T)-SF	9	8.94	29.462	804
CCSD-SF	23	9.15	24.186	742
CP-CCSD-SF	23	9.23	22.882	674
CCSD(T)-SF	23	8.86	28.990	870
CP-CCSD(T)-SF	23	8.93	28.196	749

The perturbative triples, on the other hand, have a substantial impact on the spectroscopic parameters. We therefore restrict the following discussion to results obtained at the CCSD(T) level. A comparison of the spin-free CCSD(T) correlating nine electrons with corresponding calculations including SOC (Table 5) shows that spin-dependent terms are of minor importance for the ground-state spectroscopic parameters. In contrast, both the choice of the basis set and one-particle spinor basis have a significant effect on the equilibrium distance and dissociation energy. Augmentation of the basis set by polarization functions on both atoms (ext_bas) leads to a bond contraction as well as to a bond strengthening. Similar trends are found when the Yb 6p shell is included in the spinor optimization step. Although the CCSD(T) calculations based on a (3in5) averaged spinor basis yield the most attractive potential, the results need to be regarded with caution because of the use of a single-reference method. This choice of one-particle basis is more appropiate for a multireference correlation approach.

The MRCI results for the ground state (Table 6) reproduce very well the spectroscopic values derived from the CCSD(T) calculations. We find a slightly shorter bond and a higher

TABLE 5: Spectroscopic Values for the 1 0.5 Ground State Calculated at the CCSD and CCSD(T) Level with Nine Explicitly Correlated Electrons and Including SOC[a]

method	basis set (av. in DCHF)	corr el	R_e (bohr)	ω_e (cm^{-1})	D_e (cm^{-1})
CCSD-SOC	min_bas (3in 2)	9	9.25	24.073	591
CCSD(T)-SOC	min_bas (3in2)	9	8.98	28.620	795
CCSD-SOC	min_bas (3in5)	9	9.15	25.572	654
CCSD(T)-SOC	min_bas (3in5)	9	8.89	30.214	828
CCSD-SOC	ext_bas (3in2)	9	9.17	24.969	603
CCSD(T)-SOC	ext_bas (3in2)	9	8.90	29.888	826
CCSD-SOC	ext_bas (3in5)	9	9.08	26.443	670
CCSD(T)-SOC	ext_bas (3in5)	9	8.82	31.321	868

[a] The spinor basis was derived from average-of-configurations DCHF calculations, distributing either three electrons in two Kramers pairs (3in2) or three electrons in five Kramers pairs (3in5). A CP correction was not applied.

TABLE 6: Spectroscopic Constants for the Ground and Three Lowest Excited States (Ω Designation) of RbYb Calculated at the MRCI S6_(3in8)_SD Level with Nine Explicitly Correlated Electrons[a]

	state	$\Lambda-\Sigma$[b]	R_e (bohr)	ω_e (cm^{-1})	D_e (cm^{-1})	T_v (cm^{-1})	T_e (cm^{-1})
1	0.5	$^2\Sigma^+$	8.85	29.751	865	0	0
2	0.5	$^2\Pi$	7.40	69.294	7735	7387	5794
1	1.5	$^2\Pi$	7.43	69.322	7164	8104	6581
3	0.5	$^2\Sigma^+$	8.43	52.789	4423	9431	9326
1	0.5(CP)	$^2\Sigma^+$	8.88	29.458	844	0	0
2	0.5(CP)	$^2\Pi$	7.40	69.441	7688	7441	5819
1	1.5(CP)	$^2\Pi$	7.44	69.181	7131	8153	6592
3	0.5(CP)	$^2\Sigma^+$	8.44	52.284	4388	9451	9339

[a] CP-corrected values are given in the lower part of the table. [b] leading $\Lambda-\Sigma$ configuration

dissociation energy of 844 cm^{-1} in relation to the CP-CCSD(T)-SF value of 804 cm^{-1} (Table 4). Typically, CCSD(T) is expected to result in larger binding energies than CI. A thorough analysis of the MRCI wave function reveals, however, substantial multiconfigurational character. The leading configuration consists of a doubly occupied Yb 6s Kramers pair and a bonding orbital composed of Rb 5s and Yb $6p_{1/2}$. In addition, large coefficients are found for single excitations from the bonding orbital as well as double excitations from the Yb 6s shell. The simultaneous occurrence of polarizing and correlating excitations are indicative of the importance of triples as observed in the CC calculations.

From the benchmark calculations on the molecular ground state in connection with a balanced description of the atomic limit (see Table 2) we conclude that with the chosen MRCI setup high accuracy can be achieved for both ground and low-lying excited states.

3.3. Excited-State Potentials. We now discuss in more detail the lower part of the electronic excitation spectrum of the RbYb molecule. Figure 2 displays the calculated potential energy curves for the three lowest excited states corresponding to the atomic Rb $5p_{3/2,1/2}$ and Yb $6s^2_{1/2}$ dissociation channels. The results for the spectroscopic constants of these states are compiled in Table 6 where data are listed with and without a CP correction, respectively.

The three electronically excited states can be divided into two classes, as illustrated in Figure 2. The second state with Ω quantum number 0.5 (denoted in the following by 2 0.5) and the lowest state with $\Omega = 1.5$ (1 1.5) display similar shapes with pronounced potential wells centered around 7.40 bohr (2 0.5) and 7.44 bohr (1 1.5), respectively, and a harmonic frequency ω_e of ca. 69 cm^{-1} derived from the CP-corrected data. Both states are deeply bound with a D_e of 7688 and 7131 cm^{-1}, respectively, whereas the 3 0.5 excited state has a considerably lower binding energy of 4388 cm^{-1}. We find for the latter excited state an equilibrium bond length R_e of 8.44 bohr that is significantly longer compared to the excited states mentioned before but much closer to the minimum internuclear distance of the ground state. This geometric shift is furthermore in agreement with a small difference of ≈112 cm^{-1} between the vertical T_v and adiabatic T_e excitation energies compared to the much larger difference for the other two states.

Comparison of the CP-corrected excited-state spectroscopic constants with their uncorrected counterparts in Table 6 reveals that the excited-state bond distances are less sensitive to basis set superposition errors than the ground-state bond distance. The RbYb bond in the ground state, e.g., decontracts by ≈0.03 bohr upon CP correction whereas the largest shift for an excited state is found to be around 0.01 bohr. Moreover, the adiabatic transition energies T_e are hardly affected by the CP correction with changes of the order of 10−20 cm^{-1}.

3.4. Vibrational Overlaps. Nemitz proposed a two-step mechanism for the production of ultracold RbYb molecules in the rovibronic ground state.[58] Initially, the molecule is prepared in a highly excited rovibrational level close to the dissociation limit of the electronic ground state. Interaction of the molecule with laser light of two different wavelengths promotes RbYb in a first step to some vibrational level of an electronically excited state correlating with the Rb(^{2}P) + Yb(^{1}S) atomic levels from which the population is pumped down in a second step to the rovibronic ground state of the molecule. For experimental realization of this scheme, knowledge of the vibrational overlaps between the electronically excited- and ground-state potential wells is of utmost importance. We expect that the dominating difference for a transition probability will be the FCF since all transitions are dipole allowed. We have therefore computed FCFs between vibrational wave functions of the electronic ground state and those of the three lowest electronically excited states. These calculations were perfomed for the ^{87}Rb and ^{176}Yb isotopes since these are favorably employed in experiment.[20]

In Table 7 selected FCFs between the rovibronic ground state (1 0.5, $v = 0$) and vibrational levels of the electronically excited states are listed. (Complete tables of the FCFs are available upon request.) As may be expected from the small geometrical shift between the 1 0.5 and 3 0.5 potential energy wells (see section 3.3), large Franck−Condon overlaps for the lowest vibrational levels of the 3 0.5 state are obtained. For the first excited 2 0.5 as well as the 1 1.5 state significant FCFs are observed for a wide range of vibrational states due to the large spatial extent of the electronic ground state as the maximum amplitude of the $v = 0$ wave function coincides approximately with the outer turning points of these excited-state vibrational wave functions.

FCFs between the calculated highest vibrational state ($v = 69$) of the electronic ground state were found to be on the order of 10^{-4} to 10^{-6} for the 2 0.5, 1 1.5, and 3 0.5 electronic states, as shown in Table 8. Contrary to the situation for the 2 0.5 and 1 1.5 states, none of the vibrational levels of the 3 0.5 state has non-negligible FCFs with the $v = 0$ and $v = 69$ levels of the electronic ground state at the same time. This is, however, a requirement for an effective experimental excitation/deexcitation process.

Our findings thus support a postulated two-step scheme mentioned before aiming at reaching the lowest rovibrational

TABLE 7: Selected Franck−Condon Factors between the Rovibronic Ground State and Vibrationally Excited States (v) of the Electronically Excited States of $^{87}Rb^{176}Yb$

state	v	ΔE (cm^{-1})	FC factor
1 0.5−2 0.5	0	5839	3.4D−11
1 0.5−2 0.5	1	5908	7.8D−10
1 0.5−2 0.5	2	5976	8.9D−09
1 0.5−2 0.5	14	6777	7.1D−03
1 0.5−2 0.5	15	6842	1.1D−02
1 0.5−2 0.5	16	6907	1.7D−02
1 0.5−2 0.5	23	7357	7.5D−02
1 0.5−2 0.5	24	7421	7.8D−02
1 0.5−2 0.5	25	7484	7.7D−02
1 0.5−2 0.5	35	8105	1.2D−02
1 0.5−2 0.5	36	8165	8.1D−03
1 0.5−2 0.5	37	8226	5.6D−03
1 0.5−1 1.5	0	6612	1.0D−10
1 0.5−1 1.5	1	6681	2.2D−09
1 0.5−1 1.5	2	6749	2.4D−08
1 0.5−1 1.5	13	7483	6.4D−03
1 0.5−1 1.5	14	7549	1.1D−02
1 0.5−1 1.5	15	7614	1.6D−02
1 0.5−1 1.5	22	8063	7.6D−02
1 0.5−1 1.5	23	8127	7.9D−02
1 0.5−1 1.5	24	8190	7.8D−02
1 0.5−1 1.5	34	8810	1.2D−02
1 0.5−1 1.5	35	8870	8.1D−03
1 0.5−1 1.5	36	8931	5.5D−03
1 0.5−3 0.5	0	9350	1.5D−01
1 0.5−3 0.5	1	9403	2.3D−01
1 0.5−3 0.5	2	9454	2.3D−01
1 0.5−3 0.5	3	9506	1.7D−01
1 0.5−3 0.5	4	9557	1.0D−01
1 0.5−3 0.5	12	9964	1.2D−04
1 0.5−3 0.5	13	10014	3.9D−05
1 0.5−3 0.5	14	10064	1.3D−05
1 0.5−3 0.5	20	10359	8.0D−09
1 0.5−3 0.5	21	10407	2.2D−09
1 0.5−3 0.5	22	10456	5.7D−10

TABLE 8: Selected Franck−Condon Factors between the Highest Excited Vibrational State ($v = 69$) of the Electronic Ground State and Vibrationally Excited States (v) of the Electronically Excited States of $^{87}Rb^{176}Yb$

state	v	ΔE (cm^{-1})	FC factor
1 0.5−2 0.5	0	5007	1.7D−04
1 0.5−2 0.5	1	5076	4.9D−05
1 0.5−2 0.5	2	5144	3.1D−05
1 0.5−2 0.5	14	5945	1.2D−05
1 0.5−2 0.5	15	6010	1.5D−05
1 0.5−2 0.5	16	6075	4.3D−05
1 0.5−2 0.5	37	7394	3.4D−05
1 0.5−2 0.5	38	7454	3.5D−06
1 0.5−2 0.5	39	7515	1.4D−05
1 0.5−1 1.5	0	5780	1.9D−04
1 0.5−1 1.5	1	5848	1.5D−05
1 0.5−1 1.5	2	5917	7.1D−05
1 0.5−1 1.5	13	6651	2.8D−05
1 0.5−1 1.5	14	6716	4.1D−06
1 0.5−1 1.5	15	6782	4.5D−05
1 0.5−1 1.5	37	8159	3.4D−06
1 0.5−1 1.5	38	8219	1.4D−05
1 0.5−1 1.5	39	8279	3.7D−05
1 0.5−3 0.5	0	8518	9.6D−15
1 0.5−3 0.5	1	8570	5.8D−14
1 0.5−3 0.5	2	8622	5.1D−16
1 0.5−3 0.5	12	9132	2.7D−05
1 0.5−3 0.5	13	9182	3.3D−05
1 0.5−3 0.5	14	9231	7.9D−06
1 0.5−3 0.5	20	9527	1.4D−04
1 0.5−3 0.5	21	9575	2.0D−05
1 0.5−3 0.5	22	9623	6.3D−05

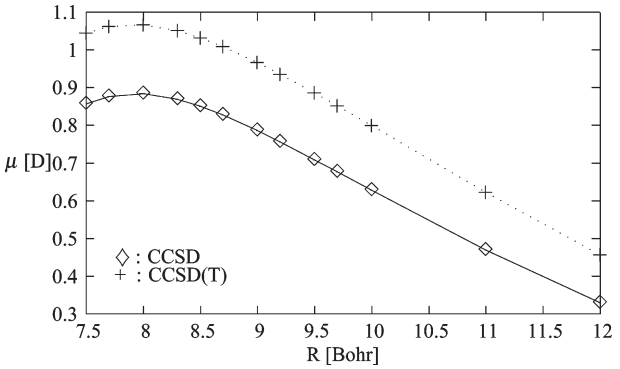

Figure 3. CCSD(T) and CCSD dipole moment curve in Debye with 23 explicitly correlated electrons. The vibrationally averaged dipole moment for CCSD and CCSD(T) is found to be 0.761 and 0.985 Debeye, respectively.

TABLE 9: Dipole Moments at R_e (μ_e) and the Vibrationally Averaged Dipole Moment μ_v for the CCSD and CCSD(T) Levels of Theory with 23 Explicitly Correlated Electrons and with CP Corrected Values

Method	μ_e (D)	μ_v (D)
CCSD-SF	0.763	0.761
CP-CCSD-SF	0.751	0.747
CCSD(T)-SF	0.987	0.985
CP-CCSD(T)-SF	0.977	0.974

level of the electronic ground state.[58] However, we propose to use either the 2 0.5 or 1 1.5 state as intermediate for this process.

3.5. Dipole Moment. Besides having a magnetic dipole moment from an unpaired electron, RbYb also exhibits an electric dipole moment of around 1 D, as illustrated in Figure 3. A fit of the CCSD and CCSD(T) dipole moment curves results in an electric dipole moment of 0.763 and 0.987 D, respectively, at the equilibrium bond distance. A slight decrease of around 0.01 D is observed if the CP correction is added to the ground state, as reported in Table 9. It should be noted that in these cases the dipole moment has not been CP corrected but has been evaluated at the CP-corrected equilibrium bond distance. In Table 9 we have also listed the vibrationally averaged dipole moment, which is only sligthly lower despite the large variation shown by the dipole moment across the rovibrational ground state.

4. Summary and Conclusions

In this study we demonstrate the capability of our relativistic all-electron quantum-chemical methodology to yield accurate ground and excited states on this new and challenging system by approaching the problem in a systematic way. We show that with our chosen MRCI model we are not only able to obtain excellent atomic data but also able to get close to the accurate CCSD(T) data around the equilibrium bond distance of the ground state. We furthermore report spectroscopic constants and Franck−Condon factors for ground and excited states.

Our coupled cluster calculations indicate that RbYb possesses a substantial dipole moment of almost 1 D, thus making it an excellent candidate for the study of dipole−dipole interactions and considering its magnetic dipole moment, making it accessible to magneto-optical trapping. The strongest candidates for reaching the rovibronic ground state via a two-step procedure (after the initial photoassociation), judging from the determined Franck−Condon factors, appear to be the two lowest excited electronic states. For these two states we find reasonable Franck−Condon factors both for the absorption and for the

emission simultaneously. We therefore propose the following two-color process. The longer wavelength laser should excite the molecule to levels with vibrational quantum numbers in the range of $v = 15-35$ in either the 2 0.5 or 1 1.5 potential wells followed by stimulated emission to the rovibronic ground state. This mechanism will give the largest combined Franck−Condon overlap. This picture can, however, change depending on how well the ground state is determined. For example, a shorter equilibrium bond distance for the ground state would favor the first two excited states, whereas a longer one would favor the third excited state. We have therefore performed high-level coupled cluster benchmark studies using a varying number of correlated electrons to calibrate our results.

The inclusion of higher excited states in this molecule necessitates core polarization from Yb 4f5p as these correlate to the atomic $Yb_{6s^16p^1}(^3P_{2,1,0})$ channels, thereby dramatically increasing the computational demand of the problem. Moreover, an accurate description of the $Rb_{4d^1}(^2D_{5/2,3/2})$ atomic limit, which will lie between the $Yb_{6s^16p^1}(^3P_{1,0})$ and $Yb_{6s^16p^1}(^3P_2)$ channels, would require additional higher angular momentum functions to be included in the basis set on Rb. Furthermore, Yb 4f−5d excitations need to be taken into account that are extremely difficult to compute properly. From the methodological aspect one would here also come to the limit of CI because with 31 explicitly correlated electrons size-extensivity errors would likely become sizable. A change to a size-extensive method would then be desirable. Such an approach is currently being investigated by extending the newly implemented general-order four-component multireference coupled cluster[39] to allow for the treatment of excited states.

Acknowledgment. We thank Axel Görlitz and his co-workers for inspiration, for helpful discussions, and for sharing their early findings with us. Financial support of this project by the Deutsche Forschungsgemeinschaft (reference number FL 256/5-1) and through the priority program SPP 1145, grant no. FL 356/2 is gratefully acknowledged. We also thank the Zentrum für Informations- und Medientechnologie (ZIM) at the Heinrich Heine University for providing computational time.

References and Notes

(1) Dulieu, O.; Raoult, M.; Tiemann, E. *J. Phys. B* **2006**, *39* (19).
(2) Cornell, E. A.; Wieman, C. E. *Comput. Phys. Commun.* **2002**, *3*, 476.
(3) Doyle, J.; Friedrich, B.; Krems, R. V.; Masnou-Seeuws, F. *Eur. Phys. J. D* **2004**, *31*, 149.
(4) Hudson, J. J.; Sauer, B. E.; Tarbutt, M. R.; Hinds, E. A. *Phys. Rev. Lett.* **2002**, *89*, 023003.
(5) Regan, B. C.; Commins, E. D.; Schmidt, C. J.; DeMille, D. *Phys. Rev. Lett.* **2002**, *88*, 071805.
(6) Zelevinsky, T.; Kotochigova, S.; Ye, J. *Phys. Rev. Lett.* **2008**, *100*, 043201.
(7) Schiller, S.; Korobov, V. *Phys. Rev. A* **2005**, *71*, 032505.
(8) Stwalley, W. C.; Wang, H. *J. Mol. Spectrosc.* **1999**, *195*, 194.
(9) Weinstein, J. D.; deCarvalho, R.; Guillet, T.; Friedrich, B.; Doyle, J. M. *Nature* **1998**, *395*, 148.
(10) Bethlem, H. L.; Berden, G.; Meijer, G. *Phys. Rev. Lett.* **1999**, *83*, 1558.
(11) Köhler, T.; Góral, K.; Julienne, P. S. *Rev. Mod. Phys.* **2006**, *78*, 1311.
(12) Korek, M.; Allouche, A. R.; Fakhreddine, K.; Chaalan, A. *Can. J. Phys.* **2000**, *78*, 977.
(13) Edvardsson, D.; Lunell, S.; Marian, C. M. *Mol. Phys.* **2003**, *101*, 2381.
(14) Knecht, S.; Jensen, H. J. A.; Fleig, T. *J. Chem. Phys.* **2008**, *128*, 014108.
(15) Le Roy, R. J. *LEVEL, A Computer Program for Solving the Radial Schrödinger Equation for Bound and Quasibound Levels*, Release 8.0; University of Waterloo: Waterloo, CA, 2007; http://leroy.uwaterloo.ca/programs/.
(16) Azizi, S.; Aymar, M.; Dulieu, O. *Eur. Phys. J. D* **2004**, *31*, 195.
(17) Sørensen, L. K.; Fleig, T.; Olsen, J. *J. Phys. B* **2009**, *42*, 165102.
(18) Aymar, M.; Dulieu, O. *J. Chem. Phys.* **2005**, *122*, 204302.
(19) Aymar, M.; Dulieu, O.; Spiegelman, F. *J. Phys. B* **2006**, *39*, S905.
(20) Nemitz, N.; Baumer, F.; Münchow, F.; Tassy, S.; Görlitz, A. *Phys. Rev. A* **2009**, *79*, 061403.
(21) Micheli, A.; Brennen, G. K.; Zoller, P. *Nature* **2006**, *2*, 341.
(22) Tassy, S.; Nemitz, N.; Baumer, F.; Höhl, C.; Batär; Görlitz, A. arXiv:0709.0827v1 [physics.atom-ph], 2007.
(23) Dyall, K. G. *J. Chem. Phys.* **1994**, *100*, 2118.
(24) Eliav, E.; Kaldor, U.; Ishikawa, Y. *Phys. Rev. A* **1995**, *52*, 291.
(25) Eliav, E.; Kaldor, U.; Ishikawa, Y. *Phys. Rev. A* **1994**, *50*, 1121.
(26) Visscher, L.; Dyall, K. G.; Lee, T. J. *Int. J. Quantum Chem.: Quantum Chem. Symp.* **1995**, *29*, 411.
(27) Visscher, L.; Lee, T. J.; Dyall, K. G. *J. Chem. Phys.* **1996**, *105*, 8769.
(28) DIRAC, a relativistic ab initio electronic structure program, Release DIRAC08(2008), written by L. Visscher, H. J. Aa. Jensen, and T. Saue, with new contributions from R. Bast, S. Dubillard, K. G. Dyall, U. Ekström, E. Eliav, T. Fleig, A. S. P. Gomes, T. U. Helgaker, J. Henriksson, M. Iliaš, Ch. R. Jacob, S. Knecht, P. Norman, J. Olsen, M. Pernpointner, K. Ruud, P. Sałek, and J. Sikkema (see http://dirac.chem.sdu.dk).
(29) Fleig, T.; Olsen, J.; Marian, C. M. *J. Chem. Phys.* **2001**, *114*, 4775.
(30) Fleig, T.; Olsen, J.; Visscher, L. *J. Chem. Phys.* **2003**, *119*, 2963.
(31) Fleig, T.; Jensen, H. J.; Olsen, J.; Visscher, L. *J. Chem. Phys.* **2006**, *124*, 104106.
(32) Pitzer, R. M.; Winter, N. W. *J. Phys. Chem.* **1988**, *92*, 3061.
(33) Yabushita, S.; Zhang, Z.; Pitzer, R. M. *J. Phys. Chem.* **1999**, *103*, 5791.
(34) Knecht, S.; Jensen, H. J. A.; Fleig, T. Large-Scale Parallel Configuration Interaction. II.Four-component double-group general active space implementation with application to BiH. *J. Chem. Phys.*, submitted for publication.
(35) Tilson, J. L.; Ermler, W. C.; Pitzer, R. M. *Comput. Phys. Commun.* **2000**, *128*, 128.
(36) Thyssen, J.; Fleig, T.; Jensen, H. J. A. *J. Chem. Phys.* **2008**, *129*, 034109.
(37) Knecht, S.; Jensen, H. J.; Sørensen, L. K. Four-component MP2 natural orbitals: An efficient way of selecting appropiate active spaces for coupled cluster and multiconfigurational self-consistent field calculations, in preparation.
(38) LUCIA, a general CI code written by J. Olsen (University of Aarhus) with contributions from H. Larsen and M. Fülscher.
(39) Sørensen, L. K.; Olsen, J.; Fleig, T. Kramers-Restricted Generalized Active Space Coupled Cluster. Implementation and Initial Application on BiH, manuscript in preparation.
(40) Fleig, T.; Sørensen, L. K.; Olsen, J. *Theor. Chem. Acc.* **2007**, *118*, 347 DOI: 10.1007/s00214-007-0265-y.
(41) Olsen, J. *J. Chem. Phys.* **2000**, *113*, 7140.
(42) Kallay, M.; Surjan, P. *J. Chem. Phys.* **2001**, *115*, 2945.
(43) Auer, A. A.; et al. *Mol. Phys.* **2006**, *2*, 211.
(44) Knecht, S.; Jensen, H. J. A general-purpose parallel four-component Kramers-restricted CI property module, unpublished work.
(45) Gomes, A. S. P.; Dyall, K. G. Manuscript in preparation. Available from the Dirac web site, http://dirac.chem.sdu.dk.
(46) Dyall, K. *J. Phys. Chem. A* **2009**, in press.
(47) Dyall, K. G. *Theor. Chim. Acta* **1998**, *99*, 366.
(48) Pulay, P. Analytical derivative techniques and the calculation of vibrational spectra. In *Modern Electronic Structure Theory, Part II*; Yarkony, D. R., Ed.; World Scientific Publishing Co. Pte. Ltd.: Singapore, 1995; Vol. 2, p 1191.
(49) http://old.iupac.org/reports/periodic_table.
(50) Sioutis, I.; Pitzer, R. M. *J. Phys. Chem. A* **2006**, *110*, 12528.
(51) Halkier, A.; Klopper, W.; Helgaker, T.; Jørgensen, P.; Taylor, P. R. *J. Chem. Phys.* **1999**, *111*, 9157.
(52) Boys, S. F.; Bernardi, F. *Mol. Phys.* **1970**, *19*, 553.
(53) van Duijneveldt, F. B.; van Duijneveldt-van de Rijdt, J. G. C. M.; van Lenthe, J. H *Chem. Rev.* **1994**, *94*, 1873.
(54) Chałasiński, G.; Szczęśniak, M. M. *Chem. Rev.* **2000**, *100*, 4227.
(55) Giese, T. J.; York, D. M. *Int. J. Quantum Chem.* **2004**, *98*, 388.
(56) Laschuk, E. F.; Martins, M. M.; Evangelisti, S. *Int. J. Quantum Chem.* **2003**, *95*, 303.
(57) Lim, I. S.; Lee, W. C.; Lee, Y. S. *J. Chem. Phys.* **2006**, *124*, 234307.
(58) Nemitz, N. *Dissertation, Mathematisch-Naturwissenschaftliche Fakultät*; Heinrich-Heine-Universität Düsseldorf: Düsseldorf, Germany, 2008.
(59) Ralchenko, Yu.; Kramida, A. E.; Reader, J.; NIST ASD Team. *NIST Atomic Spectra Database (version 3.1.5)*; National Institute of Standards and Technology: Gaithersburg, MD, May 3, 2009; http://physics.nist.gov/asd3.

JP904914M

Paper 4

André Severo Pereira Gomes, Lucas Visscher, Hélène Bolvin, Trond Saue, Stefan Knecht, Timo Fleig, and Ephraim Eliav

The electronic structure of the triiodide ion from relativistic correlated calculations: A comparison of different methodologies.

unpublished manuscript.

The Electronic Structure of the Triiodide ion from Relativistic Correlated Calculations: A Comparison of Different Methodologies

André Severo Pereira Gomes,[a,b], Lucas Visscher[a], Hélène Bolvin[b], Trond Saue[b], Stefan Knecht[c], Timo Fleig[c,d] and Ephraim Eliav[e*]

[a] *Department of Theoretical Chemistry, Faculty of Sciences, Amsterdam Center for Multiscale Modeling, Vrije Universiteit Amsterdam, De Boelelaan 1083, 1081 HV Amsterdam, The Netherlands*

[b] *Laboratoire de Chimie Quantique, Institut de Chimie de Strasbourg, LC3-URM 7177 CNRS/Université Louis Pasteur, 4 rue Blaise Pascal, F-67000 Strasbourg, France*

[c] *Institute of Theoretical and Computational Chemistry, Heinrich-Heine-University Duesseldorf, Universitaetsstr. 1 D-40225 Duesseldorf, Germany*

[d] *Laboratoire de Chimie et Physique Quantiques, I.R.S.A.M.C., Université Paul Sabatier, 118 Route de Narbonne, F-31062 Toulouse, France*

[e] *School of Chemistry, Tel Aviv University, 69978 Tel Aviv, Israel*

(Dated: September 23, 2009)

The triiodide ion I_3^- exhibits a complex photodissociation behavior, the dynamics of which are not yet fully understood. This complexity is due to the fact that various dissociation channels are accessible under experimental conditions. As a first step towards determining the full potential energy surfaces of this species for subsequent simulations of its dissociation processes, we investigate the performance of different electronic structure methods (Time-Dependent Density Functional Theory, Complete Active Space Perturbation Theory to 2nd order (CASPT2) , Fock space Coupled cluster and Multi-Reference Configuration Interaction) in describing the ground and excited states of the triiodide ion along the symmetrical dissociation

path. This is a first step towards the determination of the full potential energy surface of this species for subsequent simulations of its dissociation process. Most of our methods include scalar relativity and spin-orbit coupling in the orbital optimization, providing useful benchmark data for the more common two-step approaches in which spin-obit coupling is introduced in the configuration interaction. Indeed our calculations indicate that the Spin-Orbit-CASPT2 method gives good agreement with Fock-space coupled cluster at significantly lower cost. It can thereby be applied in regions where the Fock space calculations are difficult to converge.

I. INTRODUCTION

Recent years have seen extraordinary advances in experimental techniques to probe chemical processes such as reaction dynamics in very short timeframes. A wide range of techniques based upon pump-probe schemes[1], where the species under consideration are put in a nonstationary state by one light source (pump) and monitored by another (probe), allow researchers to gain information regarding the dynamical behavior of the system as complementary to whatever information can be obtained by more conventional spectroscopic techniques. A particularly interesting field, where such fast techniques are very helpful, is the study of the dynamics of stable negative ions[2]. One is often not interested in the anions themselves but rather on using them, in combination with spectroscopic techniques based upon photodetachment or photodissociation processes, to access species that isolated would not be stable enough for measurements.

Some ionic species, however, are important in their own right, apart from being used as precursors to other systems. A very well-known example is the triiodide ion (I_3^-). From a chemist's point of view[3], this relatively simple system is very interesting as it is (a) a structural analogue of a transition state in S_N2 reactions; and (b) an example of hyperconjugation, due to its three-center four-electron bond and associated violation of the octet rule. The widely accepted bonding picture of I_3^- is that of a (σ, π) system arising from the combinations of $5p$ orbitals on the three iodine atoms. In ΛS-coupling the ground state con-

*Corresponding author: Lucas Visscher E-mail:visscher@chem.vu.nl

figuration is accordingly $\sigma_u^2\pi_u^4\pi_g^4\pi_u^{*4}\sigma_g^2$ where the *gerade* orbitals are essentially non-bonding and the LUMO the anti-bonding σ_u^*. Some DFT functionals place the anti-bonding π_u^* rather than σ_g^2 as the HOMO, while Spin-Orbit Coupling (SOC) effects induce some mixing between the σ and π orbitals.

While early experimental information on the electronic structure of I_3^- was obtained from UV spectroscopy[4], more detailed information has been gained from photodissociation studies in more recent works. These studies have originally been performed in solution[5–9]. Questions arose as to whether it would be possible for the system to display a bent configuration at equilibrium, instead of the linear one proposed initially (the latter being the most accepted configuration). By contrast, experiments on the system in the gas-phase by Neumark and coworkers[10–12], and by Nakanishi and coworkers[13], strongly suggest that the ground state for this species is linear and centrosymmetric.

Compared to the wealth of experimental data on the triiodine species, relatively few theoretical studies have been performed. Kosloff and coworkers[14] have, at about the time of the gas-phase experiments by Neumark[10, 11], presented an extensive study of the potential energy curves of the I_3^-, I_2 and I_2^- species, which are thought to be involved in the photodissociation dynamics of I_3^-. Their results, obtained with a combination of MultiReference Configuration Interaction (MRCI) calculations and a diatomics-in-molecule (DIM) treatment where SOC effects were included, were the most accurate published at the time. However, the authors themselves considered the basis set used in the DIM treatment relatively small easily allowing for quantitative improvements on this early study. More recently, as a complement to their experimental work, Nakanishi and coworkers[13] have also performed Spin-Orbit Configuration Interaction (SO-CI) calculations which explored not only the potential along the symmetric stretch of I_3^- but also along the asymmetric stretch. Given the limited accuracy of the SO-CI method and the still rather modest basis set size, also this theoretical investigation still leaves room for improvement.

Accordingly, the theoretical studies performed so far, albeit very helpful in understanding some aspects of the experimental data (such as the kind of states involved in the two experimentally observed absorption bands), are not sufficiently accurate for a direct comparison with experiment in terms of quantities associated with the dynamical behavior of the system, such as branching ratios. To enable this kind of analysis, it should be possible to calculate the whole of the potential energy accurately in order to avoid artifacts in

the dynamics. This has motivated us to investigate the use of different methodologies for describing the electronic structure of the triiodide species, with the goal of arriving at a faithful representation of the potential energy surface for the system that can later be used in dynamical studies, e.g. by wave-packet dynamics.

Even though I_3^- can be considered a closed shell species and experimental evidence indicates two-body dissociation into closed-shell species as well, it is important to account for SOC to achieve an accurate description of the full potential energy surfaces. The reason is that I_3^- consists of heavy elements for which spin-orbit effects are intrinsically important and have a significant impact on transition probabilities and intersystem crossings in the excitation/deexcitation processes. Apart from including SOC, theoretical methods should be able to describe the full PES and account for dynamical electron correlation at a reasonable cost, given the amount of calculations involved in determining a full potential energy surface.

As not all methods will fit this description we have chosen to compare expensive but accurate multireference Coupled Cluster (CC) and Configuration Interactions (CI) at selected points along the symmetric stretch of the molecule to methods that will allow full coverage of the ground and excited state potential energy surfaces. The wave function based methods employed were: (a) the Intermediate Hamiltonian Fock-space coupled cluster method of Eliav, Kaldor and coworkers[15–17]; (b) the relativistic multireference CI method of Fleig and coworkers[18, 19];and (c) the Spin-Orbit Complete Active Space (CAS) Perturbation Theory to 2nd order (PT2) method (SO-CASPT2) of Roos and coworkers[20, 21]. Apart from these, we decided to also explore the more economial time-dependent DFT (TDDFT) method[22] as this method provides a simple orbital picture for the excitation spectra. These TDDFT calculations are of course not expected to yield better results than any of the methods above due to the well-known shortcomings (as, for instance, in describing charge-transfer (CT) excitations [23, 24] or that, within the adiabatic approximation, TDDFT can only describe single excitations[25–27]), of the current-day functionals.

The paper is organized as follows: in section II we present the details of the calculations performed with the different methodologies; in section III we compare the performance of the different methods in calculating excitation energies of I_3^-, both at selected bond lengths and at the equilibrium geometries for the symmetric configuration. We also take the opportunity to discuss results for the triiodide radical (I_3), a species that was experimentally observed

in photoionization studies involving I_3^- in the gas phase[28, 29], and that has also been investigated theoretically by Kosloff and coworkers. Finally, in section IV we assess the relative strengths and weaknesses of each method and provide concluding remarks.

II. COMPUTATIONAL DETAILS

All calculations described here have been performed along the symmetric stretch coordinate, with I–I bond lengths $r_{\text{I-I}}$ in the range of [2.60 : 6.00] Å. In order to compare the different methodologies we have chosen two geometries in which to calculate the vertical excitation energies, apart from those obtained at the equilibrium structures for the different methods. These geometries are $r = 2.84$ and 2.93 Å, corresponding to bond lengths in the vicinity of the equilibrium geometries for I_3 (from the MRCI calculations of Kosloff and coworkers[14] and I_3^- (equilibrium geometry reported from solid-state studies [30]), respectively.

A. IHFSCC

Intermediate Hamiltonian Fock-space coupled cluster[15–17] (IHFSCC) calculations were performed with a development version of the DIRAC[31] program. For describing the spectrum of I_3^- with the IHFSCC method we have taken the anion as a starting point, and proceed from the ground-state through the $(1h, 0p)$ and $(0h, 1p)$ sectors in order to arrive at the $(1h, 1p)$ sector and, therefore, at the excitation energies:

$$I_3^-(0h, 0p) \rightarrow \{I_3(1h, 0p), I_3^{2-}(0h, 1p)\} \rightarrow I_3^{-(*)}(1h, 1p) \tag{2.1}$$

For reasons of computational efficiency, the eXact 2-Component Hamiltonian (X2C) scheme of Iliaš and Saue[32] was used. Two-electron spin same-orbit (SSO) and spin-other orbit (SOO) contributions were included via atomic mean-field integrals obtained with the AMFI[33, 34] code.

The triple zeta basis sets of Dyall[35, 36] were employed in all calculations. These were kept uncontracted and augmented with diffuse functions. Given the flexibility of such basis sets with respect to adding correlating functions, two different sets were defined: a valence correlation set ("aVTZ"), where one correlating f-type function was added to the augmented

SCF set, yielding a (29s22p16d2f) basis set; and a core-valence correlating set ("aCVTZ"), which is a superset of aVTZ with additional $2f1g$ set of functions added.

In combination with these two sets different correlation spaces were employed: the first ("Q_1") is used together with basis set aVTZ and includes the orbitals with orbital energies (ϵ) between -1 and 4 hartree. This means that in the occupied orbital space the σ, π bonding system and three other σ-type orbitals arising from the $5s5p$ orbitals of iodine are present. The second correlation space ("Q_2") is used together with basis set aCVTZ and includes the orbitals with orbital energies between -3 and 12 hartree. This corresponds to enlarging Q_1 by including the occupied $4d$ electrons of iodine apart from more virtual orbitals. The combinations aVTZ/Q_1 and aCVTZ/Q_2 will be referred to as IHFSCC(a) and IHFSCC(b), respectively.

A crucial ingredient of IHFSCC calculations to prevent convergence problems due to intruder states is the definition of the model (P_m) and intermediate (P_I) spaces that comprise the active space $P = P_m + P_I$ [16, 17]. After testing different spaces at the fixed geometries mentioned above, we found that convergence problems were generally avoided for $r < 4$ Å, when the P_m space contained 8 occupied (one σ_g, one π_g, two π_u and one σ_u orbitals) and 11 virtual orbitals (two σ_g, one π_g, three σ_u and two π_u orbitals) with a full P space containing 11 occupied (5 of g and 6 of u parity) and 22 virtual (12 of g and 10 of u parity) orbitals. For bond lengths larger than 3.58 Å, however, it was not possible to obtain convergence for the $(1h, 1p)$ sector for this partition.

B. MRCI

Multireference Configuration Interaction (MRCI) calculations have been carried out with the relativistic double group CI program `LUCIAREL` [18, 19] which recently has been extended [37, 38] for parallel computer applications. In all of the calculations reported here the "aCVTZ" basis set and the eXact 2-Component (X2C) Hamiltonian including 2-electron SSO and SOO corrections provided by the AMFI[33, 34] code have been employed.

The molecular spinors for the CI calculations have been obtained by an average-of-configuration Hartree-Fock calculation, where the open shells were defined as the 8 occupied Kramers pairs as in the CC application above, and in addition the antibonding σ_u orbital, corresponding to an active subspace with 16 electrons in 9 Kramers pairs. This type of

Hartree-Fock wave function comprises a good starting point for relativistic MRCI studies when ground and electronically excited states are under investigation, since it provides a balanced description of these states. The concept of General Active Spaces (GAS) has been employed for constructing the CI expansion. In the present case, all Slater determinants with zero, one, and two particles in the external space (truncated at 3 hartrees) were included and all possible active-space distributions were allowed for the remaining electrons. These active-space distributions were defined by a CAS space corresponding to the above space used in the average-of-configuration Hartree-Fock calculation (16 electrons in 9 Kramers pairs, or 15 electrons in 9 Kramers pairs in the case of neutral I_3, "MRCI(a)"), and an additional space including the iodine 5s orbitals where a restriction of up to two holes was imposed ("MRCI(b)"). The resulting relativistic CI wave function describes the correlation of 16 (15 in the case of neutral I_3) or 22 electrons and consists of roughly 77 million Slater determinants in the latter case.

C. CASPT2

Calculations with the CASPT2 method were carried out with the MOLCAS code [39] (version 7.0), within the CASSCF/CASPT2/SO-RASSI approach. In this approach, scalar relativistic effects are included in the CASSCF[20] and CASPT2[21] calculations via the Douglas-Kroll-Hess[40] Hamiltonian, and in a subsequent calculation the CASPT2 spin-free states are used by the RASSI program to set up a spin-orbit coupling Hamiltonian[41]. In this Hamiltonian the one- and two-electron spin-orbit integrals are calculated in a mean-field fashion via the AMFI[33, 34] code. The basis set used in these calculations was the ANO-RCC[42] set.

The CASSCF active space used consisted of 16 electrons in the 9 orbitals arising from the $5p$ orbitals of the three iodine atoms. We have kept the core orbitals (i.e. up to and including the $3d$ orbitals) frozen in the CASSCF (and subsequent CASPT2) calculations. The CASSCF states that entered the multi-state CASPT2 calculations have been obtained from state-averaged calculations over nine (9) roots for $^1\Sigma$, six (6) roots for $^1\Pi$, eight (8) roots for $^3\Sigma$ and six (6) roots for $^3\Pi$, respectively. In the CASPT2 calculations an IPEA shift of 0.25 a.u. was used [43].

D. TDDFT

Time-dependent DFT (TDDFT) calculations[22] were carried out with the ADF[44] code. We used the statistical averaging of model orbital potentials (SAOP) [45], in combination with the TZ2P basis set[46]. Scalar relativistic and spin-orbit effects were included via the zeroth-order regular approximation (ZORA) [47, 48]. In the TDDFT calculations non-collinear spin magnetization was used.

III. RESULTS AND DISCUSSION

In this section we discuss the results for the triiodide ion species obtained with the different methods. We begin by investigating the performance of the different methods in determining ground-state spectroscopic constants, before addressing the electronic spectrum. Given the exploratory nature of this paper, we will only compare methods for selected structures along the symmetric stretch coordinate, thereby restricting ourselves to a part of the full potential energy surface.

We will focus mainly on vertical excitations calculated at selected geometries, but will also address "adiabatic" excitations for this particular cut of the surface, as a way to gain insight on how the different methods represent the overall shape of the surfaces. Finally, we will take a more detailed look the 0_u states, in particular the absorbing 0_u^+ states, comparing the energetics and the excitation picture, in terms of the respective molecular orbitals for the different methods, before discussing the triiodine radical.

A. Ground-state Spectroscopic constants for I_3^-

The ground-state spectroscopic constants of I_3^- obtained here are shown in table I. We take the experimental value[30] in the solid state ($r_e = 2.93$ Å) as a measure, since to the best of our knowledge, there are no experimental bond lengths for the triiodide ion in gas-phase.

In this case, CASPT2 shows a slight (about 0.02 Å) underestimation, whereas IHFSCC(a) and MRCI(a) show a similar overestimation (about 0.04-0.05 Å). DFT, in turn, overestimates r_e by about 0.07 Å. We should thereby note, however, that the SAOP functional was not derived with the aim of providing accurate structures. If a larger degree of electron correlation is taken into account in the coupled cluster case, as done for IHFSCC (b) –

where the $4d$ shell is included in the occupied space and the virtual space is truncated at a higher energy – the obtained bond length is in good agreement with experiment, with a deviation of less than 0.02 Å. The MRCI results of Kosloff including spin-orbit coupling are roughly in between the two IHFSCC results, whereas the spin-free MRCI values match the experimental number. The rather good agreement of wavefunction-based methods and the experimental structure thus suggests that environmental effects on the bond length are small.

A similar picture is seen for the harmonic frequencies. Discrepancies between MRCI, CASPT2, IHFSCC and both experiment[49] and the spin-free MRCI calculations of Kosloff are of the order of a few cm^{-1}, whereas DFT underestimates the frequency by 10 cm^{-1}. The spin-orbit numbers of Kosloff, on the other hand, show rather large discrepancies (17 cm^{-1}), which may be due to artifacts arising from their diatomics-in-molecules treatment.

B. Benchmark Calculations of the Electronic Spectra of I_3^-

In the comparison of calculated spectra, we have chosen to use two sets of geometries as reference: the first uses the experimental bond length ($r = 2.93$ Å) for all methods, whereas in the second the equilibrium geometries for the individual methods (taken from table I) are used. The corresponding spectra can be found in tables II and III, respectively.

In order to make the discussion easier, we will take IHFSCC(b) as the reference and discuss the performance of the other methods relative to it. Moreover, we restrict ourselves to the first 18 excited states, which go up to about 4.5 – 5.0 eV. This is due to the increasing importance of double excitations for higher energies, which are readily captured by MRCI and CASPT2 but neither by TDDFT nor by the IHFSCC calculations on the $(1h, 1p)$ sector of Fock-space. This renders the comparison of the different methods less useful than that for these lower states, which are dominated by single excitations.

1. Vertical excitations

Inspecting first table II, we immediately see some general trends: CASPT2 and MRCI tend to overestimate the IHFSCC excitation energies, whereas TDDFT shows the lowest excitation energies among all methods considered. One can also see that the degree of elec-

tron correlation introduced by the different methods affects distinct regions of the spectrum differently. For the lowest 10 excited states, the ordering of states is consistent with most methods whereas for higher states, which are energetically much closer to each other, small variations in the correlation treatment result in significant reorderings.

It is, however, rather difficult to obtain a clear picture of the performance of the methods by such an inspection alone. We have therefore followed the approach of Helgaker and coworkers[50] and performed a statistical analysis of the errors for each method; in particular, we calculated the mean error $\bar{\Delta}$ and its standard deviation Δ_{std}, as well as the mean absolute error $\bar{\Delta}_{\mathrm{abs}}$ and the maximum absolute error Δ_{max} for the corresponding excited states taking IHFSCC(b) as a reference. These quantities can be found at the bottom of table I.

From this analysis, it becomes clear that IHFSCC(a) setup yields only small deviations relative to the larger IHFSCC(b) calculation. This is quantified by the small mean errors (signed and absolute) and a small standard deviation (0.02 eV), suggesting that core-valence correlation does not play a prominent role in describing the transitions to low-lying excited states. TDDFT underestimates ($\bar{\Delta} = 0.24$ eV) the excitation energies, but perhaps more worrisome is that Δ_{std} is rather large (0.24 eV), indicating large non-systematic errors. At this geometry CASPT2 reproduces better the IHFSCC(b) reference than the MRCI approaches. The mean error of MRCI(b) is much larger than that of CASPT2, although Δ_{std} is in both cases essentially the same and about half of the value for TDDFT. Not correlating the 5s electrons, as done in the smaller MRCI(a) setup, increases the mean error of MRCI to about the same size as found in TDDFT, but the modest value of Δ_{std} indicates still a rather systematic deviation, similar to CASPT2 and MRCI(b). The systematic nature of the errors for MRCI is also seen by inspecting $\bar{\Delta}_{\mathrm{abs}}$, the magnitude of which is about the same as the corresponding $\bar{\Delta}$.

While it is beyond the scope of this paper to present a detailed analysis of the difference between IHFSCC and other methods, it is nevertheless instructive to consider comparisons of excitation energies calculated by IHFSCC and the linear response coupled cluster (LRCC) method done by various authors[50–54]. From those studies it becomes clear that LRCC and IHFSCC may yield significantly different excitation energies. Some evidence from recent studies for different molecular systems performed by some of us[55] as well as by other authors[56–59] seems to point to a systematic upwards shift in LRCC excitation energies compared to IHFSCC ones, similar to what is observed here when comparing MRCI and

IHFSCC. This could be consistent with the different parametrization used in describing the excitations from the ground to the excited states (linear in MRCI and LRCC, exponential for IHFSCC). It is less straightforward to rationalize the discrepancies between CASPT2 and IHFSCC as these methods describe the ground state with a rather different wave function. Based upon previous experience[55, 60–62] we expect CASPT2 results for low-lying excited states to deviate up to a few tenths of an eV from IHFSCC, but is more difficult to predict either an increase or a decrease of the excitation energies.

Since the comparison given above was done at the fixed experimental distance that is not optimal for any of the methods, we consider in table III also the results obtained at the equilibrium geometries obtained for the different methods (given previously in table I). The statistical analysis here reveals a very similar picture as in table II with respect to the standard deviation for all methods. The mean and maximum errors change considerably relative to the previous table, however. For TDDFT the underestimation of the excitation energies increases by going to the longer equilibrium distance of that method. For CASPT2, that has an optimal bondlength shorter than the experimental distance, the agreement with IHFSCC(b) (that has a longer bondlength) becomes less good. Shifting to its longer bondlength, MRCI(a) now approaches IHFSCC(a) although the maximum error is still quite large. The IHFSCC(a) results, finally, again indicate that core-valence correlation (correlating deeper than the 5s) could be disregarded when constructing the full potential energy surfaces.

The statistical analysis at these selected geometries indicates that both MRCI and CASPT2 are able to provide a balanced treatment of the ground and excited state surfaces. A problem with MRCI(a), the only feasible CI approach to cover the whole surface, is the fact that the optically active states (indicated in boldface in both tables II and III) that are well described with IHFSCC(b) exhibit relatively large errors when treated with MRCI(a). While the IHFSCC(b) reference calculations reproduces both experimentally observed transitions quite well (3.38-3.41 eV and 4.22-4.28 eV for the first and second 0_u^+ states, respectively[4]), MRCI(a) describes the first 0_u^+ (3.47 eV) rather well but places the second at too high energy (4.67 eV). CASPT2, due to the general upward shift discussed above, overestimates both excitation energies but shows a systematic error that leaves the splitting between these states in good agreement with IHFSCC(b).

2. *Explorations of the dissociative region*

The discussion so far has dealt with geometries at and close to the ground-state equilibrium structures. However, in order to be useful in modeling the dissociation process of I_3^- the potential surfaces of the excited states far from the equilibrium region have to be properly described as well. In order to probe the relative accuracy of the methods, we have chosen to investigate displacements along the symmetric stretch coordinate. This represents a one-dimensional cut through the full three-dimensional surface enabling us to define local minima (and harmonic frequencies) for the different excited states in this restricted geometry. One should thereby keep in mind, however, that such extrema do not necessarily correspond to the true spectroscopic constants for the corresponding states as we did not investigate the curvature of the surface in directions orthogonal to the symmetric stretch coordinate.

A further restriction in the current study is the presence of intruder states that made it impossible to convergence the IHFSCC calculations at internuclear distances larger than 3.6 Å . This means that we can only compare with the IHFSCC(b) reference at relatively short distances. Similarly we could not obtain TDDFT results beyond about 3.9 Å due to triplet instabilities. Both problems do not appear in the CASPT2 and MRCI(a) calculations for which we obtained information also for large I-I internuclear distances. This part of the surface is relevant due to conical intersections involving the 0_u^+ states that are of importance in the photodissociation process. Our CASPT2 results indicate that for the optically active 0_u^+ states a slice of a conical intersection between the second and third 0_u^+ occurs near $r = 3.8$ Å, as can be seen in figure 1. This is in line with the findings of Nakanishi and coworkers[13], who have observed a number of conical intersections and avoided crossings **in this region** *check this !* in their SO-CI calculations.

As the MRCI(b) calculations are computationally too expensive to cover the whole surface we will in the following focus on CASPT2 but present MRCI(a) calculations to allow for some comparison with the MRCI approach.

With respect to bond lengths given in table IV, we observe that CASPT2 tends to consistently underestimate the bond lenghts compared to IHFSCC(b) by about 0.036 Å (in line with the difference of 0.034 Å for the ground state), whereas MRCI(a) overestimates them by about 0.06 Å, in both cases with rather small standard errors. The differences between

IHFSCC(a) and IHFSCC(b) are again not very significant, and will **not be shown***sorry, can we put them back in (LV)*. TDDFT gives too long bond lengths ($\bar{\Delta} \simeq 0.2$ Å) in line with the overestimation seen in the ground state.

For harmonic frequencies, both CASPT2 and MRCI(a) overall reproduce rather well the IHFSCC(b) frequencies, with relatively small mean errors ($\bar{\Delta}$ = 2 and -12 cm^{-1}, respectively). What is striking is that, in spite of the small $\bar{\Delta}$ for frequencies, the corresponding values of $\Delta_{\rm std}$ are relatively high (and about the same as $\bar{\Delta}_{\rm abs}$). The calculated harmonic frequencies for the wavefunction-based methods agree rather well, and generally lie between 60 and 80 cm^{-1}*in the table we have very different values, going down to 28 cm and varying wildly between methods, these fits really need checking, or we should omit frequencies entirely as they are not guaranteed to correspond to minima anyhow*, giving us confidence that the three methods are able to provide a fairly consistent description of the shape of the potentials at the vicinity of the corresponding minima.*we should discuss symmetry breaking here as it may affect frequencies*

The rather systematic behavior of MRCI(a) and CASPT2 carries over to the $\bar{\Delta}$ and $\Delta_{\rm std}$ values for the excitation energies that may be compared with the analysis given for the vertical excitations (table III). This is particularly the case for CASPT2, which shows essentially the same $\bar{\Delta}$, $\Delta_{\rm std}$ and $\bar{\Delta}_{\rm abs}$ values as before. And, while the CASPT2 excitation energies show good agreement with IHFSCC(b) and can very well be used as they are, this systematic nature of the errors can be perhaps exploited to further bring the results close to IHFSCC(b) by applying global shifts to the CASPT2 potential energy surfaces. *here I really need the final fitted data to say something meaningful*

Such an approximation is demonstrated in figure 1, where we show, for the optically active 0_u^+ states the IHFSCC(b) cuts of the potential energy surface along corresponding cuts of the CASPT2 potential, after a shift of 0.15 eV was applied to the excited states. In the latter case we have also shifted the bond lengths by 0.035 Å to compensate for the underestimation of the bond lenghts in CASPT2. After these corrections, we observe a very good agreement for the ground and excited states, with rather small discrepancies for the second 0_u^+ state. Agreement for the first 0_u^+ state, however, seems to be somewhat poorer than for the second.**the figure captions are not consistent, check whether this is the new picture**

3. A closer look on 0_u^+ states

The two strong, allowed transitions for I_3^- occur from the $\Omega = 0_g^+$ ground state to two states with $\Omega = 0_u^+$. Table V displays the dominant contributions to these transitions. If available we also show oscillator strengths for the corresponding transitions. Since the CASPT2 calculations were done in a two-step fashion we can also analyze the composition of these excited states in terms of spinfree states. To a first approximation one can view these states as $^3\Pi_u$ and $^1\Sigma_u^+$, the former borrowing intensity from the latter through the spin-orbit coupling. This picture correlates very well with the DIM-SO results of Kosloff and coworkers[14]. In an orbital picture all methods give the same description, with different mixing of the two transitions from the occupied σ_g and π_g orbitals to the σ_u `LUMO`.

In the IHFSCC(b) calculations two additional excitations appear that can be interpreted as providing orbital relaxation of the `LUMO`. Since the DFT calculations also include spin-orbit coupling at the SCF stage we see a similar picture as for IHFSCC and MRCI, except that relaxation effects do not play an important role (since the virtual orbitals see the same potential as the occupied ones).

The peak separation energies for I_3^- are experimentally found to be in the 0.78–0.90 eV range, depending on the environment in which the triiodide species is embedded [4, 6]. Their relatively narrow range of variation in very different media justifies the assumption that gas-phase values should fall into a similar range.

Inspecting the lowest two 0_u^+ states, we observe that the TDDFT (SAOP) energy difference for the vertical excitation is much too high (1.47 eV) compared to the experimental values. The vertical peak separations for CASPT2 and IHFSCC(b), on the other hand, are in very good agreement with experiment (0.94 and 0.91 eV respectively). This is significantly better than the results of Kosloff and coworkers[14], for which the peak separation is 0.99 eV, and rather similar to the results of Nakanishi and coworkers[13], who obtained a value of 0.91 eV based on vertical excitation energies. The peak separation of 1.14 eV from the MRCI(a) results, on the other hand, does not match the experiment very well, as already discussed above.

C. Benchmark Calculations on I_3: Electronic Spectra and Electron affinities

Given that the IHFSCC results for the $(1h, 0p)$ sector are generated as by-products of the excitation energies determination for I_3^-, we can also present spectroscopic constants and vertical and adiabatic excitation energies for this species, calculated with IHFSCC(b). We furthermore provide a comparison of this radical IHFSCC, CASPT2, and MRCI at $r = 2.84$ Å, which is the geometry employed by Kosloff and co-workers[14] for the same system. These results are also shown in table VI.

The excitation energies calculated at $r = 2.84$ Å are in good agreement with those of Kosloff *et al.*, and, for the first two excited states, also with the experimental data. The $\Omega = 3/2_g$ third excited state has a much longer bondlength than the ground state which may explain the 0.1 to 0.2 eV overestimation found relative to the experimental value when calculated as vertical excitation. The adiabatic results for IHFSCC(b) indeed show a decrease of 0.10 eV from the vertical to the adiabatic excitation energy.

In line with the discussion above, we see that the results obtained with the different methods are fairly consistent. We find a ground state with $\Omega = 3/2_u$, followed by states of $\Omega = 1/2_g, 1/2_u$, $3/2_g$ and $1/2_g$, respectively, in agreement with the experimental assignment[28, 29].

The CASPT2 excitation energies are lower than those of IHFSCC(b) by about 0.1–0.2 eV with the exception of the first excited state, which is higher for CASPT2. In this case, however, MRCI and IHFSCC are much more alike than for I_3^-, with discrepancies generally smaller than 0.1 eV. This strong similarity could be due to the fact that, for the $(1h, 0p)$ sector used here the exponential parametrization of IHFSCC for the excited states is truncated at the linear term and therefore essentially the same as in MRCI [51–54].

From the IHFSCC(b) calculations we furthermore obtain an adiabatic (vertical) electron affinity (AE) of 4.29 eV (4.20 eV) which compares well with the adiabatic AE of 4.15 $\pm$0.12 eV, including zero-point vibrational corrections, obtained experimentally from a thermodynamic cycle [63], as well as the vertical detachment energy of I_3^- of 4.25 eV reported by Choi *et al.* [29].

IV. CONCLUSIONS

We have performed correlated electronic structure calculations including spin-orbit effects at high levels of theory on the triiodide ion (I_3^-) and the radical (I_3). The agreement between the different wavefunction-based methodologies employed is reasonable, as is their agreement with experimental results. An exploratory TDDFT calculation with the SAOP functional provides a qualitatively correct picture not too far from equilibrium distance but shows unsystematic errors that prohibit use in quantitative description.

With respect to I_3^-, of the different methodologies evaluated, it can be said that the Intermediate Hamiltonian Fock-space coupled cluster is the method that most accurately and consistently provides a picture which is both qualitative and quantitatively correct for the excitation processes taking place in the initial steps in the photodissociation of the triiodide ion and the triiodine radical. This method is not applicable to the complete potential energy surface, but we have been able to show that other wavefunction-based methods can reproduce the benchmark IHFSCC results rather well.

While it can be argued that for the triiodide species MRCI is slightly more accurate than CASPT2 with perturbative inclusion of spin-orbit effects, the latter has two interesting advantages: for one thing, it is computationally much more efficient than MRCI, and for another its errors seems to be very systematic for all electronic states considered. This systematic nature of errors is observed, in particular for energies, allowing for global correction to be applied to the potential energy surfaces in order to bring them in agreement with IHFSCC. The situation is somewhat different for the triiodine radical, where MRCI performs clearly better than CASPT2.

V. ACKNOWLEDGEMENTS

We wish to thank Prof. Ronnie Kosloff for calling our attention to the need for a more accurate description of the potential energy surfaces for the triiodide dissociation problem. Moreover, we thank the DEISA Consortium (co-funded by the EU, FP6 projects 508830 / 031513), for support within the DEISA Extreme Computing Initiative (`www.deisa.org`). In particular, we wish to acknowledge the work done by Walter Lioen (SARA/NL) in improving the efficiency of the 4-index transformation code within the DIRAC program for the

architectures used.

[1] M. Fushitani, *Annu. Rep. Prog. Chem., Sect. C: Phys. Chem.*, 2008, **104**, 272–297.

[2] D. M. Neumark, *J. Chem. Phys.*, 2006, **125**, 132303.

[3] G. A. Landrum, N. Goldberg, and R. Hoffmann, *J. Chem. Soc. Dalton Trans.*, 1997, pp. 3605–3613.

[4] W. Gabes and D. J. Stufkens, *Spectrochim. Acta A*, 1974, **30**, 1835–1841.

[5] M. Mizuno, J. Tanaka, and I. Harada, *J. Phys. Chem.*, 1981, **85**, 1789–1794.

[6] H. Isci and W. R. Mason, *Inorg. Chem.*, 1985, **24**, 271–274.

[7] T. Kühne and P. Vöhringer, *J. Chem. Phys.*, 1996, **105**, 10788–10802.

[8] T. Kühne, R. Küster, and P. Vöhringer, *Chem. Phys.*, 1998, **233**, 10788–10802.

[9] T. Kühne and P. Vöhringer, *J. Phys. Chem. A*, 1998, **102**, 4177–4185.

[10] M. T. Zanni, B. J. Greenblatt, A. V. Davis, and D. M. Neumark, *J. Chem. Phys.*, 1999, **111**, 2991–3003.

[11] H. Choi, R. T. Bise, A. A. Hoops, and D. M. Neumark, *J. Chem. Phys.*, 2004, **113**, 2255–2262.

[12] A. A. Hoops, J. R. Gascooke, A. E. Faulhaber, K. E. Kautzman, and D. M. Neumark, *J. Chem. Phys.*, 2004, **120**, 7901–7909.

[13] R. Nakanishi, N. Saitou, T. Ohno, S. Kowashi, S. Yabushita, and T. Nagata, *J. Chem. Phys.*, 2007, **126**, 204311.

[14] J. Vala, R. Kosloff, and J. N. Harvey, *J. Chem. Phys.*, 2001, **114**, 7413–7423.

[15] L. Visscher, E. Eliav, and U. Kaldor, *J. Chem. Phys.*, 2001, **115**(21), 9720–9726.

[16] A. Landau, E. Eliav, Y. Ishikawa, and U. Kaldor, *J. Chem. Phys.*, 2000, **113**, 9905–9910.

[17] A. Landau, E. Eliav, Y. Ishikawa, and U. Kaldor, *J. Chem. Phys.*, 2001, **115**, 6862–6865.

[18] T. Fleig, J. Olsen, and L. Visscher, *J. Chem. Phys.*, 2003, **119**, 2963.

[19] T. Fleig, H. J. Aa. Jensen, J. Olsen, and L. Visscher, *J. Chem. Phys.*, 2006, **124**, 104106.

[20] B. O. Roos, P. R. Taylor, and P. E. M. Siegbahn, *Chem. Phys.*, 1980, **48**, 157.

[21] K. Andersson, P.-A. Malmqvist, B. O. Roos, A. J. Sadlej, and K. Wolinski, *J. Phys. Chem.*, 1990, **94**, 5483.

[22] E. K. U. Gross and W. Kohn, *Adv. Quant. Chem.*, 1990, **21**, 255.

[23] D. Tozer, *J. Chem. Phys.*, 2003, **119**, 12697–12699.

[24] M. E. Casida, F. Gutierrez, J. Guan, F.-X. Gadea, D. Salahub, and J.-P. Daudey, *J. Chem. Phys.*, 2000, **113**, 7062–7071.

[25] M. E. Casida, *J. Chem. Phys.*, 2005, **122**, 054111.

[26] D. J. Tozer and N. C. Handy, *Phys. Chem. Chem. Phys.*, 2000, **2**, 2117.

[27] N. T. Maitra, F. Zhang, R. J. Cave, and K. Burke, *J. Chem. Phys.*, 2004, **120**, 5932.

[28] T. R. Taylor, K. R. Asmis, M. T. Zanni, and D. M. Neumark, *J. Chem. Phys.*, 1999, **110**, 7607–7609.

[29] H. Choi, T. R. Taylor, R. R. Bise, A. A. Hoops, and D. M. Neumark, *J. Chem. Phys.*, 2000, **113**, 8608–8614.

[30] T. Migchelsen and A. Vos, *Acta Cryst.*, 1967, **23**, 796–804.

[31] DIRAC, a relativistic ab initio electronic structure program, Release DIRAC04.0 written by H. J. Aa. Jensen, T. Saue, and L. Visscher with contributions from V. Bakken, E. Eliav, T. Enevoldsen, T. Fleig, O. Fossgaard, T. Helgaker, J. Laerdahl, C. V. Larsen, P. Norman, J. Olsen, M. Pernpointner, J. K. Pedersen, K. Ruud, P. Salek, J. N. P. van Stralen, J. Thyssen, O. Visser, and T. Winther., 2004.

[32] M. Iliaš and T. Saue, *J. Chem. Phys.*, 2007, **126**, 064102.

[33] AMFI: An atomic mean-field code, B. Schimmelpfennig, Stockholm, Sweden, 1996.

[34] B. A. Hess, C. M. Marian, U. Wahlgren, and O. Gropen, *Chem. Phys. Lett.*, 1996, **251**, 365–371.

[35] K. G. Dyall, *Theor. Chem. Acc.*, 2002, **108**, 335.

[36] K. G. Dyall, *Theor. Chem. Acc.*, 2006, **115**, 441.

[37] S. Knecht, H. J. Aa. Jensen, and T. Fleig, *J. Chem. Phys.*, 2008, **128**, 014108.

[38] S. Knecht, H. J. Aa. Jensen, and T. Fleig, *J. Chem. Phys.*, 2009, **submitted for publication**.

[39] G. Karlström, R. Lindh, P.-A. Malmqvist, B. O. Roos, U. Ryde, V. Veryazov, P.-O. Widmark, M. Cossi, B. Schimmelpfennig, P. Neogrady, and L. Seijo, *Comput. Mater. Sci.*, 2003, **28**, 222.

[40] B. A. Hess, *Phys. Rev. A*, 1986, **33**, 3742.

[41] P.-A. Malmqvist, B. O. Roos, and B. Schimmelpfennig, *Chem. Phys. Lett.*, 2002, **357**, 230.

[42] B. O. Roos, R. Lindh, P. Malmqvist, V. Veryazov, and P. O. Widmark, *J. Phys. Chem. A*, 2005, **108**, 2851.

[43] G. Ghigo, B. O. Roos, and P.-A. Malmqvist, *Chem. Phys. Lett.*, 2004, **396**, 142.

[44] ADF, Amsterdam density functional program Theoretical Chemistry, Vrije Universiteit Ams-

terdam, URL: http://www.scm.com, 2007.

[45] P. R. T. Schipper, O. V. Gritsenko, S. J. A. van Gisbergen, and E. J. Baerends, *J. Chem. Phys.*, 2000, **112**, 1344–1352.

[46] E. van Lenthe and E. J. Baerends, *J. Comput. Chem.*, 2003, **24**, 1142–1156.

[47] E. van Lenthe, J. G. Snijders, and E. J. Baerends, *J. Chem. Phys.*, 1996, **105**, 6505–6516.

[48] E. van Lenthe, J. G. Snijders, and E. J. Baerends, *J. Chem. Phys.*, 1996, **105**, 6505–6516.

[49] M. T. Zanni, V. S. Batista, W. H. Miller, B. J. Greenblatt, A. V. Davis, and D. M. Neumark, *J. Chem. Phys.*, 1999, **110**, 3748.

[50] T. Helgaker, P. Jørgensen, and J. Olsen, *Molecular Electronic Structure Theory*, John Wiley & Sons, Chichester, 2000.

[51] R. J. Bartlett and M. Musial, *Rev. Mod. Phys.*, 2007, **79**, 291–351.

[52] L. Meissner and R. J. Bartlett, *J. Chem. Phys.*, 1991, **94**, 6670–6676.

[53] L. Meissner and R. J. Bartlett, *J. Chem. Phys.*, 1995, **102**, 7490–7498.

[54] D. Mukhopadhyay, S. Mukhopadhyay, R. Chaudhuri, and D. Mukherjee, *Theor. Chim. Acta*, 1991, **80**, 441–467.

[55] F. Real, A. S. P. Gomes, L. Visscher, V. Vallet, and E. Eliav, *J. Phys. Chem. A*, 2009, **in press**.

[56] L. Meissner, *J. Chem. Phys.*, 1998, **108**, 9227–9235.

[57] M. Musial and R. J. Bartlett, *J. Chem. Phys.*, 2008, **129**, 044101.

[58] M. Musial and R. J. Bartlett, *J. Chem. Phys.*, 2008, **129**, 134105.

[59] M. Musial and R. J. Bartlett, *Chem. Phys. Lett.*, 2008, **457**, 267–270.

[60] I. Infante, A. S. P. Gomes, and L. Visscher, *J. Chem. Phys.*, 2006, **125**, 074301.

[61] G. La Macchia, I. Infante, R. Juraj, J. K. Gibson, and L. Gagliardi, *Phys. Chem. Chem. Phys.*, 2008, **10**, 7278–7283.

[62] F. Notter, S. Dubillard, and H. Bolvin, *J. Chem. Phys.*, 2008, **128**, 164315.

[63] K. Do, T. P. Klein, C. A. Pommerening, and L. S. Sunderlin, *J. Am. Soc. Mass Spectrom.*, 1997, **8**, 688.

TABLE I: Ground-state spectroscopic constants (r_e in Å and ω_e in cm^{-1}) of I_3^- calculated with the DFT, MRCI (a), CASPT2 and IHFSCC(a,b) methods

Method	r_e	ω_e
DFT	3.007	102
MRCI (a)	2.982	108
CASPT2	2.888	119
IHFSCC (a)	2.971	112
IHFSCC (b)	2.946	114
MRCI (ref. [14], Spin-Free)	2.930	114
DIM+SO (ref. [14])	2.966	95
Experimental (ref. [30])	2.93	112±1

TABLE II: Comparison of vertical excitation energies T_v (in eV) obtained with the different methods (TDDFT, MRCI(a and b), CASPT2, IHFSCC(a and b)) for I_3^- at $r_1 = r_2 = 2.93$ Å. States of the same symmetry as those for the optically active excited states are shown in boldface. Statistical measures of the error compared to IHFSCC(b) are also shown (see text for discussion).

	TDDFT		MRCI(a)		MRCI(b)		CASPT2		IHFSCC(a)		IHFSCC(b)	
State	Ω	T_v	Ω	T_v	Ω	T_v	Ω	T_v	Ω	T_v	Ω	T_v
1	2_g	1.92	2_g	2.32	2_g	2.30	2_g	2.27	2_g	2.10	2_g	2.05
2	1_g	2.04	1_g	2.44	0_u^-	2.40	1_g	2.35	1_g	2.23	1_g	2.18
3	0_u^-	2.42	0_u^-	2.47	1_u	2.41	0_u^-	2.49	0_u^-	2.26	0_u^-	2.20
4	1_u	2.43	1_u	2.48	1_g	2.41	1_u	2.49	1_u	2.27	1_u	2.20
5	0_g^-	2.50	0_g^-	2.94	0_g^-	2.91	0_g^-	2.79	0_g^-	2.68	0_g^-	2.64
6	0_g^+	2.56	0_g^+	2.98	0_g^+	2.95	0_g^+	2.85	0_g^+	2.73	0_g^+	2.69
7	1_g	2.70	1_g	3.13	1_g	3.08	1_g	2.88	1_g	2.90	1_g	2.86
8	2_u	2.61	2_u	3.25	2_u	3.21	2_u	3.13	2_u	3.22	2_u	3.17
9	1_u	2.72	1_u	3.30	1_u	3.25	1_u	3.13	1_u	3.30	1_u	3.24
10	$\mathbf{0_u^+}$	**3.14**	$\mathbf{0_u^+}$	**3.71**	$\mathbf{0_u^+}$	**3.66**	$\mathbf{0_u^+}$	**3.54**	$\mathbf{0_u^+}$	**3.52**	$\mathbf{0_u^+}$	**3.51**
11	2_g	3.50	0_u^-	4.04	0_u^-	3.98	0_u^-	3.82	0_u^-	3.95	2_g	3.88
12	0_u^-	3.42	1_u	4.09	1_u	4.02	1_u	3.83	2_g	3.96	0_u^-	3.91
13	1_g	3.63	2_g	4.19	2_g	4.16	2_g	4.01	1_u	4.03	1_g	4.00
14	1_u	3.56	1_g	4.29	1_g	4.25	1_g	4.08	1_g	4.07	1_u	4.00
15	$\mathbf{0_u^+}$	**4.46**	0_g^-	4.81	$\mathbf{0_u^+}$	**4.75**	$\mathbf{0_u^+}$	**4.52**	$\mathbf{0_u^+}$	**4.33**	$\mathbf{0_u^+}$	**4.33**
16	0_g^-	4.10	0_g^+	4.82	0_g^-	4.77	0_g^-	4.55	0_g^-	4.54	0_g^-	4.48
17	0_g^+	4.11	$\mathbf{0_u^+}$	**4.83**	0_g^+	4.78	0_g^+	4.57	0_g^+	4.54	0_g^+	4.48
18	1_g	4.34	1_g	4.96	1_g	4.91	1_g	4.63	2_u	4.72	1_g	4.68
$\bar{\Delta}$		-0.24		0.25		0.20		0.08		0.05		
Δ_{std}		0.24		0.11		0.11		0.16		0.02		
$\bar{\Delta}_{\text{abs}}$		0.31		0.25		0.21		0.13		0.05		
Δ_{max}		0.56		0.50		0.41		0.29		0.08		

TABLE III: Vertical (T_v) excitation energies (in eV) calculated with the TDDFT, MRCI (a), CASPT2 and IHFSCC(a and b) methods for I_3^- calculated at the optimum bond length for each method. States of the same symmetry as those for the optically active excited states are shown in boldface. Statistical measures of the error compared to IHFSCC(b) are also shown (see text for discussion).

	TDDFT		MRCI(a)		CASPT2		IHFSCC(a)		IHFSCC(b)	
State	Ω	T_v	Ω	T_v	Ω	T_v	Ω	T_v	Ω	T_v
1	2_g	1.67	2_g	2.15	2_g	2.41	2_g	1.98	2_g	2.00
2	1_g	1.78	1_g	2.27	1_g	2.48	1_g	2.10	1_g	2.13
3	0_u^-	2.13	0_u^-	2.28	0_u^-	2.65	0_u^-	2.11	0_u^-	2.13
4	1_u	2.14	1_u	2.28	1_u	2.65	1_u	2.12	1_u	2.14
5	0_g^-	2.24	0_g^-	2.77	0_g^-	2.93	0_g^-	2.55	0_g^-	2.58
6	2_u	2.26	0_g^+	2.81	0_g^+	2.99	0_g^+	2.60	0_g^+	2.64
7	0_g^+	2.31	1_g	2.94	1_g	3.03	1_g	2.77	1_g	2.81
8	1_u	2.38	2_u	3.00	2_u	3.33	2_u	3.04	2_u	3.10
9	1_g	2.44	1_u	3.05	1_u	3.34	1_u	3.11	1_u	3.17
10	$\mathbf{0_u^+}$	**2.82**	$\mathbf{0_u^+}$	**3.47**	$\mathbf{0_u^+}$	**3.74**	$\mathbf{0_u^+}$	**3.44**	$\mathbf{0_u^+}$	**3.36**
11	2_g	3.07	0_u^-	3.79	0_u^-	4.01	2_g	3.73	2_g	3.79
12	0_u^-	3.09	1_u	3.84	1_u	4.03	0_u^-	3.77	0_u^-	3.84
13	1_g	3.20	2_g	3.89	2_g	4.26	1_g	3.84	1_g	3.90
14	1_u	3.22	1_g	3.98	1_g	4.33	1_u	3.85	1_u	3.93
15	0_g^-	3.66	0_g^-	4.52	$\mathbf{0_u^+}$	**4.68**	$\mathbf{0_u^+}$	**4.17**	$\mathbf{0_u^+}$	**4.27**
16	0_g^+	3.68	0_g^+	4.52	0_g^-	4.79	0_g^-	4.31	0_g^-	4.38
17	1_g	3.91	$\mathbf{0_u^+}$	**4.61**	0_g^+	4.81	0_g^+	4.32	0_g^+	4.39
18	$\mathbf{0_u^+}$	**4.29**	1_g	4.65	1_g	4.88	1_g	4.50	1_g	4.59
$\bar{\Delta}$		-0.49		0.09		0.34		-0.05		
Δ_{std}		0.29		0.12		0.38		0.04		
$\bar{\Delta}_{\mathrm{abs}}$		0.49		0.13		0.34		0.06		
Δ_{max}		0.84		0.34		0.52		0.10		

TABLE IV: Spectroscopic constants (r_e in Å and ω_e in cm^{-1}) and adiabatic (T_e) excitation energies (in eV) for the ten lowest excited states of I_3^-, calculated with the TDDFT, MRCI (a), CASPT2 and IHFSCC (b) methods. The lowest, optically active 0_u^+ state is shown in boldface. Statistical measures of the error compared to IHFSCC(b) are also shown (see text for discussion).

	TDDFT				MRCI (a)				CASPT2				IHFSCC (b)			
State	Ω	r_e	ω_e	T_e	Ω	r_e	ω_e	T_e	Ω	r_e	ω_e	T_e	Ω	r_e	ω_e	T_e
1	2_g	3.442	54	1.19	0_u^-	3.501	56	1.53	1_u	3.366	63	1.82	0_u^-	3.419	60	1.45
2	1_g	3.462	52	1.29	1_u	3.503	56	1.53	2_g	3.233	76	1.82	1_u	3.414	61	1.46
3	0_u^-	3.720	23	1.38	2_g	3.383	61	1.64	0_u^-	3.362	63	1.83	2_g	3.245	83	1.59
4	1_u	3.696	28	1.38	1_g	3.421	56	1.71	1_g	3.251	73	1.87	1_g	3.255	80	1.71
5	2_u	3.615	46	1.41	2_u	3.644	47	1.89	1_u	3.481	57	2.18	0_g^-	3.358	53	2.07
6	1_u	3.669	40	1.52	1_u	3.657	47	1.89	2_u	3.472	58	2.21	1_g	3.512	28	2.20
7	0_g^-	3.554	38	1.68	0_g^-	3.478	48	2.16	0_g^-	3.272	70	2.28	2_u	3.448	65	2.22
8	1_g	3.771	52	1.81	1_g	3.562	43	2.22	1_g	3.315	63	2.32	0_g^+	3.240	84	2.24
9	0_g^+	3.388	63	1.88	0_g^+	3.388	62	2.28	0_g^+	3.242	76	2.38	1_u	3.462	67	2.26
10	$\mathbf{0_u^+}$	**3.513**	**57**	**2.10**	$\mathbf{0_u^+}$	**3.731**	**34**	**2.36**	$\mathbf{0_u^+}$	**3.501**	**50**	**2.64**	$\mathbf{0_u^+}$	**3.496**	**49**	**2.61**
$\bar{\Delta}$		0.198	-18	-0.42		0.142	-12	-0.06		-0.036	2	0.15				
Δ_{std}		0.080	19	0.24		0.058	12	0.18		0.067	14	0.15				
$\bar{\Delta}_{\text{abs}}$		0.198	24	0.42		0.142	15	0.13		0.045	10	0.17				
Δ_{max}		0.301	37	0.83		0.235	24	0.37		0.197	35	0.38				

TABLE V: Character of 0_u^+ states of I_3^- for TDDFT, IHFSCC(b), CASPT2 and MRCI(a) at the respective ground state equilibrium geometries. These are given in terms of contributions from one-electron (for TDDFT, IHFSCC and MRCI, where spin-orbit coupling is included at the SCF level) or many-electron states (for CASPT2). The oscillator strengths f associated to the transition from the ground state to these excited states are also shown (where available) along with the vertical excitation energy. The experimental absorption maxima are found at: (a) 3.41 and 4.22 eV in CH_2Cl_2 (solution); and (b) 3.38 and 4.28 eV in Et_4NI_3 (solid state)[4].

Method	State	Excited state composition	T_v (eV)	f
TDDFT	0_u^+	$51\%\ \sigma_{1/2g} \rightarrow \sigma^*_{1/2u} + 49\%\ \pi_{1/2g} \rightarrow \sigma^*_{1/2u}$	2.82	0.09
	0_u^+	$45\%\ \sigma_{1/2g} \rightarrow \sigma^*_{1/2u} + 50\%\ \pi_{1/2g} \rightarrow \sigma^*_{1/2u}$	4.29	1.54
MRCI	0_u^+	$46\%\ \sigma_{1/2g} \rightarrow \sigma^*_{1/2u} + 30\%\ \pi_{1/2g} \rightarrow \sigma^*_{1/2u} + 7\%\ (\pi^1_{1/2g}\pi^1_{1/2u} \rightarrow \sigma^{*\,2}_{1/2u})$	3.47	n/a[1]
	0_u^+	$29\%\ \sigma_{1/2g} \rightarrow \sigma^*_{1/2u} + 47\%\ \pi_{1/2g} \rightarrow \sigma^*_{1/2u} + 6\%\ (\sigma^1_{1/2g}\sigma^1_{1/2u} \rightarrow \sigma^{*\,2}_{1/2u})$	4.61	n/a[1]
IHFSCC	0_u^+	$40\%\ \sigma_{1/2g} \rightarrow \sigma^*_{1/2u}$ (LUMO) $+ 19\%\ \pi_{1/2g} \rightarrow \sigma^*_{1/2u}$ (LUMO) $+ 22\%\ \sigma_{1/2g} \rightarrow \sigma^*_{1/2u} + 15\%\ \pi_{1/2g} \rightarrow \sigma^*_{1/2u}$	3.36	n/a[1]
	0_u^+	$26\%\ \sigma_{1/2g} \rightarrow \sigma^*_{1/2u}$ (LUMO) $+ 36\%\ \pi_{1/2g} \rightarrow \sigma^*_{1/2u}$ (LUMO) $+\ 8\%\ \sigma_{1/2g} \rightarrow \sigma^*_{1/2u} + 24\%\ \pi_{1/2g} \rightarrow \sigma^*_{1/2u}$	4.27	n/a[1]
CASPT2	0_u^+	$14\%\ ^1\Sigma_u^+\ (89\%\ \sigma_g \rightarrow \sigma_u^*) + 86\%\ ^3\Pi_u\ (89\%\ \pi_g \rightarrow \sigma_u^*)$	3.59	0.43
	0_u^+	$84\%\ ^1\Sigma_u^+\ (89\%\ \sigma_g \rightarrow \sigma_u^*) + 14\%\ ^3\Pi_u\ (89\%\ \pi_g \rightarrow \sigma_u^*)$	4.53	2.29

[1] not available

TABLE VI: Comparison of excitation energies T_v (in eV) for different methods (CASPT2, IHFSCC (a,b), MRCI (a) for neutral I_3 at $r_1 = r_2 = 2.84$ Å. Vertical (T_v) and adiabatic (T_e) excitation energies, as well as electron affinities (EA) are shown for IHFSCC (b).

	MRCI[1]	MRCI (a)	CASPT2	IHFSCC (a)	Experimental			IHFSCC (b)					
State (Ω)	T_v ($r_1 = r_2 = 2.84$ Å)				ω_e	T_e	EA[2]	R_e	ω_e	T_v^3	T_v	T_e	EA[4]
X $(3/2_u)$	0.00	0.00	0.00	0.00	115±5	0.00	4.15±0.12	2.828	132	0.00	0.00	0.00	4.29
A $(1/2_g)$	0.28	0.33	0.40	0.27		0.28		2.884	113	0.24	0.25	0.23	
B $(1/2_u)$	0.61	0.65	0.56	0.64		0.62		2.837	129	0.65	0.65	0.65	
C $(3/2_g)$	0.78	0.78	0.77	0.88		0.68		2.951	115	0.86	0.88	0.78	
D $(1/2_g)$	1.62	1.63	1.54	1.68				2.933	118	1.68	1.70	1.62	

[1] Results from Kosloff, ref. [14], at $r_1 = r_2 = 2.836$ Å.

[2] Ref.[63]; vertical detachment energy of I_3^-: 4.25 eV (ref.[29])

[3] Calculated at $r_1 = r_2 = 2.84$ Å.

[4] Value for the adiabatic EA. Vertical processes: IP(I_3^-) = 4.39 eV, EA(I_3) = 4.20 eV.

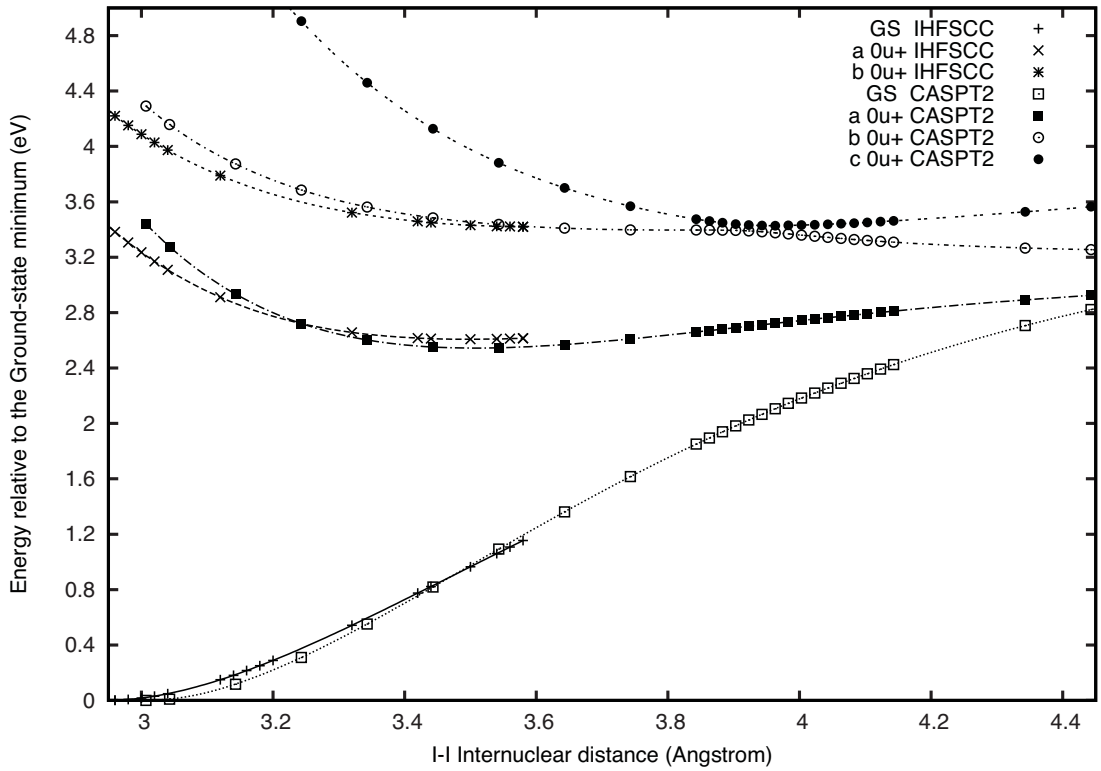

FIG. 1: Potential energy curves along the symmetric stretch coordinate for the ground-state (GS, 0_g^+) and lower 0_u^+ states (the first two corresponding to the optically active states) from CASPT2 and IHFSCC(b) calculations. All potentials were scaled so that the ground state minimum corresponds to the origin; the CASPT2 excited states were further shifted (a) downwards by 0.5 eV and (b) towards larger internuclear distances by 0.14 Å(the ground-state geometry for CASPT2 was shifted by 0.08 Å), to compensate the systematic errors compared to IHFSCC(b).

Paper 5

Stefan Knecht, Lasse Kragh Sørensen, Hans Jørgen Aagaard Jensen, Timo Fleig, and Christel M. Marian

Four-component relativistic configuration interaction and coupled cluster calculations on the ground and excited states of the $(RbBa)^+$ molecule.

submitted to J. Phys. B: At. Mol. Opt. Phys..

Four-component relativistic Configuration Interaction and Coupled Cluster calculations on the ground and excited states of the $(RbBa)^+$ molecular ion.

.

S Knecht[1], L K Sørensen[1], H J Aa Jensen[2], T Fleig [3] and C M Marian[1]

[1] Theoretical and Computational Chemistry, Heinrich Heine University Düsseldorf, Universitätsstraße 1, D-40225 Düsseldorf, Germany

[2] Department of Physics and Chemistry, University of Southern Denmark, DK-5230 Odense M, Denmark

[3] Laboratoire de Chimie et Physique Quantiques, I.R.S.A.M.C., Université Paul Sabatier, Toulouse III, route de Narbonne 118, 31062 Toulouse Cedex 04, France

E-mail:
stefan@theochem.uni-duesseldorf.de,lasse@theochem.uni-duesseldorf.de,
hjj@ifk.sdu.dk,timo.fleig@irsamc.ups-tlse.fr,cm@theochem.uni-duesseldorf.de

Abstract. Collisions of ultracold Ba^+ ions on a Rb Bose-Einstein condensate have been suggested as a possible benchmark system for ultracold ion-neutral collision experiments, however, *a priori* knowledge of the possible processes is desirable. For this purpose we here present high-level four-component coupled cluster and multi-reference configuration interaction calculations of potential energy curves, dipole moment, and spectroscopic constants of the experimentally interesting low-lying electronic states of the $(RbBa)^+$ molecule. Our results show significant avoided crossings between the $^3\Sigma^+_{1,0^-}$ Rb + Ba^+ entrance channels and low-lying charge transfer $^3\Pi_{1,0^-}$ states of the Rb^+ and $Ba_{6s^1 5d^1}(^3D)$ atomic channels, indicating that a fast non-radiative charge transfer could be possible. For the ground state population analysis shows that the ground state deviates significantly from a pure Rb^+ + Ba interaction but instead a partially covalent polar bond is formed. This finding is corroborated by the electric dipole moment which is found only to be 4.5 D at the equlibrium bond distance, compared with the 14 D for a pure Rb^+ + Ba interaction, thereby supporting the view of a partial charge transfer between the two atoms.

PACS numbers: 31.15.ae, 31.15.ag, 31.15.aj, 31.15.am, 31.15.bw, 31.15.vj, 31.15.vn, 33.15.Fm, 34.70.+e

Submitted to: *J. Phys. B: At. Mol. Opt. Phys.*

1. Introduction

The study of reactive collisions at very low temperatures is a promising new direction in the field of cold and ultracold quantum matter. This temperature regime comprises a unique environment to investigate, *i.a.*, the quantum mechanical details of chemical reactions, ultimately aiming at a controlled chemistry at the quantum level [1]. Other interesting prospects concern the possibility of testing fundamental symmetries in nature [2, 3] or the spacetime independence of electron and nuclear masses [4].

Ion-neutral interactions are distinguished from neutral-neutral collisions in that the interaction of the former is long-range, in general leading to large collision cross sections [5] and entailing the possibility of charge transfer between the collision partners [6]. Quite a number of experimental and theoretical studies of ion-neutral reactions exist, but the low-energy regime has only been addressed recently, *e.g.* in references [7, 8, 5]. Due to the complexity of the level of ab-initio electronic-structure calculations needed for determining the accurate short-range potentials, most of these studies considered few-electron systems. The limited number of investigations on many-electron systems involving a cationic reaction partner, such as the studies on $(NaNa)^+$ and $(NaCa)^+$ [6, 9], employ rather approximate potentials involving parameters taken from experiment.

Also other aspects of ion-neutral collisions beside the charge-transfer processes have received attention. The formation of a postulated mesoscopic molecular bound state arising from a single trapped ion in a sea of ultracold atoms [10] comprises an intriguing finding. In this context, the collision kinetics and electronic potential energy curves of the molecular benchmark system $(RbBa)^+$, starting from a Ba^+ ion that interacts with a Bose-Einstein condensate of neutral Rb atoms, are of great interest [11]. The $(RbBa)^+$ system is valence isoelectronic with the $(MgK)^+$, $(MgCs)^+$, and $(NaCa)^+$ systems which have been considered in earlier experiments [12, 13, 9]. The associated theoretical investigations were mainly carried out using large-core pseudopotentials and neglecting spin-orbit coupling. In these systems, the lowest-lying electronic states are characterized as Σ states, which is also true for the $(RbBa)^+$ molecular ion [14] and most likely also for another heavier species of interest, $(MgCs)^+$. The neglect of spin-orbit interaction is reasonable in the determination of such Σ states, since it affects these states only through higher-order couplings to excited states of different angular momentum projection onto the internuclear axis. For the $(RbBa)^+$ molecular ion, however, electronic states of projection $\Lambda > 0$ play a role for the lowest dissociation channels to the different atomic fragments [14]. An understanding of experiments involving the lower dissociation channels of $(RbBa)^+$ which come to lie in an energy window of about 2 eV, therefore necessitates inclusion of spin-orbit interaction in the electronic-structure calculations.

The objective of this study has been to investigate the electronic excited states lying close to the Rb + Ba^+ entrance channel and expected to have a complicated distance dependence, to form a firm basis for design of ultracold collision experiments for this system. One aim here was the search for possible charge transfer mechanism from Rb to Ba^+ by a characterization of the excited states. Another closely related

aim was the search for metastable excited states which could be used for creating a mesoscopic molecular bound state with the Rb Bose-Einstein condensate. To obtain this objective we extend an earlier scalar relativistic study [14] to also include the spin-orbit interaction, which we will show to be imperative for an understanding of the charge transfer mechanisms in $(RbBa)^+$ at ultracold experimental conditions.

Since two heavy atoms are involved we apply quantum-chemical methods which treat electron correlation and relativistic effects on the same footing. Relativistic coupled cluster and configuration interaction approaches are used in a complementary fashion, the details of which are described in the following section. In the main body of the paper (section 3) we achieve high accuracy by first a systematic study of the ground and excited states of the atoms and, in addition, of the electronic ground state of the molecule. Based on these results, a final multi-reference configuration interaction (MRCI) model expansion is chosen which can deliver accurate spectroscopic values for the states in question and describe well the relevant avoided crossings of the potential curves. We present and discuss electronic molecular potentials obtained with the MRCI model and point to possible radiative as well as non-radiative charge transfer processes which can occur. We also investigate the ground state dipole moment as a function of distance to visualize effects of any covalent character in the ground state. In the final section we summarize and draw conclusions.

2. Theory and Computational Details

2.1. Hamiltonian operator

Atomic excitation energies along with ionization potentials suggest a rich manifold of low-lying excited states with angular momentum projection greater than zero in the region around the Rb_{5s^1} + $Ba^+_{6s^1}$ entrance channel. This was confirmed by the calculations in a previous study [14] where the nine lowest-lying molecular electronic states of the $(RbBa)^+$ ion were calculated employing a spinfree Hamiltonian. These spinfree states will split into their Ω components upon taking into consideration spin-orbit coupling. Since these high angular momentum states are possible candidates for a charge transfer from Ba^+ to Rb, which could be lead to a transition to the electronic ground state, it is therefore essential to account properly for the various Ω components of these higher angular momentum states to aid the interpretation of ongoing experiments [11]. We therefore here extend the spinfree investigation to account for spin-orbit interactions in the rigorous four-component Dirac-Coulomb framework. All classes of two-electron integrals were included, also the integrals involving four small-component indices and spin-orbit, except where otherwise noted.

2.2. Correlation Methods and Setup

In the study of the ground state properties we used the `RELCCSD` module [15, 16] which can perform coupled cluster single doubles (CCSD) and perturbative triples (CCSD(T))

calculations and is available in the DIRAC08 quantum chemistry program package [17]. Since the dominant relativistic contribution for the ground state of $(RbBa)^+$ is scalar relativistic we employed the computationally cheaper spinfree Dirac-Coulomb Hamiltonian by Dyall [18] in the ground-state calculations. This was checked against the Dirac-Coulomb (DC) Hamiltonian as shown in Table 1, and the spin-orbit effect on the ground state potential was found to be well within the expected error bounds for the spectroscopic properties. We therefore consistently used the spinfree Hamiltonian for the ground-state calculations since the time consuming part in the CCSD and CCSD(T) with the DC Hamiltonian is the flipping of the Kramers projection to describe the in this case negligible spin-orbit contribution to the electronic potential. Along the entire potential energy curve we used closed-shell spinfree Dirac-Coulomb Hartree Fock (SF-DCHF) for the generation of molecular spinors. This was employed since the ground state is dominated by a single determinant. The CCSD(T) furthermore served to validate the quality of the MRCI calculations.

In the coupled cluster and MRCI treatments we decided to correlate the valence and outer core electrons, i.e. the $4p$ shell on Rb^+ and the $5p$ and $6s$ shells on Ba. Recent studies on LiCs [19] showed that the correlation of the core $4d$ shell on Cs had very little impact on the spectroscopic values, and this would then be expected also to be the case for the $3d$ shell on Rb and the $4d$ shell on Ba. The LiCs study also showed that the energetically lower lying $5s$ outer core on Cs contracted the bond by about 0.02 bohr which is expected to carry over for the outer core $4s$ Rb and $5s$ Ba.

Ground- and excited-state wavefunctions along with vertical and adiabatic excitation energies have been calculated with the recently parallelized [20] relativistic double group large-scale MRCI program LUCIAREL[21, 22, 23]. This code is able to routinely handle large CI expansions ($> 10^9$ determinants) on standard Linux-based clusters. This CI program will be made available in the forthcoming release of the DIRAC program package. By exploiting the generalized active space (GAS) concept in the CI, a flexible correlation treatment is possible. The orbital space can be divided into any number of sub-orbital spaces and any restrictions can be imposed on the allowed excitations between these sub-orbital spaces. The molecular spinors can in the developers version of DIRAC be obtained from either DCHF, Kramers-restricted multi-configurational self-consistent-field (KR-MCSCF), [24] or natural MP2 spinors [25]. We found that the best way to obtain accurate excitation energies in this case was to start from a closed shell DCHF. The Ω quantum number for a given electronic state has been assigned by calculating the expectation value for the $\hat{j}_z$ operator [26].

In the MRCI calculations we included the Rb $5s5p$ and the Ba $5d6s6p$ spinors (of which only Ba $6s$ is formally occupied in the ground state) in the active space, yielding a distribution of two valence electrons in 13 Kramers pairs. Single holes in the Rb $4p$ and Ba $5p$ shells were included to describe outer-core polarization, and single and doubles into the energy selected virtual spinors (see section 2.3) were included to account for dynamic correlation. In our notation we dub this computational scheme S12_(2in13)_SD which follows the notation of GAS1_(GAS2)_GAS3 laid out in earlier publications [27].

2.3. Basis sets and basis set superposition error

All calculations were performed using uncontracted scalar Gaussian type orbitals (GTO) large component basis sets. The small component basis functions were generated by restricted kinetic balance condition [28]. For all the ground-state coupled cluster calculations we used extended TZ basis sets by Dyall [29]. For Rb the $(29s21p15d2f)$ basis set is his TZ basis set extended with his correlating and polarizing functions for the valence and the $4s4p$ shells, since this choice of basis set has been shown to perform well in a recently published paper on RbYb [27]. For Ba we added Dyall's correlating and polarizing functions for the valence and the $5s5p$ shells to form an $(31s25p18d3f)$ extended TZ basis set. The polarizing functions were added to ensure accurate dipole moments for the electronic ground state.

For the MRCI calculations, where the focus was on proper treatment of all low-lying excited states, we followed the scheme in Ref. [30], and the Ba basis set was further augmented with one diffuse d, f, and g function with exponents of 0.036645714, 0.3000341, and 0.76354824, respectively, in the MRCI treatment. This was done in order to properly describe excitations to the Ba $5d$ shell which plays a crucial role in the charge transfer from Rb to Ba^+ and could enable a transition to electronic ground state. The polarizing functions were, on the other hand, not included since no electric properties were calculated with the MRCI. This setup results in a total of $(28s20p14d1f)$ for Rb and $(30s24p18d3f1g)$ for Ba. This basis set has been used in all MRCI calculations.

The threshold for the truncation of the virtual spinors in all the correlated calculations was set at 18 Hartree. The validity of this choice was checked for the ground state at the CCSD and CCSD(T) levels using the approximation to the small-component density by Visscher [31]. To this end, complete potential energy curves with a truncation of the virtuals at 42 Hartree were also constructed. As seen from the results in Table 2 the truncation errors in the spectroscopic parameters derived from these calculations are more than a factor of 100 smaller than the difference between CCSD and CCSD(T).

The basis set superposition error (BSSE) in the electronic ground state was accounted for by applying the counterpoise (CP) correction as suggested by Boys and Bernardi [32].

2.4. Dipole moments

Dipole moments along the ground state potential energy curve were calculated using the finite-field technique where we varied the electric field along the bond axis (chosen as z). For the dipole moment a seven-point numerical derivative has in previous publications [27, 19] been shown not to be the limiting factor for the accuracy of the dipole moment and will therefore also be used here. The field strengths used were ± 0.0001, ± 0.0002, and ± 0.0004 $\mathrm{E}_h\,\mathrm{e}^{-1}\,\mathrm{bohr}^{-1}$ to form the numerical derivative of the energy with respect to electric field taken at zero field strength. The origin of the molecular coordinate system was chosen to lie in the center of mass. In this way we could calculate the dipole moment at different internuclear distances with the WFFIT program from Sadlej [33], and this

has been done at the CCSD and CCSD(T) levels of theory for the ground state.

3. Results

Table 3 compiles the atomic configurations and terms as well as their corresponding molecular states that form the lower part of the electronic spectrum of the $(RbBa)^+$ molecular ion up to $\approx$ 14000 cm^{-1} above the ground state. These molecular states include also the Σ states correlated with the entrance channel for the envisaged collision experiments involving an ultracold ionized trapped barium atom and a Bose-Einstein condensate of neutral rubidium atoms. In the following we shall elaborate on our results for all the molecular states located below the entrance channel plus d channels associated with the $Rb^+_{5s^0}(^1S_0)$ + $Ba_{6s^1 5d^1}(^3D_{1,2,3}$; $^1D_2)$ atomic limits listed in Table 3. As our results discussed in Section 3.3 show, notable interactions between electronic states of the same Ω quantum number are observed for the molecular states correlating with these channels. It is therefore anticipated that radiative as well as non-radiative transitions will play a crucial role in the charge transfer process from Rb + Ba^+ to Rb^+ + Ba and of the life time of the different states in the excited state manifold.

3.1. Atomic calculations and ionization potentials

Table 4 compiles our results of atomic and atomic-like excitation energies of the lowest Ba atomic transitions as well as previous theoretical work and experimental data. Comparisons of our atomic MRCI S6_(2in9)_SD and the atomic-like molecular MRCI S12_(2in13)_SD results show that the dissociation limit is reached at an internuclear separation of 50 bohr. From previous studies on transition metals it is known that ns^2(n-1)d^m $\rightarrow$ ns^1(n-1)d^{m+1} excitations are difficult to describe in general within an MRCI approach because of the slow convergence of the dynamical electron correlation contributions [34]. Multireference CC approaches, such as for example the Fock-space CCSD (FSCCSD) or the intermediate Hamiltonian IHFSCCSD methods [35, 36, 37], are better at describing dynamical electron correlation energies. They are therefore expected to yield closer agreement with experiments, as the results in Table 4 confirm. In view of these difficulties for MRCI the deviations of our computed ^{3}D and ^{1}D excitation energies from the experimental values on the order of a few 100 cm^{-1} are satisfactory. The fine-structure splittings of these terms are even reproduced within a few tens of cm^{-1}(see Table 4). Furthermore, the good agreement of our calculated $Ba_{6s^1 6p^1}(^3P)$ energies to experiments shows that the chosen basis set and correlation treatment are adequate.

In addition to the energetic location of the low-lying neutral Ba channels, the differential ionization potential of Rb and Ba is of vital importance for an unbiased description of the $(RbBa)^+$ molecular states. Our computed ΔIP (IP(Ba)-IP(Rb)) value of 8454 cm^{-1} is in excellent agreement with experiment (8344 cm^{-1}) [38]. This ΔIP was calculated as the excitation energy in the atomic-like limit at 50 bohr of a molecular calculation. The Ba^+ + Rb entrance channel is thus placed only slightly below the

$Ba_{6s^15p^1}(^3D_1)$ + $Rb^+_{5s^0}$ atomic channel. This is in contrast to the lighter homologs $(NaCa)^+$, $(MgK)^+$ and $(MgCs)^+$ where the corresponding energy gap is much larger.

3.2. Ground state potential

In Table 1 we report our calculated MRCI spectroscopic constants for the $^1\Sigma^+_{0^+}$ ground state of $(RbBa)^+$ and compare with values derived from our four-component CCSD and CCSD(T) calculations. In agreement with the findings of an earlier study on RbYb [27], counterpoise correction has only a minor effect on the spectroscopic constants of the ground state. Inspecting Table 1, it is comforting that the present spin-dependent MRCI S12_(2in13)_SD approach compares favorably to the more sophisticated CCSD(T) method. The deviation of 0.03 bohr in the equilibrium bond distance R_e is small for such a weakly-bound molecular ion with $R_e = 8.75$ bohr. Moreover, the harmonic frequency ω_e as well as the dissociation energy D_e agree perfectly with the CCSD(T) values. The differences between the spin-free and spin-dependent MRCI results are mainly attributed to AO basis set effects since in the spin-free case an ANO-RCC basis set with a truncation of the virtual space at 5 E_h was used. As could be expected for a "Σ" state, spin-orbit coupling hardly affects the calculated spectroscopic parameters as seen for the coupled cluster calculations. In contrast we see a substantial contraction of the equlibrium distance and an increase of the dissociation energy by about 150 cm^{-1} when triple excitations are included perturbatively in the coupled cluster treatment. This finding is in line with what has also been observed for other weakly bound systems like LiCs [19] and RbYb [27] where a CCSD treatment was also found to be insufficient.

In the MRCI expansion the ground state is dominated by the reference determinant which has a CI coefficient of 0.94 around equlibrium. A Mulliken population analysis of the underlying DCHF wave function reveals that the highest occupied molecular orbital (HOMO) is not a purely atomic Ba $6s$ Kramers pair, the Ba $6s$ spinors are populated by 1.5 electrons. Roughly 0.4 electrons have been transferred to a Rb σ-type orbital. The remaining 0.1 electrons reside in the Ba $5d_\sigma$ that is also involved in the binding. The second largest CI coefficient of about -0.1 is found for the double exication to the lowest unoccupied molecular orbital (LUMO), which the Mulliken population analysis again reveals to be significantly mixed. The LUMO is composed of Rb $5s(0.613)$, Ba $6p_z(0.209)$, $6s(0.150)$, and $5d_{xx}$, $5d_{yy}(0.011)$. We furthermore see many single and double excitations to molecular spinors which are made up of Rb $5s$ and $5p$ and Ba $6s$, $6p$, and $5d$ atomic spinors. This large mixing of the atomic spinors is what lead to the choice of including all these spinors in the active space of the MRCI calculations and why we are confident that the MRCI with this active space performs well for the low-lying states. Upon dissociation we observe that the HOMO becomes more and more atomic and locates on Ba.

The mixing with the Rb $5s$ and $5p$ in HOMO also means that the ground state cannot be considered to be just a charge – induced dipole $1/R^4$ interaction between Rb^+ and Ba but that there is a significant amount of the valence electron density residing

on the Rb atom. The charge transfer is perhaps not so large that one would talk about a bond in a chemical sense but we find that the bond is significantly stronger than what would be expected from a charge induced dipole interaction. With a dissociation energy of around 5000 cm^{-1} (see Table 1) this is in fact directly comparable to the dissociation energy of the LiCs alkali dimer where D_e is measured to 5875.455 cm^{-1} [39]. The picture of a partially covalent polar bond is also confirmed by the dipole moment which is significantly influenced by the charge distribution in the molecule (see Section 3.4).

3.3. Excited state potentials

In contrast to the ground state, accounting for spin-orbit coupling in the excited states clearly yields a more complex picture for the potential energy curves of the electronic excited states of the molecular ion $(RbBa)^+$ compared to the spinfree calculations[14]. The avoided crossings between the $^3\Sigma^+_{0^-}$-$^3\Pi_{0^-}$ states and the $^3\Sigma^+_1$-$^3\Pi_1$ states are easily discernible in Figure 1 and in the enlargement of the critical region in Figure 2. Of course, in the spinfree calculations all these curves cross, and it is thus evident that proper treatment of spin-orbit coupling is mandatory for explanation and prediction of outcomes of ultracold reactive collisions of Ba^+ on a Rb Bose-Einstein condensate. An even more pronounced avoided crossing between the $^1\Sigma^+$ of the entrance channel and the $^1\Sigma^+$ of the $Ba_{6s^15d^1}(^1D)$ channel is also visually identifiable in Figure 1. Unlike the above mentioned avoided crossings this one would also be present in a non-relativistic or scalar relativistic calculation. The spin-orbit splitting of the calculated scalar-relativistic states is sizeable, in particular for the $^3\Delta$ and $^3\Pi$ states which are split into their $\Omega = 1, 2, 3$ and $\Omega = 0^+, 0^-, 1, 2$ components (see Figure 1 and Table 5). This splitting of the $^3\Delta$ and $^3\Pi$ into their Ω components is of 250 and 80 cm^{-1} respectively at the ground state equilibrium bond distance. While some of the Ω components are degenerate in the atomic limit because they belong to the same atomic J level, the molecular field gives a spin-orbit splitting also of these components. The $^3\Sigma^+$ state originating from the $Ba_{6s^15d^1}(^3D)$ channel exhibits very irregular behaviour due to avoided crossings, and it is therefore not meaningful to give an estimate of the molecular spin orbit splitting of this state.

Most of the electronically excited states exhibit strong multiconfigurational character and are thus more difficult to describe in a molecular orbital picture. We will therefore discuss their electronic structure in a more qualitative way. The lowest excited $\Omega = 0^-$ and $\Omega = 1$ states all correlate to a $^3\Sigma^+$ state in the Λ-S representation (see Table 3). In the dissociation limit their electronic structure corresponds to Ba^+ + Rb. At shorter nuclear distances more and more $Ba_{6s^15d^1_\sigma}(^3D)$ character is mixed in. In the Franck-Condon region the wave function has nearly equal contributions from these two configurations. At about 7.75 bohr the $^3\Sigma^+$ components undergo an avoided crossing with the $\Omega = 0^-$ and $\Omega = 1$ of a $^3\Pi$ state (see Figure 2). The $^3\Pi$ state has a significantly shorter equilibrium distance than the other states originating from the $Ba_{6s^15d^1}(^3D)$ +

Rb^+ channel (see Table 5). This can be traced back to the strong admixture of Ba $6p_\pi$ and Rb $5p_\pi$ character into the Ba $5d_\pi$ spinor.

The non-adiabatic interaction between the $^3\Sigma^+$ and $^3\Pi$ states is anticipated to have significant impact on the charge-transfer process. In the entrance channel the system is prepared initially in a highly excited vibrational level of the $^3\Sigma^+$ potential. At short internuclear separation the non-adiabatic interaction yields a finite probability for a non-radiative transition to the $^3\Pi$ potential which in turn can relax to the electronic ground state by emission of a photon.

At an internuclear distance of 15 to 16 bohr we see the $^1\Sigma^+$ of the entrance channel crossing the $\Omega = 0^+$ of a $^3\Pi$ state (see Figure 1). While formally it would not be allowed for two $\Omega = 0^+$ state to cross it appears that for this charge transfer process the non-adiabatic coupling matrix element or off diagonal element between the two states is so small we cannot visibly see any effect of it. A clear avoided crossing in the 12 to 13 bohr range between the $^1\Sigma^+$ and the higher lying $\Omega = 0^+$ of a $^1\Sigma^+$ from the $Ba_{6s^15d^1}(^1D)$ but also $\Omega = 0^+$ of a $^3\Pi$ of the $Ba_{6s^16p^1}(^3P)$ is observed. These avoided crossing helps making the $^1\Sigma^+$ of the entrance channel a metastable state which is in contrast to what is observed in the lighter homologs where this is a dissociative state.

The remaning states correlating with the ^3D channel are dominated by configurations in which the Ba $6d_\sigma$ spinor is singly occupied. As seen from Table 5 the Ω components of the $^3\Delta$ state are markedly split by spin-orbit, but exhibit equal equilibrium distances, indicating no differential spin-orbit coupling to other $^s\Lambda$ states.

3.4. Dipole moment

Finally, we show in Figure 3 the dipole moment curve of the molecular ground state of $(RbBa)^+$ calculated at the four-component CCSD(T) level with origin at the center of mass. The corresponding curve at the CCSD level (not shown) is almost identical, supporting that the CCSD(T) curve is converged. For a charge distribution corresponding purely to Rb^+ and and Ba a dipole moment of around 14 Debye could be expected at an internuclear separation of 8.75 bohr (see Fig. 3). Due to a partial electron transfer from Ba to Rb^+ (*cf.* dicussion in section 3.2), the dipole moment of the electronic ground state is significantly lower at the equlibrium distance. As seen in Table 6 we find a vibrationally averaged dipole moment of 4.53 Debey at the counterpoise corrected CCSD(T) level. Since the dipole moment function is almost linear around the rovibrational ground state we only see a minor difference between the vibrationally averaged dipole moment and the dipole moment taken at the electronic equilibrium distance as shown in Table 6. It should be noted that in perfect agreement with the theory, an asymptotic behavior of the dipole moment is obtained for large internuclear distances.

4. Summary and Prospects

In an earlier study on the valence isoelectronic system $(NaCa)^+$ of $(RbBa)^+$, a radiative lifetime of charge transfer in the order of 10^4 s to 10^6 s for the $A\ ^1\Sigma^+$ to the $X\ ^1\Sigma^+$ is found by Makarov *et. al* [9]. The $A\ ^1\Sigma^+$ (and most likely also the $a\ ^3\Sigma^+$) electronic states of $(NaCa)^+$ are thus very long-lived metastable species. This occurs since there is no close lying P states mixing into the excited Σ states, making both radiative transitions electric dipole forbidden and for the $a\ ^3\Sigma^+$ also spin forbidden. This is in great contrast to what is observed in $(RbBa)^+$. The non-adiabatic interaction in the short range of the potential (see Figure 2) between the $^3\Sigma^+_{1,0^-}$ and $^3\Pi_{1,0^-}$ states is expected to lead to a non-radiative charge transfer from the $^3\Sigma^+_{1,0^-}$ entrance channel to the $^3\Pi_{1,0^-}$ states. While transition from the $^3\Pi_{1,0^-}$ states to the ground state in $(RbBa)^+$ is also in a scalar-relativistic approximation electric dipole and spin forbidden, the large mixing of the Ba $5d_\pi$ with the close lying Ba $6p_\pi$ and Rb $5p_\pi$ spinors induced by spin-orbit coupling will greatly decrease the radiative lifetime.

The expected fast non-radiative charge transfer to the $^3\Pi_{1,0^-}$ states may not be experimentally desirable since it will irreversibly 'destroy' the Ba ion. Furthermore the shorter lifetime of the $^3\Pi_{1,0^-}$ states may not be long enough to consider the states metastable for all experiments in question [11]. With the transition dipole moments it would be possible to go from the present qualitative analysis to more quantitative predictions of life times. This is clearly of interest, and this has prompted us to start the development of a MRCI transition dipole moment module [40]. Since Ba is a special case among the alkaline earth metals with its low lying D shell it presents a unique opportunity to study non-radiative charge transfer processes in the excited state manifold thereby making $(RbBa)^+$ experimentally very interesting.

The $(RbBa)^+$ ground state is found to form a partially covalent polar bond stronger than expected. While the dissociation energy is comprable to the LiCs alkali dimer the harmonic frequency is only one third of the LiCs value, showing that the two bonds are significantly different. The broader $(RbBa)^+$ potential shows the longer ranging charge induced dipole interaction against the neutral dissociation of LiCs. We furthermore show that the electronic ground state possesses a dipole moment significantly smaller than what a charge-dipole interaction would lead one to expect. We attribute this finding to a partial charge transfer from Ba to Rb^+.

In this study we demonstrate the capability of our relativistic all-electron quantum-chemical methodology to yield accurate ground and excited states. We show that these methods are capable of handling both neutral and complex ionized systems from the atomic limit all the way in the short range potential. This is seen from the accurate differential ionization potential ΔIP, atomic excitation energies and fine structure splitting but it is primarily the ability to handle the complicated excited state potentials of highly multiconfigurational character. We show that with our chosen MRCI model we can handle the above along with reproducing the accurate CCSD(T) data for the spectroscopic properties of the ground state.

Acknowledgments

Financial support of this project by the Deutsche Forschungsgemeinschaft (reference number FL 256/5-1), SFB 663 and through the priority program SPP 1145, grant no. FL 356/2 is greatfully acknowledged. A generous allotment of computing time from the Danish Center for Scientific Computing is gratefully acknowledged. Further computational support and infrastructure was provided by the "Zentrum fuer Informations- und Medientechnologie" (ZIM) at the Heinrich Heine University Düsseldorf (Germany).

Table 1. Spectroscopic values for the $\Omega = 0^+$ ground state calculated at the spin-dependent MRCI S12_(2in13)_SD level in comparison to CC results, both at the spin-free (SF) and spin-dependent levels, and results from earlier spin-free MRCI SF-SD16_(2in7)_SD where an ANO-RCC basis was used and with a truncation of the virtual space at 5 E_h. Counterpoise corrections ("cp-" prefix) have also been tested.

Method	R_e[bohr]	ω_e [cm^{-1}]	D_e [cm^{-1}]
SF-SD16_(2in7)_SD [14]	8.75	54.327	5509
S12_(2in13)_SD	8.72	51.773	5055
SF-CCSD	8.80	52.171	4887
CCSD	8.80	52.187	4886
SF-CCSD(T)	8.75	52.785	5035
CCSD(T)	8.75	52.799	5034
cp-SF-CCSD	8.81	52.145	4877
cp-CCSD	8.80	52.161	4876
cp-SF-CCSD(T)	8.76	52.755	5023
cp-CCSD(T)	8.76	52.768	5022

Table 2. Spectroscopic values for the $\Omega = 0^+$ ground state calculated with the spin-free (SF) CCSD and CCSD(T) methods, with an energy truncation threshold for active virtual spinors at 18 and 42 Hartree, and using the Visscher small component approximation[31].

Method	Virtuals truncation	R_e[bohr]	ω_e [cm^{-1}]
SF-CCSD	18	8.8027	52.179
SF-CCSD	42	8.8025	52.179
SF-CCSD(T)	18	8.7528	52.794
SF-CCSD(T)	42	8.7526	52.795

Table 3. A selection of molecular electronic states in the $\Lambda - S$ coupling picture and associated atomic dissociation channels in an energy range of up to ≈ 14000 cm^{-1}.

Atomic $^{(2S+1)}L_J$	Molecular $^{(2S+1)}\Lambda_\Omega$
$Rb^+_{5s^0}$ ($^1S_0$) + Ba_{6s^2} ($^1S_0$)	$^1\Sigma^+_{0^+}$
Rb_{5s^1} ($^2S_{1/2}$) + $Ba^+_{6s^1}$ ($^2S_{1/2}$)	$^3\Sigma^+_{1,0^-}$, $^1\Sigma^+_{0^+}$
$Rb^+_{5s^0}$ ($^1S_0$) + $Ba_{6s^15d^1}$ ($^3D_{1,2,3}$)	$^3\Delta_{3,2,1}$, $^3\Pi_{2,1,0^+,0^-}$, $^3\Sigma^+_{1,0^-}$
$Rb^+_{5s^0}$ ($^1S_0$) + $Ba_{6s^15d^1}$ ($^1D_2$)	$^1\Delta_2$, $^1\Pi_1$, $^1\Sigma^+_{0^+}$
$Rb^+_{5s^0}$ ($^1S_0$) + $Ba_{6s^16p^1}$ ($^3P_{0,1,2}$)	$^3\Pi_{2,1,0^+,0^-}$, $^3\Sigma^+_{1,0^-}$

Table 4. Excitation energies T in cm^{-1} for the lowest $Ba_{6s^2}(^1S_0) \rightarrow Ba_{6s^15d^1}(^3D_{1,2,3})$, $Ba_{6s^2}(^1S_0) \rightarrow Ba_{6s^15d^1}(^1D_2)$ and $Ba_{6s^2}(^1S_0) \rightarrow Ba_{6s^16p^1}(^3P_{0,1,2})$, electronic transitions calculated at the atomic MRCI S6_(2in9)_SD and atomic-like S12_(2in13)_SD (molecular calculation; values taken at $R = 50$ bohr) levels. The active space in the atomic calculation includes the same Ba shells and the same truncation threshold for the virtual spinors as in the molecular case. Details on the molecular computational level are given in the text. The MRCI results are compared to previous theoretical and experimental data. In the atomic-like "J states" (Ω) the individual M_j components are almost degenerate at $R = 50$ bohr with deviations on the order of $4-8$ cm^{-1} from the lowest to highest M_j component. We here show the energies of the lowest M_j values in the table.

	$^1S_0$	$^3D_{1,2,3}$			$^1D_2$	$^3P_{0,1,2}$		
Method	$J=0$	$J=1$	$J=2$	$J=3$	$J=2$	$J=0$	$J=1$	$J=2$
Experiment [41]	0	9034	9216	9597	11395	12266	12637	13515
Atomic calculations								
S6_(2in9)_SD	0	8627	8809	9175	11197	12732	13091	13944
FSCCSD [36]	0	9075	9260	9639	11621	12423	12802	13793
IHFSCCSD [36]	0	9117	9296	9677	11426	12397	12728	13610
Molecular calculation at $R = 50$ bohr								
S12_(2in13)_SD	0	8619	8812	9174	11198	12736	13109	13936

Table 5. Spectroscopic constants for the ground and lowest excited states (Ω designation) of $(RbBa)^+$ calculated at the MRCI S12_(2in13)_SD level with 14 explicitly correlated electrons.

State	Ω	$\Lambda - S^a$	R_e [bohr]	ω_e [cm^{-1}]	D_e [cm^{-1}]	T_v [cm^{-1}]	T_e [cm^{-1}]
1	0^+	$^1\Sigma^+$	8.72	52	5055	0	0
2	0^-	$^3\Sigma^+$	9.22	45	6889	6711	6621
3	1	$^3\Sigma^+$	9.22	45	6871	6737	6638
4	0^+	$^3\Pi$	8.28	52	5899	7865	7775
5	0^-	$^3\Pi$	8.40	53	5980	7939	7878
6	1	$^3\Pi$	8.28	56	5742	8022	7932
7	2	$^3\Pi$	8.28	52	6702	8109	7156
8	1	$^3\Delta$	9.22	43	4302	9653	9556
9	2	$^3\Delta$	9.22	43	4500	9809	9721
10	3	$^3\Delta$	9.22	43	4157	10165	10064
11	2	$^1\Delta$	9.22	43	5887	10440	10365
12	1	$^3\Sigma^+$	9.22	37	2258	12047	11963
13	0^-	$^3\Sigma^+$	9.03	44	2216	12053	12005
14	0^+	$^1\Sigma^+$	9.77	39	-	13030	12601
15	1	$^1\Pi$	9.72	40	3566	13112	12687

[a] leading $\Lambda - S$ projection

Table 6. Dipole moments at R_e (μ_e) and the vibrationally averaged dipole moment μ_v for the CCSD and CCSD(T) levels of theory and with counterpoise (cp) corrected values.

Method	μ_e [D]	μ_v [D]
SF-CCSD	4.528	4.550
cp-SF-CCSD	4.533	4.556
SF-CCSD(T)	4.507	4.528
cp-SF-CCSD(T)	4.514	4.534

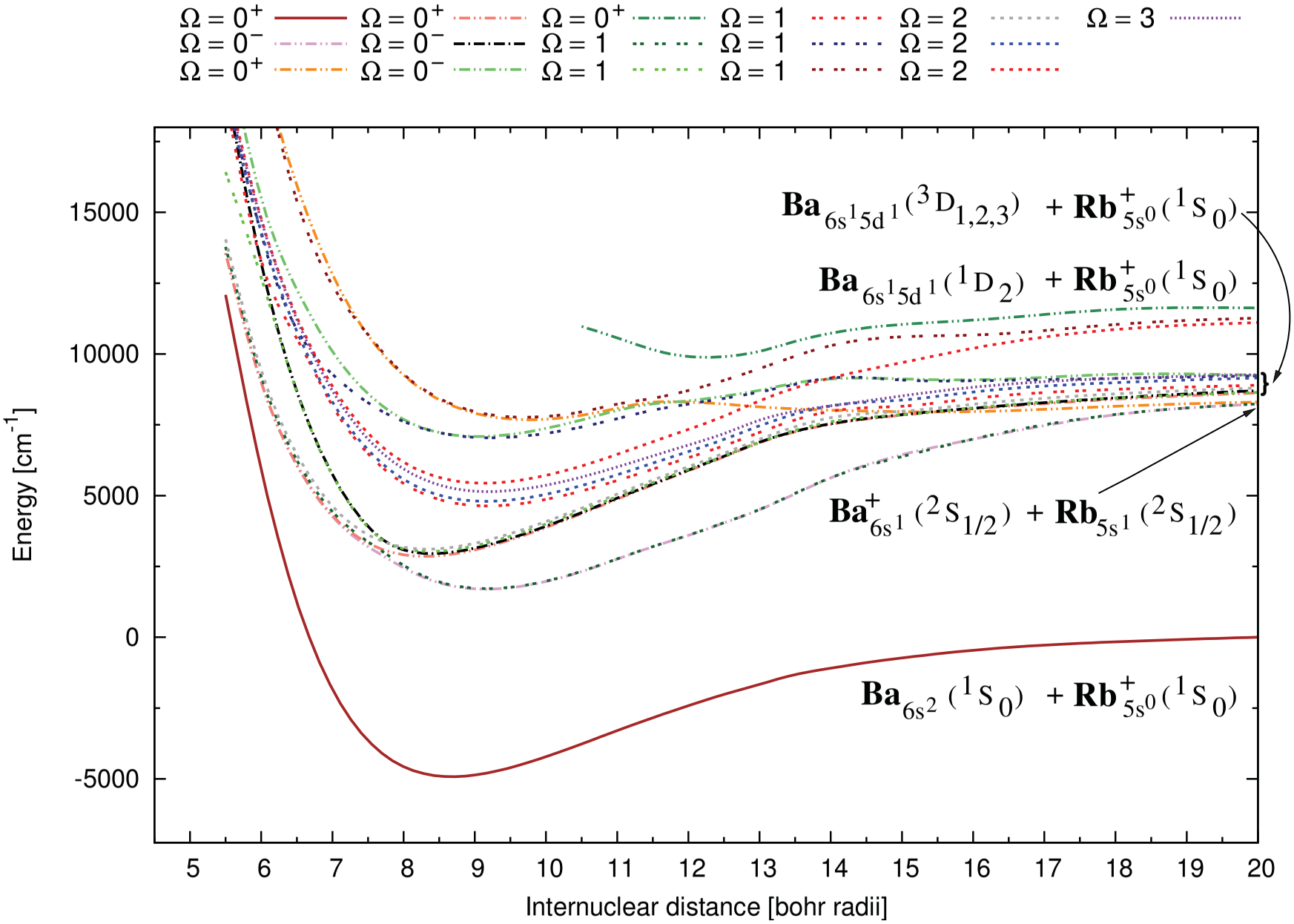

Figure 1. Potential energy curves of the ground and low-lying states (Ω designation) of $(RbBa)^+$ computed at the four-component MRCI S12_(2in13)_SD level (see text for more details). Atomic dissociation channels for the states are indicated in the picture (see Table 3 for details).

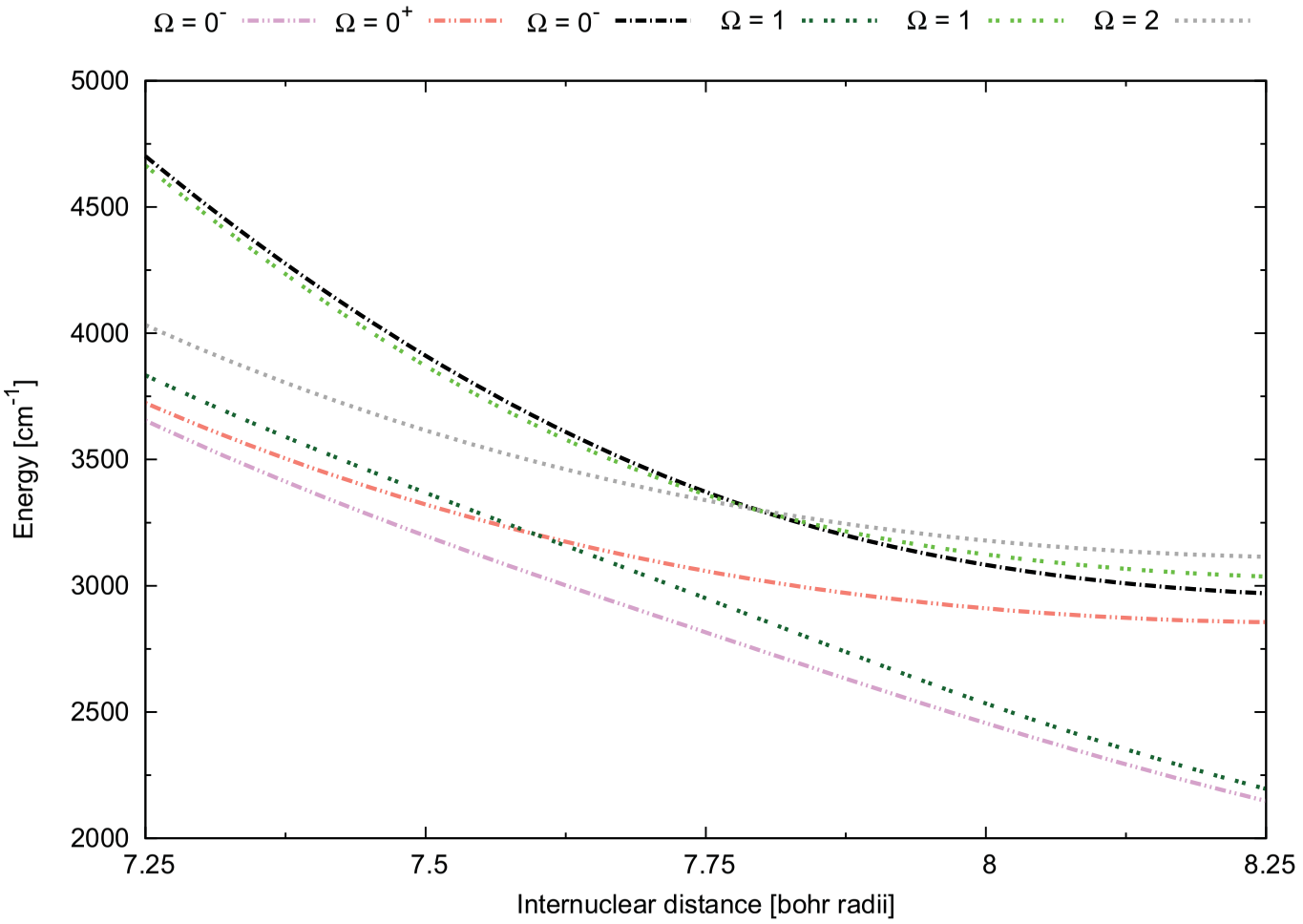

Figure 2. Close up of the avoided crossings between the $^3\Sigma^+_{1,0^-}$ Rb + Ba^+ entrance channels and and low-lying charge transfer $^3\Pi_{1,0^-}$ states of the Rb^+ and $Ba_{6s^15d^1}(^3D)$ atomic channels.

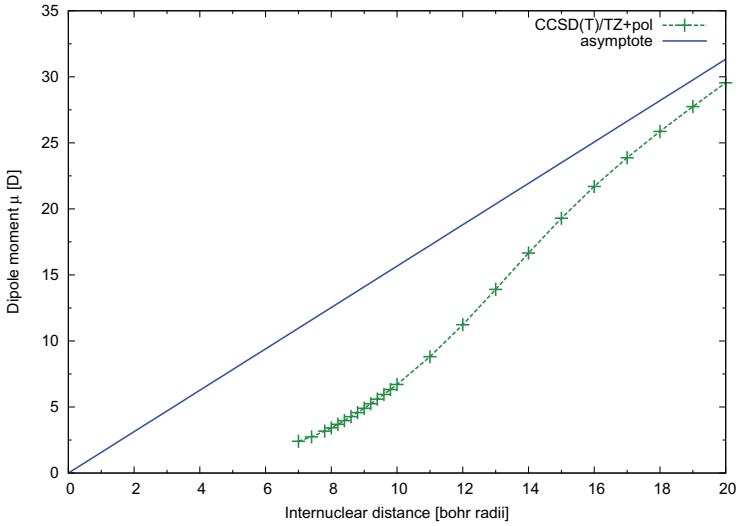

Figure 3. Four-component CCSD(T) dipole moment curve (in Debye) of the molecular ground state with calculated with 14 explicitly correlated electrons. The straight line (blue) indicates the asymptotic limit of the dipole moment μ for a charged system in the center-of-mass coordinates.

[1] J Doyle, B Friedrich, R V Krems, and F Masnou-Seeuws. Quo vadis, cold molecules? *Eur. Phys. J. D*, 31:149, 2004.

[2] J J Hudson, B E Sauer, M R Tarbutt, and E A Hinds. Measurement of the Electron Electric Dipole Moment Using YbF Molecules. *Phys. Rev. Lett.*, 89:023003, 2002.

[3] B C Regan, E D Commins, C J Schmidt, and D DeMille. New Limit on the Electron Electric Dipole Moment. *Phys. Rev. Lett.*, 88:071805, 2002.

[4] S Schiller and V Korobov. Tests of time independence of the electron and nuclear masses with ultracold molecules. *Phys. Rev. A*, 71:032505, 2005.

[5] E Bodo and F A Gianturco. Ultra low-energy behavior of an ionic replacement reaction $^3He^4He^+ + {}^4He \rightarrow {}^4He_2^+ + {}^3He$. *Phys. Rev. A*, 73:032702, 2006.

[6] R Côté and A Dalgarno. Ultracold atom-ion collisions. *Phys. Rev. A*, 62:012709, 2000.

[7] P E Siska. Cold and ultracold ion-neutral inelastic collisions: Spin-orbit relaxation in He + Ne^+. *J. Chem. Phys.*, 115:4527, 2001.

[8] E Wells, K D Carnes, B D Esry, and I Ben-Itzhak. Charge Transfer and Elastic Scattering in Very Slow H^++D(1s) Half Collisions. *Phys. Rev. Lett.*, 86:4803, 2001.

[9] O. P. Makarov, R. Côté, H. Michels, and W. W. Smith. Radiative charge-transfer lifetime of the excited state of $(NaCa)^+$. *Phys. Rev. A*, 67:042705, 2003.

[10] R. Coté, V. Kharchenko, and M. D. Lukin. Mesocopic molecular ions in Bose-Einstein condensates. *Phys. Rev. Lett.*, 89:093001, 2002.

[11] J. Hecker Denschlag. University of Innsbruck (now University of Ulm), private communication, 2009. Project BaRbIe: An ion in a sea of ultracold neutral atoms, see also http://www.uibk.ac.at/exphys/ultracold/projects/barbi/index.html.

[12] M. Sabidó, J. de Andrés, J. Sogas, M. Alberti, J. M. Bofill, and A. Aguilar. Inelastic electronic excitation and electron transfer processes in collisions between $Mg(3^1S_0)$ atoms and $K^+(^1s_0)$ ions studied by crossed beams in the 0.10-3.80-kev energy range. *J. Chem. Phys.*, 123:124314, 2005.

[13] M. Sabidó, J. de Andrés, J. Sogas, M. Alberti, J. M. Bofill, and A. Aguilar. Crossed ion-atom beam study of the inelastic collision processes between neutral $Mg(3^1S_0)$ atoms and $Cs^+(^1s_0)$ ions in the 0.05-4.20 kev energy range. *Phys. Chem. Chem. Phys.*, 7:310, 2005.

[14] S Knecht, H J Aa Jensen, and T Fleig. Large-scale parallel configuration interaction. I. Nonrelativistic and scalar-relativistic general active space implementation with application to $(Rb-Ba)^+$. *J. Chem. Phys.*, 128:014108, 2008.

[15] L Visscher, K G Dyall, and T J Lee. Kramers-restricted closed-shell CCSD theory. *Int. J. Quantum Chem.: Quantum Chem. Symp.*, 29:411, 1995.

[16] L Visscher, T J Lee, and K G Dyall. Formulation and implementation of a relativistic unrestricted coupled-cluster method including noniterative connected triples. *J. Chem. Phys.*, 105:8769, 1996.

[17] DIRAC, a relativistic ab initio electronic structure program, Release DIRAC08 (2008), written by L. Visscher, H. J. Aa. Jensen, and T. Saue, with new contributions from R. Bast, S. Dubillard, K. G. Dyall, U. Ekström, E. Eliav, T. Fleig, A. S. P. Gomes, T. U. Helgaker, J. Henriksson, M. Iliaš, Ch. R. Jacob, S. Knecht, P. Norman, J. Olsen, M. Pernpointner, K. Ruud, P. Sałek, and J. Sikkema (see http://dirac.chem.sdu.dk).

[18] K G Dyall. An exact separation of the spin-free and spin-dependent terms of the Dirac-Coulomb-Breit Hamiltonian. *J. Chem. Phys.*, 100:2118, 1994.

[19] L K Sørensen, T Fleig, and J Olsen. Spectroscopic and Electric Properties of the LiCs Molecule. A Coupled Cluster Study Including Higher Excitations. *J. Phys. B*, 42:165102, 2009.

[20] S Knecht, H J Aa Jensen, and T Fleig. Large-scale parallel configuration interaction. II.Four-component double-group general active space implementation with application to BiH, 2009. Submitted.

[21] T Fleig, J Olsen, and C M Marian. The generalized active space concept for the relativistic treatment of electron correlation. I. Kramers-restricted two-component configuration interaction.

J. Chem. Phys., 114:4775, 2001.

[22] T Fleig, J Olsen, and L Visscher. The generalized active space concept for the relativistic treatment of electron correlation. II: Large-scale configuration interaction implementation based on relativistic 2- and 4-spinors and its application. *J. Chem. Phys.*, 119:2963, 2003.

[23] T Fleig, H J Aa Jensen, J Olsen, and L Visscher. The generalized active space concept for the relativistic treatment of electron correlation. III: Large-scale configuration interaction and multi-configuration self-consistent-field four-component methods with application to UO_2. *J. Chem. Phys.*, 124:104106, 2006.

[24] J. Thyssen, T. Fleig, and H. J. Aa. Jensen. A direct relativistic four-component multi-configuration self-consistent-field method for molecules. *J. Chem. Phys.*, 129:034109, 2008.

[25] S. Knecht, H. J. Aa Jensen, and L. K. Sørensen. Four-component MP2 natural orbitals: An efficient way of selecting appropiate active spaces for coupled cluster and multiconfigurational self-consistent field calculations, 2009. unpublished work.

[26] Stefan R. Knecht. *Parallel Relativistic Multiconfiguration Methods: New Powerful Tools for Heavy-Element Electronic-Structure Studies.* Dissertation, Mathematisch-Naturwissenschaftliche Fakultät, Heinrich-Heine-Universität Düsseldorf, 2009.

[27] L. K. Sørensen, S. Knecht, T. Fleig, and C. M. Marian. Four-Component Relativistic Coupled Cluster and Configuration Interaction Calculations on the Ground and Excited States of the RbYb Molecule. *J. Phys. Chem. A*, 2009. (8 pages) *Available online*, DOI: 10.1021/jp904914m.

[28] L Visscher and T Saue. Approximate relativistic electronic structure methods based on the quaternion modified Dirac equation. *J. Chem. Phys.*, 113:3996, 2000.

[29] K.G. Dyall. Relativistic double-zeta, triple-zeta, and quadruple-zeta basis sets for the 4s, 5s, 6s, and 7s elements. *J. Phys. Chem. A*, page in press, 2009. (8 pages) *Available online*, DOI: 10.1021/jp905057q. Basis sets available from the Dirac web site, http://dirac.chem.sdu.dk.

[30] I. S. Lim, H. Stoll, and P. Schwerdtfeger. Relativistic small-core energy-consistent pseudopotentials for the alkaline-earth elements from Ca to Ra. *J. Chem. Phys.*, 124:034107, 2006.

[31] L Visscher. Approximate molecular relativistic Dirac-Coulomb calculations using a simple Coulombic correction. *Theoret. Chem. Acc.*, 98:68, 1997.

[32] S F Boys and F Bernardi. The calculation of small molecular interactions by the differences of separate total energies. Some procedures with reduced errors. *Mol. Phys.*, 19:553, 1970.

[33] Andrzej Sadlej. Program WFFIT. University of Torun.

[34] Jr. C. W. Bauschlicher, S. P. Walch, and H. Partridge. On correlation in the first row transition metal atoms. *J. Chem. Phys.*, 76:1033–1039, 1982.

[35] L. Visscher, E. Eliav, and U. Kaldor. Formulation and implementation of the relativistic Fock-space coupled cluster method for molecules. *J. Chem. Phys.*, 115(21):9720–9726, 2001.

[36] A. Landau, E. Eliav, Y. Ishikawa, and U. Kaldor. Intermediate Hamiltonian Fock-space coupled-cluster method: Excitation energies of barium and radium. *J. Chem. Phys.*, 113:9905–9910, 2000.

[37] A. Landau, E. Eliav, Y. Ishikawa, and U. Kaldor. Intermediate Hamiltonian Fock-space coupled cluster method in the one-hole one-particle sector: Excitation energies of xenon and radon. *J. Chem. Phys.*, 115:6862–6865, 2001.

[38] *NIST Chemistry WebBook* (version 69, 2005) National Institute of Standards and Technology, Gaithersburg, MD.

[39] P Staanum, A Pashov, H Knöckel, and E Tiemann. $X^1\Sigma^+$ and $a^3\Sigma^+$ states of LiCs studied by Fourier-transform spectroscopy. *Phys. Rev. A*, 75:042513, 2007.

[40] S. Knecht and H. J. Aa Jensen. A general-purpose parallel four-component Kramers-restricted CI property module. unpublished work.

[41] Y. Ralchenko, A. E. Kramida, J. Reader, and NIST ASD Team (2008). NIST Atomic Spectra Database (version 3.1.5). Available: http://physics.nist.gov/asd3 (retrieved May 3rd, 2009). National Institute of Standards and Technology, Gaithersburg, MD.